This electronic thesis or dissertation has been downloaded from the King's Research Portal at https://kclpure.kcl.ac.uk/portal/



Strong correlations in Lanthanide Interfaces and Metal Oxides

Banerjee, Debalina

Awarding institution:
King's College London

The copyright of this thesis rests with the author and no quotation from it or information derived from it may be published without proper acknowledgement.

END USER LICENCE AGREEMENT



Unless another licence is stated on the immediately following page this work is licensed

under a Creative Commons Attribution-NonCommercial-NoDerivatives 4.0 International

licence. https://creativecommons.org/licenses/by-nc-nd/4.0/

You are free to copy, distribute and transmit the work

Under the following conditions:

- Attribution: You must attribute the work in the manner specified by the author (but not in any way that suggests that they endorse you or your use of the work).
- Non Commercial: You may not use this work for commercial purposes.
- No Derivative Works - You may not alter, transform, or build upon this work.

Any of these conditions can be waived if you receive permission from the author. Your fair dealings and other rights are in no way affected by the above.

Take down policy

If you believe that this document breaches copyright please contact librarypure@kcl.ac.uk providing details, and we will remove access to the work immediately and investigate your claim.

Download date: 08. Oct. 2023

Strong correlations in Lanthanide Interfaces and Metal Oxides

DEBALINA BANERJEE

Department of Physics



This dissertation is submitted for the degree of Doctor of Philosophy

December 2022

Abstract

A complete canonical description for why the world and its constituents behave the way they do is a daunting undertaking. Unexpectedly it is so even though the nature and the mathematical form of electronic interactions that account for the energy scales relevant for everyday life, and by that scope the realm of condensed matter physics and material science, have been known for about a century now. The difficulty is that for a collection of large number of many-body entities which can be electrons or atoms, emergent phenomena arise with features that cannot be comprehended by the underlying laws. This makes the contemporary theoretical condensed matter research dealing with electronic structures a scientific exercise in comparison of various levels of approximations.

The primary overarching challenge to the theoretical understanding of materials can be attributed to the mathematical and computational complexity that arises in the calculation of the electron-electron interaction term in a realistic set-up. When the effect of this term dominates the behaviour of a material, the material is said to be strongly correlated. One such class of materials are lanthanides and lanthanide metal oxides. Lanthanide compounds are usually associated with a complex phase diagram often involving metal-insulator transitions under a range of conditions viable for industrial applications where mean-field approaches fail. This thesis addresses the realistic modelling of their electronic structure in bulk and as thin films taking into account the effects of interfaces as is needed for understanding the origin of observed behaviours and their applications.

We start with a discussion of the various models, approximations, and formalism used throughout this thesis. We further follow it with the study of a model 4-layer correlated interface described by a Hubbard-like Hamiltonian intending to set the premise for realistic calculations. We analyse how the interplay of various kinetic energy terms and strong correlations influence the observation of Mott transition in this model system. We interpret this simplified set-up as a quantum double-well and investigate the impact of correlations and bias on resonant tunnelling conditions.

Following this we study Samarium monochalcogenides which show a pressure induced isostructural insulator to metal transition characterised by the presence of an intermediate valence state at higher pressure that cannot be captured by density functional theory. These materials, particularly SmS and SmSe, have been proposed to

serve as the piezoresistive component of an alternative form of technology that uses piezoelectric transistors. This transistor operation is based on the compression of the piezoresistive component by the piezoelectric part which undergoes an insulator to metal transition either continuously or discontinuously and therefore can serve as switches or memory elements, respectively.

The failure of the mean-field corrections incorporated within density functional theory is ascribed to the presence of strongly correlated Sm-$4f$ orbitals which lead us to the use of dynamical mean field theory corrections. As a direct outcome of including the charge and spin fluctuations incorporated in dynamical mean field theory framework within the scope of the Hubbard-I approximation, we see the emergence of insulating and metallic phases with increasing pressure as a function of changing valence. This is accompanied by significantly improved predictions of the equilibrium lattice constants and bulk moduli for SmS, SmSe, and SmTe verifying experiments. We then perform nudged elastic band analysis that reveals that the insulating states are characterised by a finite quasiparticle weight that decreases as the gap closes with pressure rendering the transition to be not Mott-like. As a result, our work classifies these materials as correlated band insulators.

Since we observe the $4f$ electrons becoming more localised in their high pressure metallic state, we study their behaviour in a piezoresistive element-like set-up where we simulate a few layers of Sm-monochalcogenides in a heterostructure set up with tungsten leads. We find that in the thin film configuration where the transport mechanism becomes tunnelling, the $4f$ electrons do participate in transmission at and around the Fermi level and thus applying the appropriate level of theory is crucial to the prediction of length scales for their use as piezoresistive elements. We analyse the behaviour of the f-states around the interface, obtain the transmission through the junction at equilibrium and compare transmission ratios at different junction length scales to define an OFF state for the use of SmSe as a piezoresistive element in transistor type operations.

We then look at lanthanum metal oxides and the role of correlations and defects in determining their experimentally observed properties. The first set of such materials investigated are two double perovskites La_2TiFeO_6 and La_2VCuO_6 which are candidates for promising spintronic applications if the charge ordering between Ti-Fe and V-Cu could be controlled experimentally. However after obtaining these structures with pulsed laser deposition and studying their properties experimentally, no ordered phases could be found and only partial charge transfer could be observed. We first study their ground state properties that show a competition between two different charge transfer type phases are responsible for the observed disorder in La_2VCuO_6. For La_2TiFeO_6, we employ random structure search and find that multiple low lying phases with comparable frequencies lead to a high configurational entropy. On studying the entropy forming ability of all 400 optimised structures, we find that the disorder and accompanying partial charge transfer so observed experimentally could be attributed to the high value

of configurational entropy which is enhanced by the presence of Lanthanum vacancies to a larger extent and also over oxygenation to a lesser extent.

Finally we consider CeO_2 and its mixed metal oxide with Zr doping called zirconia to understand and compare the role of oxygen vacancies that leads to their use as heterogeneous catalysts. We compare the qualitative and quantitative results from density functional theory with and without incorporation of a static Coulomb repulsion term to account for the strong electronic correlations in Ce. We compute formation energies for oxygen defects and find that both DFT and DFT+U show Zr adsorbed on CeO_2 is energetically favourable for vacancy formation although surprisingly the inclusion of the effect of correlations in the DFT+U framework reduces this favourability. However this is restored on including the effect of lattice dynamics stemming from the observation of soft phonon mediated symmetry breaking that facilitates this vacancy formation along with an increase in effective mass.

The research elaborated in this thesis emphasises the role of different levels of state-of-the-art theoretical methods in incorporating the effect of strong correlations. We comment on the success of these approaches in determining structural transitions, associated device scaling, and vacancy effects for various ongoing industry relevant applications using lanthanides in bulk, as thin films, and lanthanide metal oxides, respectively. This provides an overview for conceptual understanding of the impact of many-body effects in the design and use of these materials for practical applications.

to ***Luna*** *&* ***Debasis***

মা ও বাপি কে

Declaration

I declare that the work contained in this dissertation was carried out by myself except where explicitly stated otherwise and has been written by myself. The research was conducted between October 2018 and December 2022 at the department of Physics, Kings College London under the supervision of

- Dr Cédric Weber (first supervisor) and Prof. Mark van Schilfgaarde (second supervisor) between October 2018 and January 2022
- Prof. Mark van Schilfgaarde (first supervisor), Dr Joe Bhaseen (second supervisor) and Dr Cédric Weber (third supervisor) between January 2022 and December 2022
- Dr Ivan Rungger (National Physical Laboratory supervisor)

This thesis is submitted to the King's College London in accordance with the requirements for award of the degree of Doctorate of Philosophy. It has not been submitted for any other degree or professional qualification. The copyright of this thesis rests with the author and no quotation from it or information derived from it may be published without proper acknowledgement.

This PhD was funded by Engineering and Physical Sciences Research (EPSRC) through the NPIF grant [EP/R512552/1] and the CANES CDT grant [EP/L015854/1] and was associated with the EU Horizon2020 research and innovation programme within the PETMEM project [No.688282].

A part of the work done during this PhD was in collaboration with teams working with the Innovate UK programme via the QUANTIFI project [Reference: 133986].

The industrial collaborations that formed a part of this thesis are listed below with an explicit mention of the contributions made and softwares used by me and by collaborators involved in the project.

1. National Physical Laboratory
   Hampton Road, Teddington, Middlesex, TW11 0LW
   Tel: 020 8977 3222

   - **Debalina Banerjee**: SIESTA (DFT, DFT+U) simulations and analysis
   - (NPL Supervisor) Dr Ivan Rungger: SMEAGOL simulations and analysis

2. Happy Electron
   32 Telford Way, London, W3 7XS, UK
   (Merged with Arrival, Beaumont House, Kensington Village, London W14 8TS)

   - **Debalina Banerjee**: Quantum Espresso (DFT, DFPT), thermo_pw, AIRSS simulations and analysis
   - (Happy Electron supervisor) Dr Edoardo Fertitta: Quantum Espresso, AIRSS, analysis
   - Sample preparation and analysis: Dr Sujit Das
   - Other experimental work and analysis: Dr Farbod Ebrahimi, Dr Kai Du, Dr He Tian
   - Research design: Prof. Peter Littlewood, Prof. Chris J. Pickard, Prof. Ramamoorthy Ramesh, Dr Clément Barraud, Dr David Dubbink, Dr Cédric Weber

3. Johnson Matthey Technology Centre
   Blounts Ct Rd, Sonning Common, Reading RG4 9NH, UK
   &
   Rahko Limited
   46 Clifton Terrace, Finsbury Park, London N4 3JP, UK
   &
   Amazon Web Services
   EMEA Sarl, UK Branch, 1 Principal Place, Worship Street, London, EC2A 2FA, UK

   - **Debalina Banerjee**: VASP (DFT, DFT+U, DFPT), Questaal (QSGW) simulations and analysis
   - Dr Rachel N. Kerber and Dr Pál D. Mezei: Quantum Espresso, DCore and project charge
   - Dr Christopher Downing: Quantum Espresso
   - Dr Dimitar Pashov: Questaal
   - Research design: Dr Glenn Jones, Dr Cédric Weber
   - *NOTE: Results obtained with DCore and Questaal have not been reported in this thesis.*

This dissertation contains material appearing in the following articles:

- *Study of disorder in pulsed laser deposited double perovskite oxides by first-principle structure prediction*
  Edoardo Fertitta, Sujit Das, **Debalina Banerjee**, Farbod Ebrahimi, Clément

Barraud, Kai Du, He Tian, Chris J. Pickard, Cedric Weber, Ramamoorthy Ramesh, Peter Littlewood and David Dubbink
npj Computational Materials volume 7, Article number: 92 (2021)

- *Pressure-induced electronic transitions in samarium monochalcogenides*
  Debalina Banerjee, Evgeny Plekhanov, Ivan Rungger, and Cedric Weber
  Phys. Rev. B 105, 195135 (2022)

- *Transmission across Samarium monochalcogenide based thin film heterostructures*
  Debalina Banerjee, Ivan Rungger
  (in preparation)

- *Density functional theory and dynamical mean field theory study of catalytically relevant d and f-type transition metal oxides*
  Rachel N. Kerber, Pál D. Mezei, Christopher Downing, **Debalina Banerjee**, Dimitar Pashov, Cédric Weber, Glenn Jones
  (in preparation)

Debalina Banerjee
December 2022

Acknowledgements

When I look back at the past four years, I realise that this thesis, would not have been possible without the help and support of many people, and I am forever grateful. First and foremost, to my previous first supervisor Dr Cedric Weber under whose guidance most of my PhD journey was spent. I am thankful for the opportunity to work on various interesting projects which shaped my scientific vision. In seeming deadlocks Cedric always found the next thing to try, another outlook to investigate. He inspired me to look beyond the immediateness of my field and to strive to connect the dots. I would then thank my NPL supervisor Dr Ivan Rungger for showing me the ropes and answering my questions patiently at a time they were still forming shape. The experience of working at NPL with him gave me a first-hand perspective of how science in industry works and taught me the importance of being aware of the audience when discussing my research. Thanks to Prof Mark van Schilfgaarde, my current first supervisor for shouldering the academic responsibilities at a very crucial stage. I express my heartfelt gratitude to Dr Jan M. Tomczak for his guidance and presence during the last year of my PhD. Jan's feedback during this year and his patient consideration of an apprentice scientist's ideas has inspired me to be a physicist like him. I am thankful to my thesis examiners, Dr Gilberto Teobaldi and Dr Andrea Floris, for accepting the roles, the very interesting discussion during the thesis defence and valuable feedback on the research conducted.

I would thank Dr Edoardo Fertitta, my internship supervisor at Happy Electron who motivated me to have a structured approach towards research. I am indebted to Dr Rachel Kerber at Johnson Matthey for finding time even in her very busy schedule during the last stretch of my thesis. From an accomplished woman scientist like her I learnt the virtue of kindness. I am also grateful to Dr Hrishit Banerjee for his advice and remarks on my thesis, for always answering my questions patiently and adding another layer of insight to them. I would thank Dr Dimitar Pashov and Dr Evgeny Plekhanov for their support during various projects. My gratitude extends to all my collaborators whose feedback shaped my scientific vision. My appreciation extends to Dr Joe Bhaseen and Dr Chris Lorenz of the CANES CDT for their constant encouragement and for providing a stimulating multi-disciplinary environment. A big thanks to our amazing CANES centre managers Dr Valeria De Marco, Dr Jemma Trick, and the brilliant Joanna Pauk, for their timely and proficient help and support throughout.

I would acknowledge EPSRC, UKRI, NPL, the EU Horizon2020 programme and the PETMEM project for providing financial support during the PhD, and indirect support from the Innovate UK programme via the QUANTIFI project. I extend my gratitude to the support teams at the HPC services ARCHER, CSD3, King's HPC facilities CREATE and Gravity, the UK MMM HPC hubs Young and Thomas.

My deepest thanks to my therapist, Lynette Pitre. A PhD is a character-building endeavour that demands one to take their mental health seriously. Having a constructive dynamic with Lynette has helped me cultivate the much-needed life-skills to be a better scientist.

Now to my lovelies, my friends. First in this line of appreciation is, undoubtedly, and definitely, Matt, one of my best friends, my confidant, colleague, advisor, one of the most gifted and intelligent people I know, a fellow cafe haunt-er and almost-more-vigorous-than-me-now chai enthusiast. When I am old and sixty and looking back at this time, I will remember our first conversations on science, PhD, mental health and life, words of wisdom worth at least fifty years from a boy who looked fifteen. You are the best thing about London! A big heart for Sigrid, my first friend in London crafted with carefully curated German perfection, a better-than-Indian spice tolerance, and the most heartfelt greeting card messages with an extra hour for choosing where to eat. Dánke to Basita. We (re-)started and are finishing our academic journeys together. You inspire me to aim higher and work harder. Blagodarya to Elena, for being the happy laughter to my cynical satire and the pepper tears to my chai. An equally weighted combination of inshallah, mashallah and alhamdulliah to THE cheese-lover Araf, for being the kid whom initially I had to keep alive from Araf-designed accidents but who then reincarnated into my dearest friend who checked up on bad days, discussed Green's functions and made elaborate plans that we both eventually and definitely cancelled. Thanks to Pastor Sarah for her infinite enthusiasm for life, and efforts in keeping our diverse world together and a happy place. Your rational but still loving attitudes to life have sometimes stopped me, from flowing away with the waves to the sea(!), a part-time PhD hobby.

Thanks to Nadia, Sarbajaya, Monalisa Di, Semanti, Madhurima, and Sanchari. Love to Amal, Sabir and Sanchi, for always being there. Thanks to Mayank, Soumik, Sriluckshmy for being the touch of home in England. A thankful shoutout to my group mates at Kings, Evan, Francois, Hovan, Zelong, for always keeping the morale high and everyone in CANES especially Cohort IV (vive la D&D!).

My deepest gratitude to S K Gummadi sir, my first inspiration, who motivated us to always be curious, and all my KVS teachers. A note of thanks to all my Bethune teachers especially Dr Ajita Sengupta ma'am, Dr Ratna Koley ma'am, Dr Keya Bose ma'am and Mainak Gupta sir. My sincere thanks to the faculty at SNBNCBS especially Prof Arup Kumar Raychaudhuri sir, who inspired me to always connect theory and experiments for a wholesome understanding of the physics behind, Prof Amitabha Lahiri sir for teaching me that there is an art to asking questions, to Prof Priya Mahadevan ma'am for being an early role model and Prof Punyabrata Pradhan sir who taught me that one must be proactive in science.

Now back to the old drawing board. Thanks to Mimi for being the first PhD I saw up close. Enormous thanks to dadai, late Shri Mrityunjoy Chatterjee and mama urf chele, Tapeshwar Chatterjee. You were the comfortable cushions of support. And finally, to the loves of my life, my Ma and Bapi, Luna Banerjee and Debasis Banerjee. Your boundless, selfless love, the sacrifices that you made so that your daughter could have her own wings in a world which is tad prejudiced against girls, not caring about people's opinion or your own comforts, your long-standing determination, dedication is my inexhaustible source of inspiration. You are my hope, you are love, you are the reason my earth goes around the sun and why I do science, why I live, and you are life. I love you and thank you.

Preface

A note for the reader

In this thesis, I tried to explain the foundational aspects of my work in detail. On a more personal note, I relished the whole process of working on the thesis, disentangling the intricate gossamer of how the *actual* effect of strong correlations, different transport mechanisms, lattice dynamics bloom in various degrees of approximations in theoretical modelling and then through a delicate equipoise of conversations between theoreticians and experimentalists which frame what that *actual* picture is. Fascinatingly with big discoveries, that *actual* picture changes, and the beauty is that we gain understanding from those changes, adapt and science progresses. The years I spent on this thesis made this realisation stronger, and were fun. The primary purpose of this thesis is to be a scientific publication and describe the research carried out throughout this doctoral program. However, I saw that it is mostly PhD students, like me, or beginners in a field who read published theses as in terms of detail they act as bridges between textbooks and papers. With this argument I come to the secondary objective of this thesis. I have tried to use a writing style that is mostly formal for describing the science correctly as done in most theses, but at places, especially in the introduction and the theory sections, is also informal with a dash of humour. It is to make the story of research not found in usual textbooks more fun, welcoming and warm for an imaginary audience of trainees like me who sometimes deal with an impostor's syndrome for various reasons and have difficulty asking questions. Setting this as a secondary aim is a small attempt by a mere beginner to address these rather big issues on a mini-scale, and I will gladly take criticisms on it. With this personal note, let us begin the thesis and I wish you will have an enjoyable experience in reading it as much as I did performing the research.

List of Figures

1.1 A schematic representation showcasing the different facets of condensed matter research aimed at the study and design of new materials. 2
1.2 A simplified schematic representation of the band theory of solids. . . . 8
1.3 Schematic representation of *(above)* the band theoretical description of metal, semiconductor and insulator, and *(below)* how the Coulomb interaction terms give rise to Mott-insulating behaviour. 9
2.1 Flowchart illustrating the self-consistent iterative scheme to solve the Kohn-sham equations in the density functional theory framework. . . . 22
2.2 A caricature showing three major (not exhaustive, often overlapping) categories of computational methods used for real materials in ascending order of information retained and computational complexity. 33
2.3 The 'Hamiltonian space sun'- a cartoon depicting the big *fictitious* world of model Hamiltonians that describes various physical phases and phase transitions as one goes from one model Hamiltonian to another. The grey arrows signify the presence of many such models[1]. Inspired by Prof. Vijay Shenoy's '*Pancha-Bhuta-Chitra*' [79]. 38
2.4 Schematic depiction of origin and relevance of correlations for a square lattice with a single orbital on each site. If an electron will hop to the next nn site is decided by the Pauli exclusion principle along with the filling and its impact on the t vs U competition. For low filling, the likelihood of hopping is higher representing a weakly correlated case. Near half-filling the competition between $-t$ and $+U$ becomes important representing strong correlations and subtle changes in the system environment like temperature, pressure can give rise to different phases with characteristic properties. 40
2.5 The DFT+U self-consistent iterative scheme implementing the simplified rotationally invariant formulation discussed in section 2.9.3 and eq.(2.76) using the FLL double counting correction scheme. 46
2.6 The general dynamical mean field theory (DMFT) self-consistent iterative scheme. 53

2.7 (a) Spectral function $A(\omega)$ obtained using Padé approximation [112] for a Hubbard Hamiltonian on the Bethe lattice at half-filling with $t = 1$, $\beta = 20$, half-bandwidth $W = 2t = 2$, depicting the onset and completion of a Mott transition as U increases from 0 to 8. Depiction of (b) imaginary Green's function, and (c) Self-Energy in Matsubara frequencies as the system moves from metallic to insulating regime. 59
2.8 Schematic representation of electron transport via (a) thermionic emission, (b) single barrier quantum tunnelling, and (c) resonance tunnelling through a double-barrier quantum well. 62
2.9 Sketch of a two-terminal transport junction with semi-infinite left (H_L) and right (H_R) leads connected via an extended molecule in the middle (H_M) coupled to the left and the right leads by H_{LM} and H_{RM}, respectively. 66
2.10 Polymorphic behaviour is usually heavily influenced by defects and disorder in a material. Entropy can be used as a descriptor a disordered state. The interplay of these concepts is crucial when investigating the role of structural degrees of freedom in determining physical properties of a material. 73
2.11 A sketch of the potential energy landscape of a material exhibiting polymorphism. Each local minima corresponds to a different polymorphic configuration C_i. The volume of the phase space at a local minimum is called its basin of attraction. 74
2.12 A sketch of enthalpy per particle for an arbitrary material showing polymorphic behaviour. The i^{th} configuration C_i has enthalpy H_i, hypervolume of the basin of attraction V_i, and probability and frequency of occurrences P_i and f_i, respectively. 75
2.13 Configurations per energy plotted as a function of energy starting from ground state for two different materials with different values of entropy forming ability (EFA) descriptors. For a wider spectrum *(lower half)* EFA is higher highlighting that going from one metastable configuration to another is more difficult energetically. 78
3.1 Chapter objectives and keyword map: highlighting the main questions asked, topics addressed and keywords used. 81
3.2 A model interface with four layers identified by different hopping parameters t, t_{perp} and t_{tun}, extending periodically in the x-y plane but finite along the z(c)-axis, the direction of transport. Layers L_1, L_4 represent identical leads forming interfaces with the film layers L_2, L_3 separated by an insulating buffer layer. U is the onsite Coulomb repulsion used to model interactions. 83

3.3 Graphical re-interpretation of the original 4-layer real space system with a 4-site Hamiltonian in mixed space with spatial x-y contributions represented in reciprocal space and z-direction in real space, the direction of voltage(V) application. The buffer layer has been considered to be vacuum. Colours mark equivalent sites (layers). 85
3.4 The DMFT loop to solve the model interface set-up based on the IPT solver with self-consistency defined by accuracy in Matsubara self-energy ($\Sigma(i\omega)$). 87
3.5 Metallic and insulating solutions obtained with DMFT within the IPT approximation for $t = 1$, $t_{\text{perp}} = 0.2$, $t_{\text{tun}} = 0.05$, $\beta = 40$, $N_{k_x} = N_{k_y} = 20$. The system is metallic for $U < 10$, the Mott transition occurs between $U = 10 - 12$, and the system becomes insulating for $U > 12$, independent of the starting point. 88
3.6 Observation of hysteresis surrounding the metastable Mott regimes with $t = 1$, $t_{\text{perp}} = 1$, $\beta = 20$, $(N_{k_x}, N_{k_y}) = (20, 20)$. $\Sigma = M$ and $\Sigma = I$ correspond to initiating a DMFT run with a metallic (M) and an insulating (I) self-energy, respectively. 89
3.7 Schematic depiction of the role of t_{perp} and t_{tun} in lifting the degeneracy between the 4 sites in absence of any on-site interactions or external bias for situations when t_{perp} being larger than t_{tun} by an order of magnitude. 90
3.8 The change in density of states (DOS) with the applied voltage at the band limit ($\Sigma(i\omega) = 0,\ U = 0$) with $t = 0,\ t_{\text{perp}} = 0.5,\ t_{\text{tun}} = 0.02,\ \eta = 0.025$. The voltage induced insulator to metal transition happens at $V = \pm 1$. 91
3.9 The change in density of states at the Fermi level (DOS_{E_F}) with applied voltage for $U = 0,\ t = 0.,\ t_{\text{perp}} = 0.5,\ t_{\text{tun}} = 0.02,\ \eta = 0.025$. The DOS_{E_F} increases with $|V|$ and reaches a peak at $V = \pm 1$ corresponding to the occurrence of resonant tunnelling (RT), as also observed in fig.(3.10). 92
3.10 The peak in transmission T across sites 2-3 (blue) and 1-4 (orange) at the Fermi level, E_F, with the applied Voltage for $U = 0,\ t = 0.,\ t_{\text{perp}} = 0.5,\ t_{\text{tun}} = 0.02,\ \eta = 0.025$. This peak confirms the observation of resonant tunnelling (RT). 92
3.11 Evolution of the spectral function with applied voltage in the atomic limit with $\Sigma(i\omega)$ given by eq.(3.25) and with $U = 1,\ t = 0,\ t_{\text{perp}} = 0.5,\ t_{\text{tun}} = 0.02,\ \eta = 0.025$. The presence of interactions exhibit a more complex evolution of DOS with V. 93
3.12 Multiple peaks in transmission between layers 2-3 (blue) and 1-4 (orange) are observed with increasing V at the simplified atomic limit where $\Sigma(i\omega)$ is given by eq.(3.25) and $U = 1,\ t = 0.,\ t_{\text{perp}} = 0.5,\ t_{\text{tun}} = 0.02,\ \eta = 0.025$. 94

3.13 Evolution of the spectral function (DOS) with ω with increasing V. The DOS at E_F slowly increases with V till $V = 0.6$ corresponding to the first peak in transmission T. At $V = 1$, T vanishes again before reaching its maximum at $V = 1.6$. 95
3.14 Role of the hopping along z-direction within sites 1-2 and 3-4 in controlling the splitting of the Hubbard peaks at $t = 0.$, $t_{\text{tun}} = 0.02$, $\eta = 0.025$. 95
3.15 Role of the hopping along z-direction within sites 2-3 representing atoms of the thin film at the interface in controlling the peak density of the Hubbard peaks at $t = 0.$, $t_{\text{perp}} = 0.5$, $\eta = 0.025$. 96
4.1 Chapter objectives and keyword map: highlighting the main questions asked, topics addressed and keywords used. 98
4.2 Microprocessor scaling trends in microchip transistor density, single thread performance of SPECint units, computer clock frequencies and power consumption, and processor logic core density between 1970 and 2020. (Figure from: [179]) 100
4.3 Schematic depiction of the operational principle of a piezoelectric transistor (PET). The entire structure is clamped on a high yield material (HYM) with input applied via the gate to the piezoelectric (PE) material connected to the piezoresistive (PR) film via the *common*. The PR insulator ($V = 0$, OFF-state) to metal ($V > 0$, ON-state) transition is detected by the *sense*. 101
4.4 Representative plots depicting the variation of resistivity (ρ) with pressure (p). (*left*) SmSe shows a continuous, reversible insulator to metal transition as the $4f$-$5d$ band gap closes, suitable for switching operations [195]. (*right*) SmS shows a discontinuous, hysteretic transition, suited for memory based device applications [182]. Red and green shaded regions identify insulating and metallic regimes, respectively. 103
4.5 *(left)* The rock salt like structure of Samarium monochalcogenides in the cubic *Fm-3m* space group. *(right)* The primitive cell used for DFT+DMFT simulations. 106
4.6 Total energy (E_{tot}) curves plotted as a function of the lattice constant (a) obtained using DFT with and without spin-orbit coupling (SOC) [231] corrections for SmS as implemented in plane wave basis code VASP [232], [233] using the projected augmented wave (PAW) [234], [235] PBE [43] potentials. 107
4.7 Density of states for SmS obtained with (a) DFT, (b) DFT+DMFT for the Sm-$4f^6$ configuration corresponding to ambient pressure insulating black phase, (c) magnified version of (b) showing the existence of a finite band gap with the vertical dashed lines delimiting the gap, (d) DFT+DMFT corresponding to the onset of high-pressure metallicity with intermediate Sm-$4f$ valence of 5.24(2) in the golden phase. 109

4.8 Comparison between DFT and DFT+DMFT predictions of total energy (E_{tot}) curves plotted as a function of lattice constant (a) and fitted with a Birch-Murnaghan [241], [242] equation of state for (a) SmS, (b) SmSe, and (c) SmTe. Arrows mark the experimental values for respective lattice constants under ambient conditions. 110
4.9 (*Left column*) Density of states obtained with DFT+DMFT corresponding to the ambient pressure insulating states for (a) SmS, (c) SmSe, and (e) SmTe, and (*right column*) the high-pressure intermediate valence metallic states with insets focusing on the behaviour of Sm-4f peaks around the Fermi level for (b) SmS, (d) SmSe, and (f) SmTe, respectively, with the vertical dashed lines delimiting the band gap. . . 111
4.10 A comparison between the density of states for different values Hund's coupling, J, for SmS with $J = 0.3$ eV, and (b) $J = 0.8355$ eV. The final choice of $J = 0.3$ is based on correct reproduction of the Sm-4f and S-p hybridisation and band gap consistent with experimental observations. 112
4.11 (a) Total quasiparticle weight (Z), (b) Sm-4f electron-occupancy (n_f), (c) total density of states at the Fermi level ($\rho(E_F)$) along the NEB-like path going from the insulating state ($\lambda = 0$) to the metallic state ($\lambda = 1$) for SmS, SmSe and SmTe. SmS, SmSe and SmTe are represented by colours magenta, blue and black, respectively. 113
4.12 (*Left*) Difference in the density of states obtained with DFT+DMFT at high temperature (T = 0.05 eV, *solid lines, unshaded*) and room temperature (T = 0.026 eV, *dashed lines, shaded*) corresponding to the ambient pressure insulating states for (a) SmS, (c) SmSe, and (e) SmTe, and (*right*) the high-pressure intermediate valence metallic states for (b) SmS, (d) SmSe, and (f) SmTe. Lowering the temperature result only in small shifts in the DOS but no significant qualitative differences. 114
5.1 Chapter objectives and keyword map: highlighting the main questions asked, topics addressed and keywords used. 118
5.2 (a) Single-ζ (SZ), (b) single-ζ polarised (SZP), (c) double-ζ (DZ), (d) double-ζ polarised (DZP) bases for bulk W. Corresponding lattice constants, energies and bulk moduli compared to the experimental values are reported in tab.(5.2). 126
5.3 Structural relaxation of bulk W for various basis sizes, shapes and ranges obtained using DFT-GGA and fitted with Birch-Murnaghan [241], [242] equation of state. SZ, SZP, DZ, and DZP refer to single-ζ, single-ζ polarised, double-ζ, and double-ζ polarised basis sets, respectively. Split is a user-defined basis optimised with respect to the number of l-shells with respective number of ζs and their cut-off radii (r_c). 130

5.4 Final optimised split-valence LNAO basis for (a) W comprised of double ζs for $6s$, single ζ for $6p$, and double ζs for $5d$ orbitals, (b) Sm composed of Sm double ζs for $6s$, single ζ for $5d$ and $4f$, and single ζ polarised for $6p$, and (c)/(d) S/Se constituted by double ζs each for $3s/4s$ and $3p/4p$ along with a single ζ for $3d/4d$. (e)/(f) depict default Siesta split-valence LNAO S/Se basis where the radial cut-offs for $3s/4s$ orbitals are less by 0.7 Å than $3p/4p$ and $3d/4d$ with the $3d/4d$ orbitals taken to be polarised. 131

5.5 The difference in predicted lattice constants for (a) SmS and (b) SmSe with each of the default Siesta S, Se basis as shown in fig.(5.4e, f) and the corrected basis as shown in fig.(5.4c, d). 132

5.6 The difference in predicted lattice constant values for SmSe with the system taken to be non-spin polarised (non-SP) and spin-polarised (SP) with LDA and GGA. 133

5.7 DFT based energy minimisation for (a) W, (b) SmS, and (c) SmSe with the final basis as described in fig.(5.4a, b, c, d) with LDA and GGA pseudopotentials. 134

5.8 (a) *Front-view* of a W bcc unit cell [261] with W atoms in blue. The a-b axes refer to the x-y plane or the plane of the paper. Shades of blue depict the depth along the c(z)-axis. (b) The blue dotted line connects 4 W-atoms in a plane with the $5th$ W-atom at the face-centre. This corresponds to the orientation of the W-atoms at the interface. (c) *Front-view* of SmX NaCl-like structure with Sm, and X=S, Se atoms in magenta and green, respectively. The Sm-Sm, X-X distance $d < 2a$ (d_1 for SmS, d_2 for SmSe). The W-SmX cross-section made to match the distance between W atoms at the ends of the square ($a\sqrt{2}$) in (b) to the 1st-nn distance ($d/\sqrt{2}$) of Sm-Sm, X-X. 135

5.9 Relaxing a_z of the substrate W with respect to the new a_x, a_y set as per the reference thin film bulk lattice minimum denoted by the figure legend. 137

5.10 The (a), (c) side-views and (b), (d) top-views of the *top* and *hollow* configurations of the W-SmX interface [261], respectively with magenta, green and blue atoms representing Sm, X = S or Se and W, respectively. The shaded planes show the respective layer cross-sections. In (a), (b) Sm and X atoms sit right on top of all five W atoms. In (c), (d) the Sm and X atoms sit between the boundary W-atoms. There can be infinitely many configurations where the Sm or X atoms sit somewhere in-between. 138

5.11 W-SmX (X = S, Se) interface distance relaxation. The minimum d is used as the interface lead-film distance in transport calculations. 139

5.12 The W-SmX interface [261] for the *hollow* configuration with 6 SmX film layers and 7 W lead layers. The Sm, X and W atoms are denoted by the colours magenta, green and blue, respectively. 140

5.13 Concurrence of minimum energy and zero pressure state for thinfilm materials used (a) SmS, (b) SmSe 140
5.14 Structure of the W-SmSe-W junction with the W and SmSe as electrode and film materials respectively for the *hollow* configuration. The interface is optimised with Siesta to be used with SMEAGOL by collaborators at NPL for transport calculations. The atoms in blue, magenta and green stand for W, Sm and Se, respectively. 141
5.15 Partial density of states (PDOS) obtained with SMEAGOL with (a) DFT and (b) 1-shot DFT+DMFT using the Hubbard-1 solver as implemented in SMEAGOL for a heterostructure with 8 monolayers (ML) of SmSe with W semi-infinite electrodes, a DMFT-$U = 8.1$ eV on Sm-4f orbitals, Hund's coupling, $J = 0.8$ eV, and nominal valence of 5.5. (Simulation and figure by: Dr. Ivan Rungger) 142
5.16 Partial density of states (PDOS) obtained with the SMEAGOL implementation of DFT+DMFT using the Hubbard-1 solver with charge self-consistency for a W-SmSe-W heterostructure with 8 monolayers (ML) of SmSe and semi-infinite W leads, DMFT-$U = 8.1$ eV on Sm-4f orbitals, a Hund's coupling, $J = 0.8$ eV, and nominal valence of 6. (Simulation and figure by: Dr. Ivan Rungger) 144
5.17 (a) Structure of the W-SmSe-W junction with W atoms (blue) as electrodes and SmSe (magenta, green) as the sandwiched film with shaded regions in xy-plane. Layer 1 is the first SmSe layer at the metal interface of length $d_l = 2.5255$ nm and layer 4 is the layer in the middle. (b) Partial density of states (PDOS) of Sm-4f levels for 4 consecutive layers of SmSe showing the evolution of occupied Sm-4f levels in energy with distance from the interface. (Simulation and figure of (b) by Dr. Ivan Rungger) 145
5.18 Comparison between transmission plotted as a function of energy from the Fermi level for W-SmSe-W heterostructure with (a) 8 monolayers (ML), and (b) 16 MLs of SmSe as the PR thin-film with DMFT-Hubbard1 solver and DFT+U+SOC with the basis as described in 5.4 compared with the DFT results obtained without the contribution of f-orbitals. (Simulation and figure by: Dr. Ivan Rungger) 146
6.1 Chapter objectives and keyword map: highlighting the main questions asked, topics addressed and keywords used. 151
6.2 The prototypical perovskite structure of $CaTiO_3$ (ABX_3) [264]. 152
6.3 The rock-salt phase of La_2TiFeO_6, a double-perovskite comprising of two formula units. The atoms are identified by colours as - La:green, Ti:blue, Fe:brown, and O:red. The above structure corresponds to the charge-transfer type ground state with $a^-b^-c^+$ octahedral rotations with Ti, Fe in 4+, 2+ states, respectively. 153

6.4 Summary of experimental workflow and methods used to synthesise and study of La_2TiFeO_6 (LTFO) and La_2VCuO_6 (LVCO) aimed at controlling the B-site charge transfer and ordering by varying internal pressure. See tab.(I) for further details. 155
6.5 Energy difference per formula unit (f.u.) of the ground state of the rock-salt and layered phases plotted as a function of strain in bulk (zero strain), strained on $SrTiO_3$ (100) and on $LaAlO_3$ (100), respectively. For La_2TiFeO_6, the charge transfer phases correspond to Ti^{4+} and Fe^{2+}, and the non-charge transfer phases stand for Ti^{3+} and Fe^{3+} oxidation states. For La_2VCuO_6, the charge transfer phases with oxidation states V^{4+} and Cu^{2+} refer to the G-type magnetic states whereas V^{5+} and Cu^{+} refer to the non-magnetic non-charge transfer phases. (reprinted from coauthored citation [272]) 157
6.6 Frequency of occurrence plotted as a function of the energy (H, enthalpy at zero pressure) difference within 400 meV of the ground state among all La_2TiFeO_6 double perovskite structures captured by AIRSS. The $P2_1/C$ rock-salt and the layered orders correspond to the ground state with the lowest frequency and the highest energy state with highest frequency. Along with three new B-site ordered structures, these low-lying competing phases are associated with higher configurational entropy and observed experimental disorder. The atoms are identified by colours- La:green, Ti:blue, Fe:brown, and O:red. (reprinted from coauthored citation [272]) 160
6.7 An AIRSS optimised configuration of $La_2TiFeO_{6.5}$ with an extra O-atom between two edge sharing B-site octahedra accounting for 8% overoxygenation representing the PLD growth in oxygen-rich conditions. The atoms are identified by their colours- La:green, Ti:blue, Fe:brown, and O:red. (reprinted from coauthored citation [272]) 162
6.8 (*Central panel*) Entropy Forming Ability (EFA) computed within the energy window of 0-400 meV for La_2TiFeO_6 depicted by the colour gradient proportional to the EFA values. The EFA is explicitly dependent on the defect chemical potential via the defect formation energies. The dashed white lines denote the value of the chemical potential where the defects emerge and accentuate the disorder. (*Corner panels*) The change of EFA with energy for four combinations of defect chemical potentials. The green shaded region corresponds to the energy window of 0-400 eV where the low-lying competing structures are observed. (reprinted from coauthored citation [272]) 164

6.9 Volume distribution of AIRSS optimised structures for $La_{1.5}TiFeO_6$, $La_2TiFeO_{6.5}$ and La_2TiFeO_6 in La-poor and O-poor conditions. The green shaded region corresponds to the energy window of 0-400 eV. The blue shaded region between $\sim 1 - 1.5$ eV corresponds to the expanse with highest concentration of minima responsible for the incoming EFA peak at ~ 1.1 eV in the upper left corner panel of fig.(6.8). (reprinted from coauthored citation [272]) 165
6.10 Distribution of magnetic moments of La_2TiFeO_6, $La_{1.5}TiFeO_6$ and $La_2TiFeO_{6.5}$ as function of energy. In La_2TiFeO_6, the charge transfer type Fe^{2+} and Ti^{4+} states are most favoured. Oxidised Fe^{3+} states emerge more when defects are included. (reprinted from coauthored citation [272]) 166
6.11 Atom resolved phonon density of states obtained using DFPT for the La_2TiFeO_6 rock-salt and layered structures. (reprinted from coauthored citation [272]) 167
6.12 Evolution of vibrational entropy of La_2TiFeO_6 rock-salt and layered structures with temperature within the quasi-harmonic approximation. The entropies for both the structures are almost identical as the largest contribution arises from the La-cage as observed in fig.(6.11). (reprinted from coauthored citation [272]) 168
6.13 Projected density of states for ceria (CeO_2) as obtained with a 4-formula unit supercell of Ce_4O_8 with (a) DFT, (b) DFT+U, $U = 5$ eV. (Simulation by Dr. Rachel Kerber, JM. See footnotes 3 and 4) 172
6.14 Projected density of states for ceria-zirconia ($ZrCe_3O_8$) in the fluorite structure with (a) DFT, (b) DFT+U, $U = 5$ eV. (Simulation by Dr. Rachel Kerber, JM. See footnotes 3 and 4) 173
6.15 (a) Energy difference of the structure displaced Δd times with respect to the original structure in the direction of the soft-mode. The red point signifies no convergence. (b) Phonon eigenvalues in meV at Gamma (0,0,0) point for ceria and zirconia-ceria oxides. (c) Relaxed structure of $ZrCe_3O_8$ corresponding to the large soft phonon mode, with the new structure formed by tilted oxygen (red) planes. (d) Density of states corresponding to the old $ZrCe_3O_8$ *(straight lines)* and the new displaced relaxed *(dashed lines)* structures denoting the structure induced energetic stabilisation. 177

II.1 Layer dependent projected density of states (PDOS) obtained with DFT+U+SOC (spin orbit corrections) with U=6 eV for (a) bulk SmSe, (b) the 4^{th} layer of SmSe in an 8-monolayer film, and (c) the 1^{st} layer of SmSe . Study of the layer dependence of DOS shows that at the 4^{th} layer, the DOS becomes visibly similar to the bulk. (Simulation and figure by: Dr. Ivan Rungger) 188

III.1 Projected density of states for ceria with 12.5% oxygen vacancy with a Ce_4O_7 supercell with (a) DFT, and (b) DFT+U with $U = 5$ eV. (Simulation by Dr. Rachel Kerber, JM. See footnotes 3 and 4) 190
III.2 Band-structure for various ceria oxides: (a)Ce_4O_8 bulk, (b) Ce_4O_7 with 12.5% O-vacancy, (c) $ZrCe_3O_8$ bulk, and (d) $ZrCe_3O_7$ with 12.5% O-vacancy obtained with DFT as implemented in Quantum Espresso code with plane-wave basis and PBE functional and other comparable parameters as obtained with VASP as described in 6.5.2. E_F, CB and VB stand for the Fermi level, conduction band and valence band respectively. (Simulation by Dr. Rachel Kerber, JM. See footnotes 3 and 4) 191

List of Tables

2.1 A summary of three widely used basis types, their benefits and pitfalls. 26

4.1 Comparison of experimental data [198], [239], [244], [243] with DFT and DFT+DMFT predictions for lattice constant (a) and bulk-modulus (B_0) for SmS, SmSe, and SmTe, along with DFT+DMFT predicted Sm-4f occupation (n_f). Red and green cells mark insulating and metallic phases respectively, either predicted or observed. 110

5.1 Predicted scales for PR functionality for various tiers of technology [248], [249]. 119

5.2 Comparative study of different multiple-ζ bases for predicting equilibrium total energy (E_{tot}), lattice constant (a), and bulk modulus (B), obtained by fitting a Birch-Murnaghan [241], [242] equation of state to the energy-volume curve, for W. 130

5.3 Comaprision of lattice structures of (a) W, (b) SmS, (c) SmSe obtained with LDA and GGA with experimental predictions [198], [239], [244], [243] 134

5.4 A summary of lattice size mismatch at the interface between the lead W and the films of SmS and SmSe, respectively. 137

5.5 The variation of total energy difference for the *top* and the *hollow* configurations of W-SmS interface for three selected distances. 138

5.6 Predicted junction length scales (d_l) for OFF-state PR functionality corresponding to memory and transistor operations for SmSe. 149

6.1 Experimentally obtained lattice parameters for LTFO and LVCO using XPS 155

6.2 Bond distance ranges for La_2TiFeO_6 and La_2VCuO_6 for charge transfer (CT) and non charge transfer (No CT) states each for the rock-salt (RS) and layered (L) type B-site ordering. The ranges include the zero strain bulk structures and those strained on STO (100) and LAO (100) as shown in fig.(6.5) 157

6.3 Estimated chemical potential bounds obtained from reference $LaFeO_3$ formation [279] in La-poor and O-rich conditions. 163

6.4 Estimated chemical potential bounds obtained from reference $LaFeO_3$ formation [279] in La-rich and O-poor conditions. 163

6.5 Percent volume collapse ($\Delta V\%$) observed in relaxed volume for structure S2 from the relaxed volume of structure S1 for each respective method with $\pm$ corresponding to an enlargement or collapse of volume respectively. 175

6.6 Defect formation energy (in eV) for oxygen vacancy for ceria and ceria-zirconia starting from an oxygen reference state calculated by difference of total energies of electronic relaxation of H_2O and H_2. A different reference state, like the oxygen molecule in triplet form, will shift all the above energies by a constant for the method used. 176

I.1 A quick overview of experimental methods concerning the work done and compared with in this thesis for the *lay-person* theorist. It includes a brief description of the experimental method and its usual application with a mention of where and how that was used in this thesis. 186

Contents

Abstract i
Declaration v
Acknowledgements viii
Preface x
List of Figures xi
List of Tables xxi
Contents xxiii

1 Introduction **1**
1.1 A sketch of the origins 3
1.2 Post-Schrödinger and pre-Kohn theories 5
1.3 Mean field treatment 6
1.4 Correlations 7
1.5 Strong correlations in materials 8
1.6 Structure of the thesis 10

2 Theory **13**
2.1 The solid-state Hamiltonian 14
2.2 Density Functional Theory 15
2.2.1 Density based formalism 17
2.2.2 Hohenberg-Kohn theorems 19
2.2.3 Kohn-Sham approach 20
2.2.4 Exchange correlation functionals 21
2.3 Basis Sets 23
2.3.1 Atomic sphere basis 24
2.3.2 Plane wave basis 24
2.3.3 Localised basis 25
2.4 Pseudopotentials 27
2.4.1 Pros of DFT 30
2.4.2 Limitations of DFT 30
2.5 Beyond DFT 33
2.6 Green's Functions 34
2.6.1 A brief review 34

2.6.2 Electron Green's function . . . 36
2.7 Model Hamiltonians : a quick review . . . 38
2.8 Hubbard Model: revisiting strong correlations . . . 39
2.9 DFT+U . . . 42
2.9.1 A DFT+U description . . . 43
2.9.2 Double counting correction . . . 45
2.9.3 A simpler DFT+U formulation . . . 46
2.10 Dynamical Mean Field Theory . . . 48
2.10.1 Anderson Impurity Model . . . 48
2.10.2 Impurity mapping and self-consistency . . . 50
2.10.3 DFT+DMFT . . . 54
2.10.4 Hubbard-I solver . . . 55
2.10.5 Iterated Perturbation Theory (IPT) solver . . . 57
2.10.6 Mott transition . . . 59
2.11 Transport . . . 61
2.11.1 Thermionic emission . . . 61
2.11.2 Tunnelling . . . 63
2.11.3 Resonant Tunnelling . . . 63
2.11.4 Landauer-Büttiker formalism . . . 65
2.11.5 Non-equilibrium Green's function (NEGF) . . . 66
2.12 Lattice dynamics . . . 69
2.13 Density functional perturbation theory (DFPT) . . . 70
2.13.1 Energy functional expansion . . . 71
2.13.2 Self-consistent linear response . . . 72
2.14 Theoretical markers of disorder . . . 72
2.14.1 Relative frequency of occurrence . . . 74
2.14.2 Entropy Forming ability . . . 77

3 Modelling Interfaces for Nanotechnology 80
3.1 Introduction . . . 82
3.2 A model interface . . . 83
3.3 Observing the Mott transition . . . 86
3.4 Transition and Tunnelling . . . 88
3.5 Resonant Tunnelling and the Mott transition . . . 90
3.6 Conclusion . . . 96

4 Pressure induced electronic transitions in Samarium monochalcogenides 97
4.1 Introduction . . . 99
4.1.1 Piezoelectric Transistor . . . 99
4.1.2 Piezoresistivity in Samarium monochalcogenides . . . 101
4.1.3 Lanthanides . . . 103

4.2 Samarium Monochalcogenides: a brief survey . . . 104
4.3 Computational Details . . . 106
4.3.1 DFT based study . . . 106
4.3.2 Spin-Orbit Coupling . . . 107
4.3.3 Hubbard-I approximation . . . 108
4.4 DMFT Results . . . 108
4.5 Nudged Elastic Band analysis . . . 113
4.6 Conclusion and Discussion . . . 115

5 Transmission across Samarium monochalcogenide based thin film heterostructures 117
5.1 Introduction . . . 119
5.1.1 Experimental details . . . 119
5.1.2 Elastic properties . . . 120
5.1.3 Transport mechanism . . . 121
5.1.4 Role of electronic structure in transport . . . 122
5.1.5 Objectives and approximations . . . 122
5.2 Localised numerical atomic orbitals . . . 123
5.3 Preambular transport with DFT . . . 127
5.3.1 Choice of electrodes . . . 128
5.4 Overview of simulation approach . . . 129
5.4.1 Basis optimisation . . . 129
5.4.2 Setting up the interface . . . 135
5.4.3 Calibrating the pressure . . . 140
5.5 Quantum Transport with DFT and DMFT . . . 141
5.6 Conclusion and outlook . . . 147
5.7 Future plan of action . . . 149

6 Disorder and defects in rare-earth metal oxide structures 150
6.1 Introduction . . . 152
6.1.1 Disorder in Double perovskite oxides . . . 152
6.2 Experimental observations . . . 154
6.3 Ordered phases . . . 156
6.4 Disordered phases . . . 158
6.4.1 Relative frequency of occurrence . . . 159
6.4.2 Entropy Forming Ability (EFA) and the role of defects . . . 161
6.4.3 Vibrational entropy and long-range order . . . 167
6.5 Soft phonons in lanthanides . . . 169
6.5.1 Catalytically relevant oxides . . . 171
6.5.2 Ceria . . . 172
6.5.3 Zirconia-ceria oxide . . . 173

6.5.4 Oxygen vacancies . . . 174
6.5.5 Soft phonon modes . . . 176
6.6 Conclusion and outlook . . . 178

7 Conclusion & Outlook **180**
7.1 Conclusion . . . 181
7.2 Outlook . . . 183

I A quick overview of experimental methods for theorists **185**

II Precursor to many-body quantum transport **187**

III Ceria **190**
III.1 Projected DOS for ceria compounds . . . 190
III.2 Bandstructures for ceria compounds . . . 191

References . . . 192

The middle-earth of correlations . . . xvii

Chapter 1

Introduction

At the heart of contemporary research in condensed matter physics lies the quest to understand *why electrons behave the way they do*? Condensed matter physics in its more general definition describes how *condensed* matter like a solid or a liquid arises from its constituents with specific model(s) of interactions between them. Historically, this terminology was a re-branding of the emerging field of solid state physics in the post world war period that was slowly merging the rift between academic interests and industrial applications [1]. One of the first and most important symbols of this paradigm shift came with the quick award of the 1956 Nobel prize [2] for the invention of transistor in 1947 at the Bell labs. It not only had far-reaching academic as well as industrial but also deep sociological impact in shaping the narrative of the next century [3]. The success of the transistor allowed research in 'solids' to become more flexible as opposed to just 'metals' that were considered to be a prime focus of interest for industrial research. Given these duplex channels of interest, it isn't surprising that condensed matter research has the highest numbers of active researchers in the world across a wide range of sub-fields in the present times [4].

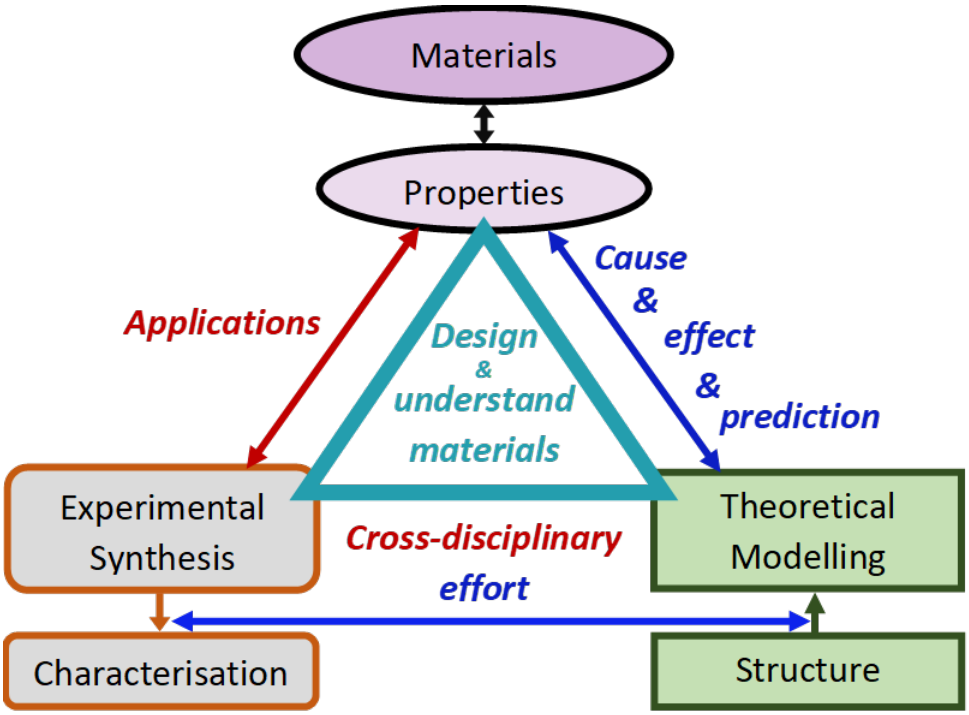


Figure 1.1: A schematic representation showcasing the different facets of condensed matter research aimed at the study and design of new materials.

A prime inspiration for a large section of the condensed matter community in present times is the search for new materials with desired properties. This exploration is deeply intertwined with the need for a deeper understanding of *emergent* behaviour in materials, a pursuit that requires joint efforts from both experimentalists and theoreticians as schematically represented in fig.(1.1) and thus, is truly interdisciplinary in nature. The objective of the scientific work performed as a part of this thesis is theoretical

modelling of a set of materials in view of their practical applications with a focus on understanding the physical origin of observed properties based on electronic structure.

1.1 A sketch of the origins

Before we delve deeper into a discussion of which theories are employed in studying the emergent phenomena from electronic structure, we consider a more philosophical view of our choices of interpretations in brief. An understanding of the physical origin of material properties that formulates the core of this thesis has in the course of time been approached in two ways. In the reductionist hypothesis it was argued that excluding some exceptional circumstances the visible universe could be explained by a set of fundamental laws, or interactions, or particles, or entities in general. However P. W. Anderson, whose work forms the basis of one of the methods we have used in this thesis, argued in his famous 1972 Science paper 'More is different' [5] that,

> *The reductionist hypothesis does not by any means imply a 'constructionist' one: The ability to reduce everything to simple fundamental laws does not imply the possibility to start from those laws and reconstruct the universe.*

In the world of condensed matter Anderson's view is usually agreed upon well. The strongest case, which might have also inspired Anderson, was the confirmation of quarks in 1968 where today's elementary nature of nucleons transformed into tomorrow's compound many-body entities. At this juncture, one cannot stop but be curious of how this dichotomy between the elementary and composite particles shape the understanding of *the theory of everything* in this universe. But for practical matters of interest and for the problems investigated in this thesis, the wonderfully successful standard model with its quarks and baryons and leptons and mesons in every colour or spin or fashion does little to explain why and how samarium monochalcogenides shows a pressure induced insulator to metal transition, why ammonia can tunnel between the two its tetrahedral configurations with a high frequency and thus have an average of zero electrical dipole moment where larger molecules, such as sugar, cannot, and numerous other questions like that. Thus, even though theories about fundamental particles and interactions stand on *correct* and *accurate* grounds, to understand an aggregate of atoms they are insufficient[1]. In another famous article titled 'Theory of Everything', R. B. Laughlin and David Pines [7] say,

> *We have succeeded in reducing all of ordinary physical behaviour to a simple, correct Theory of Everything only to discover that it has revealed exactly nothing about many things of great importance.*

[1] Some authors claim that this is closely related to the interpretations of quantum mechanical measurement processes and the relation between quantum mechanics to classical mechanics [6].

However the situation is not that dire. It has been observed that stages of hierarchy can be defined based on energy scales. Theories usually work well within a certain scale mostly because they are designed for that scale aided by approximations, many-a-times that approximation being the choice of a perturbative variable, and thus holds the fort of validity. The physics of each scale, Anderson argued, is *fundamental*. Laughlin and Pines summarise this beautifully as,

> *Thus, with increasing complication at each stage, we go up the hierarchy of the sciences. We expect to encounter fascinating and, I believe, very fundamental questions at each stage in fitting together less complicated pieces into the more complicated system and understanding basically new types of behaviour which can result.*

How these two viewpoints stand and progress with the advance of science is an interesting open question that perhaps has to be left to time and more progress in science as of now. With this understanding we go back to our realm of condensed matter that has close ties with industry. Although not exclusively, but condensed matter applications usually correspond to energy scales of regular life, in other words the energy scales than can affect a chemical bond. It means that the systems that we will describe in this thesis will comprise of a collection of atoms. The way atoms interact or are impacted at this level of hierarchy is by sharing or donating electrons, or more generally by changes or *nuances* in their electronic structure, studying which for certain choices of materials form the basis of this thesis which is why we start with the Schrödinger equation [8].

The Schrödinger equation is *reductionist* in the sense that it is a mathematical description of a system composed of many particles in a quantum mechanical system, a system scale where the Planck's constant holds direct relevance. For a single non-relativistic particle in real space we can write,

$$i\hbar\frac{\partial}{\partial t}\Psi(\mathbf{r},t) = \left[-\frac{\hbar^2}{2m}\nabla^2 + V(\mathbf{r},t)\right]\Psi(\mathbf{r},t) \tag{1.1}$$

where $\Psi(\mathbf{r},t)$ is the wave-function at position $\mathbf{r}$ and time t, m is the mass of the particle and $V(\mathbf{r},t)$ is the potential that essentially contains information about the impact of the particle's environment on it and $\hbar$ is the reduced Plank's constant. Shortly after its formulation Paul Dirac who was jointly awarded the Nobel prize in physics with Schrödinger echoed the problems with reductionist philosophy and remarked [9] that,

> *The underlying physical laws necessary for the mathematical theory of a large part of physics and the whole of chemistry are thus completely known, and the difficulty is only that the exact application of these laws leads to equations much too complicated to be soluble. It therefore becomes desirable that approximate practical methods of applying quantum mechanics should be developed, which can lead to an explanation of the main features of complex atomic systems without too much computation.*

And indeed, solving eq.(1.1) for the simplest system even with the help of best high performance computers, as elaborated in page 16, is almost impossible without many other approximations which are more *constructionist* in nature. Realistic description of materials in this thesis start with such 'approximate practical methods' that are made and applied on the Schrödinger equation in due course and discussed in detail in chapter 2 that make this problem tractable.

1.2 Post-Schrödinger and pre-Kohn theories

A year after Schrödinger equation, D. L. Hartree made an attempt to find an approximate solution for the time-independent Schrödinger equation by assuming that the many-body ground state $\Psi(\mathbf{r}_1\sigma_1, \cdots, \mathbf{r}_N\sigma_N)$ for a specific nuclear configuration can be represented by a product of orthonormal one electron orbitals $\psi_i(\mathbf{r}_i\sigma_i)$ that themselves are a product of the spatial orbitals $\phi_i(\mathbf{r})$ and respective spin functions $\chi_i(\sigma)$[10] as,

$$H\Psi(\mathbf{r}_1\sigma_1, \cdots, \mathbf{r}_N\sigma_N) = E\Psi(\mathbf{r}_1\sigma_1, \cdots, \mathbf{r}_N\sigma_N) = E\prod_{i=1}^{N}\psi_i(\mathbf{r}_i\sigma_i) = E\prod_{i=1}^{N}\phi_i(\mathbf{r})\chi_i(\sigma) \tag{1.2}$$

He used the idea of **self-consistency** pioneered by Robert Bruce Lindsay [11] and started with an initial guess of *trial* one electron orbital functions which were used to evaluate the space charge distribution and the associated time-independent potential. This was then used to find a new set of wave-functions till the initial and the *final* wave-functions and potentials agreed within a defined accuracy. This way of solving the Schrödinger equation with various approximations in a self-consistent manner makes the crux of most computational methods used in theoretical condensed matter today including the ones employed in this thesis based on electron density or Green's functions. However, at the time of Hartree working on this problem Pauli's exclusion principle [12] had just been invented and was still in its older formulation and it wasn't directly evident that the electron wave-function should be antisymmetric. It was applied in Hartree's formulation as an external condition that multiple occupancy of spin orbitals must be avoided.

$$\Psi(\mathbf{r}_1, \mathbf{r}_2, \cdots, \mathbf{r}_N) = \frac{1}{\sqrt{N}}\begin{vmatrix} \phi_1(\mathbf{r}_1) & \phi_1(\mathbf{r}_2) & \cdots & \phi_1(\mathbf{r}_N) \\ \phi_2(\mathbf{r}_1) & \phi_2(\mathbf{r}_2) & \cdots & \phi_2(\mathbf{r}_N) \\ . & . & & . \\ . & . & & . \\ . & . & & . \\ \phi_N(\mathbf{r}_1) & \phi_N(\mathbf{r}_2) & \cdots & \phi_N(\mathbf{r}_N) \end{vmatrix} \tag{1.3}$$

In 1930, J C Slater [13] and V A Fock [14] independently showed that as per the then complete Pauli's exclusion principle in order to respect quantum statistics the wave-

function had to be anti-symmetric in nature for an exchange of position coordinates. The solution was to use the wave-function as a Slater product of one electron orbitals as eq.(1.3).

Solving the above *ansatz* for an anti-symmetrised wave-function made up of one-electron orbitals in a self-consistent manner became one of the most successful theories in quantum chemistry called the Hartree-Fock theory so much so that it is still in use at many levels [15]. The specificity of the Fermi-Dirac statistics followed by electrons, or fermions in general, that led to the Aufbau principle, can be called an emergent outcome of a system of identical particles under the Pauli exclusion principle. This was the first *many-body* effect, as per the use of the term in the contemporary condensed matter world. It led to the modern version of the periodic table, filling of the atomic orbitals and an understanding of chemical bonding. As a result it had a direct impact on determining energetics and properties of materials. While Hartree-Fock successfully accounted for the Fermi-Dirac statistics, it was an inherently mean-field approximation which we discuss in further details in the next section.

1.3 Mean field treatment

The use of the Slater determinant in the form of eq.(1.3) or an equivalent definition gives the exact wave-function of an electronic system obeying Fermi-Dirac statistics only when the electrons are non-interacting. In presence of electron-electron interactions the factorisation of the many-body wave function into single particle orbitals isn't guaranteed and thus is no longer exact and becomes an approximation. The Hartree-Fock field that is determined self-consistently using this expansion, inherits this strong approximation implicitly. With this the Hartree-Fock method essentially becomes a mean-field treatment where a multi-electron problem is reduced to a one-electron problem where each electron interacts with the rest of the world via an average or, mean field which is determined self-consistently. How it becomes a mean field treatment becomes clearer when the Coulomb interaction term, denoted by H_{int}, is written in the second quantised notation which is also the notation of choice when dealing with model Hamiltonians.

$$H_{\text{int}} = \frac{1}{2} \sum_{i,j,k,l} \langle\ i\ j\ |\ U\ |\ k\ l\ \rangle\ c_i^\dagger\ c_j^\dagger\ c_l\ c_k \tag{1.4}$$

where $c_i^\dagger, c_i$ are fermion creation and annihilation operator at site i, and U is the Coulomb interaction. The mathematical or computational evaluation of the quartic term $c_i^\dagger\ c_j^\dagger\ c_l\ c_k$ is difficult and warrants approximation. In the mean-field treatment one replaces this term with its pairwise average as,

$$\langle c_i^\dagger\ c_j^\dagger\ c_l\ c_k\rangle = \begin{cases} \langle c_i^\dagger c_k\rangle\ c_j^\dagger c_l + c_i^\dagger c_k\ \langle c_j^\dagger c_l\rangle - \langle c_i^\dagger c_k\rangle\ \langle c_j^\dagger c_l\rangle & \text{contains 'direct' terms} \\ -\langle c_i^\dagger c_l\rangle\ c_j^\dagger c_k - c_i^\dagger c_l\ \langle c_j^\dagger c_k\rangle + \langle c_i^\dagger c_l\rangle\ \langle c_j^\dagger c_k\rangle & \text{contains 'exchange' terms} \end{cases} \tag{1.5}$$

where the third and the sixth terms are just constant additions to the total energy. If the pairwise-averages above are performed using single Slater determinants as eq.(1.3), the Hartree-Fock Hamiltonian is obtained where the direct and the exchange terms above match those mentioned in eq.(2.68) in chapter 2. This is why Hartree-Fock theory is often called the mean-field theory of electrons.

1.4 Correlations

In general, in mathematical and natural sciences two quantities A and B are said to be correlated when

$$\langle\ A\ B\ \rangle \neq \langle\ A\ \rangle\langle\ B\ \rangle \tag{1.6}$$

i.e., average of a product is not equal to the product of averages. Averages in quantum mechanics are used for calculating physical observables, and thus the literature of **correlations** in physics morphs into a study of terms like eq.(1.4) where formalism are developed to capture the effects beyond factorisation approximations like the Hartree-Fock theory. In Ashcroft-Mermin [16], a textbook that will complete its 50$^{\text{th}}$ year of reign in the solid-state world 4 years from now, defines the correlation energy of an electronic system as the difference between the system's *exact* energy and its Hartree-Fock energy.

For electrons in a specific atomic orbital this becomes,

$$\langle\ n_\uparrow\ n_\downarrow\ \rangle \neq \langle\ n_\uparrow\ \rangle\langle\ n_\downarrow\ \rangle \tag{1.7}$$

where n_σ is the number operator for electrons with spin σ in that atomic orbital. The equality only holds when the *second* electron doesn't care if the atomic orbital is filled or not. It can be rephrased by saying that the behaviour of one electron is not independent of the behaviour of another.

Ideally all electronic systems are by definition correlated. But the correlation can be weak or strong. The relative success of mean-field approximations can be said to depend on this degree of correlation. A large part of condensed matter research, especially computational research in solids, which frames the points of address in this thesis, starts with electrons in a periodic potential. A consequence of this is that then electrons can be described by one-particle Bloch states [17] delocalised over the system and can be worked upon to various degrees by classical computers. Such a description, usually known as the independent electron approximation, is widely used by various mean-field treatments where the electrons feel each other only via (1) the Pauli exclusion principle

built into the formalism, and (2) an effective mean field potential. The theories that constitute this picture are often said to contribute to the *standard model* description of solids [18] where the interactions are weak and can be treated either with mean field approaches or static corrections to an effective mean field as done by density functional theory or by perturbative approaches beyond mean field.

1.5 Strong correlations in materials

A study of the impact of correlations, especially strong correlations, forms the leading theme of this thesis. To aid its study and understanding we first started with our practical and application-inspired interest, then we discussed the scientific and philosophical origins of the idea of emergence and its *fundamental* nature, following we looked at some initial developments of theories in brief and discussed their classification as mean field approaches and finally we discussed correlations[2]. From philosophies and theories we come back to materials, to practical life and an aspect of science that tries to answer the calls of society's needs[3] together with its job of quenching the curiosity of the human mind.

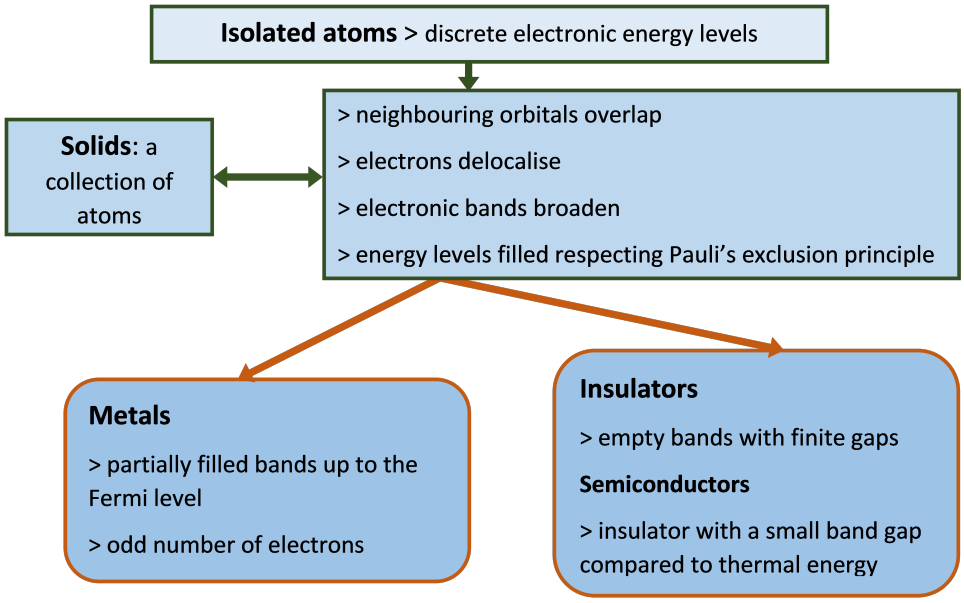


Figure 1.2: A simplified schematic representation of the band theory of solids.

[2]The path traversed to arrive at this point has slightly been like a meandering post-work, post-dinner evening walk in your neighbourhood. But to support this route taken we go back to Richard Feynman who said,

> *Study hard what interests you the most in the most undisciplined, irreverent and original manner possible.*

and that's what we did. Just followed perhaps the most famous Nobel laureate's instruction, nothing more!

[3], and funds,

Theories using the independent electron approximation were very successful with understanding semiconductor behaviour in the post world war era, especially the band theory summarised in fig.(1.2). It was phenomenally successful, was applied to explain the electrical resistance, optical absorption spectra for solid-state devices like a traditional transistor, solar cells, etc., and thus formed the framework on which the silicon valley and the entire microelectronic industry was built and is still in use. But as experiments advanced along with quantum mechanical explanations of observed phenomena, new materials, phenomena with increasing complexity were discovered with novel electronic properties suited for specific promising applications that required new conceptual developments.

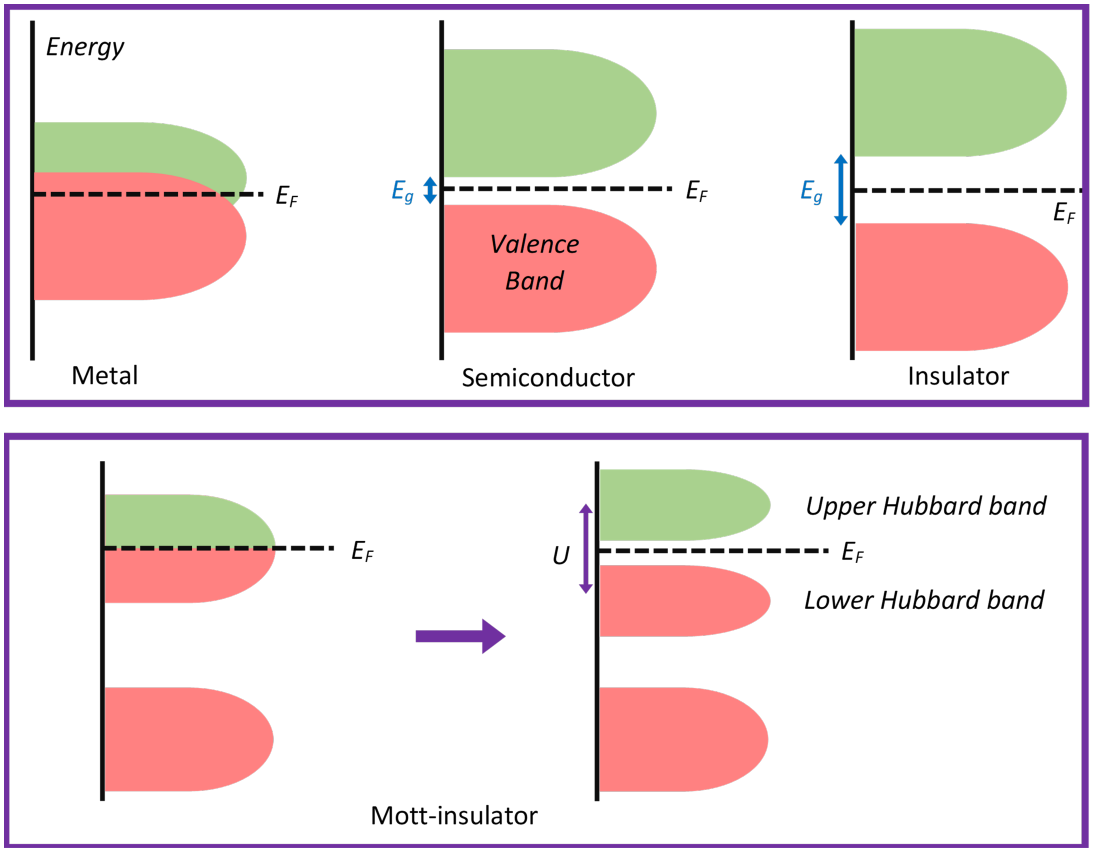


Figure 1.3: Schematic representation of *(above)* the band theoretical description of metal, semiconductor and insulator, and *(below)* how the Coulomb interaction terms give rise to Mott-insulating behaviour.

One significant mismatch was for transition metal monoxides like FeO, NiO, CoO which band theory predicted to be metallic but were in fact antiferromagnetic insulators. In 1963 the Hubbard model formulated independently by Martin Gutzwiller [19], Junjiro Kanamori [20] and, John Hubbard [21] was used to show how the competition between the Coulomb repulsion and the kinetic energy changed the band theory predicted ground state. The Hubbard model accounting for the Coulomb repulsion splits the erstwhile partially occupied single band in the band-theory picture to upper and

lower Hubbard bands separated by a gap, as depicted in fig.(1.3). Of these the lower Hubbard band is filled while the upper Hubbard band is empty leading to an insulating behaviour whose origin is at the electron-electron interaction term. This model and its physics has been discussed in detail in section 2.8. An additional but very important outcome of the Hubbard model was that band theory almost only allowed for paramagnetic metals and diamagnetic insulators, but the presence and strength of the Coulomb interaction led to the possibility of insulating states with almost a spectrum of magnetic properties as Curie paramagnetism, antiferromagnetism and even ferromagnetism [22]. In another instance to explain type-I superconductivity it was found that the electronic correlations could also extend to macroscopic distances. The celebrated BCS theory of John Bardeen [23], Leon Cooper [24] and Robert Schrieffer [25] successfully laid down that if the electron-phonon interaction dominated the electronic Coulomb repulsion, then a net attractive interaction favoured the formation of a condensed electronic state with a pair of electrons mediated by a phonon called Cooper pairs which led to a superconducting state. Another prominent discrepancy and refocusing on the role of strong correlations in academia as well as industry came in 1986 with the unexpected discovery of new high temperature copper oxide type-II superconductors [26][4] which were doped antiferromagnetic Mott insulators.

Room temperature superconductivity has potential applications as magnetically levitated vehicles, lossless power-lines, highly efficient electrical generators, some prospects which have become the need of the hour socially as well as politically owing the huge energy requirements of a fast progressing, gadget-dependent, highly populated modern society. All this resulted in materials with open d- or f-shells becoming the focus of interest and exploration for understanding novel properties like half-metallicity, spin-charge separation, a range of magnetic behaviour, tunable metal insulator transitions among others. Study of those materials became playground for how strong correlations, the competition between the kinetic energy and Coulomb terms as shown in fig.(2.4), can give rise to a complex phases that have industrially applicable relevance. Extensive technological applications, some of which we will be discussing in the next chapters, stem from such properties like the metal-insulator transition (MIT) in VO_2 that can be used to make smart windows to for an energy efficient temperature control technology [27], the MIT in $LaTiO_3$ (see chapter 6) can be used in a possible transistor design, etc. Other applications range from materials with open d or f-orbitals being used as multiferroics, as spintronic materials, spin Peierls materials, and many more.

1.6 Structure of the thesis

The work presented in this thesis can be categorised in three parts.

[4]It blew people's minds (and still does, fortunately or unfortunately) so much so that the Nobel prize was awarded the very next year of its discovery.

Chapters 1 and 2

Chapter 1 (this chapter) is the general introduction in the research field of strongly correlated systems and material science that discusses some main developments in this field, how it was shaped and arrived at this point and answers the *why* of the choice of this thesis' subject matter. In Chapter 2, we go deeper into the *how* i.e., the theories and approximations used and we describe in detail the density functional theory (DFT), Hubbard model, DFT+U formalism, dynamical mean field theory (DMFT). Along with them we discuss briefly the transport phenomena observed in models or materials studied using these theories viz., thermionic emission, quantum tunnelling, resonant tunnelling and methodologies used to study them including the Landauer-Butticker formula and non-equilibrium Green's functions (NEGF). Apart from this we also discuss density functional perturbation theory (DFPT) and methods to study disorder using density-functional based theories that we used in our study of a particular set of materials.

Chapter 3

In chapter 3 we study a Hubbard Hamiltonian defined on a 4-layer correlated interface and study the conditions on observation of Mott transition by implementing a DMFT loop in this set-up after defining a self-consistency measure. We use this set-up as a simplified model investigating the occurrence of resonant tunnelling and its relation to correlations and applied finite bias. This study is used to *set the stage* with a simplified example.

Chapters 4, 5, 6, 7

In chapter 4, we start our discussion with an alternative transistor design called a piezoelectric transistor which is based on the behaviour of Samarium monochalcogenides as piezoresistive elements. This is closely related to the presence of strongly correlated and partially filled $4f$ orbitals in Sm. We study this system in bulk using DFT and DFT+DMFT and compare our results to experiments. We discuss the presence of intermediate valence states, the role of $4f$ electrons, the nature of the transition whether it is Mott-like or not and the role of structural changes for this observed insulator to metal transition. In chapter 5, we study the behaviour of Sm-monochalcogenide thin films in a heterostructure set-up between W leads in order to analyse the thin film thickness for piezoresistive functionality corresponding to memory and transistor operations for transistor OFF state. We also investigate the role of $4f$ states in transport and the success of various level of theories in determining that. This formed a part of collaboration with our industry partners at National Physical Laboratory.

In the first half of chapter 6 we study two lanthanum metal oxides in the double perovskite structure La_2TiFeO_6 and La_2VCuO_6 initially for studying the role of charge

ordering between Ti-Fe and V-Cu for possible spintronic applications with our industry collaborators at Happy Electron Pvt. Ltd. The ordered phases could not be found experimentally and we theoretically studied the ground state and performed DFT+U based random structure search to understand the role of entropy, Lanthanum vacancies and overoxygenation in regards to the observed disorder. In the second half of this chapter we study another rare-earth oxide ceria and zirconia where the role of oxygen vacancies play a crucial role in determining their use as catalysts relevant for our industry partners at Johnson Matthey, Rahko Limited and AWS. We used DFT and DFT+U to study the vacancy formation energies, and investigated the role of soft phonon modes in facilitating the formation of vacancy formation. Finally in chapter 7, we summarised our findings and discussed further outlooks and my personal future research interests inspired by the work on this thesis.

Chapter 2

Theory

2.1 The solid-state Hamiltonian

The archipelago of subject matters that constitute each upcoming chapter all had a century old genesis. It was at the epilogue[1] of the nineteenth century. 1900 was the year that first saw the hypothesis of quantised energies by Max Planck in the form of his famous namesake postulate [28]. He tried to describe the observed spectral distribution of thermal radiation from a closed furnace i.e., the blackbody radiation, and to do that he *had to* interpret the vibrational energy of N oscillators not as a continuous, infinitely divisible quantity, but as a discrete quantity composed of an integral number of finite equal parts given by,

$$E = nh\nu \tag{2.1}$$

where n is an integer, h is the Planck's constant and ν is the frequency. This postulate at its inception still was a mathematical fiction attempting to solve the ultraviolet catastrophe and Max Planck himself was said to be baffled for why should light be 'quantised' in such energy packets [29]. Albert Einstein, in 1905, carried this idea forward by postulating that Planck's quanta were not mere fantasy but real particles called photons. He used it to explain the photoelectric effect [30] for which he was awarded the 1921 Nobel prize. This eventually led to 1924 when Louis de Broglie suggested that just as light has both wave-like and particle-like properties, electrons have wave-like properties [31]. He related the wavelength of an electron λ to its momentum p via the Planck's constant as,

$$\lambda = \frac{h}{p} \tag{2.2}$$

Further developments in the field quantum mechanics were pioneered by Bohr, Schrödinger, Dirac, Born and many others in the 20^{th} century. This eventually led to the development of many sub-fields in the study quantum systems over the next century and even the start of the efforts made in this thesis. Of all the great strides made, the one that we build our story from is the successful description of the quantum many-body Hamiltonian that describes a crystal in the non-relativistic regime. This equation can be said to be essentially been known since the birth of the Schrödinger equation.

Thus, the simple non-relativistic time-independent Hamiltonian describing a collection of atoms composed of interacting nuclei, whose internal structures aren't considered, and interacting electrons with Coulombic interaction between them can be simply written as,

[1] Interested in the middle-earth of correlations? See III.2

$$H = -\frac{1}{2M}\sum_{I}\nabla_I^2 - \frac{1}{2m}\sum_{i}\nabla_i^2 + \frac{1}{2}\sum_{I,J}\frac{Z_I Z_J}{|\mathbf{r}_I - \mathbf{r}_J|} - \frac{1}{2}\sum_{i,I}\frac{Z_I}{|\mathbf{r}_I - \mathbf{r}_i|} + \frac{1}{2}\sum_{i,j}\frac{1}{|\mathbf{r}_i - \mathbf{r}_j|}, \tag{2.3}$$

where i, I and m, M represent the electronic and the nuclei coordinate indices and masses, respectively. Eq.(2.3) is a partial differential eigenvalue equation and the computational power required to solve such a set of equations increases faster than the square of the number of the system coordinates. To make the situation tractable the Hamiltonian is simplified using the **Born-Oppenheimer (BO) approximation** [32] which states that since the mass of an atomic nucleus is more than 1000 times the mass of an electron, the typical timescale of the nuclear motion is such that electrons relax to their ground-state configuration so rapidly that for all practical purposes the nuclear position can be assumed to be stationary for electronic motion. This decouples the electronic and nuclear degrees of freedom, and describes nuclei which move quantum mechanically in an effective potential stemming from the electrons. However usually solving for the nuclear equation isn't mostly (with many exceptions) crucial to the electronic properties as the nuclear wave functions are usually highly localised with large separations between the nuclear sites. Thus one applies the **classical nuclei approximation** that identifies the quantum mechanical average of nuclear positions with their classical positions. This makes the decoupled nuclear and electronic problem to just that electronic problem. To make our lives simpler, we choose to only deal with crystals and assume translational invariance. This leads us to Bloch's theorem and thus we can write the one-electron wave-function as a periodic function obeying the periodicity of the lattice times a plane wave. Note that unless specified, in this thesis we have adopted atomic units with $\hbar = e = m = 1$.

2.2 Density Functional Theory

The simplified Hamiltonian after the BO approximation thus looks like,

$$H = -\frac{1}{2}\sum_{i}\nabla_i^2 + \sum_{i} v(\mathbf{r}_i) + \frac{1}{2}\sum_{i,j}\frac{1}{\mathbf{r}_{ij}} + V_{nn} \tag{2.4}$$

where the first term represents the kinetic energy of the electrons, $v(\mathbf{r}_i)$ represents the *external* potential acting on the electron i due to the nuclei, the third term stands for the electron-electron interaction with $\mathbf{r}_{ij} = |\mathbf{r}_i - \mathbf{r}_j|$, and V_{nn} represents the interaction of the nuclei with one another. V_{nn} can also be extended to include other terms that are not germane to the electronic problem and can be included as an additional contribution to the total energy. The solution of eq.(2.4) will be given by the quantum mechanical wave-function $\Psi(\mathbf{r}_1, \mathbf{r}_2, \mathbf{r}_3, \cdots, \mathbf{r}_N)$ which in principle can be used to calculate a physical

observable O as,

$$\langle O \rangle = \langle \Psi | O | \Psi \rangle \tag{2.5}$$

However the story still is far from finished. Even in a single mole of an element, number of atoms are of the order of 10^{23} with each atom comprising its characteristic number of electrons. Solving such a system of differential equations is a task better not undertaken even for the simplest systems. Even for 1-particle systems under various approximations, the exact analytical solution is not available. To combat this we have three (not-exhaustive) choices.

- Numerical solution: We can solve the differential equation numerically. This although appealing is still quite hard. For example let us consider iron (Fe), one of the most common materials used which in its neutral state has a wave-function that is a function of 78 variables. If this function is to be stored for 10 values of the wave-function, information containing 10^{78} entries will be needed, which even if are reduced somewhat by symmetry will need storage to be provided by a number of atoms larger than the total number of atoms in the whole solar system. So, even if we attempt a numerical solution aided by some approximation, that approximation should *drastically* reduce the number of degrees of freedom without sacrificing important information about the physical system.

- Perturbation theory: We can approximate the Hamiltonian as,

$$H = H_0 + H_{\mathrm{PT}} \tag{2.6}$$

  where H_0 is considered the non-interacting Hamiltonian with an easy or known solution and H_{PT} is the perturbative Hamiltonian whose effect we want to understand. This is often the approach taken for model systems, as we have done in chapter 3, where a real system is reduced to a schematic model comprising usually of a few sites in a simplified geometry suited for a specific physical scenario. Then the role of various terms in the Hamiltonian are studied under varying degrees of approximations.

- Variational principle: For a given Hamiltonian, H, we can choose a trial wave-function, e.g., a Gaussian, and use that to evaluate eigenenergies as,

$$\varepsilon[\Psi] = \frac{\langle \Psi | H | \Psi \rangle}{\langle \Psi | \Psi \rangle} \tag{2.7}$$

  such that if E_0 is the actual ground state energy corresponding to the actual ground state wave-function Ψ_0 then,

$$\varepsilon = \begin{cases} = E_0 \ , \ \text{if } \Psi = \Psi_0 \\ \geq E_0 \ , \ \text{otherwise} \end{cases} \tag{2.8}$$

This is used by a large class of methods in electronic physics combined with numerical paradigms. There usually a one-particle picture is used that leads to a set of self-consistent equations which is then solved numerically. Some popular methods based on the variational principle are Hartree and Hartree-Fock methods [33], multiconfiguration methods [34], etc.

2.2.1 Density based formalism

We focus here on a subset of methods that aims at reducing the dimensionality of the problem from $3N$, where N is the number of electrons in the system, to a smaller number for better computational scaling. This is based on the idea that the expectation value of a physical quantity, as written in eq.(2.5), can be calculated not just through Ψ but also through other derived quantities from Ψ that depend on lesser number of variables. To proceed we note that the Hamiltonian described in eq.(2.4) is a sum of one and two particle operators of which the nuclear-electron interaction term has only one-particle terms and thus can be written as,

$$V_{\text{ne}} \equiv \langle\Psi|\sum_i v(\mathbf{r}_i)|\Psi\rangle = \int d\mathbf{r}\; v(\mathbf{r})\rho(\mathbf{r})\;, \text{ where} \tag{2.9}$$

$$\rho(\mathbf{r}_1) = N\int \Psi^*(\mathbf{r}_1,\mathbf{r}_2,\mathbf{r}_3,\cdots,\mathbf{r}_N)\Psi(\mathbf{r}_1,\mathbf{r}_2,\mathbf{r}_3,\cdots,\mathbf{r}_N)d\mathbf{r}_2 d\mathbf{r}_3\cdots d\mathbf{r}_N \tag{2.10}$$

$$= \langle\Psi|\sum_i \delta(\mathbf{r}_1-\mathbf{r}_i)|\Psi\rangle \tag{2.11}$$

From above equation, $\rho(\mathbf{r}_1)$ can be identified as the single-particle density operator. Similarly the two-particle electron-electron interaction term can be written as,

$$V_{\text{ee}} \equiv \langle\Psi|\,\frac{1}{2}\sum_{i,j}\frac{1}{\mathbf{r}_{ij}}\,|\Psi\rangle = \int d\mathbf{r}_1 d\mathbf{r}_2 \frac{\Gamma_2(\mathbf{r}_1,\mathbf{r}_2)}{\mathbf{r}_{12}}, \text{ where} \tag{2.12}$$

$$\Gamma_2(\mathbf{r}_1,\mathbf{r}_2) = N(N-1)\times \int \Psi^*(\mathbf{r}_1,\mathbf{r}_2,\mathbf{r}_3,\cdots,\mathbf{r}_N)\Psi(\mathbf{r}_1,\mathbf{r}_2,\mathbf{r}_3,\cdots,\mathbf{r}_N)d\mathbf{r}_3\cdots d\mathbf{r}_N \tag{2.13}$$

$$= \langle\Psi|{\sum_{i,j}}'\delta(\mathbf{r}_1-\mathbf{r}_i)\delta(\mathbf{r}_2-\mathbf{r}_j)|\Psi\rangle\;, \tag{2.14}$$

which is the two-particle density operator. The prime ($\prime$) on the summation implies that double summation is avoided. Following the similar logic, the kinetic energy can

be written as,

$$\mathrm{T} \equiv -\langle\Psi|\ \frac{1}{2}\sum_i \nabla_i^2\ |\Psi\rangle = -\frac{1}{2}\int d\mathbf{r}_1 \left[\nabla_1^2\ \gamma(\mathbf{r}_1;\mathbf{r}_1')\right]_{\mathbf{r}_1=\mathbf{r}_r'}\ ,\ \text{where} \quad (2.15)$$

$$\gamma(\mathbf{r}_1;\mathbf{r}_1') = N\int \Psi^*(\mathbf{r}_1',\mathbf{r}_2,\mathbf{r}_3,\cdots,\mathbf{r}_N)\Psi(\mathbf{r}_1,\mathbf{r}_2,\mathbf{r}_3,\cdots,\mathbf{r}_N)d\mathbf{r}_2 d\mathbf{r}_3\cdots d\mathbf{r}_N \quad (2.16)$$

$$= \langle\Psi|\sum_{i,j}{}' \delta(\mathbf{r}_1-\mathbf{r}_i)\delta(\mathbf{r}_2-\mathbf{r}_j)|\Psi\rangle\ , \quad (2.17)$$

such that $\gamma(\mathbf{r}_1;\mathbf{r}_1')$ is the reduced density matrix that reproduces the one-particle and two-particle density operators under the following conditions.

$$\rho(\mathbf{r}_1) = \gamma(\mathbf{r}_1;\mathbf{r}_1) \quad (2.18)$$

$$\Gamma_2(\mathbf{r}_1,\mathbf{r}_2) = \gamma(\mathbf{r}_1,\mathbf{r}_2;\mathbf{r}_1,\mathbf{r}_2)\ ,\ \text{where} \quad (2.19)$$

$$\gamma(\mathbf{r}_1,\mathbf{r}_2;\mathbf{r}_1',\mathbf{r}_2') = N(N-1)\times \quad (2.20)$$

$$\int \Psi^*(\mathbf{r}_1',\mathbf{r}_2',\mathbf{r}_3,\cdots,\mathbf{r}_N)\Psi(\mathbf{r}_1,\mathbf{r}_2,\mathbf{r}_3,\cdots,\mathbf{r}_N)d\mathbf{r}_3\cdots d\mathbf{r}_N \quad (2.21)$$

With this we can write the total energy in terms of either the one-particle or two-particle or reduced density matrices as,

$$E[\rho,\gamma,\Gamma_2] = T[\gamma(\mathbf{r}_1;\mathbf{r}_1')] + V_{\mathrm{ne}}[\rho(\mathbf{r})] + V_{\mathrm{ee}}[\Gamma_2(\mathbf{r}_1,\mathbf{r}_2)] + V_{\mathrm{nn}} \quad (2.22)$$

It is easy to generalise the above for a spin-polarised situation by writing the total density as a sum of the two spin components. In this manner we can bypass explicitly calculating the wave-function and practically reduce the dimensionality of our space from $3N$ (number of arguments of a wave-function) to 3 (i.e., the density, a function of each point in space). It is important to note that the above formalism is possible only if the reduced density matrices can be directly determined by minimising the energy functional which in turn implies that an antisymmetric wave-function should be available from which the reduced density matrices can be obtained at the first place. This is the N-representability problem [35]. The necessary and sufficient conditions to get $\gamma(\mathbf{r}_1;\mathbf{r}_1')$ and $\Gamma_2(\mathbf{r}_1,\mathbf{r}_2)$ are not known in general but are known for $\rho(\mathbf{r})$ and are given by,

$$\int \rho(\mathbf{r})\ d\mathbf{r} = N\ ,\quad \text{and}\ \rho\ (\mathbf{r}) \geq 0 \quad (2.23)$$

This makes the single particle electron density which is also the simplest form of reduced density in a many-particle system, a promising candidate for developing a formalism for the quantum mechanics of electrons. Another crucial advantage is that it is also a physical quantity in real three-dimensional space which makes physical

interpretations, visualisation, theoretical extensions and experimental comparisons of the solution of energy functional easier. However any formalism of quantum mechanics has to ensure that the density contains sufficient information to describe a physical system in order to calculate physical observables and it should give a quantity that can be directly calculated in theory and matched with experiments. Development of such density functional based theories started with the Thomas-Fermi method [36] in 1927. However the birth of currently the most important method also used in this thesis, the density functional theory (DFT), can be attributed to two famous theorems published in 1964.

2.2.2 Hohenberg-Kohn theorems

- **The first Hohenberg-Kohn theorem** [37] states that for a system of interacting particles in an external potential $v(\mathbf{r})$, the external potential is determined uniquely up to a constant by the ground state particle density [37]. Uniquely identifying $v(\mathbf{r})$ in turn uniquely identifies the Hamiltonian, and consequently the full many particle ground state and the energy functional $E_v(\rho)$, leading to the second theorem.

- **The second Hohenberg-Kohn theorem** states that the energy functional for the ground state that corresponds to the lowest energy will in turn uniquely identify the *true* ground state density. This set of theorems is based on the variational principle and essentially says that identical densities cannot arise from two different external potentials, and that if we have the *true* density, we can find the system ground state.

The above two theorems uniquely identify the ground state of an electronic system from a rather simple quantity viz., electron density. Now going back to eq.(2.22), we observe that to write the electron density in the first place, we need to express the electron-electron interaction term and the kinetic energy term in terms of single particle density. For the electron-electron interaction term ones uses the decomposition of the two-particle density to one particle density with an associated correlation function $f(\mathbf{r}_1, \mathbf{r}_2)$ as,

$$\Gamma_2(\mathbf{r}_1, \mathbf{r}_2) = \rho(\mathbf{r}_1)\rho(\mathbf{r}_2)[1 - f(\mathbf{r}_1, \mathbf{r}_2)] \tag{2.24}$$

and separates the classical electrostatic contribution, also called the Hartree term, from it as,

$$E_{\text{coul}}[\rho] = \frac{1}{2}\int\int \frac{\rho(\mathbf{r}_1)\rho(\mathbf{r}_2)}{\mathbf{r}_{12}} d\mathbf{r}_1\, d\mathbf{r}_2 \tag{2.25}$$

The exact kinetic energy functional $T[\rho]$ is replaced by the kinetic energy of an auxiliary

system of non-interacting particles $T_S[\rho]$ as,

$$E_v[\rho] = T_s[\rho] + \int d\mathbf{r}\ v(\mathbf{r})\rho(\mathbf{r}) + E_{\text{coul}}[\rho] + V_{\text{nn}} + E_{\text{XC}}[\rho]\ ,\ \text{where} \tag{2.26}$$

$$E_{\text{XC}}[\rho] = \{\ (T[\rho] - T_s[\rho]) + (V_{\text{ee}}[\rho] - E_{\text{coul}}[\rho])\ \} \tag{2.27}$$

is the exchange-correlation energy functional whose role we will discuss in detail in 2.2.4.

2.2.3 Kohn-Sham approach

The kinetic energy functional, as described above, is obtained by solving the one-particle Schrödinger equation for a system of non-interacting particles as,

$$\left[-\frac{1}{2}\nabla^2 + \lambda(\mathbf{r})\right]\psi_i = \epsilon_i\psi_i \tag{2.28}$$

where $\lambda(\mathbf{r})$ is chosen such that the solution of the above equation yields

$$\rho(\mathbf{r}) = \sum |\psi_i|^2 \tag{2.29}$$

and the kinetic energy functional can be evaluated by solving eq.(2.28) substituting the following equation of $T_s[\rho]$

$$T_s[\rho] = \sum_i \epsilon_i - \int d\mathbf{r}\ \lambda(\mathbf{r})\ \rho(\mathbf{r}) \tag{2.30}$$

in the expression for the total energy functional given in eq.(2.26) and minimising the equation variationally. This leads to

$$\sum_i \delta\epsilon_i = \int dr\ \rho(\mathbf{r})\ \delta\lambda(\mathbf{r})\ ,\ \text{and} \tag{2.31}$$

$$\lambda(\mathbf{r}) = v(\mathbf{r}) + \frac{\delta E_{\text{coul}}}{\delta\rho(\mathbf{r})} + \frac{\delta E_{\text{XC}}}{\delta\rho(\mathbf{r})} \tag{2.32}$$

which shows that if $\lambda(\mathbf{r})$ is chosen as per the above expression, the single particle Schrödinger equation of the auxiliary system, leads to the correct ground state density for the original system. This forms the basis for the **Kohn-Sham density functional scheme** [38] where a set of N non-linear integro-differential equations given for an auxiliary one-particle system with an effective potential v_{eff} is given by,

$$\left[\ \frac{1}{2}\nabla^2 + v_{\text{eff}}(\mathbf{r},\rho)\right]\psi_i = \epsilon_i\psi_i, \tag{2.33}$$

$$v_{\text{eff}}(\mathbf{r},\rho) = v(\mathbf{r}) + \int \frac{\rho(\mathbf{r}')}{|\mathbf{r}-\mathbf{r}'|}d\mathbf{r}' + \frac{\delta E_{\text{XC}}}{\delta\rho(\mathbf{r})} \tag{2.34}$$

are solved self-consistently by an iterative numerical method starting from a trial $\rho(\mathbf{r})$. The entire DFT formalism relies on existence of a ground state density which in reality is unknown. As discussed above $\rho(\mathbf{r})$ is obtained numerically in a self-consistent manner and thus relies heavily on the trial function. Another unknown is the exchange-correlation functional which is usually approximated as discussed in the next section.

2.2.4 Exchange correlation functionals

There exists a zoo of energy functionals, one more appropriate than the other depending on the system and the system environment. The most popular one was suggested by Kohn and Sham themselves in 1965 [38] is called the **Local Density Approximation (LDA)**. In LDA the exchange-correlation functional depends on the value of electron density at each point in space only. Usually this is derived from a homogeneous electron gas model and is written as,

$$E_{\mathrm{XC}}[\rho(\mathbf{r})] = \int \rho(\mathbf{r})\ \epsilon_{\mathrm{XC}}[\rho(\mathbf{r})]\ d\mathbf{r} \tag{2.35}$$

where $\epsilon_{\mathrm{XC}}[\rho(\mathbf{r})]$ is the exchange-correlation energy per particle of a homogeneous electron gas with charge density $\rho(\mathbf{r})$. E_{XC} can be linearly decomposable into exchange and correlation terms as,

$$E_{\mathrm{XC}} = E_{\mathrm{X}} + E_{\mathrm{C}} \tag{2.36}$$

Here the exchange term E_{X} is known for homogeneous electron gas analytically [39] whereas analytical expressions for the correlation term E_{C} in a homogeneous electron gas are only available in the high or the low density limits corresponding to infinitely weak or infinitely-strong correlation limits, respectively. Many-body perturbation theory has been successfully implemented to obtain analytical expression for full range of densities in good agreement with values obtained with quantum Monte Carlo simulations for the energy of the homogeneous electron gas [40].

LDA is often called an *uncontrolled* approximation because its validity is determined by its ability to match experimental results. Due to this reason LDA is a rather lucky approximation as there is a tendency for the exchange energy to be underestimated and the correlation energy to be overestimated [41] in such a way that the errors due to the exchange and correlation parts tend to compensate for each other to a certain degree. This stems from the assumption of homogeneity in the homogeneous electron gas approximation, and is partially corrected for by considering a functional dependence of E_{XC} on density as well as the gradient of density which corrects for changes in density away from the respective coordinate [42]. These sets of approximations are known as **generalised gradient approximations (GGA)** [43] [44].

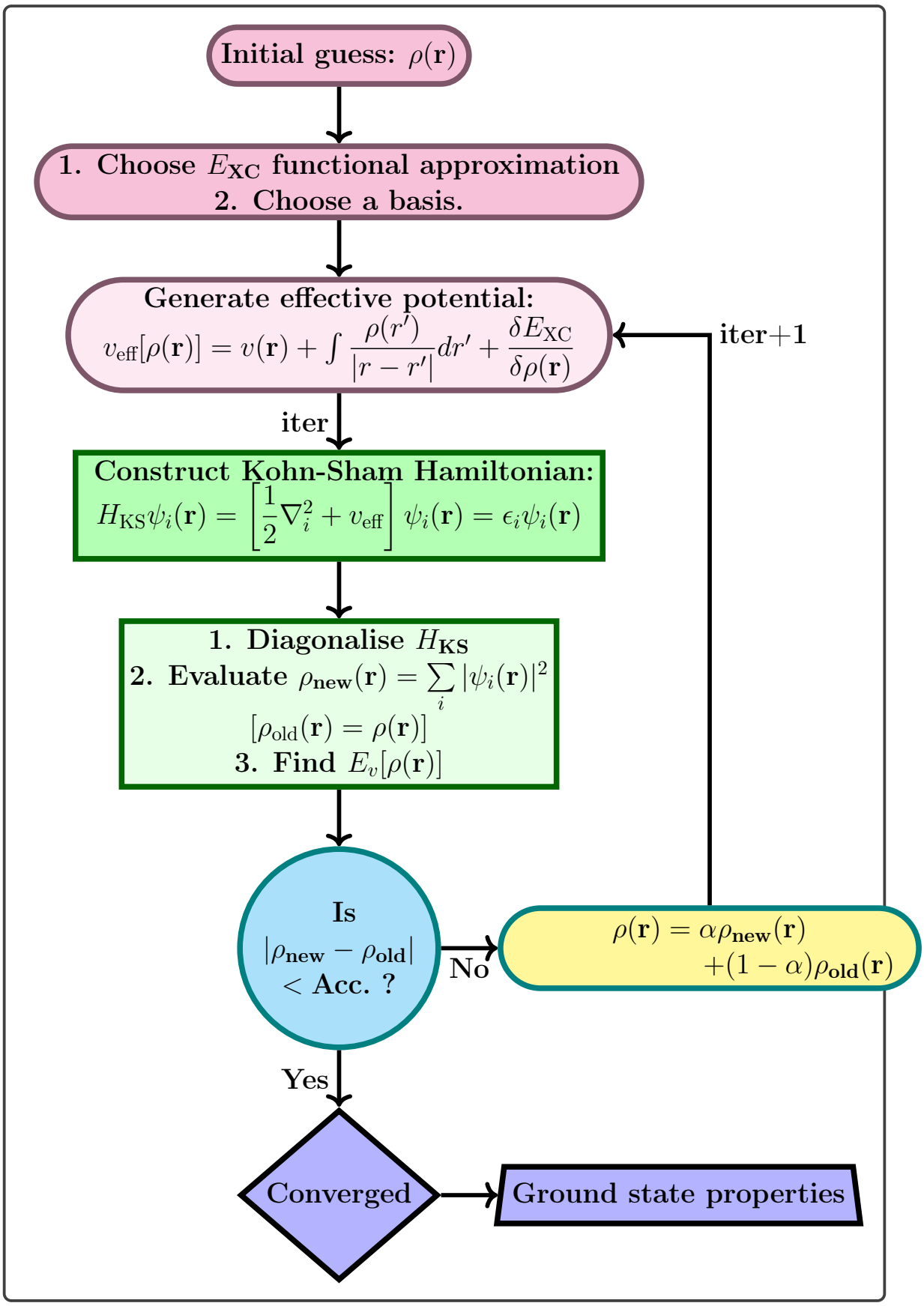


Figure 2.1: Flowchart illustrating the self-consistent iterative scheme to solve the Kohn-sham equations in the density functional theory framework.

Another class of functionals known as the **hybrid functionals** incorporate a portion of exact exchange from Hartree–Fock theory [45] with the rest of the exchange–correlation energy from *ab initio* or empirical sources [46]. The parameters determining the contribution of each individual functional are usually fitted by comparing the functional's predictions to experimental or thermochemical data [47].

The flowchart in fig.(2.1) outlines the algorithmic flow of the DFT self-consistency cycle. Note that the initial guess of the electron density is usually inspired from experiments or from the literature using values typical for a certain class of materials in specific physical situations. Another important choice in using DFT for real systems is the choice of a basis. The wave-functions are then described as a linear combination of the basis functions which are then used to evaluate density at various stages of the cycle in fig.(2.1). Basis functions relevant to this thesis have been discussed in detail in 2.3.

2.3 Basis Sets

So far in our discussion of DFT in 2.2 we saw that by following Kohn-Sham formalism, the many-body problem can be mapped to a problem of independent particles where by solving the one-particle Kohn-Sham equations we can find the eigenvectors and eigenvalues. We rewrite the Kohn-Sham equations for a given density $\rho(\mathbf{r})$,thus omitting ρ in equations, with explicit spin dependence to discuss the theory of basis sets.

$$\left[-\frac{1}{2}\nabla^2 + V_{\text{eff}}^{\sigma}(\mathbf{r})\right]\Psi_i^{\sigma}(\mathbf{r}) = \epsilon_i^{\sigma}\Psi_i^{\sigma}(\mathbf{r}) \tag{2.37}$$

But finding the eigenvector Ψ_i^{σ} is not only expensive but also inefficacious, as analysing that information freightage will not only be a challenge but physical quantities of interest can be extracted and understood by studying lesser data, and avoiding this was the main motivation behind DFT. But even though the primary quantity of interest is the density, we still need an expression of the eigenvectors to write the density as the very first step, and for further chemical analysis. The way out is obtained by expanding the eigenvectors in terms of functions of known properties or **basis sets** as,

$$\Psi_i(\mathbf{r}) = \sum_{\alpha} c_{i\alpha} f_{\alpha}(\mathbf{r}) \ , \tag{2.38}$$

where $f_\alpha(\mathbf{r})$ are the **basis functions**. In this way, the problem of finding the eigenvectors get morphed into the problem of finding some complex coefficients $c_{i\alpha}$ in the expansion of the eigenvectors in terms of their basis functions.

There are various methods based on different basis function expansions each with their own advantages and disadvantages. The choice of the basis relies heavily on the problem at hand as each method has its own reach and realm of application. So the practical choice depends on understanding the pros and cons and knowing what are

the physical quantities of interest for the problem and whether those can be computed accurately and efficiently using an expansion in a given basis set. There are three main families of DFT codes depending on their use of basis sets. We will now have a closer look at them one by one.

2.3.1 Atomic sphere basis

This definition of basis sets make the most precise and reliable pedigree among all. Here an all electron problem is solved without any pseudopotential approximations that are discussed in detail section 2.4. The primary idea is to carve the problem into spherical regions of interest i.e., the unit cell is divided into spherical regions around each nucleus where the atomic potential is much larger than elsewhere in the lattice and the features of that region are atomic-like, and atomic-like orbitals are used within the sphere to describe the system. The interstitial regions between the atoms are described by smoothly varying functions, usually plane waves with the condition that the two approximation to the basis functions match at the boundary or the sphere surface. This can be attained in many ways. One such way is using Linearised Muffin Tin Orbitals or LMTO basis. An electronic structure code using this basis is Questaal [48], [49].

2.3.2 Plane wave basis

Plane wave codes have been and still are widely used among physicists with a lot of functionalities available. In this the eigenfunctions can be written as a linear combination of plane waves like eq.(2.39).

$$\Psi_{i,\mathbf{k}}(\mathbf{r}) = \sum_{\mathbf{g}} c_{i,\mathbf{g}} \left[\frac{1}{\sqrt{\Omega}} e^{i(\mathbf{k}+\mathbf{g})\cdot\mathbf{r}} \right] \tag{2.39}$$

where the plane waves $e^{i\mathbf{g}\cdot\mathbf{r}}$ have the periodicity of the lattice obeyed by the reciprocal lattice vectors $\mathbf{g}$ occupying a volume Ω.

They are conceptually very simple with essentially Fourier transforms being used to write the eigenfunctions and thus are easy to implement. They are asymptotically complete and allow for systematic convergence which is primarily dependent on increasing the cut-off energy and making the k-mesh finer. The definition of the plane waves are also spatially unbiased with no dependence on atomic positions and related errors. Due to this reason for plane wave code every point in space has the same accuracy and vacuum costs the same computationally as matter. Given the absence of atomic structure or any radial or angular momentum function obtained as solutions of some equation, they are not suited to represent any specific function. This can have disadvantages as compared to other bases when representing, say, p_x or d_{xy} orbitals. Hundreds of plane waves are needed per atom to reach the desired accuracy in a DFT calculation and thus

are in-adequate for larger systems. Strongly localised orbitals are hard to converge as well. In spite of these shortcomings, due to its conceptual and implementation's simplicity, plane-wave basis codes are one of the most well developed and used codes in the physics community. We have used plane wave basis sets in chapters 4 and 6.

2.3.3 Localised basis

Typical DFT calculation where diagonalisation of the Hamiltonian is carried out scales in CPU load as $\mathcal{O}(N^3)$ where N is the number of particles in the system considered. This substantially limits the problems we can solve. For plane wave codes, the number of plane waves used increases with the unit cell volume irrespective of the number of atoms which limits the amount of vacuum used with system size which is particularly relevant for surfaces. A desirable scaling order is $\mathcal{O}(N)$ both in computational time and memory. This feature is called linear scaling and accessing the local behaviour of the system is its key point.

To achieve this, a large system is split in small regions or boxes whose electronic properties, interaction with neighbours are analysed. Since the system is large and divided into many regions, more number of calculations are needed corresponding to each region but the computational cost for each region is small. This is sometimes called the 'divide and rule' policy. For such a description we need a basis set of localised functions and the respective numerical prefactor for each. In order to get an efficient basis, there are two primary aspects: (i) number, and (ii) range of localisation of basis functions needed per atom. There are various available choices of basis functions in the literature, e.g., Bessel functions in overlapping sphere, non-orthogonal generalised Wannier functions, atomic orbitals, etc. In chapter 5 we have used atomic orbitals as linearised localised basis. For reasons mentioned below and in chapter 5, this particular choice of basis has many parameters to fix based on the system requirements and approximations that can substantially impact the physical quantities of interest, so we will look into these in further details.

Atomic Orbitals

A linear localised basis using atomic orbitals looks like,

$$\Phi_{Ilmn}(\mathbf{r}) = \mathbf{r}_{Iln}(|\mathbf{r}_I|)Y_{lm}(\hat{r}_I), \qquad \hat{\mathbf{r}}_I = \frac{\mathbf{r}_I}{|\mathbf{r}_I|}\ , \tag{2.40}$$

where $\mathbf{r}_{Iln}(|\mathbf{r}_I|)$ and $Y_{lm}(\hat{\mathbf{r}}_I)$ are the radial and angular momentum functions respectively. I is the atomic index, l is the angular quantum number, and m is the magnetic quantum number. Note that n has a special meaning here. It allows that for a given quantum address of I, l, m we may include more than one basis function or multiple orbitals.

Here $\mathbf{r}_{Iln}(|\mathbf{r}_I|)$ can be described in several ways. They can be linear combination of Gaussians. This particular choice is quite popular in the quantum chemistry field owing to the property that product of two Gaussians is a Gaussian which has led to development of efficient libraries for integration. Then $\mathbf{r}_{Iln}(|\mathbf{r}_I|)$ can also be expanded in terms of Slater type orbitals which resemble the shape of atomic orbitals. Another way is to numerically solve the Schrödinger equation of isolated atoms and tabulate the radial functions. Then at run-time those tables are used to interpolate in the required regime. This representation is called Numeric Atomic Orbitals (NAO) which we have used in this thesis when using the SIESTA code, explained in 5.2.

Basis type	Advantages	Disadvantages
Atomic Sphere basis	• Most accurate • Asymptotically complete • Systematic convergence possible	• Computationally expensive • Difficult implementation •$\|E_{tot}\|$ very high ⇒ if $\Delta E < \|E_{tot}\|$ substantially, the calculation must be very precise & well converged
Plane wave basis	• Widely used & well developed • Conceptually straightforward • Easy implementation • Asymptotically complete • Systematic convergence possible • No spatial dependence	• Need hundreds of plane waves for reasonable accuracy • Vacuum costs same as matter • Difficult convergence for localised orbitals • Specific functional forms not well represented (e.g., p_x)
Localised Atomic Orbital Basis	• Very efficient: few basis functions needed • Reduced CPU time & memory requirements • Vacuum almost free • High accuracy achievable • Large systems, surfaces interfaces accessible on modest platforms	• No unique basis definition • No systematic convergence • Realistic basis search needs substantial human and computational effort • Pulay terms always important

Table 2.1: A summary of three widely used basis types, their benefits and pitfalls.

Atomic orbitals usually require only 3-5 (or < 10) basis functions per atom even

when aiming for high accuracy, which is a massive reduction if one compares to plane wave basis sets which require about a hundred functions per atom. This translates to large reduction in computer time and memory, and makes bigger systems computationally accessible. Vacuum can be added almost for free, which makes electronic structure problems with surface, interfaces, molecules capable of being handled. Given we are using orbitals which are a solution of the atomic problem, physical interpretation of quantities of interest like projected density of states, population analysis are straightforward. However the choice of constructing the appropriate basis isn't unique, and thus there is no single way of attaining convergence systematically. Usually substantial human and computational effort is needed to search for good and relevant basis sets for a given configuration of atoms as will be seen later in 5.4.1. This problem is similar to pseudopotential optimisation problem, many-a-times existing alongside that. Also, since the whole paradigm is dependent on atomic positions, Pulay terms are always relevant.

2.4 Pseudopotentials

All the electrons in an atom that we want to simulate can be categorised into two parts viz., the core and the valence electrons. The core electrons are characterised by a large negative value of the nuclear potential of the order of a few hundred eV when compared to the valence electrons. In the core regions the nuclear potential also changes sharply with nuclear distance as expected from the $\frac{1}{r}$ behaviour for smaller values of r. For valence electrons, the nuclear potential changes smoothly and slowly corresponding to typical nuclear distance of > 20 Å which commensurate with the typical distances of the valence electrons from the first and second nearest-neighbours, and thus carries the most physical relevance.

If the Schrödinger equation is solved for all electrons of an atom, then the typical eigenvalues of the core electrons will be between $100 - 1000$ eV below the valence energy eigenvalues and the valence energy eigenvalues will be clustered together within a few 10s of eV. Then if we plot the radial part of the wave-function, we will see that the wave-function corresponding to core atoms go to 0 before typical valence electronic distances, and thus can be expected to be blind to the valence electrons and those belonging to the neighbouring atoms. Due to the core electrons of an atom being very localised in space and deep in energy, they are mostly imperceptive and inert to the environment and effects of valence electrons in phenomenon like chemical bonding. If we solve the Schrödinger equation for an atom, a singly positively charged (1+) ion, a doubly positively charged (2+) ion, then although the valence charge density will show drastic modifications, the core charge will remain essentially unperturbed.

Apart from this, to respect the orthogonality between different orbitals, in the small core region in space, the wave-functions will have multiple nodes with sharp oscillations.

In order to capture that *wigglesome*-effect, either a very dense real space grid will be needed or a representation in the Fourier transformed space will need large contribution from shorter wavelengths. It implies that when using a plane-wave basis, we will need a large number of plane waves to get a good approximation of the system.

If one looks at cases of interest in electronic structure calculations, the most important effect of the core electrons is nuclear screening. This and the precursory discussion along with the fact that we have to solve the Schrödinger equation for more number of electrons, makes the first-principle calculation very expensive in return for little practical significance. One solution can be to ignore the dynamics of the core electrons or as physicists say, *freeze* them, along with the nucleus, and replace their effects by an effective potential, or **pseudopotential**.

The pseudopotential is constructed to have the radial wave-function of same shape as the all electron wave function beyond a chosen cut-off radius $\mathbf{r} > \mathbf{r}_c$, but the oscillations within the core region $\mathbf{r} < \mathbf{r}_c$ are ironed out and a function that is smooth between 0 and $\mathbf{r}_c$ is chosen to replace it. As expected by design, at $\mathbf{r} > \mathbf{r}_c$, the pseudopotential has the $\frac{-Z_{ion}}{\mathbf{r}}$ characteristic behaviour.

A good pseudopotential is crucial to the physical correctness of a DFT code, both qualitatively and quantitatively, and thus there is a list of criteria for a good pseudopotential after choosing a reference atomic configuration.

1. The valence shell eigenvalues of the all electron and pseudopotential runs for the reference atomic configuration should agree reasonably well.

2. The radial wave-functions corresponding to the all electron and pseudopotential calculations should agree beyond $\mathbf{r}_c$ for each angular momentum degree of freedom.

3. The logarithmic derivative, $D_l(\mathbf{r})$, of the wave-function with respect to $\mathbf{r}$ for a particular angular momentum, as defined below, pertaining to both the methods should also agree at $\mathbf{r}_c$.
$$D_l(\mathbf{r}) = \mathbf{r}\frac{d}{d\mathbf{r}} ln[\Psi(\mathbf{r})] \tag{2.41}$$
This condition controls the smoothness and continuity of the wave-function and its derivatives. A pseudopotential has to be smooth so that it can be represented on a relatively coarse grid in real space or with a small number of plane waves.

Post this we have two choices for the kind of pseudopotential we want to choose based on the conditions it is made to satisfy. The first kind is called the norm conserving pseudopotential that we use in SIESTA, and it must satisfy the following conditions.

4. From $\mathbf{r} = 0$ to $\mathbf{r} > \mathbf{r}_c$ i.e., any distance beyond the cut-off radius, the integral of the charge density should agree for the all-electron and pseudopotenial calculations. This condition ensures that the total charge in the core-region is correct in the

pseudo-atom and normalised pseudopotential is same as the *true* orbital for $\mathbf{r} > \mathbf{r}_c$, and hence the name **norm conserving**.

5. As a corollary of the above point, the first energy derivative of the logarithmic derivative of the wave-function with respect to $\mathbf{r}$ should agree at $\mathbf{r}_c$ for the all-electron and pseudo calculations. This property is essential for the central issue of **transferability**.

   Transferability implies that the pseudopotential which has been generated for conditions based on matching with the all-electron solution for the atomic state should be applicable to a different environment of condensed systems like, solids, molecules, liquids, etc., which are the systems of interest, and it should represent accurately enough the charge densities, energies, etc.

Norm conserving pseudopotentials work well when the all electron wave-function and the pseudopotential wave function are nearly identical. However the criteria of norm conservation often requires a high plane wave basis cut-off, especially for localised orbitals. It is because the agreement of the charge density for the all electron wave function and the pseudopotential wave function occurs only when the core radius $\mathbf{r}_c$ is as large as maximum expanse of the all electron wave-function. This requirement makes computations difficult and expensive.

In 1990 in a milestone paper [50], David Vanderbilt proposed a pseudopotential scheme that overcame this challenge and allowed calculations to be performed for lower basis cut offs. The rationale is built from the observation that high cut-offs are only needed when there are some tightly bound orbitals which have substantial electron density inside the core region. For these situations the norm conservation will be violated and localised atom centric augmentation charges, which are defined as the difference between the electron density of the all electron and the pseudopotential wave-function, can be added to complement this deficit induced by the norm conservation violation. This divides the density into hard and soft parts defined as,

$$\rho(\mathbf{r}) = \sum_n \left[|\phi_n^{\mathrm{PS}}|^2 + \sum_{m,k} Q_{mk} \langle \phi_n^{\mathrm{PS}} | \beta_k \rangle \langle \beta_m | \phi_n^{\mathrm{PS}} \rangle \right] \tag{2.42}$$

Here ϕ_n^{PS} are the ultrasoft wave-functions which do not satisfy the norm conservation condition, β_m are projectors that depend on the ionic position and Q_{mk} are the augmentation function components that carry the information about the difference in all-electron and pseudopotential charge density as,

$$Q_{mk}(\mathbf{r}) = \psi_m^*(\mathbf{r})\psi_k(\mathbf{r}) - \phi_m^{\mathrm{PS}*}(\mathbf{r})\phi_k^{\mathrm{PS}}(\mathbf{r}) \tag{2.43}$$

Thus the pseudopotential wave functions can be as soft as possible within the core that removes the requirement for a large cut-off energy, and reduces computational

complexity. In this thesis, we have used norm-conserving pseudopotentials with SIESTA in chapter 5 and ultrasoft pseudopotentials with CASTEP in chapter 4, VASP and Quantum Espresso in chapter 6.

2.4.1 Pros of DFT

So far we have discussed all essential parts to understand, perform and analyse a DFT simulation. The number of papers based on DFT has seen an exponential rise since early 1990 [51]. As per google scholar database there were 23300 results that mentioned 'density functional theory' since the start of 2022, and the year still has a couple of months to end. The eminent success of DFT in the field of material science showed that a reasonable description of physical systems is possible even without the complete knowledge of the complicated many-electron wave function. This was a breakthrough for the study of real systems comprised of atoms, molecules, and even complex biological compounds.

- One prominent reason is that compared to methods based on wave functions or Green's functions, DFT is a much cheaper method as far as computational cost is concerned. It has also been aptly developed and scales well when parallelised.
- It also has many *good quality* established exchange correlation functionalals which are available and are extensively benchmarked owing to a large academic community working on and with them [52]. Sometimes, especially for LDA-based functionals, as discussed in 2.2.4, the lucky cancellations between the additive exchange and correlation part of the functionals gives very good agreements with experimental systems for a large class of weakly correlated systems where the density variations are rather small and smoothly.
- Structural properties depend primarily on ground state energetics which is determined by the ground state density. Even though DFT gets properties of excited states incorrect, as discussed in the next section in further detail, properties dependent on the ground states are very well explained. This is one reason behind the enormous success of DFT and its influence in computational electronic structure studies.

2.4.2 Limitations of DFT

The exchange-correlation zoo

In DFT there always is an ambiguity and *'tweaking'* involved in defining and using the many exchange correlation functionals [53] available across its various implementations in various codes which makes it dependent on knowing the *right* or *expected* relevant ground state properties to warrant a choice of the functional and its versions

or parameters. Also there is no systematic way to improve the physical correctness of various functionals, and the self-interaction error, described in detail in page. 32, where the electron interacts with its own charge density can be quite large. In these ways, DFT which is a prime *ab initio* method becomes less so and diminishes in its predictive powers, and sometimes even the ground state properties of weakly correlated systems show a wide variation in predicted properties depending on the exchange-correlation functional used.

Excited states

In principle DFT is strictly a ground state theory since it maps the electronic system to an auxiliary one-electron system with the same ground state electron density as the original electronic system, as discussed in 2.2. The Kohn-Sham wave-functions and the respective eigenvalues are basically Lagrange multipliers of the KS Hamiltonian and, apart from their contribution in predicting the right ground state density, are rather *fictitious* with limited physical significance [54]. This often leads to prediction of erroneous excited state properties.

Temperature in DFT

Typical Kohn-Sham DFT calculations are performed for a static crystal i.e., a crystal whose atoms are fixed at their crystallographic positions corresponding to the assumption made in the Born-Oppenheimer approximation. Sometimes in the literature, this approximation is viewed as being being equivalent to a zero temperature ground state approximation since the nuclei are assumed to not move, no lattice vibrations are considered and the lattice temperature (*not the electronic temperature*) is 0. However this is not strictly true. The BO approximation decouples the electronic and the nuclear systems and leads to two equations, discussed in further detail in section 2.12. Of those two equations, DFT solves the electronic one. The equation for the nuclei should be solved for 0 K to accurately say that an electronic structure simulation is done at 0 K.

Generally speaking, at 0 K, the atomic nuclei might move due to quantum fluctuations. But the quantum zero point motion is usually very small for *heavier* elements, and thus ignored safely in many electronic structure calculations and is the reason why DFT is called a 0 K method even while completely ignoring any consideration of the nuclear motion. But sometimes it can be significant, especially for lighter elements like hydrogen an helium [55]. Thus in this thesis, we say DFT is a static approximation, and not a 0 K approximation. Strictly speaking when looking at electronic structure properties, the lattice dynamics should not be ignored as even for heavier elements like cerium it can lead to certain effects which plainly based on DFT cannot be explained. This we have explored in the second half of chapter 6.

Defining temperature and its effects without considering nuclear motion is not a straightforward venture. Also, almost all experiments that condensed matter theorists

compare with are done at finite temperatures. Thus, including the effect of temperature while ignoring lattice vibrations is important and can be done in a few ways. One such way is Thermal DFT [56] that uses the statistical mechanical framework with a grand canonical partition function and rewrites the density functional in this framework with a temperature dependence. This interacting thermal ensemble, similar to ground state DFT formalism, is then mapped to a non-interacting ensemble with the same average particle density and temperature. The catch in the thermal DFT treatment again is to define correctly the thermal exchange correlation functionals which depend on both kinetic energy and entropic effects [57]. While finite temperature LDA is relatively well developed, GGA based approximations are not. However gradient corrections are often deemed important for ground state properties at lower to moderate temperatures but have non-trivial temperature dependence [58], and thus using ground state GGAs is a source of error to the thermal approximations of DFT. Another way to including the effect of temperature includes embedding DFT with Green's function based approaches which are discussed in detail later in this chapter.

Strongly correlated systems

Strongly-correlated systems are those which retain some of the complexities of atomic-like physics even in their crystalline state. Practically this happens when the building blocks are made up of elements with localised open shells, usually of d or f, and sometimes even of p character with their crystal structure being such that the energy bands stemming from these orbitals are are confined to a narrow energy regime [59]. DFT over delocalises these localised energy bands by underestimating the degree of correlations in these orbitals as these states cannot be represented by a single determinant of one-electron orbitals as done in DFT.

To have have a closer look at the origin of this discrepancy, we go back to eq.(2.34) in the Kohn-Sham effective potential. The second additive term is the Hartree term that describes the electrostatic potential uniquely determined by the electron density having contributions from all the electrons in the system including the electron under consideration. This makes the electron interacts with itself! This **self-interaction** is unphysical and needs to be corrected for. Ideally in DFT formalism, if we look back at when this term was introduced in eq.(2.27), the exchange correlation functional was supposed to incorporate the effects of its cancellation. But since E_{XC} itself is not exact, this cancellation is only partial. For strongly correlated systems it can become a major source of error. If one redefines the exchange-correlation functional as in the self-interaction correction (SIC) method [60], a correction of this error is possible but implementation of this method is quite cumbersome and sometimes numerically unstable. Sometimes even with SIC, the tendency for localisation is wrongly estimated. SIC has been observed to be insufficient especially for rare-earth materials [61] and transition metal oxides [62] which form two classes of materials we are interested to

study in this thesis in chapters 4, 5 and 6, respectively.

For most of these systems DFT fails to even qualitatively account for observed physical properties. However these are the classes of materials with some of the most interesting physical properties which also are technologically relevant like the property of high temperature superconductivity in cuprates [63], quantum hall effect which can serve as a reliable measure of resistance [64], battery materials with interesting thermo-electric properties like Li_xCoC_2 [65] and many others. This subclass of systems which is focused on in this thesis motivates us to look for methodologies beyond DFT that correct for many of the limitations.

2.5 Beyond DFT

The sources of errors in DFT, as we saw above, occur at different levels and often together. So it is difficult to detangle their effects and interplay. However, usually (not a strict statement) one can say that the error arising in

- ground state properties like structure, elastic constants, phonon spectra, heats of formation, defect formation energies and diffusion barriers, catalysis, etc., *primarily* stem from the ansatz for $E_{\mathrm{XC}}(\rho)$ not being good enough. For this Hybrid functionals, as discussed in 2.2.4, can be a better approximation.

- excited properties like energy bands, conductivity, magnetic excitations, photoemission and almost any spectroscopy [66] etc., can *primarily* be attributed to the Kohn-Sham eigenvalues being of limited physical significance [67].

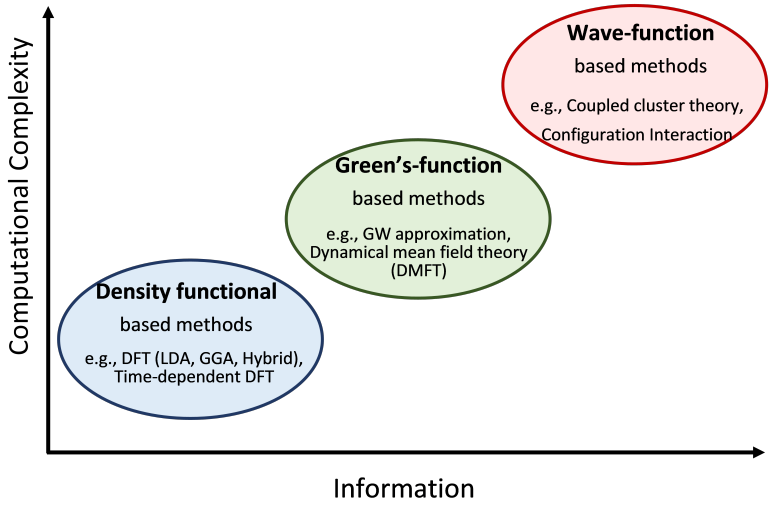


Figure 2.2: A caricature showing three major (not exhaustive, often overlapping) categories of computational methods used for real materials in ascending order of information retained and computational complexity.

The fallacies of DFT can be summarised by saying that the formalism is designed to make the electron density the fundamental variable of interest in such a way that every ψ_i feels the same v_{eff} which is an over simplification, especially when d or f electrons are present. This makes one look for methods which still retain less information than a many-body wave-function [68] but more than electron density without over-simplifying the effective potential felt by an electron. Such a class of methods are those which use a Green's function as the main variable of interest in building the formalism. Typically in terms of information retained by the formalism and computational complexity, it falls between the density functional based methods and wave-function based methods as shown schematically in fig.(2.2). Note that in fig.(2.2) wave-function based methods include only the post Hartree-Fock methods. It is so because the Hartree-Fock method, as discussed in chapter 1, is based on a single Slater determinant expansion and therefore, is relatively cheaper when compared to many Green's function based methods.

getting in the DMFT gear . . .

2.6 Green's Functions

2.6.1 A brief review

We start with a quick review of Green's functions before looking at a Green's function based method for treating correlated materials. Green's functions, originally developed by physicist, mathematician and miller George Green [69][2] were developed as auxiliary functions to solve partial differential equations with general boundary conditions. The initial applications in physics revolved around finding solutions for the differential equations for diffusion or heat conduction, Poisson equation describing the charge distributions in surfaces, propagation of waves, etc.

Formally a classical Green's function is the solution of a linear differential equation with a Dirac delta pulse $\delta(x - x')$ as the source of inhomogeneity under homogeneous boundary conditions. To elaborate further, for an inhomogeneous partial linear differential equation with $g(x)$ being its source of inhomogeneity, the particular solution $f(x)$ can be given with the help of a Green's function $G(x, x')$ which itself is defined as the solution of a differential equation with delta inhomogeneity as,

$$Df(x) = g(x) \tag{2.44}$$

$$f(x) = \int G(x, x')\, g(x')\, dx' \tag{2.45}$$

[2]This reference is a reprint of George Green's famous essay from Nottingham, 1828 titled "An Essay on the Application of mathematical Analysis to the theories of Electricity and Magnetism" published in Crelle's Journal (1850-54).

$$D\ G(x,x') \quad = \quad \delta(x-x') \tag{2.46}$$

where D denotes the general linear differential operator in variable x. This leads to traditional role of a Green's function as a mean for finding solution for linear differential equations, and as a result they are often called response functions.

The time dependent Schrödinger equation is a linear partial differential equation, first order in time and second order in space. Although it is a homogeneous equation, one can rearrange and consider the potential term as a source of inhomogeneity as,

$$\left[i\hbar\frac{\partial}{\partial t} + \frac{\hbar^2}{2m}\nabla^2\right]\Psi(\mathbf{r},t) = V(\mathbf{r},t)\ \Psi(\mathbf{r},t) \tag{2.47}$$

The difference from the classical parallel in eq.(2.44) is that now both the sides retain a functional dependence on $\Psi(\mathbf{r},t)$. This associates the need of a recursive process to find a solution for $\Psi(\mathbf{r},t)$, similar in nature to what was done for density in the context of DFT. This kind of self-consistent solution for a Green's function is achieved by using a **Dyson's equation** [70] which we will employ and discuss more in section 2.10. Therefore in a manner analogical to the classical counterpart, instead of solving the Schrödinger equation for the many-particle wave function we can solve for the quantum mechanical Green's function instead as,

$$\left[i\hbar\frac{\partial}{\partial t} + \frac{\hbar^2}{2m}\nabla^2\right]G(\mathbf{r},t;\mathbf{r}',t') = \delta(\mathbf{r}-\mathbf{r}')\ \delta(t-t') \tag{2.48}$$

and then find the wave function as the inhomogeneous solution to the Green's function as,

$$\Psi(\mathbf{r},t) = \int G(r,t;\mathbf{r}',t')\ \Psi(\mathbf{r}',t')\ d^3r' \tag{2.49}$$

This as a result leads to the interpretation of Green's functions in quantum mechanics as a quantity containing information about the evolution of or the propagation of the wave-function or of a quantum state from a given time and position $(\mathbf{r}',t')$ to $(\mathbf{r},t)$. Hence often the Green's function is called a propagator. This can be further elaborated by writing the wave-functions as state vectors in the position representation. In this representation, the wave function can be written as,

$$\Psi(\mathbf{r},t) \quad = \quad \langle\mathbf{r}|\Psi(t)\rangle = \langle\mathbf{r}|e^{-\frac{i}{\hbar}H(t-t')}\Psi(t')\rangle \tag{2.50}$$

$$= \quad \int\langle\mathbf{r}|e^{-\frac{i}{\hbar}H(t-t')}|\mathbf{r}'\rangle\langle\mathbf{r}'|\Psi(t')\rangle d^3r' \tag{2.51}$$

where $U(t,t') = e^{-\frac{i}{\hbar}H(t-t')}$ is the time evolution operator. Setting $\langle\mathbf{r},t| = \langle\mathbf{r}|e^{-\frac{i}{\hbar}Ht}$ and by comparing the above equation to eq.(2.49), the Green's function can be interpreted as the probability amplitude for finding a particle in state $\langle\mathbf{r},t|$ given that it started in state $|\mathbf{r}',t'\rangle$.

Inserting a completeness relation for the eigenstates of the Hamiltonian H with $\phi_n(r)$ being the respective eigenfunctions for a state $|n\rangle$, the Green's function can be written in the energy domain as,

$$G(\mathbf{r}, \mathbf{r}'; E) = \sum_n i \frac{\phi_n(r)\phi_n^*(r')}{E - E_n} \tag{2.52}$$

with poles at the eigenstates E_n. This was just a brief refresher of some basic concepts involving Green's functions, its physical and mathematical interpretations which are directly relevant to their use in quantum systems and the methods used in this thesis. The full formalism of quantum mechanics in terms of Green's functions includes going to the second quantised notation, restricting the definition to causal situations [71], implementing Wick's time ordering [72], developing the method in a grand canonical ensemble introducing the imaginary time axis [73], etc., and has not been extensively discussed in this thesis [3].

2.6.2 Electron Green's function

We now move directly to the causal electron Green's function which in second quantised notation and atomic units is written as,

$$G_{ij}^c(t, t') = -i \langle \mathcal{T} \langle [c_i(t),\ c_j^\dagger(t')] \rangle \tag{2.53}$$

$$\mathcal{T} [c_i(t),\ c_j^\dagger(t')] \rangle = \theta(t - t')\ c_i(t)\ c_j^\dagger(t') - \theta(t' - t)\ c_j^\dagger(t')\ c_i(t) \tag{2.54}$$

Here $\mathcal{T}$ is the time-ordering operator that ensures causal orderings (*also called later to the left rule*) using the Heaviside function θ. $c_i^\dagger(t)$ creates an electron at site i and time t, and $c_i(t)$ annihilates an electron similarly at time site i and time t. The creation and annihilation operators satisfy the fermion anticommutation relations. The above definitions lead us to the expression for the retarded Green's function defined for $t > t'$ as,

$$G_{ij}^r(t, t') = -i\ \theta(t - t') \langle \{c_i(t),\ c_j^\dagger(t')\} \rangle \tag{2.55}$$

which can be used to calculate the response of a system after it has been perturbed. The adjoint of the retarded Green's function is the advanced Green's function $G_{ij}^a(t, t')$. Note that a formalism based on Green's functions inherently has the information about **system excitations** [4], as opposed to DFT (2.4.2). Some important physical properties

[3] An excellent introductory reference is [74]

[4] The electron Green's function formalism can be built in the Heisenberg picture of motion where the Green's functions are operators ($\hat{O}$) carrying information about the system excitations whose time evolution is governed by the system Hamiltonian as,

$$i\ \frac{d\hat{O}}{dt} = [\hat{O}, H] + i\frac{\partial}{\partial t}\hat{O}(t) \tag{2.56}$$

of the Green's function can be written as,

- In absence of interactions, poles of the electron's spectral Green's function, similar to eq.(2.52), correspond exactly to the eigenenergies (ϵ_n). For an interacting system on the other hand, the poles specify the many-body excitation energies of the system.

- In the frequency domain ω, the imaginary part of the diagonal of either the retarded or the advanced Green's function gives the local density of states as,

$$\rho_i(\omega) = \mp\frac{1}{\pi}\ \mathrm{Im}\ \left\{G_{ii}^{r/a}(\omega)\right\} \tag{2.57}$$

  When the above equation is evaluated in an interacting system with inverse temperature β and partition function Z, the local density of state can be given by the Källén-Lehmann representation [75], [76] as,

$$\rho_i(\omega) = \frac{1}{Z}\sum_{nm} |\langle n|c_i(0)|m\rangle|^2\ (e^{-\beta\epsilon_n} + e^{-\beta\epsilon_m})\ \delta[\omega - (\epsilon_m - \epsilon_n)] \tag{2.58}$$

  Note that since this representation of the Green's function is built on statistical averaging between two quantum states, its evaluation for a particular system intrinsically incorporates the information about the **temperature** of the system in the density of states among other observables calculated, unlike DFT (2.4.2).

Generally the computational methods for real systems based on Green's functions can be classified in two broad categories,

- Many body perturbation theory based formalism as the GW approximation [77], fluctuating exchange theory [78]. Here the leading terms in the Dyson equation are computed. These sets of methods are good for weak and moderate correlations, however going beyond the lowest order is usually difficult and computationally challenging.

- Non-perturbative solution of a selected subspace as in the Dynamical mean field theory which we have used in this thesis in chapters 3, 4 and 5. In such a development, the whole system is partitioned into a larger uncorrelated or a weakly correlated subspace and a smaller subspace comprising of only a few degrees of freedom e.g., the d or the f orbitals in a real material where the correlations are strong. The smaller subspace is then treated at higher levels of approximations than the weakly correlated ones, accordingly.

Moving forward we will look at the Dynamical mean field theory (DMFT) that belongs to the class of non-perturbative methods that use Green's functions to solve the Schrödinger equation. But before that we will have a quick view of model Hamiltonians and a qualitative discussion on the most famous Hamiltonian in many-body physics, called the Hubbard Hamiltonian whose features lie at the basis of the DMFT treatment.

2.7 Model Hamiltonians : a quick review

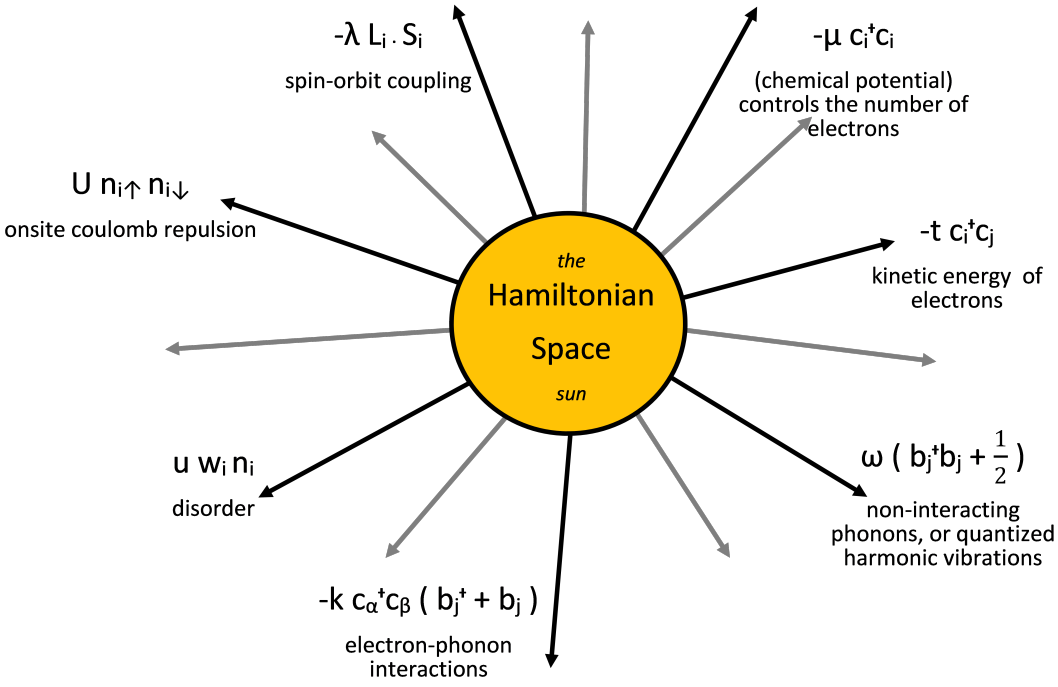


Figure 2.3: The 'Hamiltonian space sun'- a cartoon depicting the big *fictitious* world of model Hamiltonians that describes various physical phases and phase transitions as one goes from one model Hamiltonian to another. The grey arrows signify the presence of many such models[5]. Inspired by Prof. Vijay Shenoy's '*Pancha-Bhuta-Chitra*' [79].

Before we look into the DMFT formalism, we take a small detour to have a general understanding of model Hamiltonians and their relevance in the study of strongly correlated systems. This is because eventually for real materials studied in this thesis, we will use a DFT-based description first and then map it to Hubbard model (section 2.8) for a subspace of the total degrees of freedom. In chapter 6 we will terminate our study of correlations at this stage. In chapters 4 and 5 we will go further and then map the Hubbard model to an Anderson Impurity model [80] which will give us a set of equations which will then be solved self-consistently. In chapter 3, we do the same but starting from a Hubbard Hamiltonian for a simplified model system. Thus, understanding the logic of and behind multiple mappings and approximations is important to understand the physical properties of any given system.

A way to think about weak and strong correlations is to classify weakly correlated systems as those systems where the electron motion is influenced primarily by the Pauli exclusion principle [12], e.g., a simple metal like Na. On the other hand[6], we can say

[5]The model Hamiltonian terms are accompanied by their usual physical interpretations and are depicted for an intuitional understanding, and should be modified accordingly if used explicitly to solve problems.

[6]Adding to the description of strongly correlated systems discussed in 2.2.4 and simplifying it.

that strong correlations happen where the electron motion is influenced by interactions between the electrons in addition to the Pauli exclusion principle. Consider a site where an up-spin electron ($\uparrow$) is sitting. The Pauli exclusion principle allows another down-spin electron ($\downarrow$) to sit beside that $\uparrow$ electron. However because of their mutual repulsion, the $\downarrow$ electron might not want to occupy that site from energy considerations even though the exclusion principle allows for it. This competition is an instance of correlation and has a strong impact on physical properties. Modelling such competitions correctly for a specific physical scenario has a huge role in determining the validity of theories and approximations, and the validity of various model Hamiltonians.

When electrons of the order of Avogadro's number aggregate, many different *phases* can emerge with a common set of physical characteristics depending on how the electrons aggregate themselves. These phases can be a metal, a semi-metal, an insulator or semiconductor, a topological insulator [81], a superconductor, a Mott insulator [82], a magnet of a specific magnetic order among numerous others. The phases are characterised by different ways like by broken symmetry between phase transitions (ferromagnetic, superconductors), by their response, or specific properties of excitations (e.g., if the excitations are topologically protected or not), and many more. A way to understand these different phases theoretically is to write Hamiltonians designed to describe the emergent properties of a collection of electrons pertaining to a specific condition. This can be called the Hamiltonian space that physicists use to understand various phases and phase transitions as one moves from a model Hamiltonian valid for one situation to another where its validity changes and transforms to another Hamiltonian where a different set of terms hold truth. When one works with model Hamiltonians the aim becomes to identify such phases arising out of various terms, study their properties like thermodynamic properties, conductivity, susceptibility, etc., or even find a new phase by identifying the symmetries of the system and studying the limits associated with various terms for discerning the corresponding energy scales.

2.8 Hubbard Model: revisiting strong correlations

If there is a model Hamiltonian almost of legendary status in the theory of strongly correlated systems that is the Hubbard model which was independently conceived in 1963 by Martin Gutzwiller [19] , Junjiro Kanamori [20] and, John Hubbard [21]. It was designed as an extension over the tight-binding model to explain how a more correlated nature of electrons can justify the observed antiferromagnetic insulating behaviours of transition metal monoxides like FeO, NiO, and CoO, where the band treatment fails. The Hubbard Hamiltonian looks like,

$$H = -t \sum_{\langle i,j \rangle} (c^{\dagger}_{i\sigma} c_{j\sigma} + h.c.) - \mu \sum_{i} c^{\dagger}_{i\sigma} c_{i\sigma} + U \sum_{i} n_{i\uparrow} n_{i\downarrow} \tag{2.59}$$

where t is the kinetic energy term denoting the hopping between nn sites i and j with the same value for all sites, μ is the chemical potential that controls the number of particles in the system and U is the onsite Coulomb interaction term. It is one of the most deceptively simple Hamiltonians whose variations can be evoked to explain various physical phases ranging from a Mott-Hubbard insulator [83] to superconductors to the phase transition from a superfluid to a Mott insulator using the Bose-Hubbard model [84]. The Hubbard model has even inspired and has become the target of experimental realisations of *artificial model-like* systems using cold-atom optical trapping [85].

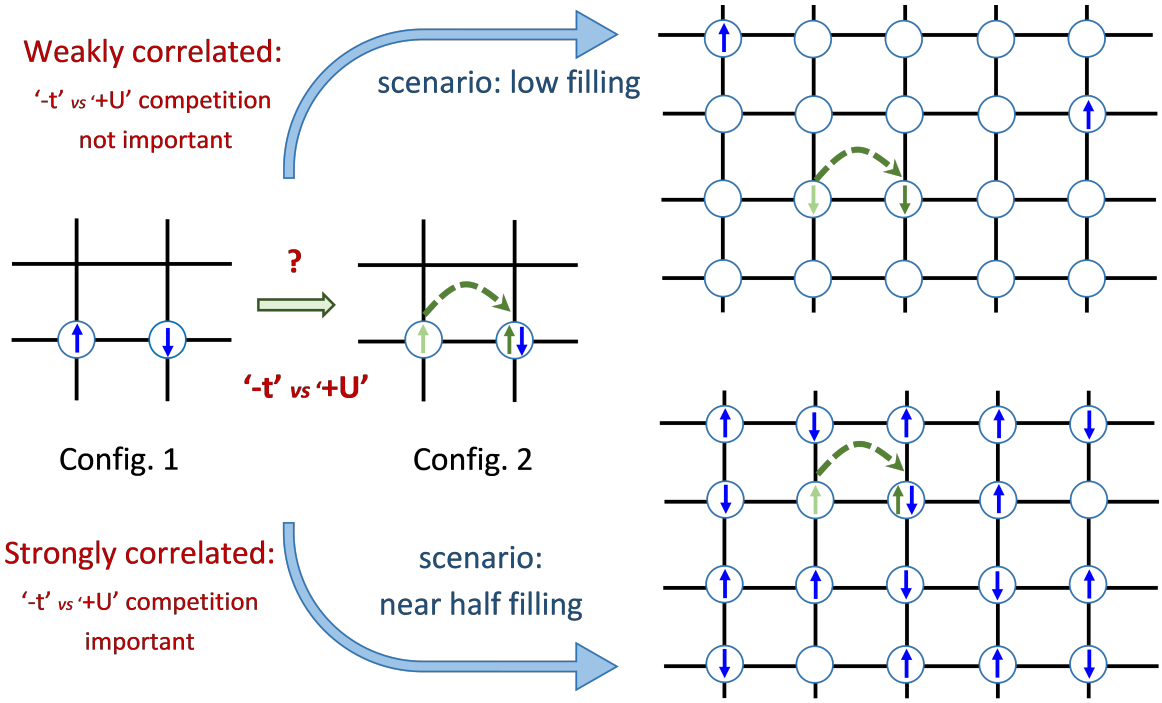


Figure 2.4: Schematic depiction of origin and relevance of correlations for a square lattice with a single orbital on each site. If an electron will hop to the next nn site is decided by the Pauli exclusion principle along with the filling and its impact on the t vs U competition. For low filling, the likelihood of hopping is higher representing a weakly correlated case. Near half-filling the competition between $-t$ and $+U$ becomes important representing strong correlations and subtle changes in the system environment like temperature, pressure can give rise to different phases with characteristic properties.

In this section we will elaborate on the idea of correlations discussed in the previous section 2.7 and use the Hubbard model to understand qualitatively how the competition between the kinetic and the Coulomb or interaction terms gives rise to the physics of strong correlations. The Coulomb interaction term for the d and the f shells are typically higher than the s or p, and hence they are more localised in space. However merely a high value of U isn't enough for a system to be in strongly correlated regime.

Suppose we have a square lattice with a single orbital present on each site. If we start from a situation like configuration 1 of fig.(2.4), then whether the electron will hop to another site allowed by the Pauli exclusion principle, as depicted by configuration 2,

or not, will be determined by the competition between t i.e., the kinetic energy term which will reduce the energy by $-t$ with that hopping, and U the interaction term which increases the energy by $+U$. Two following scenarios can explain the effect of strong correlations here.

- If the filling (the number of electrons per site) is low, i.e., if there are enough empty states available in the vicinity of an electron this "t vs U" competition has less relevance. This situation corresponds to weakly correlated systems as described by the upper right hand situation of fig.(2.4).

- If the system is near half-filling i.e., there is an average of one electron at each site then the "t vs U" competition will become relevant because each possible hopping is now associated with a possible increase in energy due to the onsite Coulomb repulsion. This corresponds to a strongly correlated scenario implying that correlations are important here and they determine system properties.

In general there is no unique quantitative limit or definition of what strong correlations are and what are their degrees, and thus just knowing the value of U is not enough. For example, sometimes a quantity like $\frac{\langle n_{\uparrow\downarrow}\rangle}{N}$, where $\uparrow,\downarrow$ denotes electron up-spin and down-spin respectively, and N is the total number of electrons, can be a measure. If at half-filling it is ~ 0, that implies a dominating effect of U, whereas a value of 0.5 implies almost non-interacting particles. One can also analyse $|\langle n_{\uparrow}\rangle - \langle n_{\downarrow}\rangle|$. If the difference is not 0, it means there is a respective degree of correlation given by the number.

Usually models work in the limit where either $t >> U$ or $U >> t$ because it is easier to apply perturbation theory in the extreme limits. Complications arise when the values of $\frac{t}{U}$ becomes finite and the two opposite effects compete[7]. This can happen when we have unoccupied d or f levels near the Fermi level in a real material. Those shells are highly localised and very atomic like, and occupy a narrow region around the Fermi level. In certain conditions it may happen that some states around the Fermi level become available[8], that will increase the likelihood of those electrons moving to those levels from the valence band by thermal energy or some other effect. This can induce an insulator to metal transition which is the basis of most industrially relevant applications. Study of strongly correlated systems also involve a quest for understanding the origin of such effects in order to get a detailed understanding of electronic structure in materials. That is also one of the broader aims of this thesis. The Hubbard model is the basis of the two methods used in this thesis to correct DFT for real materials exhibiting strong correlations. We will now discuss those two methods.

[7]Being able to capture this regime is one major success of DMFT, as will be seen in the following sections. For a quick inspirational glance, see fig.(2.7).

[8]This happens in SmS, SmSe and SmTe by application of pressure, as discussed in detail in chapter 4.

2.9 DFT+U

With the above perspective from the Hubbard model about the competition between t and U energy scales, we can interpret the failure of DFT in reproducing the correct Mott insulating behaviour as an absence of an explicit Hubbard-term (U) for the electron-electron interactions. So the next step is to add such a term and incorporate it in the DFT framework. This can be done in two ways.

1. DFT+U : Add U and then evaluate its impact in a *static* mean-field or, Hartree-Fock way as discussed below.

2. DFT+DMFT : Treat interactions as a dynamical mean field with frequency dependence (discussed in more detail in section 2.10) that is determined self-consistently.

However the new Hubbard term will be additive. We should bear in mind that this is commensurate with our previous description in section 2.4.2 where the DFT design partially takes into account the correlations. So to a certain degree the electron-electron interactions are counted twice, and thus adding a U will result in a double counting error for the correlated states which must be deducted from the total energy. Thus writing figuratively,

$$E_{\mathrm{DFT}} + \text{“}U\text{”} = E_{\mathrm{DFT}} + E_{\mathrm{Hub}} - E_{\mathrm{DC}} \tag{2.60}$$

This whole implementation is not done for all the electrons of the system, but is based on choice of the orbitals for which the DFT description is not good enough a.k.a., the correlated orbitals. Thus the implementation relies on the projection scheme. If $\mathbf{R}$ be the Bravais lattice site vector for one-particle site-centred orbitals depicted by the set of quantum numbers χ, the hopping term in analogy to t in eq.(2.59) will be given by DFT as,

$$t_{\mathbf{R}_i\mathbf{R}_j\chi_i\chi_j} = H^{\mathrm{DFT}}_{\mathbf{R}_i\mathbf{R}_j\chi_i\chi_j} = \int d\mathbf{r}\ \langle \mathbf{R}_i\chi_i|\mathbf{r}\rangle\ H^{\mathrm{DFT}}(\mathbf{r})\ \langle \mathbf{r}|\mathbf{R}_j\chi_j\rangle \tag{2.61}$$

For projecting onto the correlated sites, if ξ be the quantum numbers for site-centred correlated orbitals which for an atomic-like basis will be $\{l, m, \sigma\}$[9], the onsite-repulsive interaction term can be added on top with the double counting correction as,

$$\begin{aligned} H^{\mathrm{DFT+U}} &= \sum_{\mathbf{R}_i\mathbf{R}_j\chi_i\chi_j} H^{\mathrm{DFT}}_{\mathbf{R}_i\mathbf{R}_j\chi_i\chi_j} c^{\dagger}_{\mathbf{R}_i\chi_i} c_{\mathbf{R}_j\chi_j} \\ &+ \frac{1}{2}\sum_{\mathbf{R}}\sum_{\xi_1\xi_2\xi_3\xi_4} U_{\xi_1\xi_2\xi_3\xi_4} c^{\dagger}_{\mathbf{R}\xi_1} c^{\dagger}_{\mathbf{R}\xi_2} c_{\mathbf{R}\xi_4} c_{\mathbf{R}\xi_3} - \sum_{\mathbf{R},\xi_i} H^{\mathrm{DC}}_{\mathbf{R}\xi_i} c^{\dagger}_{\mathbf{R}\xi_i} c_{\mathbf{R}\xi_i} \end{aligned} \tag{2.62}$$

[9] We use this description when discussing DFT+U and DMFT as it makes physical interpretations easier. Also, a large part of this thesis focuses on the f-electronic systems which are more atomic-alike in nature.

2.9.1 A DFT+U description

Above in eq.(2.62), we have used a general form of Coulomb interaction at a single site. Interpretation and calculation of $U_{\xi_1\xi_2\xi_3\xi_4}$ is not always very clear or straightforward. The weakly correlated electrons treated with DFT participate in screening interactions between the correlated electrons. Thus, $U_{\xi_1\xi_2\xi_3\xi_4}$ is not the bare Coulomb repulsion but an effective interaction based on the Coulomb repulsion that also takes into account the effect of screening by other electrons. If we consider only intra-site interactions for a given shell l since those interactions are dominant[10] then,

$$U_{\xi_1\xi_2\xi_3\xi_4} = \delta_{l_1,l_2,l_3,l_4} U_{m_1\sigma_1,m_2\sigma_2,m_3\sigma_3,m_4\sigma_4} \tag{2.63}$$

For a particular orbital quantum number l with different m indices and respective σ indices, one can have

$$U_{m_1\sigma_1,m_2\sigma_2,m_3\sigma_3,m_4\sigma_4} \rightarrow \delta_{\sigma_1,\sigma_3}\delta_{\sigma_2,\sigma_4} U_{m_1\sigma_1,m_2\sigma_2,m_3\sigma_3,m_4\sigma_4} = U_{m_1\sigma_1,m_2\sigma_2,m_3\sigma_1,m_4\sigma_2} \tag{2.64}$$

From this the Hubbard term in the eq.(2.60) and eq.(2.62) can be written in a rotationally invariant scheme (rotation over the m subspace for an l) [87] with V_{ee} is the screened Coulomb interaction term in the Hamiltonian as,

$$H^{\text{Hub}} = \frac{1}{2}\sum_{\mathbf{R}} \sum_{\substack{l,\\ m_1,m_2,m_3,m_4,\\ \sigma_1,\sigma_2}} U_{m_1\sigma_1,m_2\sigma_2,m_3\sigma_1,m_4\sigma_2}\; c^\dagger_{m_1,\sigma_1}\; c^\dagger_{m_2,\sigma_2}\; c_{m_4,\sigma_2}\; c_{m_3,\sigma_1} \tag{2.65}$$

$$= \frac{1}{2}\sum_{\mathbf{R}} \sum_{\substack{l,\\ m_1,m_2,m_3,m_4,\\ \sigma_1,\sigma_2}} \begin{cases} +\langle m_1, m_2|V_{ee}|m_3, m_4\rangle\; n^{\sigma}_{m_1m_3}\; n^{-\sigma}_{m_2m_4} & (\text{when } \sigma_1 \neq \sigma_2) \\ +\Big(\langle m_1, m_2|V_{ee}|m_3, m_4\rangle & \\ \quad -\langle m_1, m_2|V_{ee}|m_3, m_4\rangle\Big)\; n^{\sigma}_{m_1m_3}\; n^{\sigma}_{m_2m_4} & (\text{when } \sigma_1 = \sigma_2) \end{cases} \tag{2.66}$$

If the integrals in eq.(2.66) are written explicitly, we can note its similar nature to the energy expression for the direct and exchange Coulomb interaction in the Hartree-Fock theory[11]. Similar to the Hartree-Fock theory, the self interaction terms cancel the corresponding exchange terms. Due to this reason, the Hubbard correction implemented

[10] This is a simplification. There can be inter-orbital or even inter-site interactions [86] that govern the physical characteristics of a system, however those have not been discussed in this thesis.

[11] In the Hartree-Fock theory with one-electron orbitals $\Phi_i(\mathbf{r})$ the direct and the exchange Coulomb interactions are,

$$J_{ij} = \int |\Phi_i(\mathbf{r})|^2 \frac{1}{|\mathbf{r}-\mathbf{r}'|} |\Phi_j(\mathbf{r}')|^2\; d\mathbf{r}d\mathbf{r}' \tag{2.67}$$

$$K_{ij} = \int \Phi^*_i(\mathbf{r})\Phi_j(\mathbf{r}) \frac{1}{|\mathbf{r}-\mathbf{r}'|} \Phi^*_j(\mathbf{r}')\Phi_i(\mathbf{r}')\; d\mathbf{r}d\mathbf{r}' \tag{2.68}$$

The Hartree-Fock theory is exact in the limit of one-electron system where the J_{ii} and K_{ii} cancel.

as above is often interpreted as a method replacing the density-density interaction with an expression similar to the Hartree-Fock method. Since we have assumed that the projected orbitals are strongly correlated and hence atomic-like, the above coefficients can be expanded in terms of spherical harmonics as usually done in the Hartree-Fock methods as,

$$\langle m_1, m_2|V_{ee}|m_3, m_4\rangle = \sum_{n=0}^{2l} a_n(m_1, m_2, m_3, m_4)F^n \ , \text{ where} \tag{2.69}$$

$$a_n(m_1, m_2, m_3, m_4) = \frac{4n}{2n+1}\sum_{q=-n}^{q=+n}\langle lm_1|Y_{nq}|lm_3\rangle \ \langle lm_2|Y^*_{nq}|lm_4\rangle \tag{2.70}$$

Here Y_{nq} are spherical harmonics, $\langle lm_1|Y_{nq}|lm_3\rangle$ are the Gaunt coefficients, and F^n are called screened Slater integrals, all of whose properties can be used to obtain [88] the following two sum rules,

$$U = \frac{1}{(2l+1)^2}\sum_{m_1\neq m_2}\langle m_1m_2|V_{ee}|m_1m_2\rangle = F^0 \text{ and} \tag{2.71}$$

$$U - J = \frac{1}{2l(2l+1)}\sum_{m_1\neq m_2}\langle m_1m_2|V_{ee}|m_1m_2\rangle - \langle m_1m_2|V_{ee}|m_2m_1\rangle \tag{2.72}$$

$$= F^0 - \frac{C}{2l}\sum_{k=2}^{2l}(C_{lkl^{000}})^2F^k \tag{2.73}$$

where $C_{lkl^{000}}$ is a Clebsch-Gordon coefficient, U is the averaged direct Coulomb integral and J is the averaged exchange integral. For correlated electrons in d and f shells, one can obtain

$$J = \begin{cases} \frac{1}{14}(F^2 + F^4) & d-\text{orbitals} \\ \frac{1}{6435}(286F^2 + 195F^4 + 250F^6) & f-\text{orbitals} \end{cases} \tag{2.74}$$

Thus, for atomic-like correlated orbitals the determination of the full 4-index U-matrix has been reduced to finding the two values of U and J.

Usually a third relation is needed to find U and J in terms of the Fs. However it has been verified both experimentally and computationally using Hartree-Fock method that the ratios between the Slater integrals F^2, F^4 and F^6 are reasonably constant within an electronic shell [89]. For transition metal oxides typically $\frac{F^4}{F^2} = 0.635$ is used [90]. Even with these conditions, the choice of the values of averaged Coulomb interaction terms isn't trivial. They can be obtained using constrained Random Phase approximation (cRPA) [91], constrained Density Functional theory (cDFT) [92], [93] or some semi-empirical procedures [94]. Usually owing to the vast literature available that has used this method, typical values are used from the literature *specific* to a particular set of orbitals in a certain class of systems, and usually if the orbitals of projection are chosen

appropriately, the results are good. Note that the above formulation assumes atomic-like orbitals and unscreened Coulomb interaction. However the formulation has been successfully adopted to be evaluated in presence of screening [88]. Unscreened values of U range within 15-20 eVs. In DFT+U with the effect of screening, the values vary within 3-8 eVs usually depending not only on the degree of localisation and correlation of the orbitals but sometimes also heavily on factors like geometry, strain, etc., for the same orbitals and the same element in same or different materials.

2.9.2 Double counting correction

The choice of double counting functional introduced in eq.(2.60) isn't unique. It can depend on the DFT exchange correlation functionals used, the projection scheme, which orbitals are treated for correlations, etc. For real materials, they are mostly chosen based on the nature of the material studied as will be discussed for the most famous choices in the literature below.

- "Around mean field" (AMF) expansion [95], [96] which assumes that the average occupation of an orbital denoted by $\{m, \sigma\}$ is independent of m. It is more suited for systems characterised by quasi-homogeneous distribution of electrons as metals[12] and weakly-correlated systems.

- "Fully localised limit" (FLL) [97] expansion which assumes that the occupation an orbital $\{m, \sigma\}$ can either be 0 or 1. It is more suited for materials with strong localisation on specific orbitals. It is the most widely used approximation and shows a better ability to capture Mott localisation and increase the band gaps with the application of U when compared to DFT.

- Held's formula [98] : Introduces average Coulomb repulsion to ascertain rotational invariance for certain Hamiltonians. It is a slightly different implementation of the FLL approximation.

In the upcoming chapters, we will be dealing mostly with f-orbitals which are highly localised in nature. Thus, we will only be discussing the FLL implementation of DFT+U in detail which is also the most popular choice of double counting such that in DFT+U or DFT+DMFT codes it sometimes isn't even explicitly mentioned. Our discussion for DFT+U so far has been for atomic-like localised orbitals as well. If eq.(2.66) is considered, the double counting correction in the FLL limit, with respective

[12] In the study of correlated systems a "metal" can be an ambiguous term. Here, it implies that the density of states or the spectral function has a finite value at the Fermi level. It is thus a blanket term that can mean a traditional metal as well as a "correlated metal" (that we discuss in section 2.10.6) that refer to a quasiparticle peak that might belong to electrons or polarons or any other quasiparticles.

total occupations $n^l = \sum_{m,\sigma} n_{lm\sigma}$ and $n^{l\sigma} = \sum_{m} n_{lm\sigma}$[13], is given by,

$$H^{\mathrm{DC}} = -\sum_{\mathbf{R},l}\left\{\frac{U^l}{2}n^l(n^l-1) - \frac{J^l}{2}[n^{l\uparrow}(n^{l\uparrow}-1) + n^{l\downarrow}(n^{l\downarrow}-1)]\right\} \tag{2.75}$$

2.9.3 A simpler DFT+U formulation

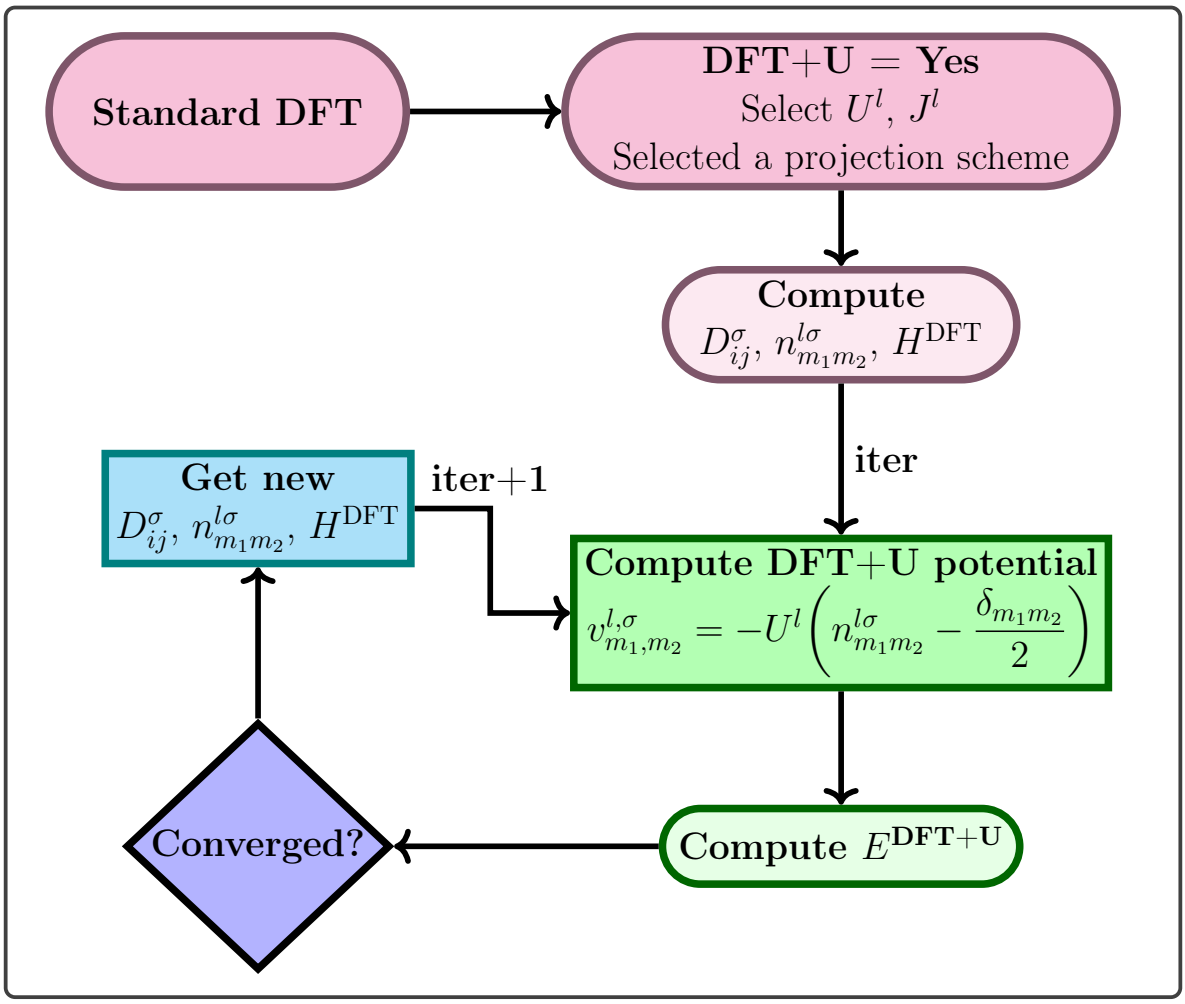


Figure 2.5: The DFT+U self-consistent iterative scheme implementing the simplified rotationally invariant formulation discussed in section 2.9.3 and eq.(2.76) using the FLL double counting correction scheme.

The rotationally invariant formulation can be cast into a simpler form with the FLL

[13]Note that usually in the literature the atomic site is denoted by I and m is used to denote magnetic quantum number for a certain angular momentum l. We have kept atomic site $\mathbf{R}$ and l and m separate here although $\mathbf{R}$ has been made redundant and is not explicitly mentioned in the right hand sides of many equations.

double counting scheme [99], [100] by retaining the lowest order Slater integral F^0 as,

$$H^{\text{DFT+U, FLL}} = H^{\text{Hub}} - H^{\text{DC}} = \sum_{\mathbf{R},l,\sigma} \frac{U^l}{2} \text{ Tr } [n^{l\sigma}(1 - n^{l\sigma})] \tag{2.76}$$

In this representation, sometimes U is replaced by a $U_{\text{eff}} = U - J$ [101]. But this formulation essentially loses the dependence on exchange Coulomb interaction J as calculated above in section 2.9.1. However J, also called the Hund's coupling, which accounts for the magnetic quantum number (m) dependent interactions, is important to find the correct ground state in multiband metals, in presence of non-collinear magnetism, in presence of strong spin-orbit coupling, [88] etc. However, the popular use of the DFT+U energy formula in eq.(2.76) is also the reason why DFT+U calculation has only a minor computational overhead when compared to DFT. It is because compared to the formulation in section 2.9.1, here no integrals need to be evaluated. One just needs to find the DFT+U occupation matrix and the energy is corrected. This is implemented in almost all popular DFT codes and is widely accessible for short computational cost when compared to DFT.

The effective potential that enters the Kohn-Sham Hamiltonian in this formulation will be,

$$v^{l,\sigma}_{m_1,m_2} = \frac{\partial H^{\text{DFT+U, FLL}}}{\partial D^{\sigma}_{ij}} = -U^l \left(n^{l\sigma}_{m_1 m_2} - \frac{\delta_{m_1 m_2}}{2} \right) \tag{2.77}$$

where D^{σ}_{ij} represents an element of the general density matrix of the system where i, j stand for the basis index on a certain atomic site [99]. For a single site, it becomes the occupation matrix. This can then be added back to the DFT Hamiltonian and following the logic of fig.(2.5), the ground state can be found self-consistently. Consequently the following can be observed.

- Occupied orbitals $\rightarrow$ occupancy $= 1 \rightarrow$ orbital energy shifted by $\dfrac{-U}{2}$
- Unoccupied orbitals $\rightarrow$ occupancy $= 0 \rightarrow$ orbital energy shifted by $\dfrac{U}{2}$

Thus DFT+U leads to a band gap opening proportional to the value of U. In this context, DFT+U with the FLL correction is often interpreted as an energy penalty on the system that forces the system to have full or empty orbitals. However this change can be very drastic and unphysical if U is too high.

Still the choice of the double counting correction is ambiguous and system dependent, the values of U and J can be a source of error [88], [101] and DFT+U does not give a systematic way to fix these *parameters*. For better a better approximation beyond DFT, we go further than such static corrections of DFT to Dynamical Mean Field Theory discussed in the following section.

2.10 Dynamical Mean Field Theory

The dynamical mean field theory essentially maps the *effective* Hubbard model to the single impurity Anderson model such that the local Green's function at a single site in the lattice is equal to the impurity Green's function of the effective impurity model. To understand this statement, we first briefly view the Anderson impurity model and then move on to the DMFT scheme of solving this mapped impurity problem.

2.10.1 Anderson Impurity Model

The second way to treat the effective Hubbard model, that we originally mapped from the electron Hamiltonian of DFT, is to map it onto a Single impurity Anderson model (SIAM). SIAM, as the name suggests, describes a single impurity embedded in an effective field. This mapping is a way to solve the Hubbard model with a mean field treatment for the selected degrees of freedom which here correspond to the quantum degrees of freedom at a cite-centred correlated orbital.

In general, the Anderson impurity model (AIM) Hamiltonian is written as,

$$\begin{aligned} H^{\text{SIAM}} &= \sum_{\xi_i\xi_j} \varepsilon_{\xi_i\xi_j} c^\dagger_{\xi_i} c_{\xi_j} + \frac{1}{2}\sum_{\mathbf{R}} \sum_{\xi_1\xi_2\xi_3\xi_4} U_{\xi_1\xi_2\xi_3\xi_4} c^\dagger_{\mathbf{R}\xi_1} c^\dagger_{\mathbf{R}\xi_2} c_{\mathbf{R}\xi_3} c_{\mathbf{R}\xi_4} \\ &+ \sum_{\mathbf{k},\sigma} \varepsilon_{\mathbf{k},\sigma} a^\dagger_{\mathbf{k},\sigma} a_{\mathbf{k},\sigma} + \sum_{\mathbf{k},\xi_i,\sigma} (V_{\mathbf{k},\sigma} a^\dagger_{\mathbf{k},\sigma} c_{\xi_i,\sigma} + \text{h.c.}) \qquad (2.78) \\ &= H^{\text{imp}} + H^{\text{bath}} + H^{\text{hyb}} \text{ , where} \qquad (2.79) \end{aligned}$$

- H^{imp} comprises of the first and the second term. The first term in eq.(2.78) corresponds to the energy of the impurity electrons that is obtained as the DFT Hamiltonian is projected onto the correlated orbitals. This term controls the chemical potential such that for the one-orbitals case it can merge with the chemical potential making it 0. The second term with the U-tensor denotes the interacting part of the atomic Hamiltonian corresponding to the interactions in the correlated orbitals. For a single orbital, this term will become $Uc^\dagger_\uparrow c_\uparrow c^\dagger_\downarrow c_\downarrow$ and $\mathbf{R}$ will be superfluous. Note that here the impurity operators are denoted by $c, c^\dagger$.

- H^{bath} is represented by the third term in eq.(2.78) that denotes the bath composed of conduction electrons i.e., all the electrons other than those considered as impurity with a generic quantum number $\mathbf{k}$ and spin quantum number σ denoted by $a, a^\dagger$.

- H^{hyb} corresponds to the last term in eq.(2.78) that denotes the hybridisation between the impurity $(c, c^\dagger)$ and the bath $(a, a^\dagger)$ with $V_{\mathbf{k},\sigma}$ being the magnitude of this hopping.

We consider the single impurity case with a single correlated orbital of interest for conceptual simplicity. The SIAM impurity Green's function can be written as,

$$G^{\text{imp}}_{\xi_1\xi_2\sigma}(\tau - \tau') = -\langle T\ c_{\xi_1\sigma}(\tau)c^{\dagger}_{\xi_2\sigma}(\tau')\rangle \tag{2.80}$$

where τ is the imaginary time in Matsubara [102] formalism with $0 < \tau < \beta$ and T is the time ordering operator which specifies that

- for $\tau > \tau'$: an electron created in orbital ξ_2 with spin σ at imaginary time τ' propagates through the system before getting annihilated in orbital ξ_1 at imaginary time τ, and
- for $\tau' > \tau$: a hole is created at imaginary time τ in orbital ξ_1 with spin σ which propagates and gets annihilated at imaginary time τ' in orbital ξ_2

It is often useful to know the non-interacting impurity Green's function for the SIAM by putting the on-site Coulomb term to 0. This can be done by writing the effective action and integrating out the bath degrees of freedom [103]. We also merge the impurity electron energy $H^{\text{at},0}$, denoted by the first term in eq.(2.78), with the chemical potential. Then we go from imaginary time τ to Matsubara frequencies, $\omega_n = \frac{(2n+1)\pi}{\beta}$, and write

$$\mathcal{G}^{\text{imp},0}_{\sigma}(i\omega_n) = \left[(i\omega_n + \mu) - H^{\text{at},0} - \Delta_{\sigma}(i\omega_n)\right]^{-1} \tag{2.81}$$

$$\Delta_{\sigma}(i\omega_n) = \sum_{\mathbf{k}} \frac{|V_{\mathbf{k},\sigma}|^2}{i\omega_n - \varepsilon_{\mathbf{k},\sigma}} \tag{2.82}$$

where Δ_σ is called the hybridisation function or the mean field that is determined by $\varepsilon_{\mathbf{k},\sigma}$ and $V_{\mathbf{k},\sigma}$, and depends on the Matsubara frequencies in the effective SIAM Hamiltonian, and signifies the background field for the impurity considered. As per many-body perturbation theory, the full interacting impurity Green's function, G^{imp}_{σ}, that includes the onsite Coulomb interaction term in SIAM can be found using the Dyson equation as,

$$G^{\text{imp}}_{\sigma}(i\omega_n) = \left[\{\mathcal{G}^{\text{imp},0}_{\sigma}(i\omega_n)\}^{-1} - \Sigma^{\text{imp}}_{\sigma}(i\omega_n)\right]^{-1} \tag{2.83}$$

where $\Sigma^{\text{imp}}_{\sigma}$ is the impurity self-energy that contains all the information about the interactions and depends only on the non-interacting Green's function $\mathcal{G}^{\text{imp},0}_{\sigma}$ and through it to the hybridisation function Δ_σ which in turn depends on $\varepsilon_{\mathbf{k},\sigma}$ and $V_{\mathbf{k},\sigma}$, and on-site Coulomb interaction term. It describes how interactions affect the propagation of electrons.

The "self" in self-energy historically comes from [104] the description of an interacting system as an electrolyte with equal number of positive and negative ions. In this portrayal each bare particle, because of the Coulomb interaction, is surrounded by a dress or a coat or a cloud of oppositely charged particles, and together with that forms a ***quasiparticle****, or a renormalised particle from field theory considerations, with the initial bare particle forming the cloud core. But this picture is valid only when there are a few quasiparticles compared to the total number of particles in the system. Due to this, the entire system isn't visualised as made up of quasiparticles but as a gedanken experiment where an extra particle is added to the electrolyte and its motion through the system is studied. This quasiparticle or quasi-ion moves through the system for a finite lifetime before undergoing collision with another quasi-ion that belongs to the system itself.*

The difference between the energy of the quasiparticle and the bare particle was called the ***"self"-energy*** *of the quasi-particle because in the above picture it seems as if the bare particle disturbs the many-body system thereby creating the quasiparticle cloud in the first place which in turn reacts and disturbs the many body system again that affects the quasiparticle's own motion. It is as if the quasiparticle is interacting with itself, changing its own energy via the many-body system due to the presence of Coulomb interactions.*

The self-energy Σ defined in this section isn't an energy term, unlike this historical definition but, as per the Dyson equation in eq.(2.83), is the inverse of the difference between the non-interacting and interacting inverse Green's functions, and thus acts as a mathematical ***measure of the many-body interactions*** *present in a system that is related to physical observables via the Green's functions.*

2.10.2 Impurity mapping and self-consistency

Now we come back to our effective Hubbard lattice problem. For the correlated orbitals in any general lattice problem, the local Green's function at a single site will be given by,

$$G^{\text{loc}}_{\mathbf{R}\sigma\xi_1\xi_2}(\tau - \tau') = -\langle T\ c_{\mathbf{R}\xi_1\sigma}(\tau) c^{\dagger}_{\mathbf{R}\xi_2\sigma}(\tau')\rangle \tag{2.84}$$

The lattice problem is often dealt with in the reciprocal space. In this space, we can denote the non-interacting lattice Green's function as,

$$G^0_{\sigma}(\mathbf{k}, i\omega_n) = \frac{1}{i\omega_n + \mu - \epsilon_{\mathbf{k},\sigma}} \tag{2.85}$$

where $\epsilon_{\mathbf{k},\sigma}$ are the Fourier transform of the hopping matrix elements. They can originate from a model Hamiltonian or can be projected from DFT to an effective Hubbard model as described in eq.(2.62). The Lattice Green's function $G_\sigma(\mathbf{k}, i\omega_n)$ for the interacting case can similarly be written by invoking the Dyson equation again as,

$$G_\sigma(\mathbf{k}, i\omega_n) = \left[\{G^0_\sigma(\mathbf{k}, i\omega_n)\}^{-1} - \Sigma_\sigma(\mathbf{k}, i\omega_n)\right]^{-1} \tag{2.86}$$

$$= \frac{1}{i\omega_n + \mu - \epsilon_{\mathbf{k},\sigma} - \Sigma_\sigma(\mathbf{k}, i\omega_n)} \tag{2.87}$$

where $\Sigma_\sigma(\mathbf{k}, i\omega_n)$ is the lattice self-energy through which the interactions enter the lattice problem. Note that in the DFT+U Hamiltonian in eq.(2.62), a static U was evaluated leading to an additive term in the energy functional that changed the effective DFT potential. In DMFT, the effect of U is incorporated in the lattice problem through the self-energy via the interacting and the non-interacting lattice Green's functions.

So now we have two sets of non-interacting, interacting Green's functions and self-energies each for the lattice and the impurity problem related to each other within the problem by the Dyson equation.

Lattice	Impurity
$G_\sigma(\mathbf{k}, i\omega_n) = [\{G^0_\sigma(\mathbf{k}, i\omega_n)\}^{-1} - \Sigma_\sigma(i\omega_n)]^{-1}$	$G^{\text{imp}}_\sigma(i\omega_n) = \left[\{\mathcal{G}^{\text{imp},0}_\sigma(i\omega_n)\}^{-1} - \Sigma^{\text{imp}}_\sigma(i\omega_n)\right]^{-1}$

By identifying a correlated orbital at a lattice site as an impurity, a self-consistent solution can be constructed such that the impurity Green's function $G^{\text{imp}}_\sigma(i\omega_n)$ is identical to the local lattice Green's function $G^{\text{loc}}_{\mathbf{R}\sigma}(i\omega_n)$ as,

$$G^{\text{imp}}_\sigma(i\omega_n) = G^{\text{loc}}_{\mathbf{R}\sigma}(i\omega_n) = \int_{\text{BZ}} d\mathbf{k}\; G_\sigma(\mathbf{k}, i\omega_n) \tag{2.88}$$

where BZ implies the Brillouin zone. This is the DMFT **self-consistency condition**. Implementing this amounts to finding a hybridisation function Δ_σ such that the above condition is obeyed. This in turn means that those $\varepsilon_{\mathbf{k},\sigma}$ and $V_{\mathbf{k},\sigma}$ values will be found iteratively which at self-consistency will respect eq.(2.88). Note that Δ_σ, that we originally interpreted as the **mean field** felt by the impurity in the AIM, is always frequency dependent either in Matsubara frequencies or imaginary time or even real frequencies, and thus is **dynamical** in nature. By that virtue, it also contains information about the temperature of the system unlike the terms in the plain DFT Hamiltonian. In reference to the Anderson impurity model of eq.(2.78), it means that the bath formed by the conduction electrons will be updated at each iteration. Since Δ_σ was identified as the background mean field, the self-consistency condition translates to finding this mean field iteratively such that the Anderson impurity model mimics the lattice environment

within a convergence criteria. Note that sometimes depending on the implementation one may also work with $\mathcal{G}_\sigma^{\text{imp},0}(i\omega_n)$ instead of the hybridisation function.

So far the representation of the original lattice is exact and the *impurity Green's function is chosen* to be equal to the lattice local Green's function. However this is not sufficient to find the solution iteratively, and another condition is needed to relate the two sets of equations. This is done with the **dynamical mean field approximation**. It identifies the lattice self-energy to be local as well by equating it to the impurity self-energy as,

$$\Sigma_{\mathbf{R}\mathbf{R}'\sigma}(i\omega_n) = \delta_{\mathbf{R}\mathbf{R}'}\Sigma_\sigma^{\text{imp}}(i\omega_n) \tag{2.89}$$

The DMFT approximation appears arbitrary but is similar to Weiss mean field theory of the Ising model where the effective field is approximated by the thermal average of the local field seen by a spin at a given site. In the reciprocal space, it means that the self-energy becomes k-independent as,

$$\Sigma_\sigma(\mathbf{k}, i\omega_n) \approx \Sigma_\sigma^{\text{imp}}(i\omega_n) \tag{2.90}$$

Note that even with this approximation, the self-energy retains a frequency dependence. This dependence extends to all the Green's functions as well, and thus the theory is **dynamical**. When DMFT is used as a correction on DFT, or for other system specific Hubbard model definitions, instead of the hybridisation function (or mean field) Δ_σ, either one of the Green's functions or the self-energy[14] becomes the term of focus which is evaluated. That quantity the takes the role of the dynamical mean field of the system that is evaluated using the above approximations self-consistently. There are three limiting cases where this approximation is exact.

1. $U = 0$: The self-energy is 0 and thus trivially local.

2. For infinite nearest neighbours or infinite dimensions, the DMFT approximation becomes exact. It was proved by Metzner and Vollhardt in 1989 [105] and is sometimes considered the first milestone of DMFT. The second milestone work happened a year later when Georges and Kotliar [106] showed that in this limit it is possible to exactly map the Hubbard model onto the Anderson impurity model.

3. Atomic limit: Here, the sites are decoupled which makes the hybridisation function 0.

$$t_{\mathbf{R}_1\xi_1\mathbf{R}_2\xi_2} \sim \delta_{\mathbf{R}_1\mathbf{R}_2} \longrightarrow \Delta_\sigma(i\omega_n) = 0 \tag{2.91}$$

   This implies that the self-energy only has on-site components and thus is local. The Hubbard-I approximation which is an approximate DMFT solver to solve the SIAM is built in this limit. We will study this in detail later.

[14] E.g., in chapter 3 the self-energy becomes the quantity of interest whose accuracy is checked and that is iterated over, as depicted in fig.(3.4).

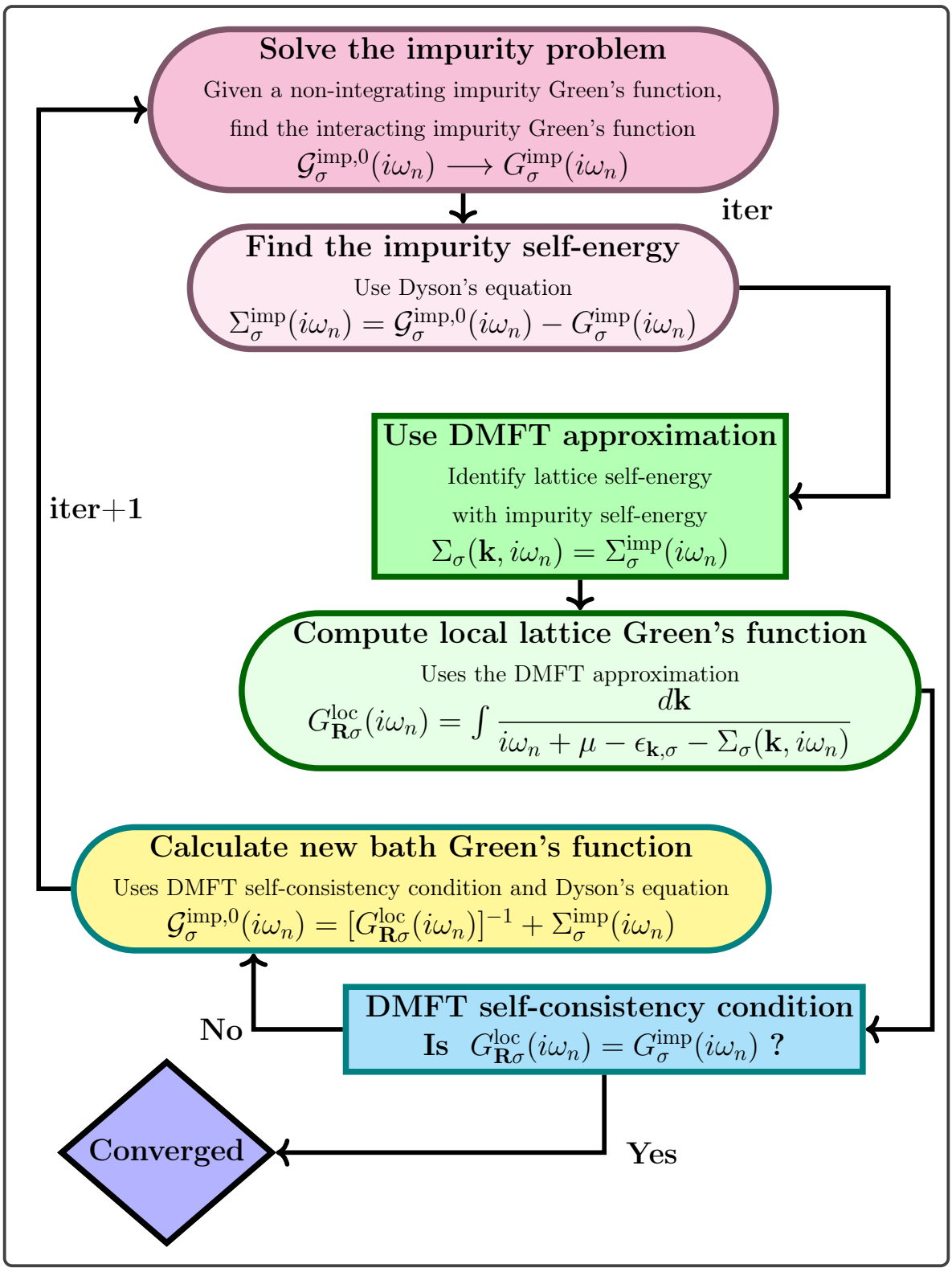


Figure 2.6: The general dynamical mean field theory (DMFT) self-consistent iterative scheme.

Thus, for a given non-interacting impurity Green's function $\mathcal{G}_\sigma^{\mathrm{imp},0}(i\omega_n)$ (called a bath Green's function after the 1$^{\mathrm{st}}$ iteration) if we can compute the interacting impurity

Green's function $G_\sigma^{\text{imp}}(i\omega_n)$ we will have a self-consistent set of equations that can be evaluated, as depicted in fig.(2.6). However finding G_σ^{imp} is usually not only the most computationally expensive problem but also that step in the DMFT cycle whose approximations determine the kind of problem one can choose to look at and the validity of the results in chosen limits. This is called the impurity problem, and can be solved with various approximations. We will discuss two impurity solvers which have been used in this thesis in detail namely the Hubbard-I solver and the Iterated Perturbation Theory (IPT) solver.

2.10.3 DFT+DMFT

Before going into the details of the DMFT-HI and IPT solvers, we will briefly discuss how the above set of equations which were obtained for a single orbital Hubbard-like model can be generalised to multi-indices. We use the notation described in section 2.9 and denote the DFT weakly correlated basis by $|\mathbf{k}, \chi\rangle$ which will play the role of the bath and the correlated orbitals by $|\mathbf{k}, \xi\rangle$ which will be corrected for using the DMFT treatment. If H^{DFT} be the converged Kohn-Sham Hamiltonian, then the one-electron Green's function will be written as,

$$G^{\text{DFT}}(i\omega_n) = [(i\omega_n + \mu) - H^{\text{DFT}} - \Sigma(i\omega_n)]^{-1} \tag{2.92}$$

We denote the original DFT basis as a global basis in quantum numbers χ. Usually in the first DMFT iteration $\Sigma = 0$. After this is obtained, a projector $\mathcal{P}_C$ is defined which projects the Kohn-Sham eigenstates to the basis of the correlated subspace. In real space, for a set of correlated orbitals represented by a generic set of quantum numbers ξ at site R it can be written as,

$$\mathcal{P}_C = \sum_{\xi} |\mathbf{R}, \xi\rangle\langle\mathbf{R}, \xi| \tag{2.93}$$

Then the single particle part of the AIM i.e., the non-interacting impurity Green's function $\mathcal{G}^{\text{imp},0}(i\omega_n)$ can be written as,

$$\mathcal{G}^{\text{imp},0}(i\omega_n) = \mathcal{P}_C \; G^{\text{DFT}}(i\omega_n) \; \mathcal{P}_C \tag{2.94}$$

This is then fed to the impurity solver and the DMFT cycle is run self-consistently. The converged set of Green's functions can then be used evaluate the charge density and obtain relevant physical parameters. This whole process is known as 1-shot DMFT. In a second way, the Kohn-Sham Hamiltonian can be written again using this new charge density, solved in the DFT approximation for the entire space of weakly and strongly correlated systems and fed back to the next DMFT cycle till an outer DFT+DMFT self-consistency is attained in the charge density. This is called charge self-consistent

DMFT.

2.10.4 Hubbard-I solver

Hubbard-I solver is an approximate solver to the single impurity Anderson model based on the Hubbard I approximation. The Hubbard-I approximation solves the impurity problem in the atomic limit, mentioned on page 52, in which the sites are assumed to be decoupled. This implies that in the effective system Hamiltonian given by the AIM in eq.(2.78), the hybridisation or the coupling term H^{hyb} between the impurity and the bath is neglected. This leads to the self-energy having only on-site components. In other words, the impurity self-energy is assumed to be same as the atomic self-energy. Together with the DMFT approximation, this results in the lattice self-energy being considered to be equal to the atomic self-energy as well as,

$$\Sigma_{\mathbf{R}\mathbf{R}'\sigma}(i\omega_n) = \delta_{\mathbf{R}\mathbf{R}'}\Sigma^{\text{At}}_{\sigma}(i\omega_n) \tag{2.95}$$

Since we assume $V_{\mathbf{k},\sigma} = 0$, this implies in the DMFT self-consistent cycle as discussed in section 2.10.2, the hybridisation function $\Delta_\sigma = 0$. This obliterates a computationally expensive quantity that needs to be found and makes this approximation very fast. However this is a rather strong approximation[15] since essentially an atomic problem is solved instead of an impurity problem and can only be applied when the correlated orbitals are atomic-like with a negligible hybridisation. This holds true mostly for rare-earth materials with $4f$-orbitals. As a result we have used DFT+DMFT with the Hubbard-I solver in this thesis in chapters 4 and 5 to study Samarium chacogenides where Sm is a rare-earth element with valence configuration [Xe] $4f^6\ 6s^2$. The various steps used in a generic implementation of the Hubbard-I DMFT solver are listed below.

1. DFT loop is run and using the converged density H^{DFT} is obtained.

2. H^{DFT} is then projected from the global basis χ onto the correlated states at site $\mathbf{R}$, $|\mathbf{R},\xi\rangle$. For lanthanides for example, this will be the subspace formed by the atomic-like $4f$ states. This gives the non-interacting atomic Hamiltonian $H^{\text{At},0}_{\mathbf{R}}$ which is then used to write the non-interacting atomic Green's function $G^{\text{At},0}(\omega)$ in real frequencies.

$$H^{\text{At},0}_{\mathbf{R}} = \sum_{\xi_1\xi_2}\langle \mathbf{R}\xi_1|H^{\text{DFT}}_{\mathbf{R}}|\mathbf{R}\xi_2\rangle c^{\dagger}_{\mathbf{R}\xi_1}c_{\mathbf{R}\xi_2} \tag{2.96}$$

$$G^{\text{At},0}(\omega) = [\ \omega + (\mu^{\text{DFT}} + \Delta\mu^{\text{At}} + \mu^{\text{DC}}) - H^{\text{At},0}_{\mathbf{R}}\ ]^{-1} \tag{2.97}$$

[15] Some people also prefer not attaching the venerated DMFT name to this solver as an eulogy to the death of the revered hybridisation term. They are, of course, correct. However as we will see later, the DMFT self-consistent cycle is still used, and since we are using this solver for $4f$ systems, we call it DMFT.

At this step the chemical potential also has to be adjusted with essentially three contributions.

(a) μ^{DFT}, which is determined by the converged DFT calculation. For a 1-shot DMFT, this is kept fixed. However, for a charge self consistent DMFT, this is readjusted to reflect the change the density of delocalised electrons by the new density of the localised or correlated electrons that is obtained from a converged DMFT run.

(b) μ^{DC}, which corrects for the Coulomb repulsion term that will be added in the next step. Its presence is to correct for a part of this repulsion that has already been accounted for in the DFT calculation. However there is no straightforward way of knowing this value, and its calculation depends on the double counting approximation used, discussed in section 2.9.2. We have used the FLL approximation throughout.

(c) μ^{At}, which ensures that the particle number remains conserved between the SIAM and the atomic model which essentially is the SIAM without the hybridisation term. E.g., in lanthanides this will take care of the correct number of f-electrons between different DMFT iterations.

μ^{DC} and μ^{At} invoke a rigid shift and in most implementations are coupled together.

3. Then the on-site Coulomb tensor is added to this Hamiltonian giving the interacting atomic Hamiltonian $H^{\mathrm{At}}_{\mathbf{R}}$ while the coupling of the impurity and the bath is ignored. This is the stage where a choice has been made to solve an atomic problem in place of an impurity problem.

$$H^{\mathrm{At}}_{\mathbf{R}} = H^{\mathrm{At},0}_{\mathbf{R}} + \frac{1}{2}\sum_{\xi_1\xi_2\xi_3\xi_4} U_{\xi_1\xi_2\xi_3\xi_4} c^{\dagger}_{\mathbf{R}\xi_1} c^{\dagger}_{\mathbf{R}\xi_2} c_{\mathbf{R}\xi_3} c_{\mathbf{R}\xi_4} - (\mu^{\mathrm{DFT}} + \Delta\mu^{\mathrm{At}} + \mu^{\mathrm{DC}}) \sum_{\xi} c^{\dagger}_{\mathbf{R}\xi} c_{\mathbf{R}\xi} \tag{2.98}$$

4. This Hamiltonian is then diagonalised giving many-body eigenvalues (E_ν) and eigenfunctions ($|\nu\rangle$) which are then used to write the interacting atomic Green's function $G^{\mathrm{At}}(\omega)$ in real frequencies using the Källén –Lehmann spectral representation [107] [76] as,

$$G^{\mathrm{At}}_{\xi_1\xi_2}(\omega) = \frac{1}{Z}\sum_{\nu'\nu} \frac{\langle\nu'|c_{\xi_1}|\nu\rangle\langle\nu|c^{\dagger}_{\xi_2}|\nu'\rangle}{\omega + E_{\nu'} - E_{\nu}} (e^{-\beta E_{\nu'}} + e^{-\beta E_{\nu}}) \tag{2.99}$$

5. The Dyson equation is then used to compute the atomic self-energy $\Sigma^{\mathrm{At}}(\omega)$ which then holds the information about the system interactions as,

$$\Sigma^{\mathrm{At}}(\omega) = [G^{\mathrm{At},0}(\omega)]^{-1} - [G^{\mathrm{At}}(\omega)]^{-1} \tag{2.100}$$

6. The impurity self-energy is then taken to be equal to the atomic self-energy. This step is often called the **Hubbard-I approximation**. However note that it stems from neglected the coupling when writing the atomic Hamiltonian by ignoring the hybridisation term in the Anderson Impurity Hamiltonian.

7. The impurity self energy is then written in terms of the global basis χ. This step is called upfolding.

8. Using this upfolded self-energy $\Sigma(\omega)$, the one electron Green's function $G(\omega)$ is written in the global basis again. In this step the atomic and the non-interacting features are recombined. This is then used to calculate the spectral function (or, electron density) as,

$$\rho(\omega) = -\frac{1}{\pi} \text{ Im } [G(\omega + i\delta)] \ , \ \delta \to 0^+ \tag{2.101}$$

   In real computations, δ is small but non-zero, and causes a broadening of the spectrum. It is often also called smearing. The chemical potential is adjusted in the global basis to account for the right number of particles. This can in general be done in two ways.

   (a) Keeping the number of delocalised electrons fixed and adjusting μ^{At} and μ^{DC}, for 1-shot DMFT in step 2 till a self-consistency in the self-energy is attained. One drawback of 1-shot DMFT is that it carries on the systematic errors introduced by, say, a faulty correlation function.

   (b) Adjusting all μ^{DFT} as well for attaining charge self-consistency in which case the density of the delicalised electrons is recalculated, and a slightly different H^{DFT} is obtained. Then step 1 is repeated until self-consistency is obtained in self-energy as well as density. As expected, this results in an outer DFT+DMFT loop in density and an inner DMFT loop in self-energy, and thus is computationally more expensive.

Since in the Hubbard-1 approximation, the coupling term of the impurity with the bath is neglected, this makes the solver most economical computationally while ignoring important physics arising from the hybridization of the correlated orbitals with the bath.

2.10.5 Iterated Perturbation Theory (IPT) solver

Iterated Perturbation Theory (IPT) solver is another approximate solver for DMFT. As the name suggests, it is based on a perturbative expansion of the self-energy in the Coulomb interaction term U till the second order in the auxiliary impurity model. It was originally designed to work at half-filling such that the self-energy becomes exact at both

the weak and strong coupling limit [108], [109]. At half-filling, the IPT approximation till the second order contribution in the Feynman diagram gives,

$$\Sigma^{\mathrm{IPT},0}(i\omega_n) \approx U^2 \int_0^\beta d\tau\ e^{i\omega_n\tau}\ \mathcal{G}^0_\sigma(\tau)\ \mathcal{G}^0_{-\sigma}(-\tau)\ \mathcal{G}^0_{-\sigma}(\tau)\ ,\ \text{with} \tag{2.102}$$

$$\mathcal{G}^0_\sigma(i\omega_n) = \frac{1}{i\omega_n + \mu_0 - \Delta_\sigma(i\omega_n)} \tag{2.103}$$

For simplicity, we only consider a system with no magnetic symmetry breaking i.e., $n_\sigma = n_{-\sigma} = n$. For such cases, beyond half-filling the expression is modified by an ansatz [110] for the self-energy,

$$\Sigma^{\mathrm{IPT}}(i\omega_n) = U\frac{n}{2} + \frac{A\ \Sigma^{\mathrm{IPT},0}(i\omega_n)}{1 - B\ \Sigma^{\mathrm{IPT},0}(i\omega_n)} \tag{2.104}$$

where A is determined from the condition that the self-energy becomes exact at high frequencies. The first term is called the Hartree term ensures the right high-frequency behaviour. Up to the order of $\frac{1}{\omega}$ one can write,

$$A = \frac{n(2-n)}{n_0(2-n_0)} \tag{2.105}$$

$$n = 2G(\tau = 0^-) \tag{2.106}$$

$$n_0 = 2\mathcal{G}^0(\tau = 0^-) \tag{2.107}$$

$$G(i\omega_n) = \sum_k \frac{1}{i\omega_n + \mu - \varepsilon_k - \Sigma^{\mathrm{IPT}}(i\omega_n)} \tag{2.108}$$

where μ is the lattice chemical potential that can be determined by fixing n. μ_0 is a free parameter which needs to be fixed by an additional condition like the Luttinger liquid theorem at low temperature [110] or by the third moment of the Green's function or simply fixing $n_0 = n$ [111]. Following this B can be evaluated from the atomic limit.

$$B = \frac{(1 - \frac{n}{2})U + \mu_0 - \mu}{\frac{n_0}{2}(1 - \frac{n_0}{2})U^2} \tag{2.109}$$

This is then fed to a DMFT loop. IPT is a an approximate but quick and relatively simple solver that gives the correct $U = 0$ and $U \to \infty$ limits. It can reproduce the main features of the Mott transitions relatively well around half-filling, as we will see in the next section. However it is a largely uncontrolled approximation with the choice of μ_0 being reflected in the solutions qualitatively. Also, its extensions beyond half-filling are not very successful and many-a-times do not interpolate well between weak and high U limits. In this thesis we have only considered IPT at half-filling in chapter 3 i.e., we have only used eq.(2.102) and eq.(2.103). The DMFT loop with the IPT solver

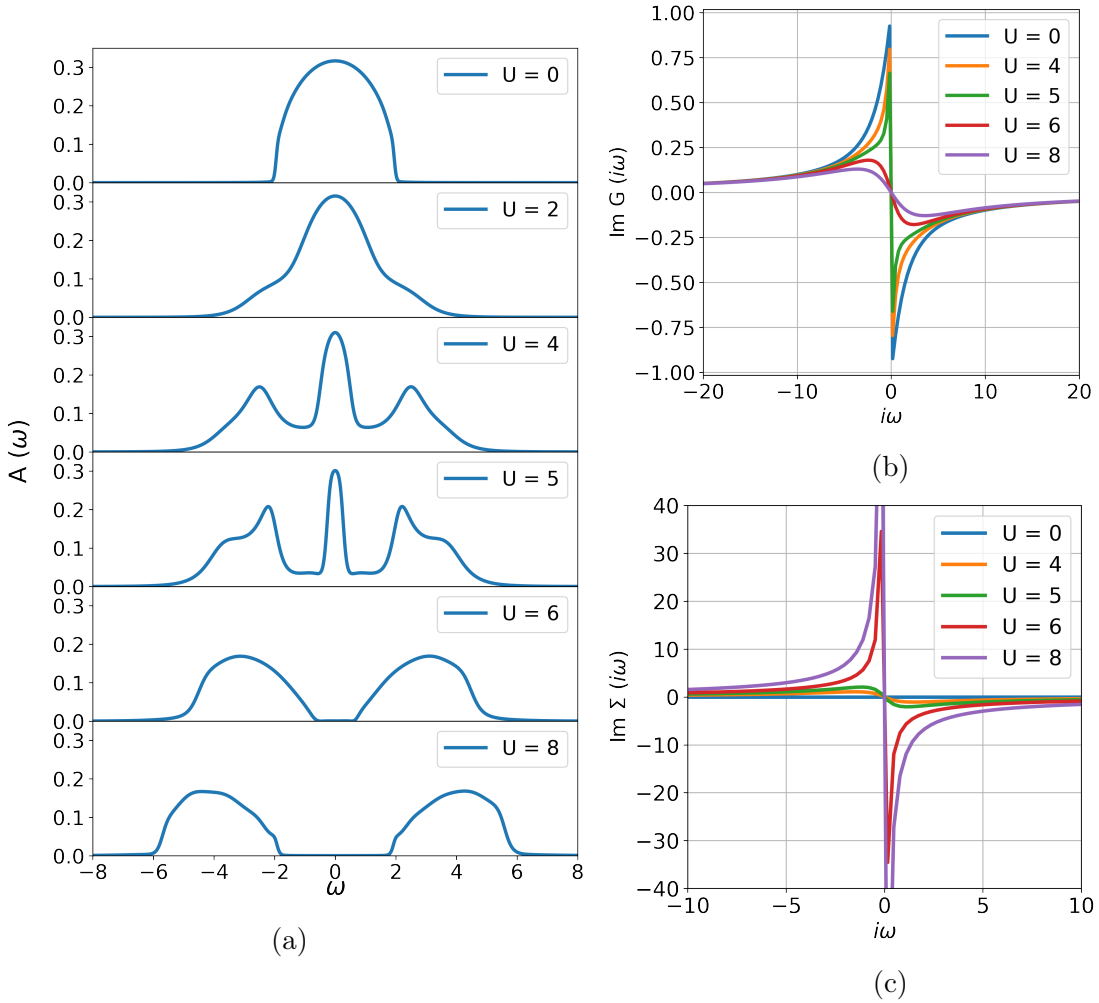


Figure 2.7: (a) Spectral function $A(\omega)$ obtained using Padé approximation [112] for a Hubbard Hamiltonian on the Bethe lattice at half-filling with $t = 1$, $\beta = 20$, half-bandwidth $W = 2t = 2$, depicting the onset and completion of a Mott transition as U increases from 0 to 8. Depiction of (b) imaginary Green's function, and (c) Self-Energy in Matsubara frequencies as the system moves from metallic to insulating regime.

for the specific model considered has been discussed in detail and shown in fig.(3.4).

2.10.6 Mott transition

We will now use an IPT based DMFT solver with the Hubbard model implemented on the Bethe lattice at half filling as a preliminary example to understand the qualitative features of a Mott transition. Bethe lattice[16], introduced by Hans Bethe in 1935 [113], with coordination number z can be thought of a *branching tree* where from each *node* emerges z-many numbers of branches. If t be the hopping, μ be the chemical potential, then in the limit of infinite coordination $z \to \infty$, the local Green's function G_{loc} in

[16] *An infinite connected cycle free graph* with all vertices having the same number of neighbours. For physicists-&-non-mathematicians: only branches, no loops, and more branches.

Matsubara frequencies is related to the non-interacting impurity Green's function as,

$$[\mathcal{G}^{\text{imp},0}(i\omega_n)]^{-1} = i\omega_n + \mu - t^2 G_{\text{loc}}(i\omega_n) \tag{2.110}$$

After executing the DMFT loop and performing analytic continuation with the Padé approximation [112] the spectral function on real frequency can be plotted as shown in fig.(2.7a). Here half-bandwidth is $W = 2t$. From there we can identify three scenarios depending on the ratio $\frac{U}{W}$. Note that the following is a qualitative discussion that can be extended to real materials and is not limited to the Bethe lattice at half-filling because it is based on the qualitative features of the spectral function plotted in fig.(2.7).

- $U << W$: When the onsite Coulomb interaction is very weak compared to the bandwidth, as when $U = 0$, or smaller values of U, the system is weakly correlated. The system is metal. DFT works well for such cases.

- $U >> W$: The Coulomb interaction is so large that the single band from $U = 0$ case now splits into two bands, called the lower and the upper Hubbard bands separated by U with peaks at $E_F \pm \frac{U}{2}$. Here only the lower Hubbard band is occupied and the system behaves as a *Mott insulator*. This splitting can be successfully described by the DFT+U method and corresponds to the scenario discussed on page 47.

- Intermediate regime: This is the most interesting regime to study strong correlations where the spectral function depicts a three peak feature. The competition between U and W is such that two Hubbard bands occur together with a peak at the Fermi level, a remnant of the weak correlation scenario. This peak is often called the quasiparticle peak which can be called a scaled reproduction of the weakly correlated peak by a factor which is interpreted as the quasiparticle weight. This regime is often called a correlated metal.

The success of DMFT lies in its ability to explain the intermediate regime. The quasiparticle weight[17] is defined as,

$$Z = \frac{1}{\left(1 - \lim\limits_{i\omega_n \to 0} \dfrac{d\{\text{Im } \Sigma(i\omega_n)\}}{d(i\omega_n)}\right)} \propto \frac{1}{m^*} \tag{2.111}$$

where m^* is the effective mass of the quasiparticle. If we refer back to fig.(2.7c) we can observe that.

- With the onset of the **Mott transition** and increasing U from 0 to 8, Im $\Sigma(i\omega_n)$ diverges as $i\omega_n \to 0$. This divergence appearing at $U = 6$ in fig.(2.7c) is concomitant with the disappearance of the three-peak feature in fig.(2.7a). At these

[17] Rather confusing nomenclature considering it is proportional of the inverse of effective mass. See [114] for a proof of this relation for Hubbard model at high dimensions.

values $Z \to 0$ i.e., the mobility of the electrons (more accurately, quasiparticles) vanishes and the system becomes a Mott insulator.

- For small values of U, Im $\Sigma(i\omega_n)$ is near 0 for $i\omega_n \to 0$. Here $Z \to 1$. The quasiparticles are mobile. The system is thus metallic in nature.

Lowering of Z from 1 or a finite value to 0 is a typical indicator of the onset and completion of a Mott transition. It qualitatively shows that the quasiparticle peak that had formed due to correlations has now vanished and there en effective renormalisation of the electron mass that manifests as a divergence in Im $\Sigma(i\omega_n)$. We have used this criteria in chapter 4 to classify the material studied.

2.11 Transport

We now briefly discuss three different transport mechanisms that have been studied or are relevant for the discussion of the problems addressed in this thesis.

2.11.1 Thermionic emission

In a material, and more commonly in a metal, at room temperature some quantum states above the Fermi level are filled respecting the Fermi-Dirac statistics. In general, as long at the temperature $T > 0$, some electrons will always occupy these quantum states. Due to random nature of electron motion and collisions, some of the electrons will invade the material or metal surface. Among those electrons, those whose kinetic energies are greater than the work function, ϕ_W, of the material will be able to escape. This transfer of the electron at the material surface will transform a part of their kinetic energy into potential energy and new found absence of an electron or the presence of a hole will increase this phenomenon further. Using statistical and quantum mechanics, it can be shown that the current density J of electrons emitted from the surface of a metal at temperature T can be expressed as per the improved Richardson equation [115] as,

$$J = (1 - R)AT^2 e^{\frac{-\phi_W}{k_B T}} \tag{2.112}$$

where r is the reflection coefficient of the metal surface, k_B is the Boltzmann constant, and A is a constant that includes the effects charge, mass and wave vector of the electron and a material-specific correction factor that includes the effect of the emitting material's bandstructure. There exists a detailed old and new literature on this equation A [116] and its application to various materials [117], [118], and is still an active field of work. As expected from the above relation, the charge flow increases dramatically with temperature. This effect is the principle behind electrons guns in cathode ray tubes, thermionic valves, thermionic diodes, etc.

Schottky emission

If a relative bias is applied such that an electric field is created at the metal surface, then the surface barrier seen by an electron at the Fermi level can be reduced by an amount $\Delta\phi_W$ proportional to the applied field. This will increase the rate of flow and thus the emission current as per the equation,

$$J = (1 - R)AT^2 e^{\frac{-(\phi_W - \Delta\phi_W)}{k_B T}} \tag{2.113}$$

This mechanism is often called Schottky emission [119], [120].

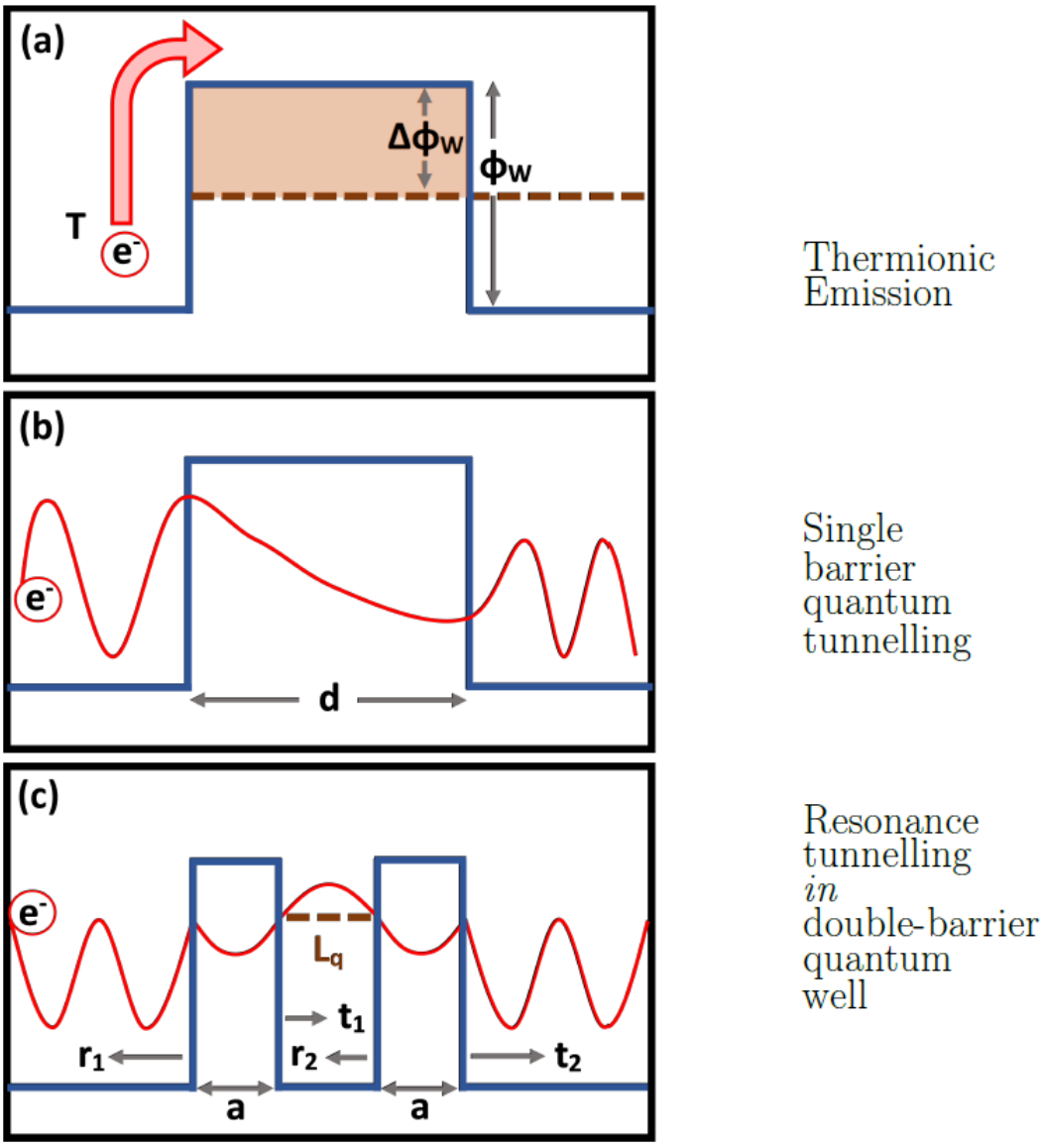


Figure 2.8: Schematic representation of electron transport via (a) thermionic emission, (b) single barrier quantum tunnelling, and (c) resonance tunnelling through a double-barrier quantum well.

2.11.2 Tunnelling

If scientists could choose a phenomena most characteristic of quantum physical structure of matter, that might very well be tunnelling. It is the phenomena where a quantum mechanical *particle*, represented by its *wavefuntion*, whose kinetic energy is less than that of a potential barrier has a finite probability to propagate through the barrier proportional to the height and the width of the barrier. Its applications range from a traditional p-n junction tunnel diode [121] to programming floating gates of flash memory [122] to visualising molecules and atoms through Scanning Tunneling Microscopy (STM) [123] to low power replacements for the CMOS technology via the quantum dot cellular automata implementation [124] or through tunnelling based field effect transistors that can be used as energy efficient switches [125]. If that wasn't enough already, it is also the reason the sun shines (courtesy: the role of quantum tunnelling in nuclear fusion [126])!

Mathematically tunnelling occurs as a simple outcome of solving the Schrödinger (usually, or even Dirac if needed) equation where the quantum mechanical current density has a probabilistic interpretation. A quantum mechanical object, respecting wave-particle duality, is incident on a potential barrier as a travelling wave part of which is reflected (R) and part is transmitted (T) typically depending on the barrier height and width in a square potential barrier. More generally transmission accross a thickness d can be given by,

$$T(E) = T_0(E)e^{\frac{-2\kappa(E)}{d}} \tag{2.114}$$

where $\kappa(E)$ is the decay coefficient which is 0 in a metallic regime and larger values indicate the onset of insulating behaviour.

In a heterostructure, as constructed in fig.(5.14), if the junction (i.e., the film) thickness is *large*, the electron transport is dominated by thermionic emission. In thermionic emission the electrons from the metal (lead) Fermi level are promoted to the conduction band by thermal activation. If the conduction band comes closer to the Fermi level, the probability of this process becomes exponentially larger. Experimentally for samples in bulk form, this effect is what is observed as the exponential increase of conductance on increasing pressure. But if the film is thin i.e., its thickness is in the nanometer scale, the mechanism is quantum tunnelling instead. In this mechanism, as discussed before as per the Landauer-Büttiker formula, the conductance is dictated by the transmission coefficient around the Fermi level.

2.11.3 Resonant Tunnelling

There can be possible scenarios where there are more than one potential barriers in the path of an electron. Let us consider the simplest case of two potential barriers. The associated electron wave-function has a finite probability to tunnel through both the

barriers. It can also be reflected back one or more times and then be transmitted with a phase factors coming from all those reflections. The total amplitude of the incident wave-function that tunnels out through the double-well barrier will be summed over all possible cases of emerging waves with different phases. For the cases when after multiple reflections between the barriers the emergent waves are mostly or all in phase depending on the incident wave-vectors and energies, there will be a constructive interference between the emergent waves for which the amplitude will be a maximum. This is the qualitative picture behind resonant tunnelling [127]. If the barrier is made symmetric, then the transmission can even be 100%.

For two barriers of equal width a as per fig.(2.8c), an incident quantum mechanical wave-function with wave-vector k and energy E can emerge eventually in the following ways. t_1, t_2 and $\mathbf{r}_1, \mathbf{r}_2$ are the transmission and reflection coefficients for the two barriers written with a subscript for the sake of generality in order to understand the role of barrier difference separately. In general, $t_l = |t_l|e^{i\psi_t}, \mathbf{r}_l = |\mathbf{r}_l|e^{i\psi_r}$ are complex with phases ψ_t and ψ_r, respectively.

- No reflection bounce: Tunnels through both the barriers one after the other with the emergent amplitude $t_1 t_2 e^{ika}$.
- Single reflection bounce: Tunnels through the first barrier, reflects off the second, reflects back off the first and finally tunnels through the second and thus accumulates a phase of $3ka$ in the emergent amplitude as $t_1\mathbf{r}_2\mathbf{r}_1 t_2 e^{i3ka}$
- Double reflection bounces: Following the pattern above, the emergent amplitude will be $t_1 t_2 \mathbf{r}_1\mathbf{r}_2\mathbf{r}_1 t_2 e^{i5ka}$
- $\cdots$

Thus, the total transmission amplitude will form a geometric series as,

$$\begin{aligned} t &= t_1 t_2 e^{ika} + t_1\mathbf{r}_2\mathbf{r}_1 t_2 e^{i3ka} + t_1 t_2 \mathbf{r}_1\mathbf{r}_2\mathbf{r}_1 t_2 e^{i5ka} + \cdots && (2.115)\\ &= t_1 t_2 e^{ika}\left[\frac{1}{(1-\mathbf{r}_1\mathbf{r}_2 e^{i2ka})}\right] && (2.116)\end{aligned}$$

The transmission probability T can be written as,

$$T = |t|^2 = \frac{|t_1|^2|t_1|^2}{1+|\mathbf{r}_1|^2|\mathbf{r}_2|^2 - 2|\mathbf{r}_1||\mathbf{r}_2|\cos(2ka+\psi_{\mathbf{r}_1}+\psi_{\mathbf{r}_2})} \quad (2.117)$$

At resonance,

$$\begin{aligned} 2ka+\psi_{\mathbf{r}_1}+\psi_{\mathbf{r}_2} &= 2n\pi && (2.118)\\ \Rightarrow T_{\text{res}} &= \frac{|t_1|^2|t_2|^2}{(1-|\mathbf{r}_1||\mathbf{r}_2|)^2} && (2.119)\end{aligned}$$

If the barriers are symmetric then $t_1 = t_2$ and $\mathbf{r}_1 = \mathbf{r}_2$, and since $|t_1|^2 + |\mathbf{r}_1|^2 = 1$ by conservation of probability,

$$T_{\text{res, DB}} = 1 \tag{2.120}$$

This is a remarkable as well as baffling result as it implies that even though the transmission through a single barrier can be small, a symmetric double barrier can almost be invisible under certain conditions.

Note that any state inside the quantum well is not a stationary state, and can eventually tunnel out. They are unbound states with a lifetime proportional to the tunnelling probability. Such states are called *quasi-bound states*. If an electron is incident on a symmetric double barrier with incident energy approximately equal to the energy of a quasi-bound state in the hollow between the two barriers, resonant tunnelling will occur. It will be as if the two potential barriers are almost absent, as depicted in fig.(2.8c). Resonant tunnelling diodes [128], [129], made up of doped semiconductors creating a complex heterostructure of potential wells are promising candidates for integrated circuit technology.

2.11.4 Landauer-Büttiker formalism

A significant contribution in the realm of nanoscale transport for mesoscopic systems, that still influences the way we think about it, came from Rolf Landauer, especially through his papers in 1957 [130] followed by 1970 [131]. The **Landauer formalism** originally studied a simplified conductor (a Fermi gas in a one-dimensional disordered lattice) connected through smooth single wires to reservoirs at different chemical potentials on its either end and related the statistical properties of a complex quantum mechanical entity, the transmission matrix of the conductor, to its electrical conductance which could be experimentally measured. This was later generalised to multi-channel systems by Büttiker *et al.* [132]. This generalised Landauer or the **Landauer-Büttiker formalism** interprets the conductance through a material as an outcome of scattering processes where electrons are injected from reservoirs onto the material and scattered back to the reservoirs from random scattering centres in the material. The current through the j^th electrode is given by,

$$I_j = \frac{2e}{h} \int \sum_{i=1}^{N} [\ T_{j,i}(\varepsilon)\ f_i(\varepsilon) - T_{i,j}(\varepsilon)\ f_j(\varepsilon)\ ]\ d\varepsilon \tag{2.121}$$

where $T_{i,j}(\varepsilon)$ is the transmission probability of an electron with energy ε from electrode j to electrode i, f_i is the Fermi distribution function of the electrode i that counts in the effect of the lead chemical potential. The multiplicative factor of 2 accounts for duplicacy induced by electron spin.

At low but finite bias $V \to 0$ and zero temperature limit $T \to 0$ in presence of two terminals, the current can be further simplified to,

$$I = \frac{2e^2}{h} T_{RL}(\varepsilon_F) V \tag{2.122}$$

where $T_{RL}(\varepsilon_F)$ represents the total left(L) to right(R) transmission probability calculated at the Fermi level ε_F

Note that the scattering centres are assumed to be static and correspond to the inherent disorder or impurities present in the conductor. These scattering states are occupied in energy according to their asymptotic occupation probability given by the lead Fermi functions (f_i). They are orthogonal and extend from the leads throughout the whole device, thus *static*. Due to this assumption within this formalism, there is no need of an actual electron to pass from one side of the device to the other.

This association between conductance that measures the ease with which electrons flow in material to its transmission probability is what lets various degrees of theory to be applied to transport and be verified from experiments. $T_{i,j}(\varepsilon)$ can be expressed in terms of the conducting region's Green's functions which factors in contributions from the leads via their self-energies and the central conductor via its Hamiltonian and self-energy. In the SMEAGOL [133] [134] implementation of DFT+NEGF, Kohn-Sham equations for an open and non-periodic system are first solved in the NEGF scheme. This gives the transmission probabilities, which are then used in the scope of the above formalism to calculate the current through a two terminal nanoscale device with a potential drop. The many-body corrections are incorporated within the NEGF framework by using a DMFT solver to get the central conductor's self-energy.

2.11.5 Non-equilibrium Green's function (NEGF)

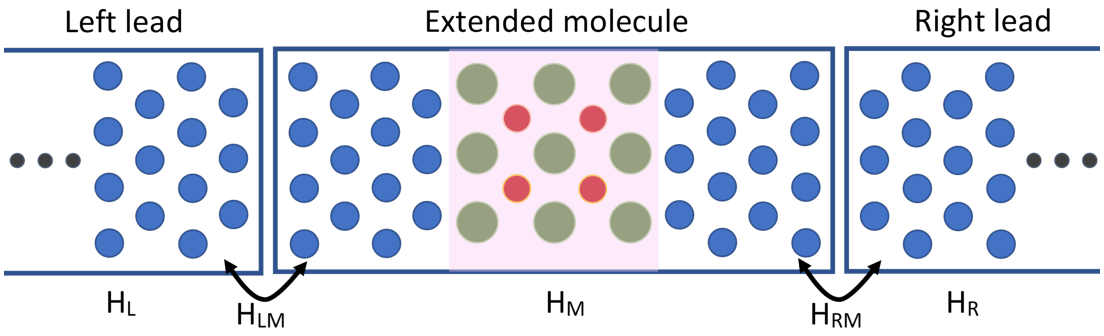


Figure 2.9: Sketch of a two-terminal transport junction with semi-infinite left (H_L) and right (H_R) leads connected via an extended molecule in the middle (H_M) coupled to the left and the right leads by H_{LM} and H_{RM}, respectively.

In this section we do a quick review of the non-equilibrium Green's function approach which is usually used to study electronic transport properties of nanojunctions. In this thesis, it has been employed in chapter 5 to study the transmission properties through an SmSe film sandwiched between leads. It essentially calculates the out of equilibrium

properties of a quantum system. As a first step in this direction, the system is divided into smaller subsystems as depicted in fig.(2.9).

- The left and the right leads are semi infinite electron reservoirs which are supposed to be in a local thermal equilibrium with a corresponding chemical potential μ_L and μ_R. Their respective Hamiltonians and self-energies are H_L, Σ_L and H_M, Σ_M. This means that all the state in the leads are occupied to their respective Fermi energies.

- The central region is often called the *extended molecule* (EM) or the scattering region is made up by the central *interacting region* (ER) and a left and a right subsystem each connected to a lead. For an isolated EM, the Hamiltonian is H_M. The leads do not interact with each other directly but are connected through the EM. The quantum states present in the scattering region can be influence by the rate of inflow and outflow from the leads.

- The coupling between the leads and the extended molecule is done by hopping matrices H_{LM} and H_{RM}. We assume the system to be Hermitian and thus,

$$H_{LM} = H_{LM}^{\dagger} \ , \text{ and } H_{RM} = H_{RM}^{\dagger} \tag{2.123}$$

The NEGF formalism can thus be used to calculate the spectrum of states in the scattering region for a given Hamiltonian, their occupation for a given configuration of the leads and current through the set-up for a given set of chemical potential and applied bias. We can use the above set-up to write the Hamiltonian and the overlap matrix for the entire system as,

$$H = \begin{pmatrix} H_L & H_{LM} & 0 \\ H_{ML} & H_M & H_{MR} \\ 0 & H_{RM} & H_R \end{pmatrix} \text{ and } S = \begin{pmatrix} S_L & S_{LM} & 0 \\ S_{ML} & S_M & S_{MR} \\ 0 & S_{RM} & S_R \end{pmatrix} \tag{2.124}$$

Using these quantities it can be shown [135] that the effective Hamiltonian and the retarded Green's function for the EM in contact with the leads for the device set-up in fig.(2.9) is given by,

$$H_{M,\text{eff}} = H_M + \Sigma_L + \Sigma_R \tag{2.125}$$

$$G_M = [(E + i\delta)S_M - H_{M,\text{eff}}]^{-1} \tag{2.126}$$

where E are the corresponding energy eigenvalues. These can be used to obtain the device wave-functions, density matrices for the leads and the scattering region. These can then be used to find the transmission coefficient and the current flowing through

the scattering region as,

$$T(E) = \text{Tr}\,[\Gamma_L G_M \Gamma_R G_M^\dagger] \tag{2.127}$$

$$I = I_L = -I_R = \frac{2e}{h}\int_{-\infty}^{\infty} dE\; T(E)\;(f_L(E) - f_R(E)) \tag{2.128}$$

where f_L and f_R are the distribution functions of the left and the right leads. This expression is the same as the one obtained in the Landauer-Büttiker way in eq.(2.121).

In implementing DFT with NEGF [133], [136], [137], the Hamiltonian H in eq.(2.125) is taken to be the DFT Hamiltonian. It is assumed that all parts of H excluding H_M do not depend on the electron density of the scattering region ρ_M. Then ρ_M is calculated from G_M via H_M which is then updated and found self-consistently. At the converged value, the transmission and/or current are calculated. Compared to the Landauer-Büttiker formalism which applies to non-interacting systems, DFT+NEGF can be used to study the transmission from the ground state of interacting electrons. However whenever a voltage bias is applied that drives the system out-of-equilibrium, the use of DFT Kohn-Sham single particle states as scattering states might not correspond to true excitation energies. This is a conceptual anomaly in this formalism. Apart from this all limitations of DFT, as discussed in section 2.4.2, are also inherited like the qualitative differences coming from the exchange-correlation degree of approximation and strong electron localisation.

One possible way to go beyond this is to use NEGF with DFT+DMFT [138]. In analogy with a usual DFT+DMFT cycle, here after the extended molecule's Green's function is obtained from the DFT Hamiltonian, it is projected onto a set of interacting orbitals for the extended molecule. This is then defined as the impurity which is treated in the many-body way, similar to fig.(2.6), which is then decoupled from the bath of non-interacting electrons. An impurity solver is used and the DMFT self-consistent cycle is invoked that gives the converged interacting many-body self-energy for extended molecule Σ_{MB}. This is the used to rewrite G_M and $T(E)$ as,

$$G_{MB} = [(E + i\delta)S_M - H_M - \Sigma_L - \Sigma_R - \Sigma_{MB}]^{-1} \tag{2.129}$$

$$T(E) = \text{Tr}\,[\Gamma_L G_{MB} \Gamma_R G_{MB}^\dagger] \tag{2.130}$$

Correct incorporation of correlation has been shown to both qualitatively and quantitatively influence results. We use NEGF with DFT and DMFT in chapter 5 with the DMFT Hubbard-I solver to study transmission through SmSe thin films. However, putting DMFT and NEGF together with DFT makes this method computationally very demanding even with high performance computing.

2.12 Lattice dynamics

We saw in the beginning of section 2.2 that the BO approximation decouples the electronic and lattice degrees of freedom that lets us build the entire DFT formulation for the electronic degrees of freedom.The ionic wave function will obey the ionic Hamiltonian as,

$$H_{\text{ion}}^{\text{full}}\ \chi(\mathbf{R}) = \left[-\frac{1}{2M}\sum_{I}\nabla_I^2 + \frac{1}{2}{\sum_{I,J}}' \frac{Z_I Z_J}{|\mathbf{R}_I - \mathbf{R}_J|} + E_n(\mathbf{R}) \right] \chi(\mathbf{R}) = \varepsilon_\chi(\mathbf{R}) \tag{2.131}$$

where $E_n(\mathbf{R})$ is the electronic energy of the n^{th} eigenstate that is obtained by the solution of the electronic Hamiltonian of eq.(2.3). For DFT, it reflects the effect of screening induced by the valence electrons on the ionic motion. We assume that for the scales relevant for ionic motion the excited states will have negligible effect, and thus we restrict ourselves to the effect of only the electronic ground state $E_0(\mathbf{R})$, which is also the most physically reliable state given by DFT. Within the adiabatic approximation, the kinetic energy of the nuclei is supposed to be a constant and subtracted from the total Hamiltonian and eventually added back later. So, the statics and dynamics of ions can be said to be governed by the last two terms of eq.(2.131) which we denote by H_{ion} which becomes the starting point of the microscopic theory of lattice dynamics.

$$H_{\text{ion}} = \frac{1}{2}{\sum_{I,J}}' \frac{Z_I Z_J}{|\mathbf{R}_I - \mathbf{R}_J|} + E_0(\mathbf{R}) \tag{2.132}$$

A systematic expansion of H_{ion} around a chosen configuration $\mathbf{R}_{0,i}$ for displacements $\mathbf{u}_i$ can be done for $\mathbf{R}_i = \mathbf{R}_{0,i} + \mathbf{u}_i$ giving,

$$H_{\text{ion}}(\mathbf{R}) = H_{\text{ion}}(\mathbf{R}_0) + \sum_{i\alpha}\Phi_{i\alpha}u_{i\alpha} + \frac{1}{2}\sum_{i\alpha j\beta}\Phi_{i\alpha j\beta}u_{i\alpha}u_{j\beta} + \cdots \tag{2.133}$$

$$\Phi_{i\alpha} = \left.\frac{\partial H_{\text{ion}}}{\partial \mathbf{r}_{i\alpha}}\right|_0 = -F_{i\alpha} \tag{2.134}$$

$$\Phi_{i\alpha j\beta} = \left.\frac{\partial^2 H_{\text{ion}}}{\partial \mathbf{r}_{i\alpha}\ \partial \mathbf{r}_{j\beta}}\right|_0 \tag{2.135}$$

where for the i^{th} atom Cartesian coordinates are denoted by α, and so on. $F_{i\alpha}$ is the negative force at a reference configuration which vanishes at equilibrium. In this context H_{ion} determines the potential energy surface (fig.(2.11)) whose local minima correspond to the relaxed structure. $\Phi_{i\alpha j\beta}$ is the harmonic force constant at the lowest order, equivalent of a spring constant, such that the force felt by an atom at a site j is

given by,

$$F_{j\beta} = -\sum_{i\alpha} \Phi_{i\alpha j\beta}\ u_{i\alpha} \tag{2.136}$$

Truncating this sum at the second order corresponds to the harmonic approximation, and thus higher order force constants are called anharmonic force constants[18].

In periodic systems, the Fourier transform of the force constant matrix weighted by the mass of the atoms (often called a mass reduced Fourier transform) is called **the Dynamical matrix**. For a description matching computations of crystals, we replace our atom index i by two indices l, κ where l denotes the unit cell of a crystal and κ identifies the atom within the unit cell. Thus the dynamical matrix is,

$$D_{\kappa\alpha\kappa'\beta}(\mathbf{q}) = \frac{1}{\sqrt{m_\kappa m_{\kappa'}}} \sum_l \Phi_{(\alpha,l\kappa)(\beta,0\kappa')} e^{-i\mathbf{q}(\mathbf{R}_{0,l\kappa} - \mathbf{R}_{0,0\kappa'})} \tag{2.137}$$

Diagonalising the above matrix amounts to solving an eigenvalue equation whose solution givee the normal modes or **phonons**. Here $\mathbf{q}$ is the phonon wave-vector. Then

$$\mathbf{D}(\mathbf{q})\mathbf{W}(\mathbf{q}) = \omega^2(\mathbf{q})\mathbf{W}(\mathbf{q}) \tag{2.138}$$

where ω^2 are the squared phonon frequencies and $\mathbf{W}$ are the eigenvectors which are the mass weighted displacement vectors for the phonon modes at $\mathbf{q}$. A harmonic phonon calculation can be done in two ways.

- Φ can be computed in real space by using numerical differentiation techniques after displacing the atoms by a small amount from their equilibrium position. These displacements are along the phonon eigenvectors and require an a priory knowledge of them from symmetry considerations. This is often called the frozen-phonon method [141]. Although this approach is conceptually simple, a major disadvantage in practical implementations is that beyond non-zero wavevector of phonons i.e., the Gamma phonons, one has to resort to supercells. A full description of the phonon spectrum will need supercells larger than the effective range of lattice interactions which isn't known beforehand.

- $\mathbf{D}(\mathbf{q})$ can be calculated in reciprocal space as used in density-functional perturbation theory (DFPT) that we will discuss in the next section.

2.13 Density functional perturbation theory (DFPT)

Density functional perturbation theory (DFPT) is based on calculation of the energy derivatives perturbatively, as the name suggests. The dynamical matrix is obtained by calculating the second derivative via eq.(2.135). These are used in a summation in

[18] Two good sets of introductory lecture notes are [139], [140]

the reciprocal space based on eq.(2.137). Thus this method can compute the dynamical matrix at arbitrary wave vectors without needing a supercell. We will discuss briefly the approach within the DFT framework. For that we go back to eq.(2.33) and eq.(2.34), and re-write the effective potential which is a functional of density $v_{\text{eff}}(\mathbf{r}, \rho)$ as a sum over an external potential $v(\mathbf{r}) = v_{\text{ext}}$ and screening v_{scr} which is the sum of the Hartree term and the exchange-correlation potential as,

$$v_{\text{eff}}(\mathbf{r}, \rho) = v(\mathbf{r}) + \int \frac{\rho(\mathbf{r}')}{|\mathbf{r} - \mathbf{r}'|} d\mathbf{r}' + \frac{\delta E_{\text{XC}}}{\delta \rho(r)} = v_{\text{ext}}(\mathbf{r}) + v_{\text{scr}}[\rho, \mathbf{r}] \tag{2.139}$$

Going back to eq.(2.4), we see that $v(\mathbf{r})$ or $v_{\text{ext}}\mathbf{r}$ is the external potential acting due to the nuclei on the electrons. So we consider $v_{\text{ext}}(\mathbf{r})$ to be dependent on a set of adiabatic parameters $\Lambda = \{\lambda_a \text{ for } a = 1, 2, 3, \cdots, p\}$.

2.13.1 Energy functional expansion

The total energy E^Λ will then be determined by each term in v^Λ_{ext} expansion corresponding to density $\rho^\Lambda(\mathbf{r})$ as,

$$E^\Lambda = F[\rho^\Lambda] + \int d^3r \ \rho^\Lambda(\mathbf{r}) + v_{\text{ext}}(\mathbf{r}) \tag{2.140}$$

Note that here the density depends on the perturbation parameter Λ via its dependence on the external potential. This makes the perturbation dependent on Λ implicitly via the density. Thus we can write,

$$\frac{\partial E^\Lambda}{\partial \lambda_a} = \int d\mathbf{r} \ \rho^\Lambda(\mathbf{r}) \ \frac{\partial v^\Lambda_{\text{ext}}(\mathbf{r})}{\partial \lambda_a} + \int d\mathbf{r} \ \frac{\delta E^\Lambda}{\delta \rho(\mathbf{r})} \frac{\partial \rho^\Lambda(\mathbf{r})}{\partial \lambda_a} \tag{2.141}$$

For each finite Λ the second term vanishes as per the Rayleigh–Ritz-Galerkin variational principle. This reproduces the Hellman-Feynman [142] equivalent in DFT construction where the first derivative of the total energy depends only on the ground state electron density. The second derivative can then be written as,

$$\frac{\partial^2 E^\Lambda}{\partial \lambda_a \partial \lambda_b} = \int d\mathbf{r} \ \frac{\partial \rho^\Lambda(\mathbf{r})}{\partial \lambda_b} \ \frac{\partial v^\Lambda_{\text{ext}}(\mathbf{r})}{\partial \lambda_a} + \int d\mathbf{r} \ \rho^\Lambda(\mathbf{r}) \ \frac{\partial^2 v^\Lambda_{\text{ext}}(\mathbf{r})}{\partial \lambda_a \partial \lambda_b} \tag{2.142}$$

From here we see that the second order energy derivative depends only on the first order derivative of the charge density in the perturbation parameters. This can be generalised and it can be shown that the $(2n+1)^{\text{th}}$ derivative of energy on perturbation parameters depend only on the derivatives up to order n in charge density due to the variational character of the problem. This is known as the **(2n+1) theorem**. This $\frac{\partial \rho^\Lambda(\mathbf{r})}{\partial \lambda_a}$ can be calculated using a self-consistent procedure in DFPT.

2.13.2 Self-consistent linear response

Now we go back to the effective DFT potential which we assume to be dependent only on the ground state electron density and write a perturbation in it as,

$$\delta v_{\text{eff}}(\mathbf{r},\rho) = \delta v_{\text{ext}}(\mathbf{r}) + \int d\mathbf{r}' \frac{\delta\rho(\mathbf{r}')}{\mathbf{r}-\mathbf{r}'} + \int d\mathbf{r}' \frac{\delta E_{\text{XC}}}{\delta\rho(\mathbf{r}')}\delta\rho(\mathbf{r}') \tag{2.143}$$

Here a slightly different formula for density is employed with a multiplicative factor f_i that also accounts for non-integer occupancy or spin degeneracy as,

$$\rho(\mathbf{r}) = \sum_i f_i |\psi_i(\mathbf{r})|^2 \tag{2.144}$$

The variation in the external potential then induces a first-order variation in the wave-functions which can be used to write the variation in density as,

$$\delta\psi_i(\mathbf{r}) = \sum_{i,j}{}' \frac{\langle j|\delta v_{\text{eff}}|i\rangle}{\epsilon_i - \epsilon_j}\psi_j(\mathbf{r}) \tag{2.145}$$

$$\delta\rho(\mathbf{r}) = \sum_{i,j}{}' \frac{f_i - f_j}{\epsilon_i - \epsilon_j}\langle j|\delta v_{\text{eff}}|\rangle\ \psi_i^*(\mathbf{r})\psi_j(\mathbf{r}) \tag{2.146}$$

Now eq.(2.143) and eq.(2.146) can be solved self-consistently to obtain the first order variation in density due to ionic perturbation. In modern DFPT formulations [143], the variation in charge density is recast in the following form form to avoid the summation over all, more specifically conduction states,

$$\delta\rho(\mathbf{r}) = 4\ \text{Re}\ \sum_v \psi_v^*\Delta\psi_v(\mathbf{r})\ ,\ \Delta\psi_v(\mathbf{r}) = P_c\frac{1}{\epsilon_v - H^{\text{DFT}}}P_c\delta v_{\text{eff}}\psi_v \tag{2.147}$$

where v represents the valence states with energy eigenvalue ϵ_v, P_c is the projector on to the conduction states, and $\Delta\psi_v(\mathbf{r})$ can be obtained from the solution of the following linear equation,

$$(H^{\text{DFT}} - \epsilon_v)P_c\ \Delta\psi_v(\mathbf{r}) = P_c\ \delta v_{\text{eff}}\ \psi_v \tag{2.148}$$

This was a brief sketch of some of the main concepts and a description of some of the main formulas used in DFPT. For an exhaustive DFPT formulation the independent works by Zein *et al.* and Baroni *et al.* can be referred to in [144], [145] and [146], [147], [143] respectively.

2.14 Theoretical markers of disorder

A recurring theme in this thesis is the significance and variability of structural degrees of freedom in determining the physical properties of a material. The most

popular example in literature is elemental carbon [148] which in the form of a diamond is the hardest known natural mineral with a band gap > 5 eV making it an excellent electrical insulator. But carbon in the form of graphite has a layered structure with individual layers of graphene bonded by relatively weaker van der Waals interactions where it becomes a valued electrical conductor. This polar opposite behaviour of carbon in its two different forms is not only interesting but also underlines the significance of material structure in determining its behaviour. Another material that shows almost prolific polymorphism and is also the cornerstone of modern semiconductor technology is elemental silicon [149]. It created an impact so significant that an epoch in modern history has been marked after silicon starting the 'silicon age'. The scientific study of Si allotropes caters to the functionality tailored search for novel materials with one of the primary aims being their use for integrated circuits and solar cells. In-spite of being a rather difficult material due to difficulty in tuning its indirect band gap, the energy landscape of Si is rich in minima, thus exhibiting a strong polymorphism where several metastable crystalline structures could be recovered in ambient conditions [150]. These two materials among a great many others inspire a field of study of such structural polymorphism that is not only relevant for their different applications but also inspires one to investigate theoretical models and experimental ways in which a relevant polymorph could be stabilised.

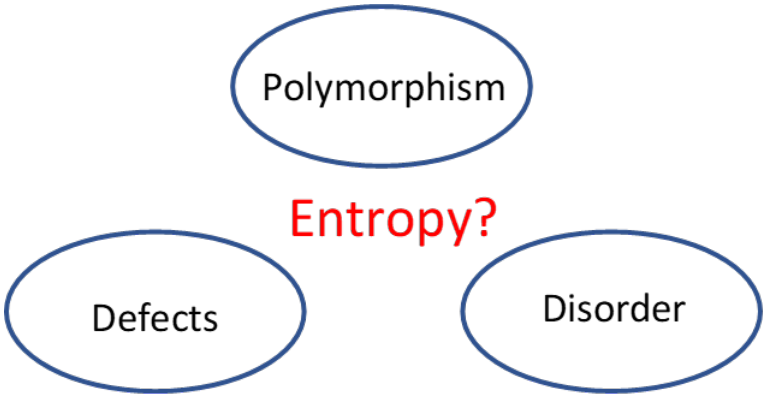


Figure 2.10: Polymorphic behaviour is usually heavily influenced by defects and disorder in a material. Entropy can be used as a descriptor a disordered state. The interplay of these concepts is crucial when investigating the role of structural degrees of freedom in determining physical properties of a material.

Polymorphic behaviour comes with a complex energy landscape with many low-lying local minima which cause this behaviour at the first place. Also when we are dealing with structural polymorphism, defects and disorder can play a crucial role in influencing the polymorphic behaviour. In this thesis we deal with crystals and thus disorder in crystals which essentially means that different isomers or conformers with the same molecular formulae and similar in energy exist together. Typically highly disordered crystalline phases are also associated with high entropies. There are various classes of high-entropy materials from high-entropy alloys to high-entropy borides and carbides

to entropy-stabilised oxides where a crystalline phase is stabilised entirely by entropic contributions. High-entropy materials are also closely linked with the active field of energy storage and conversion technologies [151]. This inspires one to investigate the role of entropy in characterising order in crystalline phases.

However both studying complex energy landscapes of polymorphs and parametrising entropy is a difficult problem because of its statistical nature and demand of a statistically large sample space in order to give a quantitative description. Recent developments in *ab-initio* high-throughput computing has opened some avenues where random sampling algorithms which are highly parallelisable on HPCs can thus sample a large enough phase space to study statistically relevant quantities. We will now have a closer look at two ways which could be used to gain further insight to the role of structural polymorphism and disorder in materials.

2.14.1 Relative frequency of occurrence

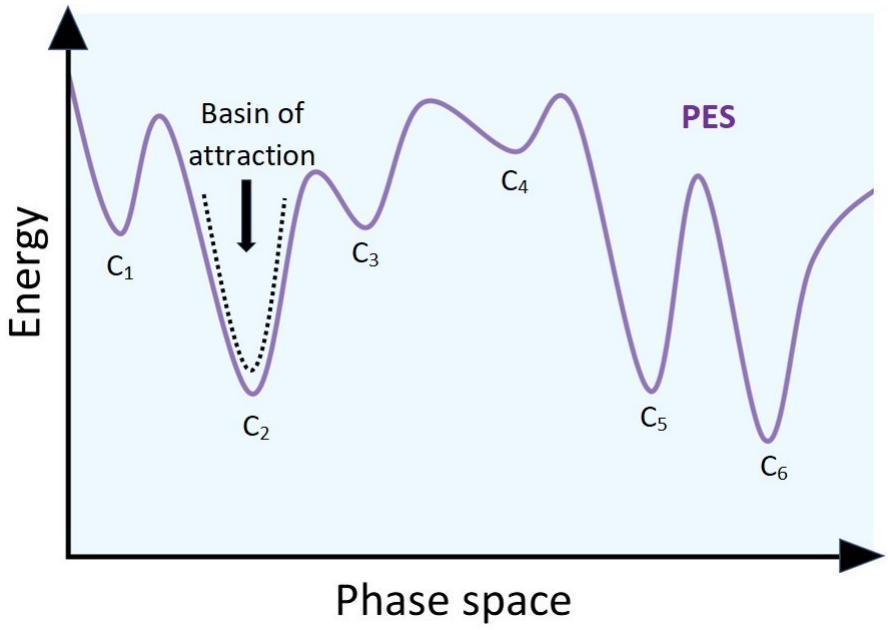


Figure 2.11: A sketch of the potential energy landscape of a material exhibiting polymorphism. Each local minima corresponds to a different polymorphic configuration C_i. The volume of the phase space at a local minimum is called its basin of attraction.

As discussed above, a topic of long term interest is the development of theoretical approaches to explore the phase space of a material exhibiting polymorphism and assist experimental realisation of materials with commercially valued properties. A principal challenge to attain this is that the number of local minima of the potential energy surface (PES) of periodic systems increase exponentially with system size. This poses serious limitations to systematic exploration of potentially interesting structures. Given the advancement in the field of first-principle methods, a big part of the current

condensed matter community works on finding correct ground state structures in the space of structural polymorphs. The prediction method used can vary from evolutionary algorithms [152] to structural prototyping [153] to random structure searches [154], [155] where an energy window is chosen above the ground state to identify the potential for an optimised structure to be experimentally realised.

Although energy about the ground state can quantify the possibility of experimental realisation, it alone is insufficient to identify viable structures. For example for MgO only the ground state rocksalt structure and for ZnO the ground state wurtzite structure and the zinc blende and rock salt structures could be experimentally realised among the predictions of many others [156]. Many other such examples exist, perhaps the most popular one being elemental silicon, which indicate that a finite set of structures for a given material have higher chance of experimental realisation than others in spite of comparable ground state energies. Keeping this in mind two other factors have been introduced that determine the likelihood of experimental realisation [156], [149]. One is the energy required to escape from a local minimum of the potential energy surface. Another one is the hypervolume of the phase space that a particular local minimum of PES occupies. This is known as the basin of attraction, as depicted in fig.(2.11). Note that to estimate the likelihood of a particular polymorph one will have to count all the symmetry equivalent basins.

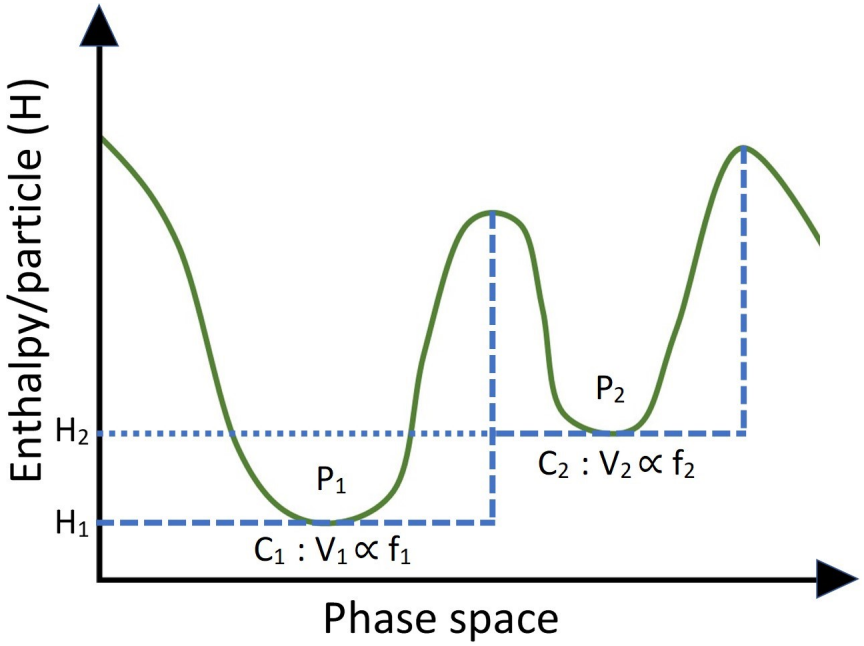


Figure 2.12: A sketch of enthalpy per particle for an arbitrary material showing polymorphic behaviour. The i^{th} configuration C_i has enthalpy H_i, hypervolume of the basin of attraction V_i, and probability and frequency of occurrences P_i and f_i, respectively.

For the the i^{th} configuration C_i, let the probability of occurrence of a particular polymorph be P_i and the observed hypervolume of the basin be V_i. To include the

effects of pressure and volume, we specify that our PES now describes the enthalpic landscape and we plot the enthalpy surface for all the possible configurations, as shown in fig.(2.12). Then, following the work of [149], an estimate for the relative probability between two nascent polymorphs with configurations C_1 and C_2 can be given by,

$$\frac{P_1}{P_2} = \frac{V_1}{V_2}\ e^{-\beta(H_1 - H_2)} \tag{2.149}$$

Note that arrival to eq.(2.149) uses a number of rather strong approximations [149]. The interactions between constituents of the system are assumed to be described in a mean field way. This allows the partition function to be independent of the number of atoms in the system. Any finite size effects have been neglected too. Along with these if we also approximate each basin of attraction to be a square well, we arrive at the above simplified equation relating the probability to hypervolume.

Now if N_1 be the number of structures in the basin of attraction for configuration C_1 i.e., in an enthalpy or energy window chosen above the minimum to define the basin of attraction, occupying its local minimum hypervolume V_1 out of N randomly generated structures, the ratio of two hypervolumes can be written as,

$$\frac{V_1}{V_2} = \lim_{N\to\infty}\ \frac{N_1/N}{N_2/N} \equiv \frac{f_1}{f_2} \tag{2.150}$$

where f_i is the frequency of occurrence of the i^{th} configuration. Thus from eq.(2.149) and eq.(2.150), we can write the probability of occurrence of a particular polymorph configuration within constant multiplicative scaling as,

$$P_i = f_i\ e^{-\beta H_i} \tag{2.151}$$

This definition of probability of occurrence leads to the following expression for free energy per particle,

$$g = -\frac{1}{\beta}\ln\left(\sum_i f_i\ e^{-\beta H_i}\right) \tag{2.152}$$

Now, if a particular state, i_{max} has the dominant contribution then to the lowest order approximation g simply becomes,

$$g \approx H_{i_{max}} - \frac{1}{\beta}\ \ln f_{i_{max}} \tag{2.153}$$

This is the resonant state, and we can identify its configurational entropy s as,

$$s = k_B\ \ln f_{i_{max}} \tag{2.154}$$

Once we have an expression for the probability of occurrence, we can estimate various thermodynamic quantities like the free energy, configurational entropy, etc. Thus one

can say that this formalism relates volume of the basin of attraction of a local minima in the configuration's energy or enthalpy surface to its frequency of occurrence which minimises its enthalpy and maximises its entropy. This can be a metric of estimating entropy related disorder in a class of systems.

Although the above formulation presents a simple expression for configurational entropy, its derivation based on the assumed mean-field-type interactions between the system constituents is always violated for strongly correlated systems which are the systems of interest in this thesis. Chemistry of surfaces and interfaces relevant to the growth of different phases will have finite size effects which have been completely neglected too. These factors need to be considered when using the above formalism to describe the entropic contribution [157], [158] or commenting on disorder or synthesisability of materials [159], and thus in such scenarios at best is used as a qualitative and not quantitative metric.

2.14.2 Entropy Forming ability

Another theoretical quantity that can be potentially useful to experimentalists studying disordered phases can be an Entropy Forming Ability (EFA) descriptor which could study a random set of possible configurations of a material and estimate the relative predisposition of that material to form a high-entropy phase.

If we take a large enough configurations of a material and draw a distribution of number of configurations per unit energy (C_E) with respect to the energy per atom (E), then we can study that energy distribution (or spectrum) and tell if the energy cost of one configuration to evolve into another metastable configuration is larger or smaller when compared to such energy spectrum for another material, as shown in fig.(2.13). A narrow spectrum will imply that going to other metastable configurations from one configuration has a lower energy cost, and hence larger entropy or randomness, which can potentially be classified by a high value of the EFA descriptor. On the contrary a wider spectrum will imply that a higher energy barrier needs to be crossed to reach the available metastable states and thus the material has a lower propensity to move to other configurations. This will have a low EFA value and these states will also show a strong preference for ordered phases.

If n geometrical configurations are sampled randomly where for the i^{th} configuration the degeneracy is g_i and the enthalpy is H_i, then we can write down the standard deviation σ of the spectrum as,

$$\sigma\{H_i(N)\} = \sqrt{\frac{\sum_{i=1}^{n} g_i \left(H_i - H_{mix}\right)}{\left(\sum_{i=1}^{n} g_i\right) - 1}}, \text{ where} \tag{2.155}$$

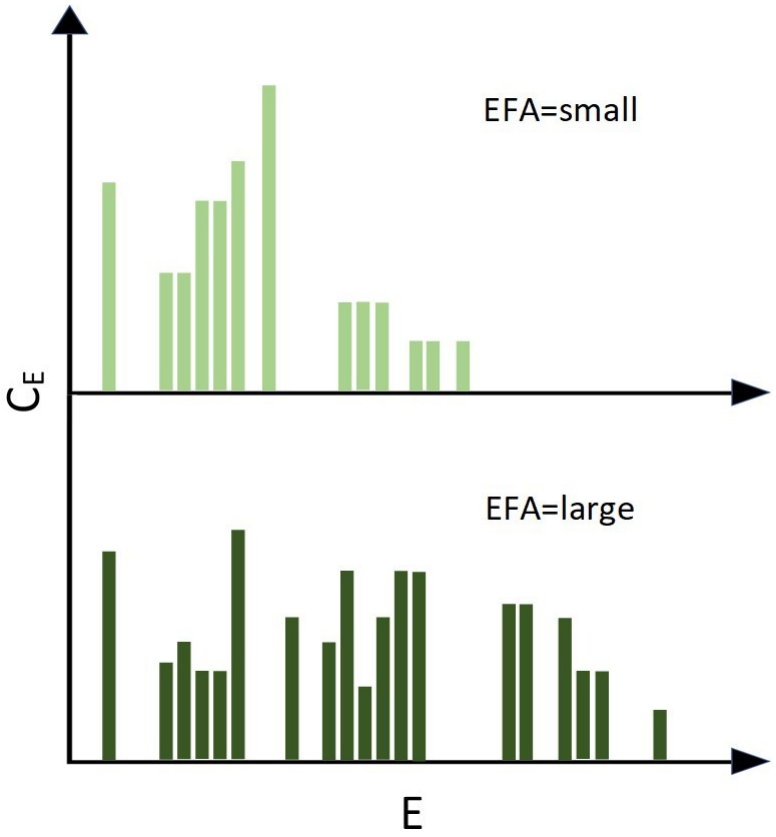


Figure 2.13: Configurations per energy plotted as a function of energy starting from ground state for two different materials with different values of entropy forming ability (EFA) descriptors. For a wider spectrum *(lower half)* EFA is higher highlighting that going from one metastable configuration to another is more difficult energetically.

$$H_{mix} = \frac{\sum_{i=1}^{n} g_i H_i}{\sum_{i=1}^{n} g_i} \tag{2.156}$$

Note that H_{mix} here refers to the average energy of the entire spectrum. But knowing the entire energy spectrum of a real material is almost impossible and thus in reality H_mix is approximated in various ways. Most commonly it refers to a reference energy that corresponds to the lowest-lying or ground state in the studied spectrum.

The standard deviation σ at zero temperature, $T = 0$, could classify the energy distribution spectrum and become a potential descriptor for the entropy S above the zero temperature ground state. At a finite temperature, a metastable disordered state occupying a place in the energy spectrum, will have a probability given by the state's degeneracy multiplied by the Boltzmann distribution. Thus, we can use $\sigma_{T=0}$ to define an entropy forming ability (EFA) for the system above state with the energy distribution

$\{H_i\}$ at the zero temperature as,

$$\text{EFA}(N) \equiv \{\sigma[\text{spectrum}(H_i(N))]_{T=0}\}^{-1} \tag{2.157}$$

with units $(\text{eV/atom})^{-1}$. Thus satisfying the intuitive hunch that a broader spectrum being more energetically expensive in terms of evolving to other metastable states and will stand for smaller keen-ness for disorder. However for a narrower spectrum configurational disorder could be easily introduced comparatively.

This recent formalism from 2018 [160] even with its simplicity has been quite successful in describing the role of disorder in carbides, high-entropy alloys and high-entropy oxides, and is one way we use to understand disorder in this thesis. But in spite of its recent success, it must be noted that EFA is a rather empirical descriptor. Comparing materials and disorder based on the spectrum of configurations, as defined in eq.(2.157), is not physically rigorous or unique. This spectrum and the associated reference state can be chosen in many ways, and at best is used as a qualitative marker of disorder.

Chapter 3

Modelling Interfaces for Nanotechnology

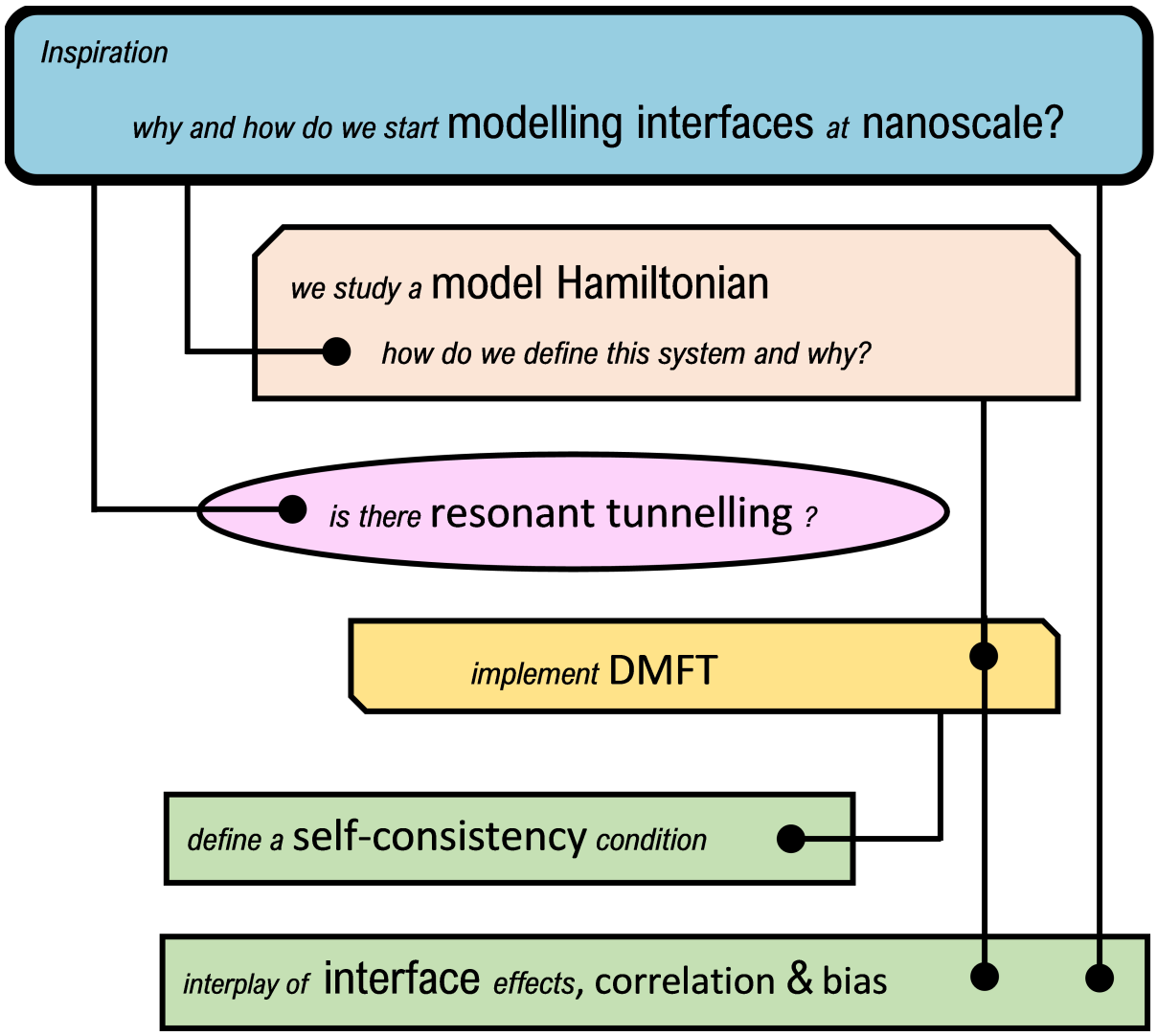


Figure 3.1: Chapter objectives and keyword map: highlighting the main questions asked, topics addressed and keywords used.

3.1 Introduction

A focal theme of this thesis is theoretical modelling of interfaces for understanding material behaviour at nanoscales. Nanostructures have dimensions ranging typically between 1-100 nm. Most common examples include graphene layers, carbon nanotubes, fullerenes, glucose molecules, and antibodies among numerous others. Research on nanostructured materials has been continuously gaining popularity over the past decade ranging from the use of multi-walled carbon nanotubes for treating cancer [161], nanosilica as an asphalt binder [162] to using nanotechnology for sustainable energy [163].

This diversity in the enhanced variety and tunability of the observed properties of nanomaterials when compared to their bulk counterparts arises from the smaller sizes of these nanoparticles. Merely due to their size, quantum effects like tunnelling and confinement become significant especially at interfaces and surfaces. Thus an interest in understanding the behaviour of nanostructures can be construed as an interest in understanding the emergent behaviour of the atoms and electrons that constitute the nanomaterials in bulk and at interfaces and surfaces.

A recent study [164] found that thermodynamically stable phases of nanoparticles correspond to a minimum in total interfacial and surface energy, and this serves as the governing rule for designing polyelemental nanoparticle interfaces. This isn't surprising as at nanoscale a large fraction of atoms are near or on the interface or surface which enhances the role of surface energetics on material properties. Tunability increases further in presence of materials with open d- or f-orbitals where correlation effects provide a nexus between surface thickness, film geometry, orbital degeneracy, applied bias, or temperature effects, to name a few controlling factors.

Applications based on electrical and optical transport in catalysis [165] and in semiconductor technology benefit most. In the semiconductor world for instance, applied positive gate voltage enhances carrier mobility resulting in a field-induced carrier delocalisation for an organic Mott insulator [166]. In another example, a field effect transistor operation could be obtained in VO_2 films grown on TiO_2 substrates by controlling collective carrier delocalisation via externally applied voltage [167]. In yet another recent work two layers of $SrVO_3$ grown on $SrTiO_3$ substrate were found to be at the verge of a Mott-Hubbard transition whose occurrence can be modulated by applied strain, electric field and temperature changes making it a prototype Mott transistor [168]. Thus understanding the physics of interfaces and surfaces and their behaviour in presence of correlations is critical in the nano-world. And more specifically designing transistor operations based on correlation effects attracts more attention now than ever. Therefore a theoretical quantum study of nanostructures focusing on a detailed and accurate modelling of nanointerfaces is interesting to not only explain the numerous observed physical phenomena but also to potentially predict properties of artificially structured nanomaterials.

3.2 A model interface

Before studying real materials and complex interplay between strong correlations, interface effects and stability of phases, we try to elucidate the concepts involved by studying a model system. This system serves as a prototype of a heterostructure comprised of a correlated material interfaced with an uncorrelated one. Our aim is to qualitatively study how equilibrium properties based on correlations are affected when a current is put through this interface by qualitatively studying the internal change of the chemical potential at the interface but without going into the details of the Keldysh formalism [169]. We try to understand the impact of various parameters, interactions, the interface structure on the density at the Fermi level and also the transmission. This also serves the purpose of building qualitative expectations for a beginner from a simple model by understanding the interplay of various parameters and interactions and then potentially studying more complex real materials.

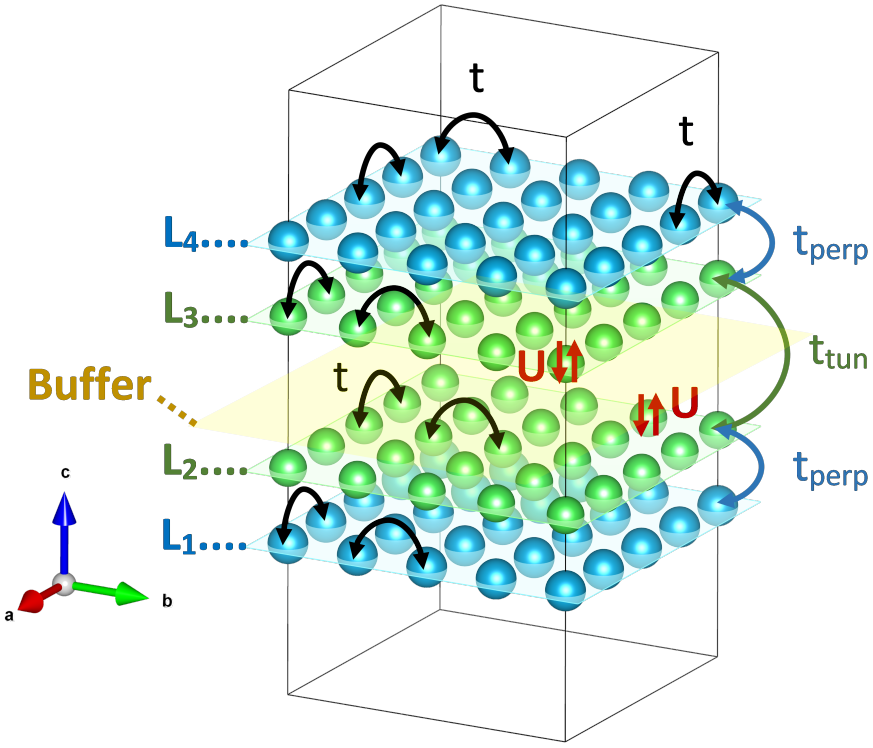


Figure 3.2: A model interface with four layers identified by different hopping parameters t, t_{perp} and t_{tun}, extending periodically in the x-y plane but finite along the z(c)-axis, the direction of transport. Layers L_1, L_4 represent identical leads forming interfaces with the film layers L_2, L_3 separated by an insulating buffer layer. U is the onsite Coulomb repulsion used to model interactions.

We thus consider a simple system of 4 layers with periodic boundary conditions in the x and y directions i.e., axes a, b in fig.(3.2) but finite length in the z-direction (c-axis) which is also the direction of transport in which the voltage will be applied. In a more realistic situation within the model, layers L_1 and L_4 will continue semi-infinitely

in each direction and will be studied as transport leads. Since in this section our aim is to decouple the effects of various parameters and interactions, as discussed before, we terminate beyond 1 layer in each direction and also make layers L_1 and L_4 identical in composition. Layers L_2 and L_3 compose the thin film layers separated by an insulating buffer layer, usually a different material than either of L_1 and L_4, that we typically want to study. The buffer layer can be taken to be vacuum as has been done here. In chapter 5, W forms the leads i.e., layers L_1 and L_4, and SmSe will be the thin film of layers L_2 and L_3 on which a voltage will be applied. Usually there are multiple layers of the film as well. In chapter 6, the correlated film is a heterostructure comprising either $LaTiO_3$ with $LaFeO_3$ or $LaVO_3$ with $LaCuO_3$.

We assume that the hopping in the x-y plane is the same for all the layers and denote that by t. The hopping between layers L_1-L_2 and L_3-L_4 is denoted by t_{perp}. The hopping in the z-direction between layer L_2-L_3 is designated by t_{tun}. Note that we have assumed that the kinetic terms in the x-y plane for all the layers are identical, and thus different from the hopping terms between layers along the z-direction. In this way we model the interactions differently along the direction of transport. This serves the purpose of simplifying our system but still keeping geometry (layer) dependent terms to study their effect on physical properties.

Even with 4 layers, the real space Hamiltonian will be infinite in x and y directions. To combat that we utilise the periodicity of this system in the x-y plane, and go to Fourier transformed space depiction of the x-y plane by noting,

$$\epsilon(k_x, k_y) = -2t\,(\cos\, k_x + \cos\, k_y) \tag{3.1}$$

where $t \geq 0$ and $k_x, k_y \in [0, \frac{2\pi}{a}]$ are points in the 2-dimensional Brillouin zone of the identical square lattice formed by all the layers with lattice constant a. If we now write down the Hamiltonian of this system, it will be in a mixed representation of both the Fourier space in x, y direction and the real space in z direction. This trick complicates the direct interpretation of physical quantities by allowing us to keep the real space description of the z-direction along with largely reducing the dimension of our Hamiltonian in x-y plane from infinite to 1. Since we have kept all the four layers at par with each other in the x-y plane with the same hopping t, this mixed representation of the Hamiltonian will not substantially effect the relevant properties of concern *(blessed by Fourier!)*. So, we end-up with essentially a 4-site 'chain' as shown in fig.(3.3) and a 4×4 Hamiltonian as,

$$H(k_x, k_y) = \begin{pmatrix} \epsilon(k_x, k_y) & -t_{\text{perp}} & 0 & 0 \\ -t_{\text{perp}} & \epsilon(k_x, k_y) & -t_{\text{tun}} & 0 \\ 0 & -t_{\text{tun}} & \epsilon(k_x, k_y) & -t_{\text{perp}} \\ 0 & 0 & -t_{\text{perp}} & \epsilon(k_x, k_y) \end{pmatrix} \tag{3.2}$$

where $t_{\text{perp}}, t_{\text{tun}} \geq 0$. This is a rather simple system that can be made serially more

complex by changing the values of various t's mimicking a desired situation. At half-filling the total number of electrons will be 4 with an average of one electron per site.

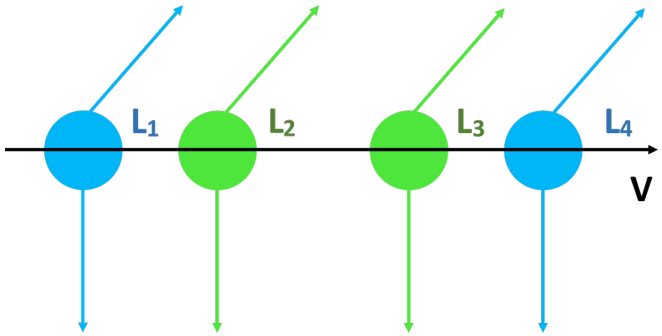


Figure 3.3: Graphical re-interpretation of the original 4-layer real space system with a 4-site Hamiltonian in mixed space with spatial x-y contributions represented in reciprocal space and z-direction in real space, the direction of voltage(V) application. The buffer layer has been considered to be vacuum. Colours mark equivalent sites (layers).

On this Hamiltonian we can apply a voltage in the z-direction applied along the matrix diagonal. We apply a step voltage V_z on the layers as,

$$V_z = \begin{pmatrix} \frac{V}{2} & 0 & 0 & 0 \\ 0 & \frac{V}{2} & 0 & 0 \\ 0 & 0 & -\frac{V}{2} & 0 \\ 0 & 0 & 0 & -\frac{V}{2} \end{pmatrix}, \; V \geq 0 \tag{3.3}$$

The lattice local Matsubara Green's function can then be written as,

$$G_{loc}(i\omega) = \sum_{k_x,k_y} [\; i\omega + \mu - H(k_x,k_y) - V_z - \Sigma(i\omega) \;]^{-1} \tag{3.4}$$

where the many-body effects have been included via the self-energy in imaginary frequency as,

$$\Sigma(i\omega) = \begin{pmatrix} \Sigma_1(i\omega) & 0 & 0 & 0 \\ 0 & \Sigma_2(i\omega) & 0 & 0 \\ 0 & 0 & \Sigma_3(i\omega) & 0 \\ 0 & 0 & 0 & \Sigma_4(i\omega) \end{pmatrix} \tag{3.5}$$

The next step is to solve for the self-energy self-consistently using DMFT within the scope of the IPT solver as discussed in 2.10.5. In general, one of the main DMFT approximations involve neglecting spatial or $k-$dependent fluctuations in the lattice

self-energy by equating it to the self-energy of the impurity as,

$$\Sigma(k, i\omega) \approx \Sigma_{imp}(i\omega) \tag{3.6}$$

In addition we have assumed that,

$$\Sigma_{ij}(i\omega) \rightarrow \Sigma_{ij}(i\omega)\delta_{ij}(i\omega) \tag{3.7}$$

It implies that we have considered each site as an impurity independently and each impurity acts as its own bath.

3.3 Observing the Mott transition

The non-interacting Green's function is based on the system description defined above. However, the value of the self-energy at the beginning of the calculation is an ambiguous point. It can be initialised with e.g., either $\Sigma = 0$ representing the non-interacting limit, or $\Sigma = \frac{U^2}{4i\omega}$ standing for the atomic limit or from a different intermediate value set as per system considerations, say, the $\Sigma(i\omega)$ from the previous iteration while solving the DMFT equations of motions self-consistently. Since we are trying to observe a metal-to-insulator transition as a function of U for a definite set of t, t_{perp} and t_{tun}, we will start from U=0 corresponding to the non-interacting limit and then slowly increase U with the initial self-energy for a particular value of U taken in the non-interacting or interacting limit or equal to the converged self-energy from the previous value in the parameter varied. Note that we simplify our toy system even further and have the same U value for all the impurity sites.

Given that we are interested in the half-filled regime where the overall number of electrons remain constant, and even with application of V, the electron occupation is only redistributed between the four layers, we will solve the Green's function using the Iterative Perturbation theory based solver at first for $V = 0$.

The transition regime depends highly on the parameters, the initial value of self-energy and the inverse temperature. This regime is metastable in nature and can show hysteresis depending on its initial conditions. For our system we observed such behaviour and an associated first order transition as depicted in fig.(3.6). As t_{tun} is switched on, the transition from the metallic to the insulating phase remains unaffected when starting from a metallic seed.

However, the insulating phase persists longer when starting from an insulating seed. We speculate that this is an artefact from our system set-up, most likely from lifting of the degeneracy. In a Hubbard model, an opposite behaviour to the change of U/t would be expected. A similar dependence of the onset of the transition can be found for t_{perp}, t and the inverse temperature β.

Also note that the calculation of error in Σ generally isn't unique. For this work,

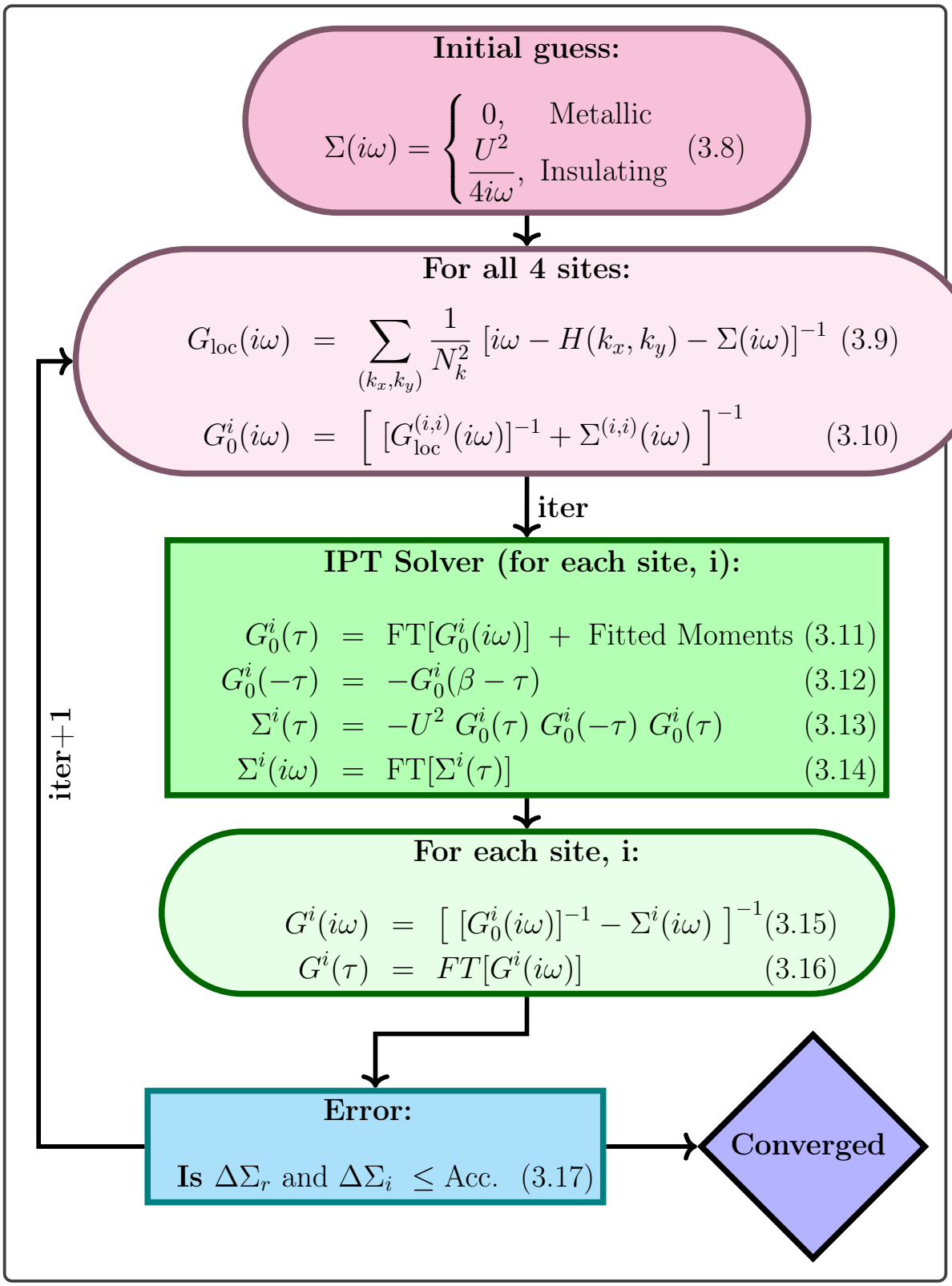


Figure 3.4: The DMFT loop to solve the model interface set-up based on the IPT solver with self-consistency defined by accuracy in Matsubara self-energy ($\Sigma(i\omega)$).

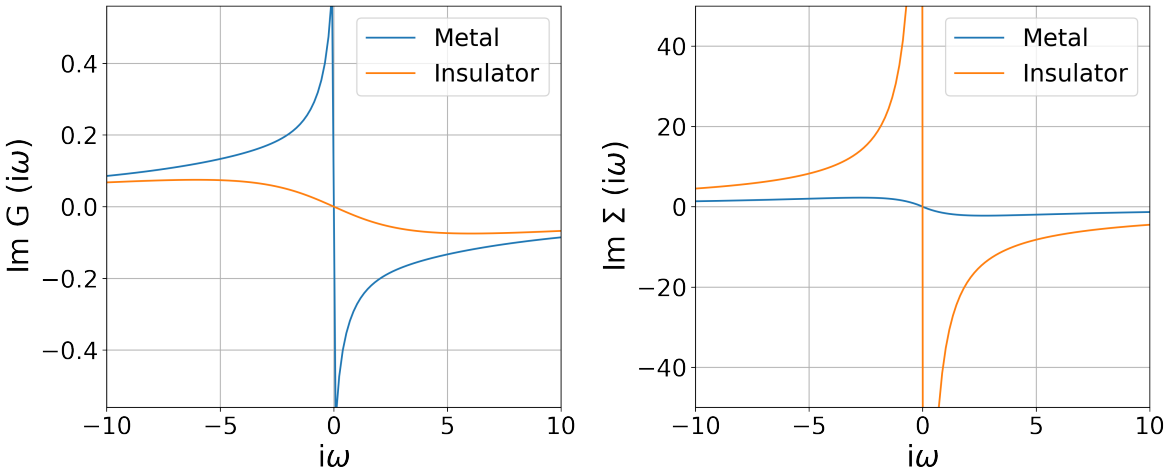


Figure 3.5: Metallic and insulating solutions obtained with DMFT within the IPT approximation for $t = 1$, $t_{\text{perp}} = 0.2$, $t_{\text{tun}} = 0.05$, $\beta = 40$, $N_{k_x} = N_{k_y} = 20$. The system is metallic for $U < 10$, the Mott transition occurs between $U = 10 - 12$, and the system becomes insulating for $U > 12$, independent of the starting point.

we define it at each iteration as,

$$\Delta\Sigma_{r/i} = \sqrt{\frac{1}{2M+1}\sum_{i=1}^{4}\left[\sum_{\omega_n=-M}^{M}\left|\left\{\text{Re/Im}\left[\Sigma_{i,\omega_n}^{k+1}\right]\right\}^2 - \left\{\text{Re/Im}\left[\Sigma_{i,\omega_n}^{k}\right]\right\}^2\right|\right]} \tag{3.18}$$

where $2M+1$ is the number of Matsubara frequencies (ω_n) used to calculate the error and is user-defined. Usually it is chosen within 30 as the change in the nature of the self-energy comes from points around 0. In $\Delta\Sigma_{r/i}$, r/i represent whether the error is calculated using the real (Re) or the imaginary (Im) part of Σ. Both errors are separately calculated and the convergence criteria, *Acc.* from fig.(3.4), is provided for both, usually $< 10^{-6}$. i denote the site number and thus goes from 1 to 4. k stands for the k^{th} iteration in the self-consistency loop. All the quantities in matsubara frequency have been calculated at 10000 frequencies between $(-150, 150)$.

There will be transitions across different scales of the parameters. However, since it is a toy system we do not investigate further the nature of transition within this system but rather use this as an archetype to motivate the investigation of the effects of electronic structure and correlations on phase transitions in 6.

3.4 Transition and Tunnelling

A second point of interest is the study of transport characteristics across this interface. As discussed in section 2.11.2, when studying transport across nano-interfaces one mechanism characteristic of quantum systems and nanostructures is quantum tun-

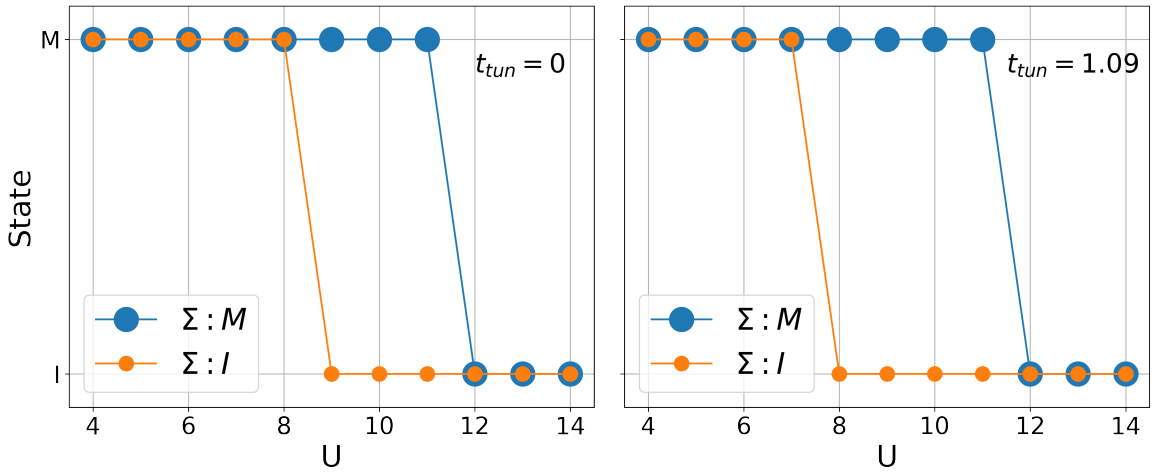


Figure 3.6: Observation of hysteresis surrounding the metastable Mott regimes with $t = 1$, $t_{\text{perp}} = 1$, $\beta = 20$, $(N_{k_x}, N_{k_y}) = (20, 20)$. $\Sigma = M$ and $\Sigma = I$ correspond to initiating a DMFT run with a metallic (M) and an insulating (I) self-energy, respectively.

nelling, a phenomenon which describes that a quantum particle has a finite probability to propagate through a potential energy barrier that is larger than its kinetic energy. It is one of the most fundamental concepts of quantum systems which differentiates them from the classical world, and we will use a specific type of quantum tunnelling to explore the role of correlations and Mott transition.

Usually the transmission coefficient or the tunnelling probability is < 1 for a single potential well structure. A special case of this happens when an electron is incident on a double well barrier such that the transmission probability is 1. This phenomena where the double well barrier is almost transparent to the electron transmission is known as resonant tunnelling (RT) [170]. This can happen when the energy of an incoming electron matches the energy of an electron confined within the double well structure, called the quasi-bound or the metastable energy level that leads to a charge transfer faster than 10^{-13} s [171]. One prominent application of this comes in the form of resonant tunnelling diodes which can potentially act as high-frequency oscillators and switching devices at Terahertz frequencies [172].

From the perspective of theoretical modelling, traditionally correlation effects have been ignored or treated in a perturbative manner in the explanation of resonant tunnelling. However a recent experimental study suggests resonant tunnelling inducing a metal-insulator transition in a heterostructure comprising of strongly correlated oxides. [173] Apart from this recent advances in experimentally fabricating complex correlated heterostructures with atomic resolution like one dimensional quantum wires [174], has in general led to an interest in theoretically studying [175], [176] the physical significance of correlations on the occurrence of resonant tunnelling and vice-versa.

But note that the computational cost increases with the dispersion of k-points in the x-y plane. Before studying the effect of a voltage bias across the interface, we simplify

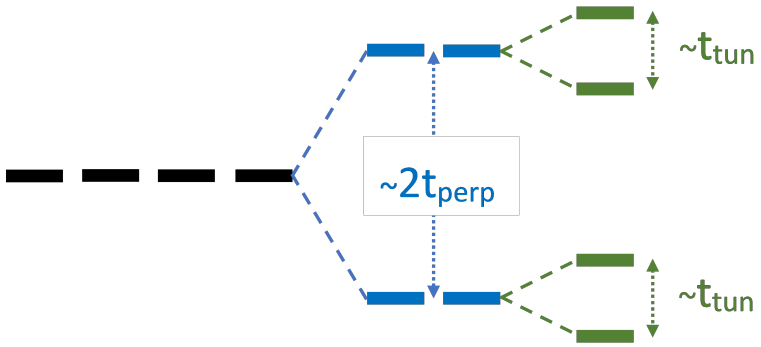


Figure 3.7: Schematic depiction of the role of t_{perp} and t_{tun} in lifting the degeneracy between the 4 sites in absence of any on-site interactions or external bias for situations when t_{perp} being larger than t_{tun} by an order of magnitude.

the system even further and replace the x-y dispersion in $\epsilon(k_x, k_y)$ by considering only a single level with energy ε. If we assume t_{tun} to be smaller by at least an order than t_{perp}, then in absence of U as per the Hamiltonian described in eq.(3.2), t_{perp} and t_{tun} have a role in lifting the degeneracy between the 4 sites as depicted in fig.(3.7). Application of a static bias, as considered in eq.(3.3), can alter the energetics of these four levels which could possibly mimic a resonant tunnelling like situation depicted in fig.(2.8) in chapter 2. But this is expected to be affected by correlations and their interplay with the hopping terms and bias[1].

As a first step to understand the interplay of resonant tunnelling and metal-insulator transitions in a correlated system, we look at our simplified model set-up and try to understand the impact of various degrees of freedom on transmission and its correspondence with the phenomena of resonant tunnelling for two limiting cases corresponding first to the complete absence of correlation i.e., the band limit ($U = 0$) followed by the Mott insulating phase where U dominates. This serves two purposes. One of building qualitative expectations for a beginner from a simple model by understanding the interplay of various parameters and interactions and then potentially studying more complex real materials in the next chapters. And the second of verifying the physics of this toy model with an experimentally observed phenomena.

3.5 Resonant Tunnelling and the Mott transition

We start with the non-interacting limit with the presence of an external voltage in the z-direction. The non-interacting Green's function can be written as,

$$G_0(\omega + i\eta) = [\ \omega + i\eta - H - V_z\ ]^{-1} \tag{3.19}$$

[1]In a real system, the simplified scenario in fig.(3.7) will be made more complex by the various $\frac{U_i}{t_i}$ ratios, where $i = 1, 2, 3, 4$ corresponding to each layer.

where $\omega,\ \eta \in \mathcal{R}$, $\eta > 0$ with ω being the frequency and η a small positive number, also called the smearing. As per our definition of V_z, the voltage barrier exists across L_2 and L_3 which now are single sites with no dispersion. The spectral function or the density of states will this be,

$$\text{DOS} = -\frac{1}{\pi}\ \text{Im}\ [\ \text{Tr}\ G_0(\omega + i\eta)\ ] \tag{3.20}$$

From our discussion in section 2.6.2, since the Green's function can be interpreted basically as a propagator, the transmission probability, also discussed in section 2.11.3, across the applied barrier can simply be written as,

$$T(\omega^+) = |G_{23}(\omega^+)|^2\ ,\ \text{where}\ \omega^+ = \omega + i\eta \tag{3.21}$$

In presence of interactions, the many-body effects will be introduced via the self-energy Σ as,

$$G_0(\omega + i\eta) = [\ \omega + i\eta - H - V_z - \Sigma(\omega + i\eta)\ ]^{-1} \tag{3.22}$$

From sections 2.11.3 and 3.4, we expect that resonant tunnelling conditions will be created when the voltage will align with one of the conduction states at the Fermi level. This should correspond to a peak in transmission across the barrier. Note that T is a function of frequency. To study the effect of voltage on the L_2-L_3 junction, we will analyze T at the Fermi level E_F. To study the effect of applied voltage via resonant tunnelling on a correlation induced metal-insulator transition, or a Mott transition, we now study two limiting cases mimicking our toy model.

1. **Non-interacting limit:**

$$\Sigma = 0 \tag{3.23}$$

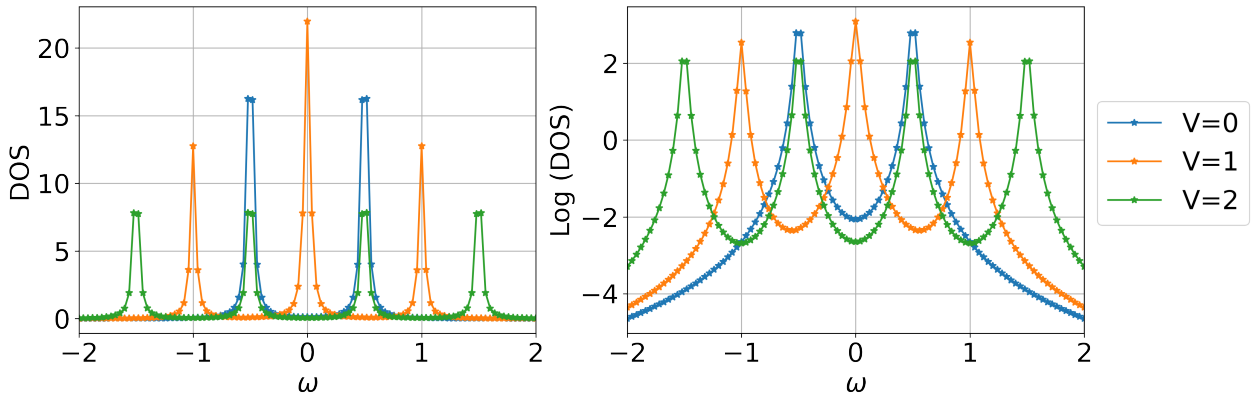


Figure 3.8: The change in density of states (DOS) with the applied voltage at the band limit ($\Sigma(i\omega) = 0,\ U = 0$) with $t = 0,\ t_{\text{perp}} = 0.5,\ t_{\text{tun}} = 0.02,\ \eta = 0.025$. The voltage induced insulator to metal transition happens at $V = \pm 1$.

We see in fig.(3.8) that in absence of voltage V, the two 1-particle levels align on either side of $\omega = 0$, and the DOS is insulating. As the magnitude of V is

increased these levels shift and at $|V| = 1$ the density of states has a peak at $\omega = 0$, and thus the material becomes metallic. Note that due to the symmetrical nature of our model, the polarity of V has no effect on the results. Also a finite value of ϵ just shifts the peaks proportionally, and thus has neglected using $t = 0$.

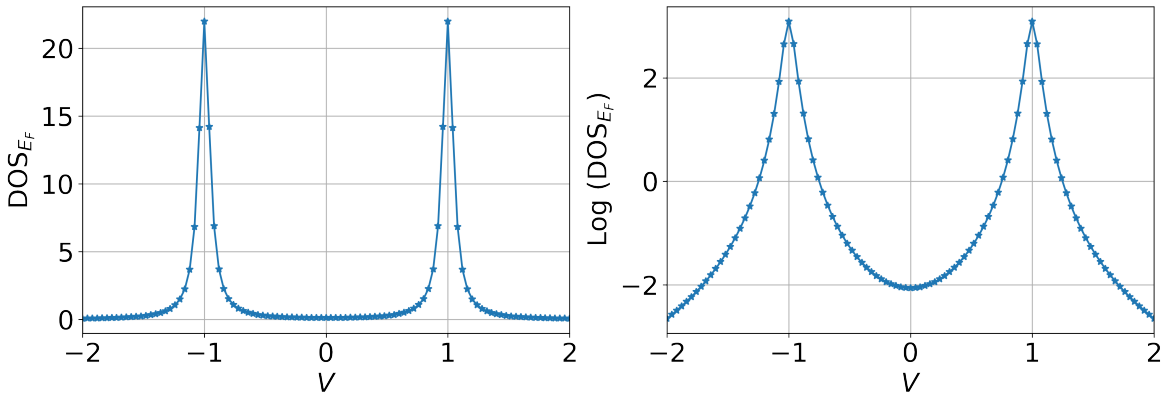


Figure 3.9: The change in density of states at the Fermi level (DOS_{E_F}) with applied voltage for $U = 0$, $t = 0.$, $t_{\text{perp}} = 0.5$, $t_{\text{tun}} = 0.02$, $\eta = 0.025$. The DOS_{E_F} increases with $|V|$ and reaches a peak at $V = \pm 1$ corresponding to the occurrence of resonant tunnelling (RT), as also observed in fig.(3.10).

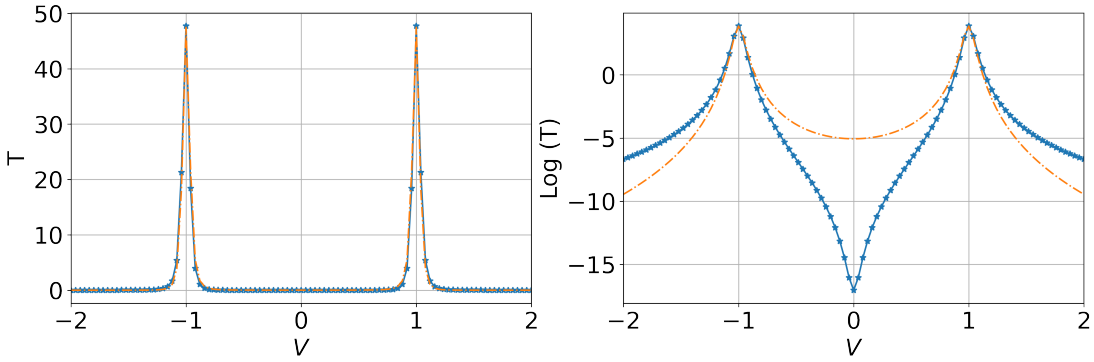


Figure 3.10: The peak in transmission T across sites 2-3 (blue) and 1-4 (orange) at the Fermi level, E_F, with the applied Voltage for $U = 0$, $t = 0.$, $t_{\text{perp}} = 0.5$, $t_{\text{tun}} = 0.02$, $\eta = 0.025$. This peak confirms the observation of resonant tunnelling (RT).

On a closer inspection, in fig.(3.9) we find that the density at the Fermi level, E_F, starts increasing as soon as voltage is slightly increased, but the peak is reached only at $V = \pm 1$. This corresponds to a peak in the transmission probability as shown in fig.(3.10), and thus stands for the occurrence of resonant tunnelling in the absence of any interactions.

2. **Atomic limit:** Usually at half-filling, the atomic limit self-energy corresponds to,

$$\Sigma = \frac{U^2}{4(\omega + i\eta)} \tag{3.24}$$

This results in poles at $\omega = \pm\frac{U}{2}$ corresponding to the upper and lower Hubbard bands. An applied voltage V will modify the self-energy and, potentially, metallise the system. As a crude approximation, we will assume that instead the form of the self energy is inert to V and the applied voltage merely shifts the Hubbard bands, as seen for the non-interacting limit in fig.(3.8). So, we include the effect of V in the atomic limit of the self-energy as,

$$\Sigma(\omega + i\eta) = \begin{pmatrix} \frac{U^2}{4(\omega + i\eta - \frac{V}{2})} & 0 & 0 & 0 \\ 0 & \frac{U^2}{4(\omega + i\eta - \frac{V}{2})} & 0 & 0 \\ 0 & 0 & \frac{U^2}{4(\omega + i\eta + \frac{V}{2})} & 0 \\ 0 & 0 & 0 & \frac{U^2}{4(\omega + i\eta + \frac{V}{2})} \end{pmatrix} \tag{3.25}$$

Note that in a DMFT loop, the self-energy will evolve at each iteration and will be dependent on V via the Green's function. Here, since we want a qualitative understanding of the effect of V on the Mott transition, have set $t = 0$ and are dealing with a finite system, we include V in the self-energy as above and need not perform DMFT runs.

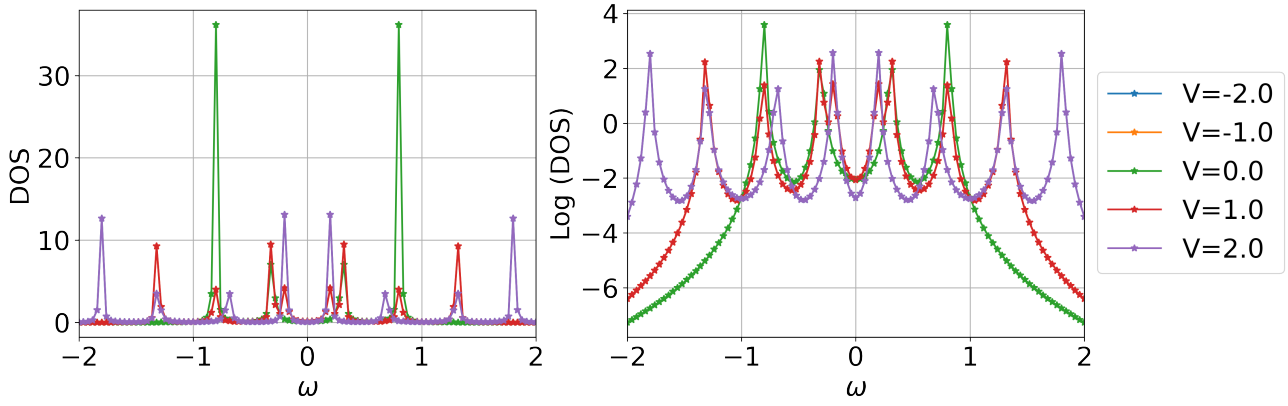


Figure 3.11: Evolution of the spectral function with applied voltage in the atomic limit with $\Sigma(i\omega)$ given by eq.(3.25) and with $U = 1, t = 0,\ t_{\text{perp}} = 0.5,\ t_{\text{tun}} = 0.02,\ \eta = 0.025$. The presence of interactions exhibit a more complex evolution of DOS with V.

In the Mott insulating phase at $V = 0$, we start with two 1 particle levels from fig.(3.8) are split into two Hubbard bands each, as seen in fig.(3.11). Application of V, splits these bands further. This causes the emergence of two new peaks and two dips in the transmission at the Fermi level and the earlier resonant tunnelling occurrence at $V = \pm 1$ changes to a more complex scenario observed in fig.(3.12).

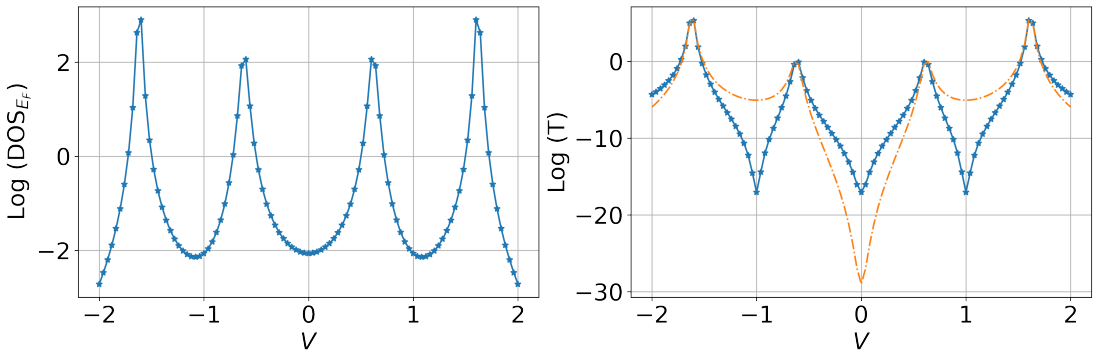


Figure 3.12: Multiple peaks in transmission between layers 2-3 (blue) and 1-4 (orange) are observed with increasing V at the simplified atomic limit where $\Sigma(i\omega)$ is given by eq.(3.25) and $U = 1$, $t = 0.$, $t_{\text{perp}} = 0.5$, $t_{\text{tun}} = 0.02$, $\eta = 0.025$.

To understand this further we look at the DOS corresponding to two minima and maxima each and an intermediate point at $V = 0, 0.3, 0.6, 1, 1.6$. As seen from fig.(3.13), each local maxima in the transmission occurs together with a sharp peak at the Fermi level at specific values of V. This corresponds to resonant tunnelling in the Mott insulating phase. Note again that in reality, the self-energy will respond to the V-induced changes, an effect that has been neglected in this simplified set-up.

Note from fig.(3.7) that the splitting of the peaks in absence of U is controlled by the various couplings between the sites or layers.

- The interface coupling between the lead and the film i.e., hopping t_{perp} between atoms of L_1-L_2 and L_3-L_4 do control the splitting between the peaks as seen in fig.(3.14).
- On the other hand, t_{tun} i.e, coupling within the film in the direction of transport i.e., between L_2 and L_3, has a smaller impact on the splitting than t_{perp} but a more significant impact on the attained density value more as seen from fig.(3.15).
- An atomic self-energy doubles the peaks with the splitting and the density dependent on the different couplings.

This complex interplay impact the resonant tunnelling conditions and invite further study in a more realistic set-up with real materials for possible device-like operations that we have discussed, for a different transistor-like operation in chapters 4 and 5.

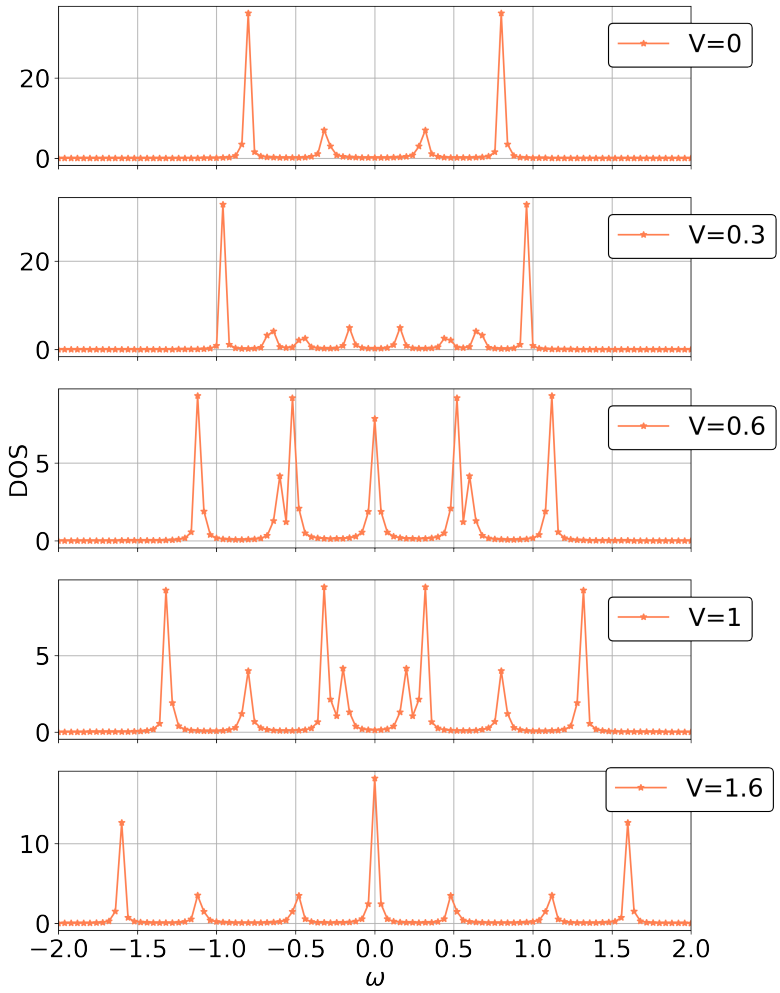


Figure 3.13: Evolution of the spectral function (DOS) with ω with increasing V. The DOS at E_F slowly increases with V till $V = 0.6$ corresponding to the first peak in transmission T. At $V = 1$, T vanishes again before reaching its maximum at $V = 1.6$.

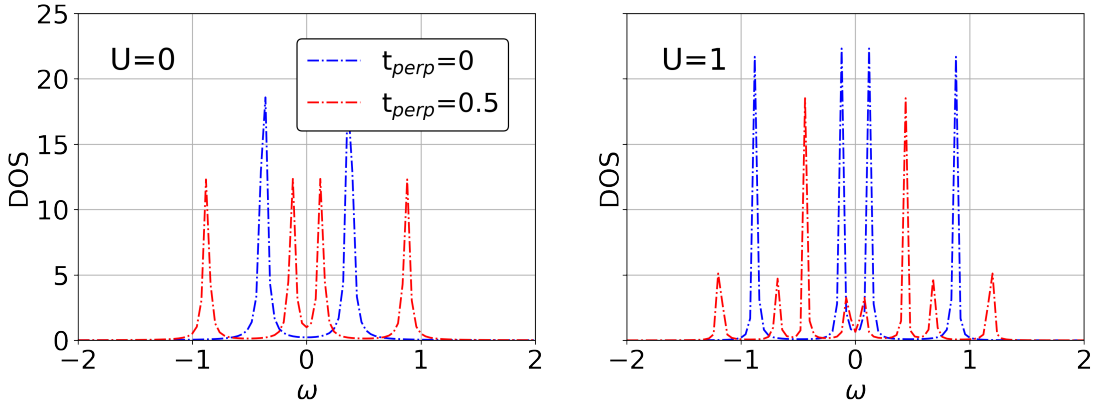


Figure 3.14: Role of the hopping along z-direction within sites 1-2 and 3-4 in controlling the splitting of the Hubbard peaks at $t = 0.$, $t_{\text{tun}} = 0.02$, $\eta = 0.025$.

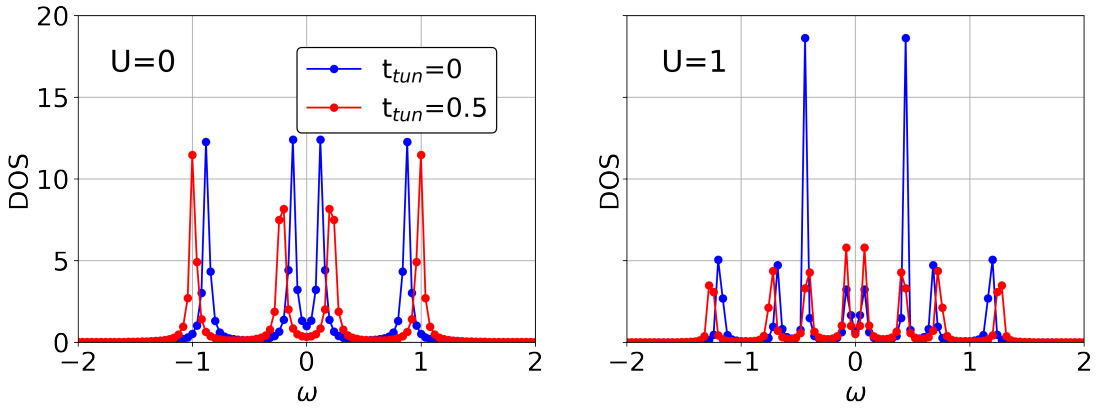


Figure 3.15: Role of the hopping along z-direction within sites 2-3 representing atoms of the thin film at the interface in controlling the peak density of the Hubbard peaks at $t = 0.,\ t_{\text{perp}} = 0.5,\ \eta = 0.025$.

3.6 Conclusion

In a nutshell, many technological applications of nanotechnology arise from a complex interplay between interface effects and correlations. We study a prototype four-layer heterostructure in a square lattice and its interfaces using a Hubbard-like Hamiltonian to understand how correlation dependent equilibrium properties change in presence of a current without going into the Keyldsh formalism. The effect of correlation is then elucidated by solving for the impurity self-energies using DMFT with an IPT solver at half-filling for various combinations of the Coulomb interaction and three hopping parameters and noting the occurrence of Mott transitions. We then study this system as a model for a quantum double well to understand how the presence of correlations through onsite-Coulomb interaction terms influence resonance tunnelling conditions in a further simplified system description of four-sites. This sets the stage to look into realistic interface set-ups where strong correlations can lead to a Mott transistor-like device operations.

Chapter 4

Pressure induced electronic transitions in Samarium monochalcogenides

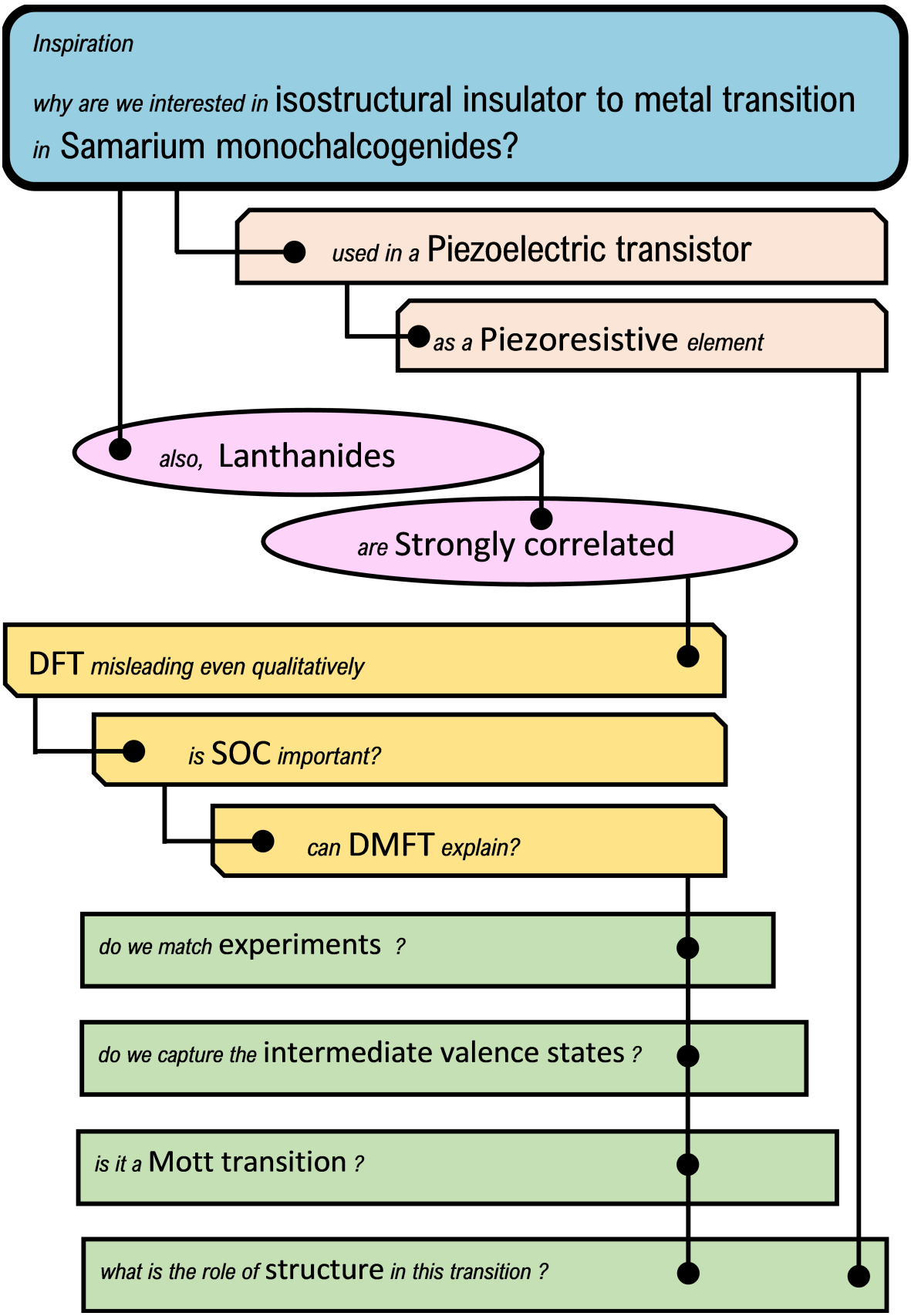


Figure 4.1: Chapter objectives and keyword map: highlighting the main questions asked, topics addressed and keywords used.

4.1 Introduction

The Moore's law [177], though not a physical law, popularly stated that the number of transistors on a microchip would double every two years and due to this, their cost will be halved. Its another postulation claimed that this growth will be exponential. Gordon Moore was the co-founder of Fairchild Inc. and Intel, two pioneer corporations involved in the manufacturing of transistors, integrated circuits (IC), and semiconductor chips. The Complementary Metal Oxide Semiconductor (CMOS) technology used in ICs framed the premise of this *law*. CMOS based devices followed the predicted trends throughout the 20^{th} century forming the grounds for the silicon era [178] and the modern Information Technology (IT) sector. In the recent decade however, although the exponential rise in the number of transistors on a chip has continued, the corresponding frequency and the power performances have saturated since early 2000s, as reported in fig. (4.2).

To understand the reason, we look deeper at CMOS based devices in which metal-oxide semiconductor field-effect transistors (MOSFET) are used as switches and amplifiers controlling the flow of electric current with an applied voltage. And although their use in integrated circuits is very well engineered for low power operation, there are system thresholds that limit their performance. In general, the power (P) is proportional to the switching frequency (ν) and the square of the voltage (V) as,

$$P \propto \nu \ , \ P \propto V^2 \tag{4.1}$$

This poses a limit on the voltages reached and on the clock-speeds of the devices that we want to make. A wider section of research in all avenues of electronic sciences focuses on improving the limitations posed by the CMOS technology for more desirable device cut-offs [180], [181]. Given the present and much required trends for future, we want a form of technology with higher clock speeds and lower power-consumption that is also potentially scalable to atomic sizes to accommodate higher transistor densities. For that one needs to arrest the switching power, which in turn requires us to steer towards a different form of technology with nanoscalability. Reaching nanoscales can possibly lead to a reduction of line voltage with dimensional scaling merely by virtue of the device size. This will make higher processor clock speeds and lower power operations accessible.

4.1.1 Piezoelectric Transistor

A possible new low-voltage switching and memory element in line with aforementioned requirements is the piezoelectric transistor (PET) [182], [183]. A PET, as depicted in fig. (4.3), is essentially a transduction device that converts an applied external voltage to stress in a piezoelectric (PE) material. The electrical input is provided via

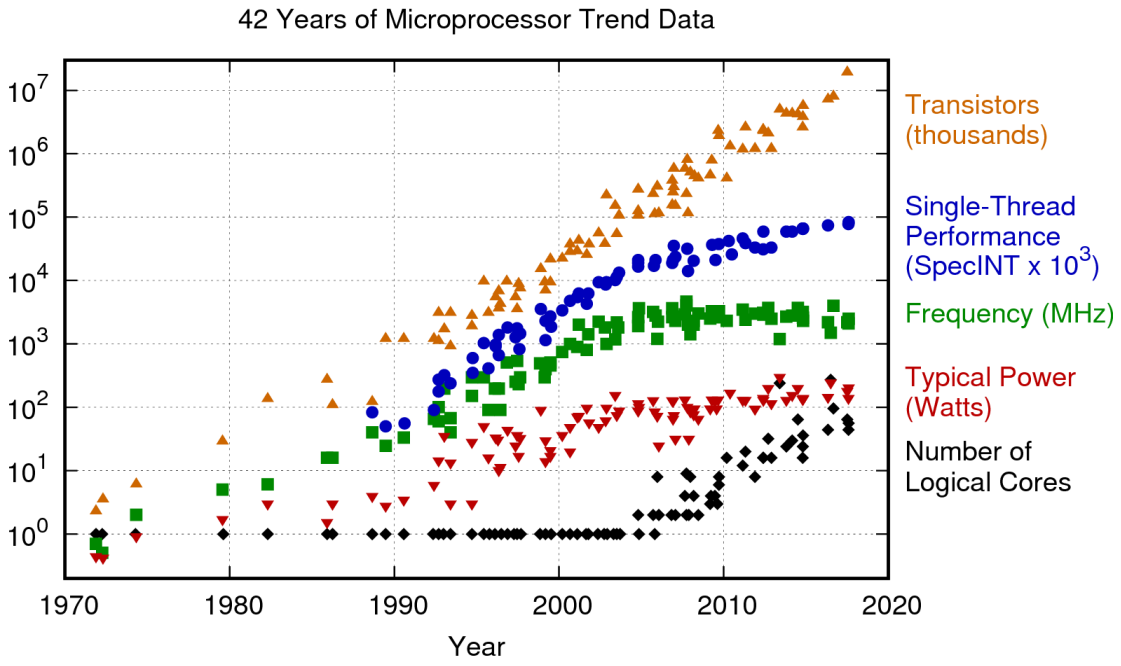


Figure 4.2: Microprocessor scaling trends in microchip transistor density, single thread performance of SPECint units, computer clock frequencies and power consumption, and processor logic core density between 1970 and 2020. (Figure from: [179])

the *gate* which the PE element converts into an acoustic pulse and it expands [184]. On expansion, the PE material which is located between the gate and the *common*, in turn compresses an adjacent piezoresistive (PR) thin film clamped on one side whose resistance changes with applied pressure. The compression of the PR thin film is usually of the order of a few nanometers [185] which thereby activates a facile insulator-metal transition that is detected by the *sense*. This set-up is vertically clamped within a rigid structure made up of a high yield material (HYM). The state of the PET in absence of any input signal corresponds to the OFF state whereas in presence of a signal the device starts conducting which corresponds to the ON state.

Depending on the nature of the transition, continuous or hysteretic, the device can be accordingly used as a switch or a memory element. The PET design is expected to allow device operations at voltages an order of magnitude lower than CMOS while reducing power by two orders and achieving frequencies up to 10 GHz [186]. It is also potentially scalable to nanometers suiting various device operation regimes as discussed in detail in section 5.1. Further applications include designing ultralow power radio frequency switches for telecommunications devices [183], low voltage gigahertz-range logic devices for portable equipment, etc.

PE materials are those materials that can convert an electrical stimulus to a mechanical response or vice-versa. Usually these are highly polar crystals like $LiGaO_2$, CdTe, $BaTiO_3$, etc., although there exists a class of non-polar piezoelectrics as well including TeO_2, $Bi_{12}GeO_{20}$, β-ZnS, etc. Generally their atomic structure is such that

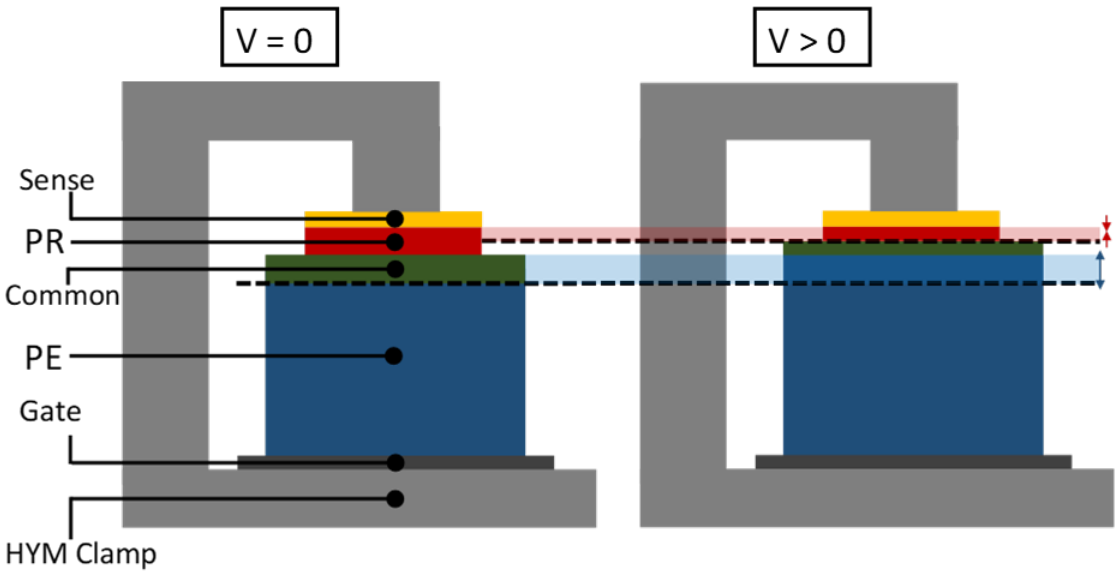


Figure 4.3: Schematic depiction of the operational principle of a piezoelectric transistor (PET). The entire structure is clamped on a high yield material (HYM) with input applied via the gate to the piezoelectric (PE) material connected to the piezoresistive (PR) film via the *common*. The PR insulator ($V = 0$, OFF-state) to metal ($V > 0$, ON-state) transition is detected by the *sense*.

ions are attracted or repelled when an electric field is applied. This distorts the interatomic bonds and thus creates a strain in the material. The study and engineering of piezoelectrics is a broad field of research in itself with some interesting applications [187] as sensors, actuators, motors, components in microelectromechanical systems (MEMS) [188], etc.

For desired clock speeds in a PET-based device, correct and well engineered integration of the PE element with the PR element remains at the core. Since a high-frequency mechanical transition in the PE element can be prone to mechanical distortions, a robust piezoelectric with a large response is needed that is well suited for the high-frequency operating regime. For this a class of PE materials called relaxor piezoelectrics like PMN-PT (lead magnesium niobate-lead titanate) [189] are used. Also certain PE element geometries like nanopillars and scaling the PET to smaller dimensions improves performance [190], [191].

4.1.2 Piezoresistivity in Samarium monochalcogenides

In general, piezoelectrics have been studied with more success and thus are better understood and engineered when compared to the more enigmatic piezoresistive materials. Piezoresistive materials, true to their nomenclature, exhibit a change in their resistance with applied pressure. First observed in silicon and germanium in the Bell labs in 1954, multiple applications [192] of piezoresistive materials have been realised so far. They serve as transducers, piezo-FETs (Field Effect Transistor), bipolar transis-

tors, as components of solid-state accelerometers and also in many MEMS applications. The performance of piezoresistivity is usually defined in terms of the ON/OFF ratio of this resistance change.

In rare-earth monochalcogenides, high-performance piezoresistivity (high ON/OFF ratio) has been observed for macroscopic single crystals at ambient pressure and temperature. In experiments done first by Jayaraman *et al.* [193], [194] in Bell Labs in 1970, it was observed that an insulating to metal transition occurs discontinuously for SmS and continuously for SmSe and SmTe with respect to pressure. The samples are initially insulating at zero pressure but increasing the pressure leads to the onset of a metallic behaviour. SmSe and SmTe show a reversible change in resistivity, but SmS shows hysteresis [195], [196]. Bulk single crystals have been found to show a change of up to 10^7 in conductivity between the insulating and the metallic states. The ambient pressure state is usually restored by thermal annealing. Similar behaviour is also shown by TmTe and SmEuS.

This piezoresistive behaviour in bulk samples has traditionally been attributed to the gradual decrease and eventual closing of the band gap between $4f$ and $5d$ bands such that the density of carriers in the conduction band increases leading to an exponential increase in conductivity. This observed change in conductance is usually attributed to the phenomenon of thermionic emission, as discussed in 2.11.1, where electrons get promoted from the Fermi level to the bottom of the Sm-$5d$ conduction bands by thermal activation. In 2013 it was found that a current through rare-earth monochalcogenide polycrystalline thin films, as thin as 8 nm, can be modulated by more than 1000 times due to a pressure-induced insulator to metal transition [197]. These findings of good piezoresistive response in rare-earth monochalcogenides both in bulk and thin film format makes them ideal PR candidates for a PET.

In this and the next chapter in this thesis, we focus on understanding the electronic origins behind this piezoresistive transition at equilibrium in two primary PR candidates for PET viz., SmS [198] for PR sensors and memory applications, and SmSe [199] for switching operations. In the current chapter, we will also study SmTe belonging to the same family of Samarium monochalcogenides, and look for trends across these materials originating in electronic structure. Note that the insulator-metal transition between zero and high pressure is isostructural in nature. It implies that bonds are only compressed and not rearranged between the low and high pressure states, and thus this transition can be cycled multiple times with thermal annealing without any fatigue induced breakdown associated with high frequency atomic motion. This is an important contributing factor that lets these materials be used as PR elements for high-frequency device operation in a PET.

The smallest element, SmS, in this series has another peculiarity. In its low pressure insulating state it is black in colour which turns golden when it becomes metallic at high pressure. A study of X-Ray absorption spectra [198] for SmS shows that the black phase corresponds to an oxidation state of Sm^{2+} whereas the golden phase is in Sm^{3+} state

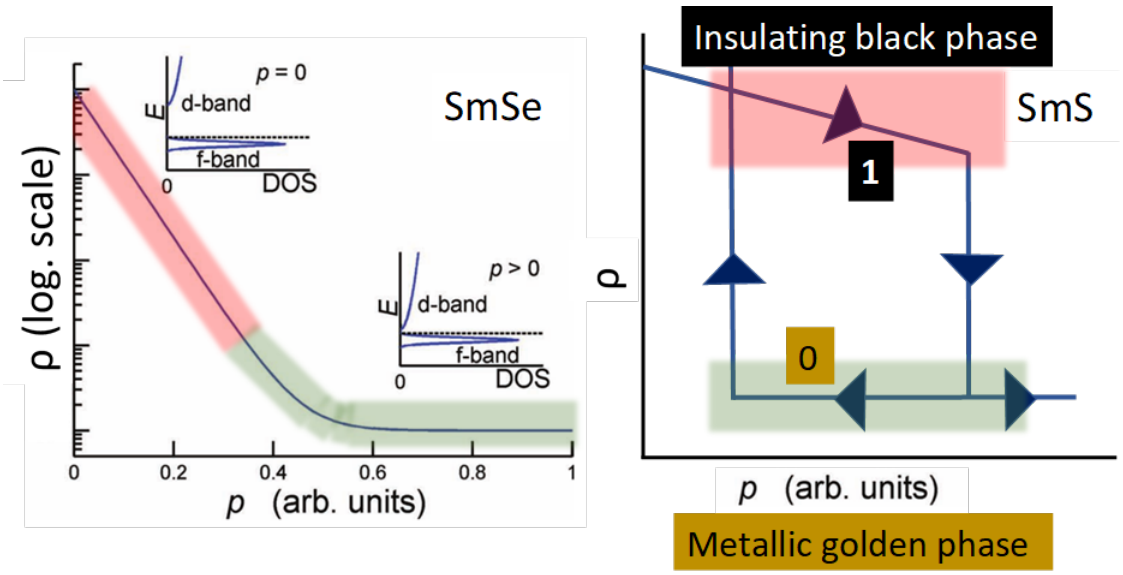


Figure 4.4: Representative plots depicting the variation of resistivity (ρ) with pressure (p). (*left*) SmSe shows a continuous, reversible insulator to metal transition as the $4f$-$5d$ band gap closes, suitable for switching operations [195]. (*right*) SmS shows a discontinuous, hysteretic transition, suited for memory based device applications [182]. Red and green shaded regions identify insulating and metallic regimes, respectively.

but they are accompanied with the observance of a mixed valent state. Intermediate valence states are also a common feature of SmSe, SmTe and SmB_6. This draws our interest in understanding the role of mixed electronic valence in these materials and their role in bringing this insulator to metal transition.

High piezoresistivity is usually associated with a change in geometry from applied mechanical stress [200]. However these observations have been made mostly in the ohmic regime. In bulk semiconductors, the change in resistance is sometimes several orders of magnitude more than that can be attributed to a purely geometrical origin [192], [197]. In early 2000s, a change of 60% piezoresistance was reported for Si nanowires when compared to bulk [201], [202] which stimulated a deeper interest in piezoresistivity in other functional materials. In this and the next chapter we study Samarium monochalcogenides in bulk and in the form of nanoscale thin films, respectively. The debate on the origin of piezoresistivity and the example of Si nanowires serve as an indirect motivation to study the electronic origins of the piezoresistive behaviour Samarium monochalcogenides and inspect the role of structure in bringing about this transition. This is also related to the mechanism of electron transport that will result in the observed behaviour. That will be discussed in further detail in chapter 5.

4.1.3 Lanthanides

Samarium (Sm:[Xe]$4^6 6s^2$) is a rare-earth material, specifically a lanthanide, with open $4f$ shells which usually govern its material properties. Lanthanides form one

of the most complex but most interesting class of materials known today to material scientists as their physical properties are the outcomes of an interplay between structure, dimensionality and strong electronic correlations. They form compounds showing interesting properties like high-T_c superconductivity [203] ($La_{1-x}Sr_xCuO_4$), rare-earth magnets [204] ($SmCo_5$, $Nd_2Fe_{14}B$), catalysis [205] and even prohibition of cancer cell growth in certain conditions [206].

These interesting and many-a-times tunable properties of lanthanides stem up from the presence of highly localised f electrons. Due to the atomic-like behaviour of the $4f$ electrons, the standard model of lanthanides [207] considers the $4f$ orbitals to be chemically inert. This approximation works well to explain why the average volume for elemental rare-earths remains almost constant with a slight decrease across the series for its trivalent elements. The constancy in volume comes from the fact that the $4f$ orbitals do not participate in bonding. As the series is traversed the hybridised [*spd*] electrons that participate in bonding experience the increase in core charge only partially as they are screened but not completely by the $4f$ electrons. However for divalent lanthanides (Eu, Yb), the volume is significantly larger as the $4f$ filling (half, full) becomes important. This signifies that although the $4f$ orbitals are atomic-like, their participation is important under certain conditions, and due to that reason a completely inert $4f$ shell based description may not be sufficient [208].

4.2 Samarium Monochalcogenides: a brief survey

After discussing in somewhat detail the industrial relevance of the choice of our materials of interest[1], now come back to theoretically understand the previously discussed piezoresistive properties of Samarium monochalcogenides. Sm-monochalcogenides have been studied with first principle approximations to varying degrees over the course of years. Density Functional theory (DFT) [37], [38] with local spin-density approximation (LSDA) using a fully relativistic Dirac LMTO band structure method [209] falsely predicts SmS, SmSe and SmTe to be metallic while largely underestimating the lattice constants. The LSDA+U approach with a $U = 6$ eV correctly predicts the band gaps under ambient conditions although the band gap, in general, depends on the value of U. However DFT+U fails to capture the mixed valent high-pressure golden phase of SmS that is observed between 6-20 kBar [193], [198]. If LSDA accounts for the self-interaction error (SIC) [210] and the theory-predicted energetics in the trivalent configuration are corrected for, better predictions for the high pressure intermediate valence state is shown. But for this the system with a total Sm-$4f$ occupation between 5 and 6 is described by considering it as an array of Sm-f^5 ions with one extra partially occupied f-band [211], [212]. In another DFT approach very good predictions

[1]This project was supported by the EU Horizon2020 research and innovation programme within the PETMEM project [No.688282].

of the lattice constants and bulk moduli are made by incorrectly making the Sm ions ferromagnetic [213].

Apart from this, the high pressure cohesive properties of SmS and SmSe have also been studied using three-body interaction potential models [214], [215]. This approach explicitly includes long-range Coulomb forces, short range overlap repulsive forces and polarizability effect [216] up to the next nearest neighbour ions but still falls short of the right qualitative explanation for both the metallic and the insulating phases which constitute the ON and OFF states in a PET configuration. Valence transitions in Sm-monochalcogenides have been studied using model Hamiltonians [217] to various extents as well with relative successes.

These methods, especially the first-principle applications on these systems generally over-delocalises the f-shells. The corrections accounted for by various approximations, although relate well for the scenarios they were specifically constructed for, cannot describe the insulator to metal transition appropriately. On the other hand, the standard model of lanthanides [207] puts the f-levels in the core. All this still leads to incorrect predictions of conductance and transmission. This entails the necessity of treating the f-levels with a full many-body Hamiltonian beyond DFT [218], leading to the use of Dynamical Mean Field Theory (DMFT) [105], [106], [219] corrections on top of DFT, and using a DFT+DMFT [220] approach to obtain the correct physics.

The application of dynamical mean-field methodology to real materials has been widely successful for cases where correlation effects are intrinsically accountable for a phenomenon that cannot be explained by the usual band theory arguments. Phase transitions and crossovers between metallic and paramagnetic insulators driven by temperature as in VO_2 [221], [222] and V_2O_3 [223], or pressure as for 3d transition metals and compounds [224], or doping as in Cr-doped V_2O_3 [225] constitute one class that falls in this category. DMFT has been previously employed with the symmetrized finite-U non-crossing approximation (SUNCA) [226] to study temperature dependence of SmS and reports a pseudogap appearing near the Fermi level with lowering of temperature after the fashion of Kondo-mixed-valent semimetallic systems.

Trailing the aforementioned motivations, in this chapter we aim to provide fully *ab initio* structural predictions for Sm-monochalcogenides, accounting for the many-body effects, within the DFT+DMFT approach. This is key for this class of materials, as they undergo structural and electronic transitions driven by pressure. We also want to understand the nature of the transition that is connected to the observance of piezoresistivity in these materials. We want to disentangle the structural and electronic aspects, and analyse the degree of agreement of our results with known experimental parameters to validate our approach. In particular, we want to understand if this insulator to metal transition is driven by charge localisation (i.e., is it Mott-like) or by structure? This will be a key point for understanding the physics of this class of systems.

4.3 Computational Details

4.3.1 DFT based study

Sm-monochalcogenides (SmX) form fcc-lattices with Sm at (0, 0, 0) and X (= S, Se, Te) at (0.5, 0.5, 0.5). The observed isostructural insulator to metal transition in SmX induced by a change in pressure is concomitant with a change in valence which is experimentally characterised by going from Sm^{2+} state at ambient pressure to Sm^{3+} state at higher pressures.

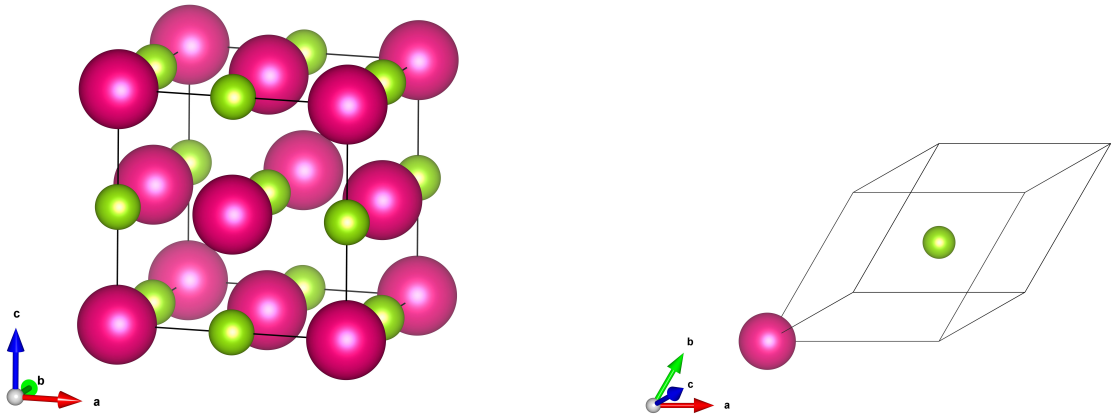


Figure 4.5: *(left)* The rock salt like structure of Samarium monochalcogenides in the cubic *Fm-3m* space group. *(right)* The primitive cell used for DFT+DMFT simulations.

We started with *ab-initio* calculations using DFT, as implemented in the plane wave basis code CASTEP [227], [228], with the PBEsol [229] functional, the Fermi-Dirac smearing scheme with a smearing width of 0.05 eV and a 19×19×19 Monkhorst k-grid [230]. We observe that, as expected from the discussion in section 4.2, DFT always converges to a metallic ground state with Sm-4f peaks at the Fermi level, as seen in fig. 4.7(a). In the literature [226], putting a tunable U_{eff} value shifts the Sm-4f levels accordingly and reproduces the correct insulating band gap but incorrect multiplet structure of the density of states. It also fails to reproduce the metallic state at higher pressures. As there is a change in valence, it is likely and also suggested from the study of X-Ray absorption data [198], that this metal-insulator transition (MIT) is accompanied by intermediate valence states which are not well captured by mean-field approximations like DFT, it being in principle a single Slater determinant approach. The presence of strongly correlated Sm-4f peaks at the Fermi level are key to these experimentally observed intermediate valence states leading to the onset of metallicity. To capture this fractional occupation state, we must look beyond such mean-field approximations warranting the need for many body corrections.

4.3.2 Spin-Orbit Coupling

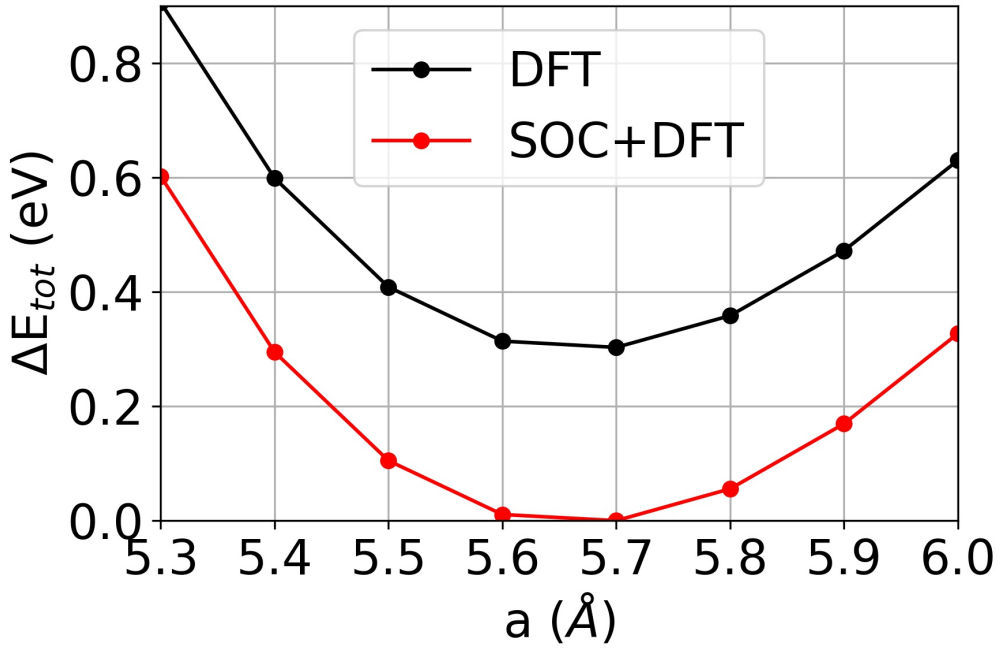


Figure 4.6: Total energy (E_{tot}) curves plotted as a function of the lattice constant (a) obtained using DFT with and without spin-orbit coupling (SOC) [231] corrections for SmS as implemented in plane wave basis code VASP [232], [233] using the projected augmented wave (PAW) [234], [235] PBE [43] potentials.

Another aspect to consider in parallel is the effect of spin-orbit coupling (SOC). Sm is a heavy fermionic element. The SOC-constant for Sm^{3+} is 1625.10 cm^{-1} [236]. Thus for optimal description of a system with Sm, SOC is deemed to be important [226]. To verify the role of SOC in this system (and only for this part of work), we move from CASTEP to the *sister*[2] plane wave basis code VASP [232], [233]. We use the projected augmented wave (PAW) [234], [235] PBE [43] potentials with the energy cut-off of 520 eV, a $19 \times 19 \times 19$ Monkhorst k-grid [230] and a smearing of 0.05 eV with the tetrahedron method and Blöchl corrections. Both with and without spin-orbit coupling [231], we optimise the structure electronically with the conjugate gradient algorithm at each value of the lattice constant.

We observe that the SOC effects, in analogy to how it is done in the standard DFT calculations, do not change predictions of any structural parameter, as seen from fig. (4.6). In general, SOC holds more relevance for the excitation properties. However in this work we aim at correctly predicting the electronic physics and cohesive properties of Sm-monochalcogenides as possible PR candidates. In other words, we are interested

[2]Since both CASTEP and VASP use plane wave basis, we expect the results to be qualitatively similar for DFT. CASTEP was not used for SOC calculations as appropriate SOC pseudopotential was not found for Sm at the time of working on this paper.

in the structural and integral properties such as total energy, and thus here the SOC contribution to the total energy can be safely neglected. The reason for this is the smallness of the SOC energy scale in comparison with the Coulomb repulsion energy of Sm-4f electrons, and the latter dominates the structural physics of SmX.

4.3.3 Hubbard-I approximation

As discussed before, DMFT has traditionally been a good tool to describe such MITs. Since the 4f-series is usually characterised by a small hybridisation, DMFT is used here within the scope of the Hubbard-I(HI) approximation. In HI approximation, as discussed in 2.10.4, after the system has been mapped to an effective single impurity Anderson model, the coupling between the bath consisting of the conduction electrons and the impurity which is essentially the correlated orbital here, is neglected. This results in approximating the self-energy of the impurity problem by the atomic self-energy by neglecting the hybridisation function. But this, rather strong, assumption makes the computational process faster as now the self-consistency criteria has one less quantity to converge on. This is usually a good approximation for rare-earths [237].

Thus, the Hubbard-I solver [238] as implemented in CASTEP is used with the ensemble density functional method to perform DMFT calculations at various values of lattice constant and valence. We set the inverse temperature $\beta = 20$, and use 2048 Matsubara frequencies to calculate the Green's functions under the fully localised limit (FLL) approximation for the double counting correction scheme that adjusts for the Hartree shift already accounted for in DFT. We use a Hund's coupling of $J = 0.3$ eV [3] and a standard value of $U = 6.1$ eV on Sm at the DMFT level. We find that for the correct ordering of X-p levels with respect to the Sm-4f states in the metallic phase, a static DFT-U of 6 eV has to be put on X. For the insulating state this U does not change the physics qualitatively around the Fermi level other than an expected small shift in the occupied p-states, and thus has been used throughout consistently[4]. Also note that, in the CASTEP implementation of the H1 solver [238], we solve for a larger $f-$multiplet subspace, we capture both the $4f_{5/2}$ and $4f_{7/2}$ multiplets without identifying them explicitly.

4.4 DMFT Results

DMFT gives us a control over the degree of correlation and valence of the system across the expected transition regime in Sm-monochalcogenides. We capture the effect of pressure via the nominal occupancy (n_{if}) which characterises the Sm-4f electronic

[3] See fig. (4.10) for further details on this choice.

[4] Since our correlated subspace of interest comprises of the Sm-4f orbitals, henceforth when we mention a DFT+DMFT study it takes into account a DFT-U on X-p orbitals, and DMFT corrections on Sm-4f orbitals.

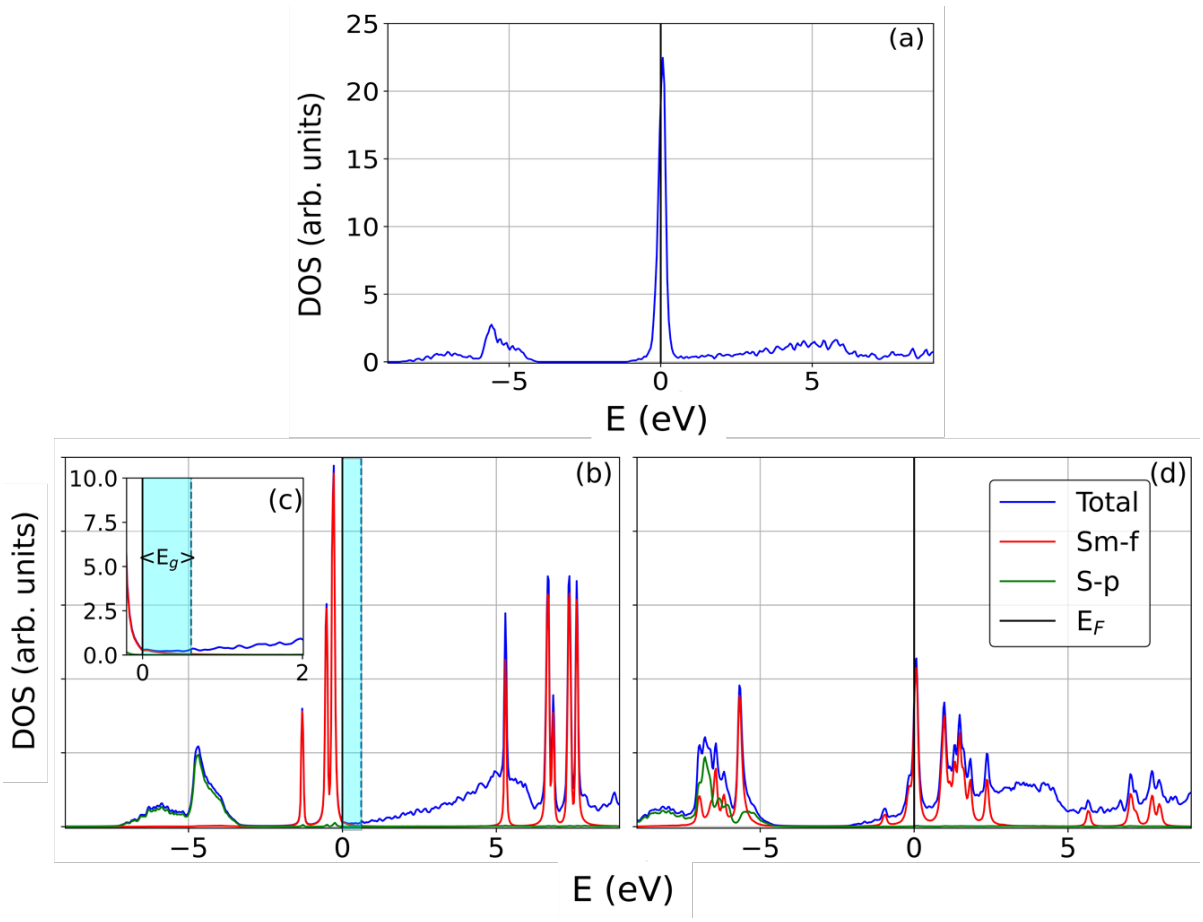


Figure 4.7: Density of states for SmS obtained with (a) DFT, (b) DFT+DMFT for the Sm-4f^6 configuration corresponding to ambient pressure insulating black phase, (c) magnified version of (b) showing the existence of a finite band gap with the vertical dashed lines delimiting the gap, (d) DFT+DMFT corresponding to the onset of high-pressure metallicity with intermediate Sm-4f valence of 5.24(2) in the golden phase.

valence and is controlled by the double counting correction as implemented in the HI solver and as discussed in 2.10.4. Note that the nominal occupancy n_{if} is different for Sm^{2+} and Sm^{3+}, respectively. We then perform energy minimisation at different values of the lattice constant to reach the electronic ground state. A clear distinction between insulating, as seen in fig. (4.7b, 4.7c), and metallic, as seen in fig. (4.7d), behaviours emerge for SmS across the insulator to metal transition regime (MIT) as the system goes from ambient to high pressure. This change in phase is accompanied by a charge difference of 0.76 which confirms the presence of an intermediate valence state for this material and matches reasonably well with the experimentally observed values of 0.62 [196], [239]. The density of states (DOS) for the SmS black phase matches well the observed ARPES spectra reported in [240]. Additionally with DMFT corrections, the subtle effects due to the paramagnetic nature of SmS also emerge associated with the presence of a local fluctuating magnetic moment between 1.96-2.12 μB, a phenomenon not well captured by DFT.

We minimise DMFT obtained total energies to relax and optimise the structures and find the ground state corresponding to the insulating phase, as seen in fig. (4.8). Following that the equilibrium lattice constants and Birch-Murnaghan [241], [242] fitted values of bulk moduli are calculated as reported in Table 4.1. These values show significant quantitative improvements over DFT predictions, and agree well with experimental results [198], [243] (Fig.4.8) for all three SmX materials.

At the onset of the metallic golden phase of SmS, we predict the fractional occupancy of 5.24(2)[5]. At the beginning of all the insulating states for SmS, SmSe and SmTe the integer occupancy of 6.00(2) is predicted. Note however that in contrast to the previous studies where a long range magnetic order [213], or spin-orbit coupling [226] or next-nearest neighbour interactions [216], [215] were invoked to reproduce experiments, in our work we recover consistent results with experimental observations without the need to specify further mechanisms at room temperature. And although PBEsol underestimates the lattice parameters, we obtain remarkable experimental agreements arising from local charge and spin fluctuation corrections using DMFT.

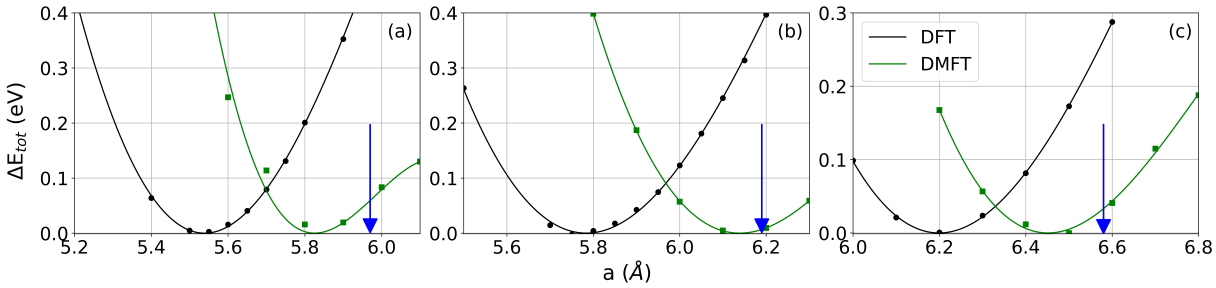


Figure 4.8: Comparison between DFT and DFT+DMFT predictions of total energy (E_{tot}) curves plotted as a function of lattice constant (a) and fitted with a Birch-Murnaghan [241], [242] equation of state for (a) SmS, (b) SmSe, and (c) SmTe. Arrows mark the experimental values for respective lattice constants under ambient conditions.

Material	a_{exp} (Å)	a_{DFT} (Å)	a_{DMFT} (Å)	n_f	B_{0-exp} (GPa)	B_{0-DMFT} (GPa)
SmS	5.97	-	5.82	6.00(2)	89.8-92	90.6
	5.7	5.54	5.68	5.24(2)	-	-
SmSe	6.19	5.78	6.14	6.00(2)	40±5	62.5
SmTe	6.58	6.2	6.45	6.00(2)	40±5	49.5

Table 4.1: Comparison of experimental data [198], [239], [244], [243] with DFT and DFT+DMFT predictions for lattice constant (a) and bulk-modulus (B_0) for SmS, SmSe, and SmTe, along with DFT+DMFT predicted Sm-4f occupation (n_f). Red and green cells mark insulating and metallic phases respectively, either predicted or observed.

[5]The number in brackets specifies the precision.

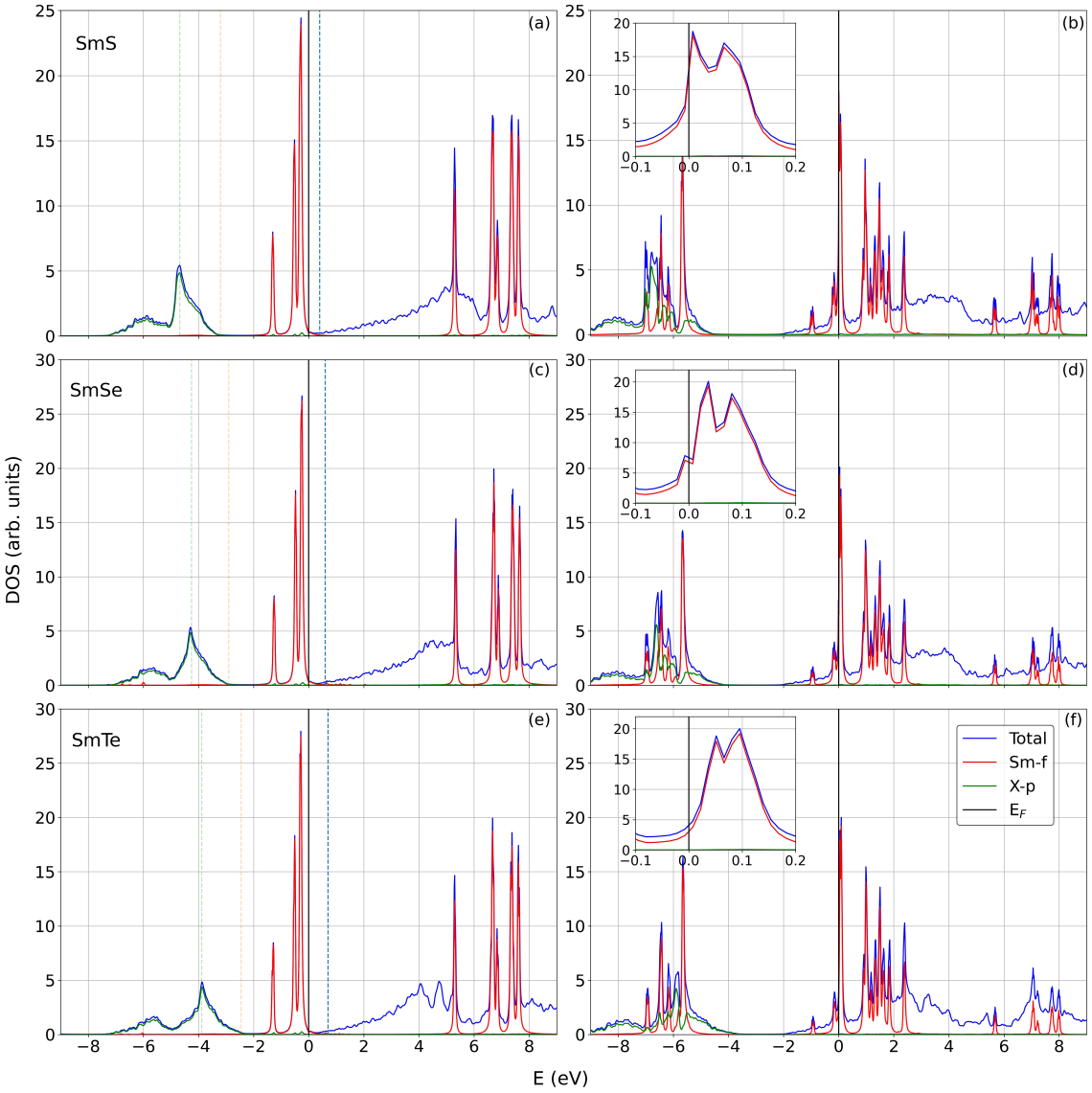


Figure 4.9: (*Left column*) Density of states obtained with DFT+DMFT corresponding to the ambient pressure insulating states for (a) SmS, (c) SmSe, and (e) SmTe, and (*right column*) the high-pressure intermediate valence metallic states with insets focusing on the behaviour of Sm-4f peaks around the Fermi level for (b) SmS, (d) SmSe, and (f) SmTe, respectively, with the vertical dashed lines delimiting the band gap.

Among the insulating states, we find the band gap to increase by approximately 50% when going from SmS to SmSe and by then $\sim$ 20% when going down from SmSe to SmTe (fig.4.9a, 4.9c, 4.9e) all of which are isovalent compounds. However even with increasing mass and more number of electrons, the qualitative natures of the density of states remains essentially the same with some little changes mostly corresponding to the occupied X-p levels which going from S to Se to Te gradually shift towards the Fermi level.

For the metallic states, we observe the sharp 4f-peaks to be almost on top of the Fermi level within 0.01 eV for SmS, and just across it within 0.1 eV for SmSe and SmTe

shifting towards the right as we go down the group (fig.4.9b, 4.9d, 4.9f). These shifts can be attributed to the previously noted increase in band gap which pushes the f-states further above the Fermi level, and is consistent with experimental observations [243], and might explain the difference between the discontinuous nature of the MIT in SmS and their continuous nature in SmSe, SmTe.

This very sharp resonance at and around the Fermi level is crucial to the onset of metallicity as small differences in pressure, temperature, disorder might shift this peak to left or right and cause huge changes in the density at the Fermi level making its position a critical parameter for transport and calorimetry. We will analyse further the role of f-electrons in conduction in the next chapter. A point to note here is that the metallic states for SmSe and SmTe have not been observed in experiments. This can be regarded as a utility of the DMFT method as we can hereby predict properties of systems which are not fully stabilised in experiments, and can use this to gauge the effect of mass contrast in these systems.

Samarium monochalcogenide systems are composed of weakly hybridised $4f$-magnetic moments. However, note that the gap in these systems is not Hubbard like, but is instead between the $4f$-states and 5d-states. To a large degree, the gap is controlled by the bandwidth of these 5d-states. The bandwidth of the upper band, which is approximately 7, 6, and 5 eV for SmS, SmSe and SmTe, respectively, is dependent on the chemistry of the chalcogenides. The $4f$-states however are very much atomic like, and as seen in our calculations remain very similar across the three materials.

Note that the value of the Hund's coupling J controls the relative position and splitting of the DOS in a particular phase. In the literature $J = 0.8$ [226] has been used for SmS. However, we find that the splitting of the states consistent with Angle resolved photoemission spectroscopy results [240] within the framework of H1 approximation as implemented in CASTEP is obtained with $J = 0.3$, which is the value used in this chapter as depicted in fig. (4.10).

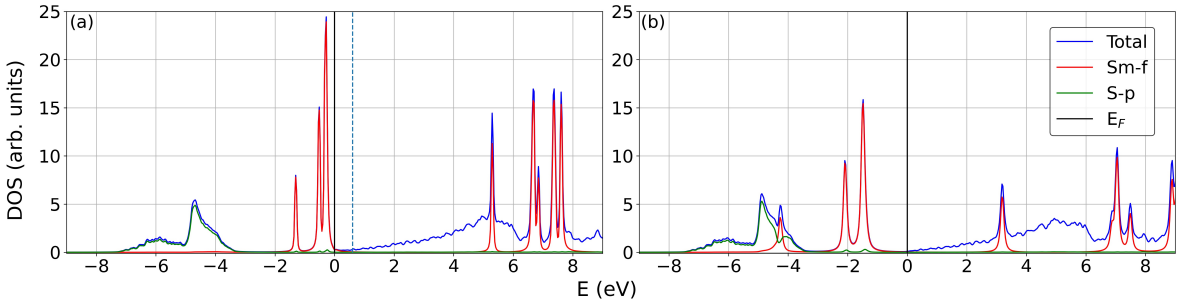


Figure 4.10: A comparison between the density of states for different values Hund's coupling, J, for SmS with $J = 0.3$ eV, and (b) $J = 0.8355$ eV. The final choice of $J = 0.3$ is based on correct reproduction of the Sm-$4f$ and S-p hybridisation and band gap consistent with experimental observations.

4.5 Nudged Elastic Band analysis

To investigate the nature of the insulator to metal transition further, we employ the likeness of a nudged elastic band (NEB) [245] method. For this first we select a path from the predicted DMFT solution for the insulating ground states ($a_{\rm ins}$, $n_{\rm i,ins}$) corresponding to the larger value of lattice constants, a, under ambient pressure for which the NEB-parameter $\lambda = 0$ is defined to be 0. We interpolate both the structural and electronic parameters i.e., the lattice constant and the double counting respectively to what we predict to be the high-pressure metallic ground states corresponding to $\lambda = 1$.

$$\lambda = \frac{a_\lambda - a_{\rm met}}{a_{\rm ins} - a_{\rm met}} = \frac{n_{i,\lambda} - n_{\rm i,met}}{n_{\rm i,ins} - n_{\rm i,met}} \tag{4.2}$$

Along this path, while going from the insulating to the metallic phases, there is a regime for SmS, SmSe and SmTe where the f-states cross the Fermi level, as seen in fig. 4.11(c). This variation of density corresponds entirely to the impurity states i.e., the $4f$ levels, for both values of temperature of $\sim$ 580 K (= 0.05 eV) as well as $\sim$ 301 K (= 0.026 eV). This confirms that the metallic conductivity in the SmS golden phase as observed in experiments [246], [247] originates from the Sm-$4f$ states.

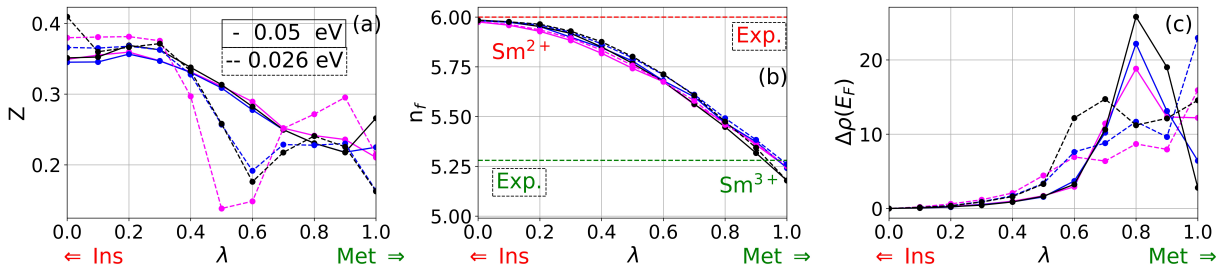


Figure 4.11: (a) Total quasiparticle weight (Z), (b) Sm-$4f$ electron-occupancy (n_f), (c) total density of states at the Fermi level ($\rho(E_F)$) along the NEB-like path going from the insulating state ($\lambda = 0$) to the metallic state ($\lambda = 1$) for SmS, SmSe and SmTe. SmS, SmSe and SmTe are represented by colours magenta, blue and black, respectively.

Additionally along this path, we observe a change in occupancy when going from the insulating and the metallic phase, which follow well the experimentally predicted valence for the insulating and the intermediate valence metallic states (fig.4.11(b)). This trend in valence remains similar for all three materials. On going to room temperature $\beta = 40$ (or $\frac{1}{\beta} \sim 0.026$ eV) and linearly interpolating as before, insulating states of SmX show a maximum change in Z by 0.031, 0.021 and 0.058, whereas the metallic phases change by 0.004, 0.061 and 0.103, respectively for SmS, SmSe and SmTe. This is consistent with the noted small shifts in the DOS at room temperature as shown in fig. 4.12 where no qualitative differences in density trends were noted.

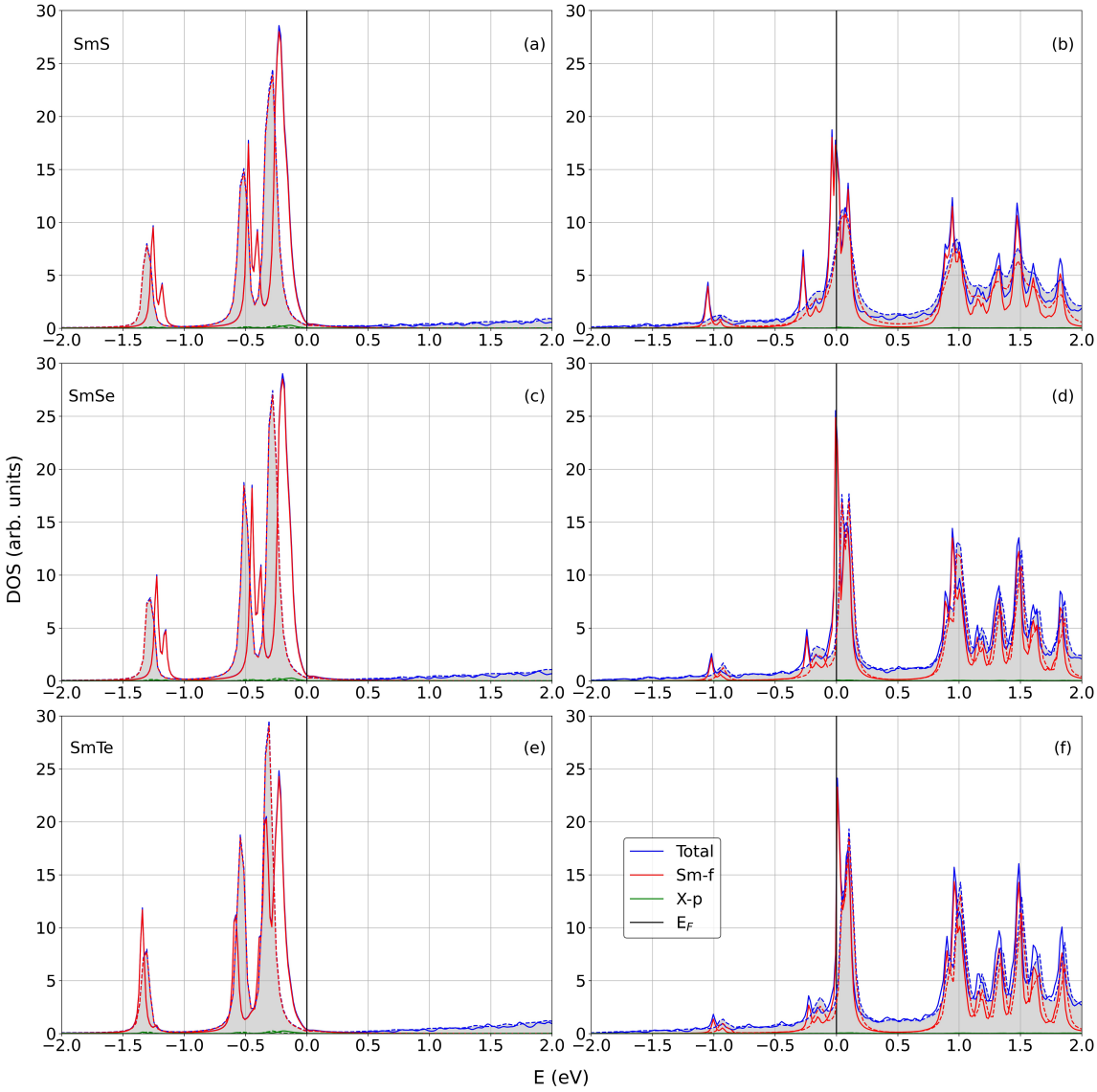


Figure 4.12: (*Left*) Difference in the density of states obtained with DFT+DMFT at high temperature (T = 0.05 eV, *solid lines, unshaded*) and room temperature (T = 0.026 eV, *dashed lines, shaded*) corresponding to the ambient pressure insulating states for (a) SmS, (c) SmSe, and (e) SmTe, and (*right*) the high-pressure intermediate valence metallic states for (b) SmS, (d) SmSe, and (f) SmTe. Lowering the temperature result only in small shifts in the DOS but no significant qualitative differences.

Note that our NEB-inspired approach interpolates linearly between the structural and electronic properties of the respective metallic and insulating equilibrium phases corresponding to different lattice constants, a, and nominal occupancies, n_{if}, respectively. Our equation of states in these two phases follow the Birch-Murnaghan [241], [242] relation, where the structure is indeed uniquely defined for each chalcogenide, but the transition from metal to insulator can be obtained by many different paths or processes with many combinations of structural deformations and associated electronic transitions. Thus we cannot infer about possible lowest energy barrier or first order

transitions or sharp discontinuity in the Sm valence.

But contrary to expectations, not only the quasiparticle weight (Z) decreases, but is also non-zero for the observed insulating phases, as seen in fig. 4.11(a)). This is observed both at room and higher temperatures. However, when we reach the predicted metallic states for SmSe and SmTe, Z goes up a little. Although the effective mass is mostly dominated by the mass renormalisation due to the f-electrons, it shows that this insulator to metal transition is not a Mott transition. Based on this behaviour, we argue that these materials are correlated band insulators, confirming ARPES results for SmS [246], where on driving towards the metallic phase the Sm-$4f$ interestingly become even more correlated. Due to this reason, we conclude that here Z is not a measure of transition. Because the $4f$ electrons become heavier, we can argue that this transition is thus not truly electronic in nature. Rather the $4f$ state cross the Fermi level because a change in structure changes the energy bands. To elaborate, on applying pressure the structure becomes compressed and as a result the density of the energy bands shift and the f-states cross the Fermi level, thus making this transition a structural transition.

In the predicted metallic states, the f-states are weakly hybridised at the Fermi level. Across the transition, the $4f$ states do cross the Fermi level but do not end up in the metastable configuration. So, the $4f$-states are across the energy barrier that separates these two phases. At some point along the NEB-like path, we are passing through a state which is reminiscent of Kondo lattices. These f-states are however very important for transport and the role of SmX as PR materials because if we gate the system, small voltages might suddenly involve the f-states in the conduction and they might start contributing more. This inspires us to study their role in thin film configurations as well as their contribution to conduction via transmission, which will be followed up in the next chapter.

4.6 Conclusion and Discussion

To conclude, we saw that the limitations posed by Joule heating at high frequency and high voltage regimes in existing CMOS based devices encourage us to look for alternative forms of technology. A piezoelectric transistor transpires as a possible substitute with possible clock speeds that can go up to GHz. However, a part of the mechanism behind a piezoelectric transistor relies on the behaviour of a piezoresistive element which undergoes an insulator to metal transition with pressure. Samarium monochalcogenides are one class of systems that exhibit this pressure induced isostructural insulator to metal transition as the band gap between Sm-$4f$ and $5d$ levels close. This transition is also associated with a concomitant change in valence. Samarium, being a lanthanide with the presence of partially filled $4f$ shells, is a material where the role of strong correlations is important. We verified that density functional theory and its static corrections, being essentially mean field levels of treatment, fail to capture

this transition as well as the presence of the intermediate valence states.

However, dynamical mean field theory based corrections correctly explain the pressure induced insulator to metal transition with the accompanying change in valence in Sm-monochalcogenides owing to its access of the fractional electronic occupations. It leads to significant improvements over the predicted values of lattice constants and bulk-moduli for the experimentally observed states as a direct result of incorporating the charge and spin fluctuations within the Hubbard-I framework. We also obtain the multiplet nature of the density of states with excellent experimental agreements in absence of any long range interactions or spin-orbit coupling, and although the Kondo-like physics is important, we find that the gap is dominated by the spectral weight of Sm-5d electrons, which is dependent on the chalcogenides S, Se, Te.

On doing nudged elastic band based analysis, we find that the quasiparticle weight remains finite for the insulating phases and decreases with pressure. This implies that the f-electrons which cross the Fermi level as the system become metallic and heavier in the metallic regime. From this observation we infer that this is not a Mott transition, and the quasiparticle weight is not an indication of the transition. As a result, we classify these materials as correlated band insulators which become metallic with pressure as the compression of the material changes the energy levels. This answers the questions asked in fig. (4.1) and gathers further interest in studying the role of the $4f$ electrons in transport where thin films of Sm-monochalcogenides are used as possible piezoresistive materials. That motivates us to go to the next chapter.

Chapter 5

Transmission across Samarium monochalcogenide based thin film heterostructures

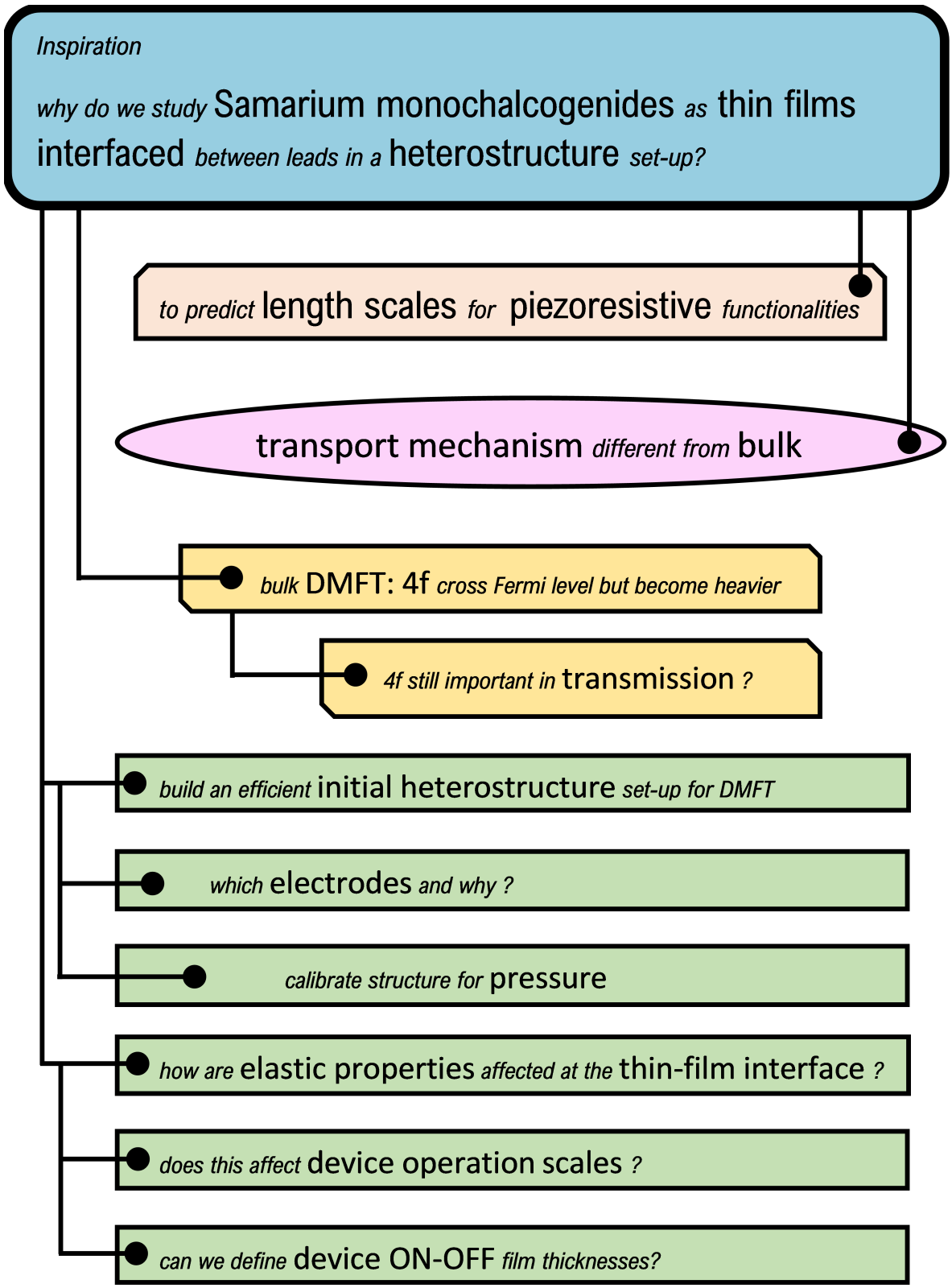


Figure 5.1: Chapter objectives and keyword map: highlighting the main questions asked, topics addressed and keywords used.

5.1 Introduction

We continue the discussion from chapter 4 where we found Piezoelectric Transistors (PET) to be one of the futuristic alternatives to the CMOS technology. In 4.1.2 we looked at how accounting for strong correlations give us better theoretical predictions for the PR material in bulk. A full understanding of the PET comprises of not only a grasp over the science of each individual component, of which the PR-element is our focus of interest, but also their collective behaviour in an experiment-like set-up simulating device operation. A complete theoretical understanding of the device operation will require development of a continuum model that relates device modelling at different scales as well as experiments. This multi-scale device modelling approach will start from atomic scale simulations of each individual component and end at full device modelling and design using finite element (FE) simulations to liaise with experimental observations.

We focus on the atomic scale simulations in this chapter. We will evaluate the PR-metal contact properties, and systematically review the scalability limit to desired device operation regimes. For this we will perform first the atomic scale simulations of the PR bulk and lead materials followed by PR-metal interfaces to eventually study their transmission and conductance as a function of thickness and strain. This will also enable determining the theoretical scalability limit in terms of minimum PR thickness required for ON-OFF device operations suited various technologies. In order to achieve a significant reduction in power consumption as compared to existing state-of-the-art transistor and memory technologies [182], the PR material should scale down as per tab.(5.1) [248], [249].

Technology	Scale (nm)
Radio frequency (RF) switches	15
Internet of Things (IoT) applications	5
Very Large Scale Integration (VLSI) units	3

Table 5.1: Predicted scales for PR functionality for various tiers of technology [248], [249].

5.1.1 Experimental details

A motivation of this project is to eventually liaise with experimentalists involved in device modelling. Thus, we first try to understand the experimental progress and limitations, and other specific details that will impact our theoretical studies.

1. Predictions in tab.(5.1) are based on extrapolations from experimental data for electron mobility, carrier concentration, and mean-free path.

2. For memory operations, the device thickness can be smaller by 1-2 nm than for transistor operations. It is so because transistors are made to operate between ON and OFF states. So, the OFF state needs to be calibrated very close to 0 and safely away from the ON state for the switching operation to be functional. However for a memory function, those two states need to be far enough to detect a change of state.

3. Most experimental works done on variation in resistance with pressure that report a response upto 10^7 were done for macroscopic single crystals [193] [194] of Samarium monochalcogenides.

4. Films as thin as 8 nm, reported in [197] for SmSe that show a piezoresistive response were polycrystalline, and a response of the order of 10^3, although interesting, is not sufficient for logic operations. Logic operations typically require a resistance modulation of 10^4.

5. The thinnest high quality pure-phase films of SmS obtained were of thickness 100 nm [250].

The projected values as per tab.(5.1) for the desired piezoresistive response are 1-2 orders of magnitude smaller than the actual material thicknesses realised so far in laboratory. Experimentally, going to thin-films of the order of a few nanometres is in itself a big challenge. As one goes down to such scales, making a clean structure with no defects as well as defining a thickness and decoupling it from the effects of the substrate become extremely difficult. Hence, predictions regarding attaining device functionality at the level of a few nanometres might be preceded by theory and then verified by experiments, and thus this work is partly speculative in nature.

5.1.2 Elastic properties

Looking back at point 1, we note that extrapolations leading to tab.(5.1) assume that bulk and elastic properties are preserved down to nanometre scales. The logic behind this assumption stems from the observation that a chemical bond is essentially a local property of a material as it depends mainly on the nearest-neighbour (nn) atoms. That is why interface effects do not always interfere with properties like bond-length. E.g., the C-C bond in benzene is $\sim$ 1.40 Å and that in graphene is $\sim$ 1.41 Å. Thus it is reasonable to surmise that although the electronic density of the interfacial layer between a metal and a semiconductor will feel the presence of the metal, 1-2 layers away as the deviation from expected variation in electronic density becomes small, we can expect to reach bulk properties. Consequently, the elastic properties after 1-2 layers will match the bulk properties stemming from the now bulk-like density of states.

This may not be the case for the PR element in the PET since the aimed scale ranges from a few to a few tens of nanometres. Unlike bulk where the effect of interfaces is

safely neglected, in a thin film set-up the validity of this assumption has to be verified explicitly. In other words, we have to find how many layers from the interface are the bulk properties restored and its impact on PR film thicknesses that can be used in a PET. As a first step in this direction, the bulk has be studied with the correct level of theory in a relatively small cell with periodic boundary conditions while ignoring the interface effects, as we did in sec.(4). This will need to be followed by a study of properties of the Sm-monochalcogenide thin-films in the heterostructure set-up which is one aim of this chapter.

Experimentally elastic properties in an ideal and perfectly crystalline film should remain the same as that of bulk after a few layers from the interface. However thin films usually are full of defects, oxidation, etc., which can substantially change its elastic properties. For instance consider a material that shows strain induced metal-insulator transition, and a substrate that induces deformities at the interface such that it in turn introduces a strain at the 1^{st} layer of the film. In a PET-like device with only a few monolayers of the concerned material, the effect of this surface induced pressure can change the metal insulating behaviour of the 1^{st} and the consequent layers and therefore the functionality of the device. Thus, although in general bulk properties are largely free from interface effects, transport properties can be heavily affected by them. Also, the thin films obtained in points 4 and 5 were polycrystalline in nature, and most theoretical studies are done with perfect crystalline structures which is another possible source of error.

5.1.3 Transport mechanism

When the PR thickness is large, the electron transport is dominated by thermionic emission, as per the mechanism discussed in 2.11.1. Here the metal electrons by virtue of thermal activation at a certain finite temperature get promoted to the Sm-5d conduction band. As the 5d states come closer to the Fermi level, the probability of this transmission process becomes larger and is reflected by the experimentally observed exponential increase of conductance with pressure.

However as per the scaling appraised in tab.(5.1), the predicted ranges are between $3 - 15$ nm. This is comparable to or less than typical electron mean free paths which vary from a few to 1000s of Angstroms. In this regime the conduction mechanism is expected to be based on quantum tunnelling as discussed in section 2.11.2, and this can induce drastic changes in conductance when compared to bulk. This advocates going beyond the semi-classical models of transport and using quantum mechanics to address conductance calculations at the nanometre scale.

In the tunnelling regime, the conductance depends on the value of the transmission coefficient around the Fermi level, both as per eq.(2.121) obtained using the Landauer-Büttiker formalism and eq.(2.128) obtained using the NEGF formalism. Even though for non-dissipative transport these equations become identical, a major difference be-

tween the two approaches is that in NEGF formalism the internal state of the conductor is taken into account unlike in the Landauer-Büttiker formalism. Thus within the NEGF framework calculating the transmission function relies on the internal electronic structure and properties of the conductor (the PR element) whose calculation in turn depends on the level of theory applied (DFT or DFT+DMFT) to study the electronic properties or write the Green's functions.

5.1.4 Role of electronic structure in transport

As we already discussed in 4.1.3, the f-orbitals are much more protected than s-, p- and d-orbitals. The atomic-like f-electrons are usually well screened from atomic interfaces, and can be considered inert in many cases. E.g., in bulk Sm, the spd-hybridised orbitals participate in bonding, not the f-electrons. Therefore for studying bonding-dependent phenomena, the standard model of Lanthanides suffices. Since the Sm-4f orbitals are not expected to participate in bonding, one can trivially expect them to be irrelevant in the transport too. However their closeness to the Fermi level suggests a strong role in transmission. In chapter 4, we saw that with increasing pressure the Sm-4f levels cross the Fermi level. This is again expected to strongly impact the transmission. A key point to inspect in this chapter is the involvement of the f-levels in transport for thin films and at interfaces.

In chapter (4), we also saw that where DFT, being a mean-field approach, fails reproduce the bulk properties of SmX, DMFT within the Hubbard-I approximation predicts the right qualitative nature and improves over quantitative predictions. Inclusion of the many body effects at the appropriate level is thus crucial for quantum transport calculations even within the NEGF framework, as described in 2.11, because the level of theory employed dictates how and to what degree are the correlations included via the self-energy which in turn affects the calculation of the transmission coefficient.

Previously we also found the transition to be structural such that with increasing pressure, the 4f-electrons become heavier. But at the same time the energy levels shift such that the system becomes conducting in bulk. This conclusion is key for transport and the role of SmX as PR films. It is so because the ideal PET device is expected to reach speeds of many GHz attaining which is expected to be easier if the transition is electronic and not structure-induced. However since the compression of the structure plays a key role in the position of the 4f-levels, studying them at the appropriate level of theory is crucial. This also imparts studying the role of defects a higher importance.

5.1.5 Objectives and approximations

Although the work with PET is the motivation, it isn't the focal point of this thesis. System integration with PE, PR elements with an element of strong correlation affecting the PR behaviour over the transport regime is an extremely challenging problem. In

this chapter we focus on doing atomistic simulations using the quantum transport code SMEAGOL [133], [136] that uses linear atomic orbitals as employed in electronic structure code SIESTA [251], [252]. We address the role of strong correlations in $4f$ orbitals and in transmission through a Sm-monochalcogenide (PR) thin film between two metal leads. However quantum transport within NEGF framework with DFT+DMFT is not only challenging conceptually owing to the many competing effects but also computationally as system sizes and associated requirements of computational power becomes substantial. We have thus decided to make the problem tractable by employing the following assumptions.

- We ignore any effect of defects as discussed in 5.1.2 or polycrystalline nature of the thin-films or oxidation at the PR-metal interface.
- We neglect any effect arising from lattice vibrations or any electron-phonon interactions.

We will now start with an overview on localised numerical atomic orbitals followed by a brief look at DFT-based predictions. We will then discuss our simulation approach in detail and look at the DMFT predictions of the transmission coefficient and associated scaling to match the desired trends reported in tab.(5.1). Alongside we will inspect the effect of interface and the conduction mechanism along with studying the role of electronic correlations especially those pertaining to the atomic-like Sm-$4f$ electrons.

5.2 Localised numerical atomic orbitals

One feature of SIESTA that enables us to tackle large scale challenging problems like doing electronic structure calculations involving hundreds of atoms is the use of atomic orbitals with a finite range as basis sets. Before going into the details of the simulation and results, we will briefly discuss the mechanism of Localised Numeric Atomic Orbitals (LNAO) in general and as implemented in SIESTA which is then used by the Quantum Transport code SMEAGOL.

In SIESTA, the Kohn-Sham Hamiltonian, as the nomenclature suggests, is numerically solved for the isolated pseudoatom with exactly the same approximations in term of the choice of exchange-correlation functional, pseudopotential, etc. as for the original system of all electrons. Note that the pseudoatoms are comprised of only the valence electrons as this method uses norm-conserving pseudopotentials to tackle the core+valence system, as described in 2.4. The use of pseudopotentials along with LNAOs makes the problem of handling about a hundred atoms and performing quantum transport calculations tractable. This is done to obtain the radial part of eq. (2.40) by solving the following equation.

$$\left(-\frac{1}{2r}\frac{d^2}{dr^2} + \frac{l(l+1)}{2r^2} + V_l(r)\right) R_l(r) = \epsilon_l R_l(r) \tag{5.1}$$

This equation is solved for r in a logarithmic radial grid using the Numerov (also known as Cowell) method. The logic behind using a logarithmic grid is that close to the origin atomic quantities oscillate rapidly and thus a denser grid is needed to capture such effects whereas they change quite smoothly far from the origin and thus a lighter grid suffices.

The $Y_{lm}(\hat{r}_I)$ are the spherical harmonics representing s, p, d, f orbitals and so on, and thus, are rather well defined and fixed. The radial part, however, can be optimised in terms of *size*, reflecting the number of atomic orbitals used, *range*, denoting their spatial extension, as well as the *shape* of the atomic orbitals used. Depending on the desired accuracy and available computational power, the number of basis sets per atom can be chosen.

• **Single-ζ (SZ)**: The minimal basis set is the Single-ζ basis which has only one radial function for each occupied valence angular momentum shell for the free pseudoatom. For example, in Si with atomic configuration $[1s^2\ 2s^2\ 2p^6]\ 3s^2\ 3p^2$, $[1s^2\ 2s^2\ 2p^6]$ are the core shells. $3s^2\ 3p^2$ make the valence shells. There is one $3s$ shell ($l = 0\ (s); m = 0$) and three $3p$ shells ($l = 1\ (p); m = -1, 0, 1$) each for $3p_x$, $3p_y$, $3p_z$. So, the minimal SZ basis will have 2 radial functions for each l with 1 and 3 m-channels for l = 0 and 1 respectively, thus counting for 4 atomic orbitals. Similarly for Fe with atomic configuration $[1s^2\ 2s^2\ 2p^6\ 3s^2\ 3p^6]\ 4s^2\ 3d^6$ the valence orbitals will be $4s^2\ 3d^6$ and thus, an Z-basis representation will have 2 radial functions for 6 atomic orbitals per Fe atom.

However note that the basis is generated for free atoms but used for solid state systems. This change of environment can be potentially problematic. For example the radial wave-function for two separate atoms when they infinitely separated differ from the situation when they are very near each other. Since we will be dealing with condensed matter systems in solids where atoms will be in close proximity to their neighbours in a unit cell, our basis needs to be constructed such that it is *adjustable* to deal with physical systems where the charge density would want to be more compressed or expanded depending on atomic positions of various neighbours. This desired property of the basis is called **Radial flexibilisation**, and is a feature of LNAOs.

• **Multiple-ζ: Double-ζ (DZ), Triple-ζ (TZ)**: Based on the above rationale, more than one radial function is added for the same angular momentum to the SZ-basis so that depending on the situation where the charge density wants to be either less or more, any of those ζ-orbitals can be appropriately used. In this way the basis is made more flexible, apt for the respective system description.

This can be done in many ways. One way is to solve the Schrödinger equation for not only the ground state but also the excited states. In a different scheme, the first ζ is taken as the atomic orbital and then its first derivative of radial shape with respect to the charge of the atom is calculated. Another method, known as the 'split-valence' method considers the linear part as a linear combination of Gaussians, takes the most extended Gaussian and consider that as the first ζ. The second ζ is chosen such that it reproduces the tail of the first ζ between a chosen radius, r_m, and the radial value where

the first ζ goes to zero, r_c. This function can be defined such that it goes smoothly (i.e., the function and its first derivative are continuous) to 0 and joins the tail of the first ζ between r_m and r_c. A possible choice can be a known function, say, a parabola. Another alternative is that the second ζ can be the difference between the first ζ and the chosen function such that it vanishes at r_m. Finally, after this choice is made, the second ζ is orthonormalised to the first ζ orbital.

• **Polarised-ζ (P) : SZP, DZP**: Similar to the size of the basis, the angular shape of the basis generated for a free pseudoatom might not meet the charge density requirements of the unit cell atomic configuration, and thus we need **angular flexibilisation** of the basis. For that shells of different atomic symmetry and polarisation than those present in the minimal basis set can be added. In Si for instance, the five unoccupied $3d$ shells can be added which are oriented differently than $3s$ and $3p$, and thus more orientations of charge density can be described more accurately. This is called **atomic polarisation**. Note that for the free atom these states are unbound and thus short cut-offs need to be provided for these orbitals by hand. A second way is to apply a small electric field to the original atomic orbital. The new solution with the electric field of the Schrödinger equation will have a different and more extended shape to the original atomic orbital. It can be shown that the new orbital can then be written as a linear combination of the original and higher-angular momentum orbitals [251]. This is known as **perturbative polarisation**. A description of how the solution of eq.(5.1) looks in terms of various choices of multiple-ζ basis can be seen in fig.(5.2).

Since there are many ways of defining an apt basis set, convergence isn't as systematic as for, say, plane wave basis. But LNAOs show good convergence with respect to basis size. Modest basis sizes of, say, DZP are comparable to large plane wave cut-offs in terms of predicting equilibrium lattice constants, total energies, bulk moduli, and thus are very accurate as well as efficient. Note that typically polarisation commands the quality of result more than basis size in multiple-ζ approach.

Implementation of linear scaling methods rely heavily on locality i.e., the spatial range of the atomic orbitals. If two orbitals are sufficiently far away, then their overlap and energy matrix elements should mostly be zero.

$$S_{\mu\nu} = \langle \Phi_\nu | \Phi_\mu \rangle = \int d\vec{r}\ \Phi^*_\nu(\vec{r})\ \Phi_\mu(\vec{r}) \ \simeq\ 0$$
$$H_{\mu\nu} = \langle \Phi_\nu | \hat{H} | \Phi_\mu \rangle = \int d\vec{r}\ \Phi^*_\nu(\vec{r})\ \hat{H}\ \Phi_\mu(\vec{r}) \ \simeq\ 0$$

If we impose that below a tolerance r_c, chosen to include a scope of neighbours, our orbitals are strictly confined i.e., $S_{\mu\nu}$ and $H_{\mu\nu}$ become zero beyond r_c, then for a large system of many atoms where the dimension of H is large, we can use linear algebra libraries for sparse matrices which makes a big and challenging system numerically pliant. But this limit is difficult to gauge and implement. One way is to choose r_c as

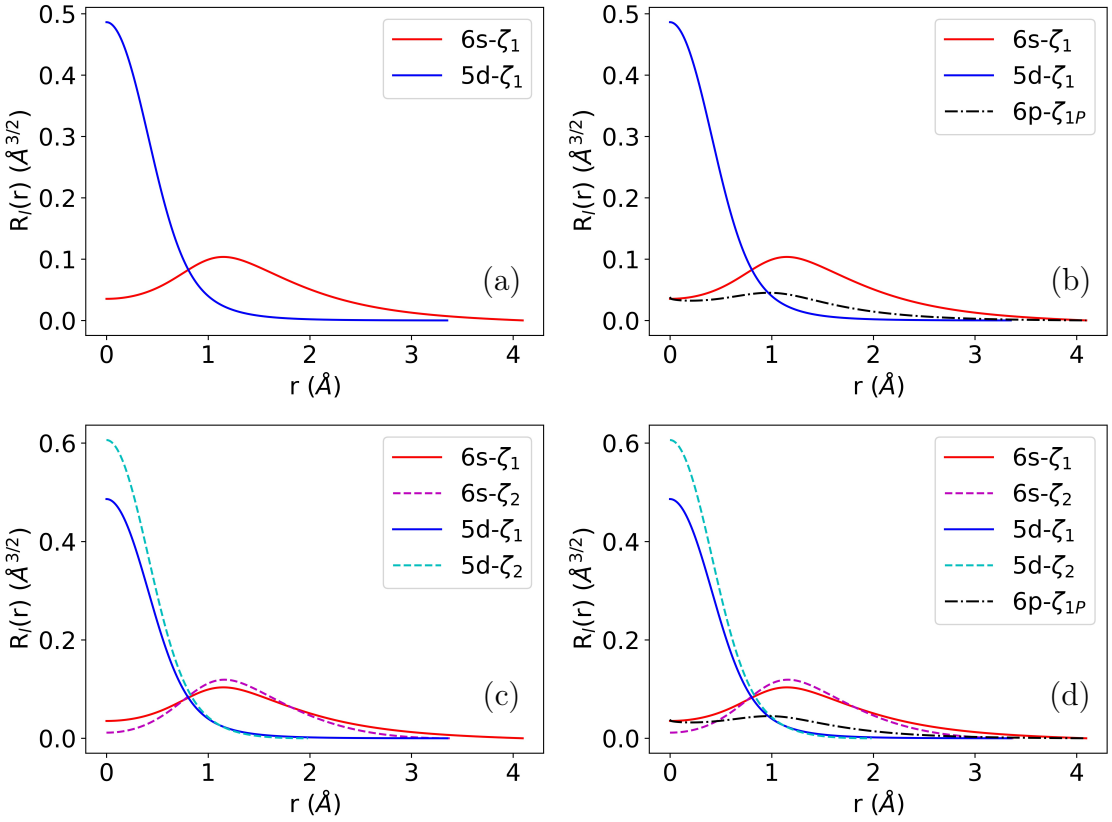


Figure 5.2: (a) Single-ζ (SZ), (b) single-ζ polarised (SZP), (c) double-ζ (DZ), (d) double-ζ polarised (DZP) bases for bulk W. Corresponding lattice constants, energies and bulk moduli compared to the experimental values are reported in tab.(5.2).

the position where an atomic orbital has a node so that we do not neglect any physical effects by ignoring the overlap. Sometimes that value is too large and of not much practical significance in which case r_c could be made smaller. However, confining the cut-off comes at a price of $\delta\epsilon_l$ increase in energy for that orbital. As expected, the larger the cut-off, the more accurate the result with more computational effort being needed.

$$\left(-\frac{1}{2r}\frac{d^2}{dr^2}+\frac{l(l+1)}{2r^2}+V_l(r)\right)R_l(r)=(\epsilon_l+\delta\epsilon_l)\;R_l(r) \tag{5.2}$$

The basis range as well as the basis shape can also be controlled by a confinement potential or added charge. If the Schrödinger equation is solved for the isolated atom in a confined potential, that can impose a strict localisation effect on the basis and change its shape. If we use the energy shift of $\delta\epsilon_l$ to define r_c for a particular confinement potential, one drawback is that the first derivative of the radial part of the basis function becomes discontinuous at r_c. This when combined with numerical grids can create numerical instabilities. To combat this, the choice of confinement potential becomes crucial. In SIESTA, the following choice is made.

$$V(r) = V_0 \frac{e^{-\frac{r_c - r_i}{r - r_i}}}{r_c - r} \tag{5.3}$$

The above choice of potential, also known as the soft-confinement potential [253], ensures that the radial part of the atomic orbital vanishes at r_c, and all its derivatives are continuous and is zero at the core. The problem is that now there are two new parameters to explore and fix. Apart from this, in systems where some atoms might become more anionic or cationic, solving the Schrödinger equation accordingly will make the orbitals more delocalised or localised respectively.

5.3 Preambular transport with DFT

A preliminary heterostructure was first set-up using artificial gold(Au)-like[1] electrodes and 8 mono layers of SmSe and then studied with DFT+U+SOC as implemented in the quantum transport code SMEAGOL [133], [136]. The details of this simulation are discussed in Appendix II. DFT+U+SOC, with $U = 6$ eV, although managed to see the band gap closing with volume compression, it failed to reflect that change in the transmission. In SMEAGOL, the total current at low bias is calculated using the Landauer-Büttiker formula, eq.(2.122), and is proportional to the transmission integrated over an energy range around the Fermi level E_F which is the range of the applied bias. As a result, this framework failed to see the expected increase in current with the closing of band gap. This is clearly wrong.

To delve into possible reasons behind this, it is important to note that the choice of the electrode metal influences directly the alignment of its Fermi level with respect to the band gap of the film. This in turn influences the calculation of conductance in both cases of the transport being governed by thermionic emission (more heavily in this case) as well as tunnelling, as discussed in 2.11.1 and 2.11.2. Thus the results rely heavily on what metal is used in the leads and the detailed structure of the metal-PR-metal interface. For these artificial Au-like leads, the lead Fermi level is pinned approximately at the top of the Sm-4f conduction band.

At any interface, say a metal-semiconductor interface, both the metal and semiconductor terminal layers are surfaces which don't have the same periodicity as the bulk. That is why there are fixed electron levels in the band gap of which the lower levels may be filled [254]. The position and occupation of these levels and their change with applied pressure, bias or doping has a serious effect on conduction properties. If the metal is changed, that will change not only the distribution of these levels in the band gap but also which levels are occupied based on the Fermi level of metal.

The position of the Fermi level is usually related to the work function of the material. In a bulk semiconductor, a change of its Fermi level often leads to an equal and opposite

[1] For further details, please see Appendix II.

change in the work function [255]. At three-dimensional surfaces things become more complicated, especially in presence of Fermi level pinning by the surface states. However recently the one-to-one equivalence of changes in the Fermi level and the work function was shown to accurately exist and hold for single layer graphene till the nanometre scale [256]. Thus we look for a lead material whose Fermi level is approximately mid-gap in 0 pressure conditions might be more suitable. This inspires us to look for a metal but whose work function is less than Au so that the energy required to remove an electron from the metallic leads is less than that of Au. A suitable material in this regards can be W(74) : $[Xe]\ 4f^{14}\ 5d^4\ 6s^2$. With different electrodes one can expect a change in the relative position of the transmission peak due to Sm-$4f$ electrons and the Fermi level as well as the the value of transmission coefficient around the Fermi level. These changes can impact highly the low voltage conductance.

Also note that the transmission takes into account the contributions from the highly localised Sm-$4f$ states as these are assumed to contribute. For these states, mean field levels of approximations as used here have been shown to be incorrect both qualitatively and quantitatively. We expect that if we include many-body corrections which approximate the localisation of the Sm-$4f$ bands better, the contribution of the Sm-$4f$ electrons might be reduced.

We also saw in chapter 4 the effects of spin-orbit corrections implemented within the DFT framework are energetically insubstantial when compared to U in determining structural properties.

Since the Au-lead Fermi level is pinned on top of the Sm-$4f$ states, both the position of the electrode Fermi level as well as the incorrect inclusion of the many-body effects in Sm-$4f$ can be the possible reasons for why even though the band gap closes with pressure in the DFT+U+SOC framework, the conductance does not take into account that change. So, we need DMFT corrections with the right electrode and a very precise construction of the heterostructure since we are working a few monolayers of a pressure dependent film.

5.3.1 Choice of electrodes

Before we go into the details of constructing a suitable heterostructure, we have to select the material to be used as electrodes or leads. When choosing a lead material, one aspect that is always taken into consideration are the structures of the leads and the film that they will have an interface with. There are no unique set of rules or effects that must always be considered and a lot depend son the problem at hand. We choose to construct our leads. There are two main reasons.

- W's lattice constant of $\sim$ 3.2 Å is such at the W-SmX cross-section is made such that the diagonal $a\sqrt{2}$ (see fig.(5.8a)) distance between W atoms matches approximately the 1st-nearest neighbour distance of of Sm-Sm, X-X (see fig.(5.8)). This is discussed in further details in 5.4.

- W has the appropriate work-function, as discussed in 5.3.

Experimental set-up

With an outlook towards PET based devices, some heterostructures were made in the University of Ghent by *Dr. Andreas Sousanis, Dr. Philippe F. Smet, and Dr. Dirk Poelman*. There for the metal substrate an alloy between W and Titanium (Ti) was used with about 90% W concentration as they have similar atomic radii [257], [258]. The alloy so formed had high W concentration and preserved the W bcc structure as seen in fig.(5.8a) and the Ti and W atoms are expected to occupy bcc sites randomly as per their relative concentration in the alloy composition. Thus the electronic properties are expected to be similar with respect to a rigid shift in the density of states with respect to the Fermi level. This reconfirms the choice of W as electrodes in this work.

Since the match is always approximate, there is no unique choice. Another choice that is being considered experimentally is Ir(77) : $[Xe]\ 4f^{14}\ 5d^7\ 6s^2$ with lattice constant ~ 3.837 Å [259], similar to W as well as a similar work-function. In this thesis, we have considered W as our material for the leads.

All this inspires the next section where we fashion our heterostructure in such a way that we avoid any side-effects coming from the choice of electrodes to be able to focus only on the property of the change of conductance coming from the electronic structure of the SmX films and be a good starting point for the DMFT calculations.

5.4 Overview of simulation approach

Since all DFT codes are parametric in nature, with SIESTA being more so due to the nature of its basis set, the choice of an appropriate values of parameters are essential to the qualitative and quantitative aspects of the results. For the following calculations, we use a mesh-cut off of 2000 Ry, the density matrix Mixing Weight of 0.01 and a Tolerance 1.0×10^{-5}, 5 Pulay steps with a 14×14×14 Monkhorst [230] k-pack at 300 K. We use a Conjugate Gradient(CG) type run with 0 CG steps with maximum displacement of 0.1 Bohr, and Maximum Force Tolerance of 0.01 eV/Ang.

Bulk calculations

5.4.1 Basis optimisation

As we discussed in 2.3.3 and 5.2, due to the lack of a systematic convergence procedure in absence of a unique definition of the basis set, localised atomic orbitals need careful selection and optimisation of the basis before starting any realistic calculations for the relevant system. The choice of the basis can heavily influence the results. Since from chapter 4 we are already aware that DMFT will be essential to find the MIT, our

Basis	ΔE_{tot} (eV)	a (Å)	B (GPa)
SZ	2.23	3.19	367.66
SZP	1.44	3.24	291.57
DZ	1.17	3.19	339.70
DZP	1.04	3.20	302.35
Split	0	3.20	325.28
Exp.	-	3.2	311.04 [ ]

Table 5.2: Comparative study of different multiple-ζ bases for predicting equilibrium total energy (E_{tot}), lattice constant (a), and bulk modulus (B), obtained by fitting a Birch-Murnaghan [241], [242] equation of state to the energy-volume curve, for W.

primary aim is to choose a basis that represents experiments and the physical system of interest well as a good starting point for the quantum transport calculations. In general, for better quality and precision one can go to multiple-ζs, polarised or extended orbital basis sets at the cost of computational time.

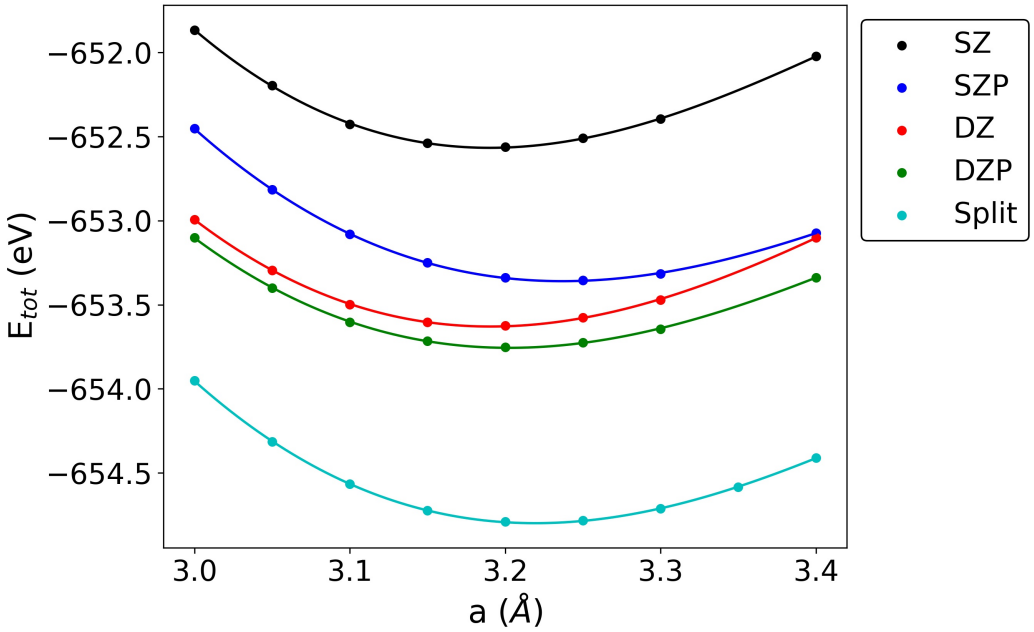


Figure 5.3: Structural relaxation of bulk W for various basis sizes, shapes and ranges obtained using DFT-GGA and fitted with Birch-Murnaghan [241], [242] equation of state. SZ, SZP, DZ, and DZP refer to single-ζ, single-ζ polarised, double-ζ, and double-ζ polarised basis sets, respectively. Split is a user-defined basis optimised with respect to the number of l-shells with respective number of ζs and their cut-off radii (r_c).

To see the effect of the basis choice on physical quantities of interest in this thesis, viz., lattice constant, a, Bulk-modulus, B, total energy, E_{tot}, we first look at the material that will be used to construct the leads i.e., W, and explore the effect of some available SIESTA basis sizes of SZ, SZP, DZ, DZP as described in fig.(5.2). From fig.(5.3) and

tab.(5.2), we see that the total energy goes down in the direction: SZ > SZP > DZ > DZP > Split. As we go from SZ to SZP, the inclusion of *Atomic Polarisation* orbitals stabilise the system energetically by ~ 0.79 eV which is a substantial reduction. Further going to DZ and DZP further improves the lattice constant and bulk modulus values.

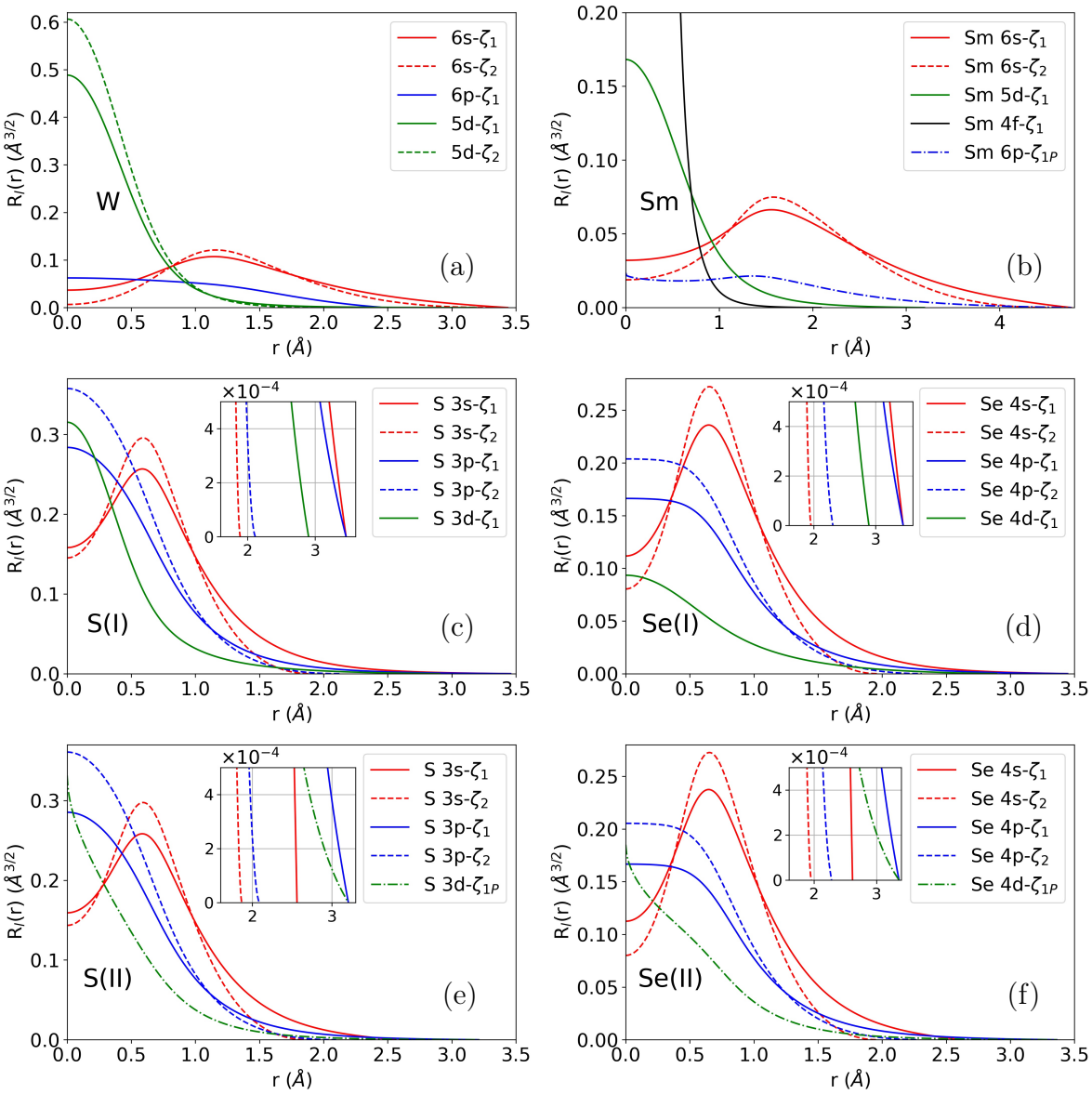


Figure 5.4: Final optimised split-valence LNAO basis for (a) W comprised of double ζs for $6s$, single ζ for $6p$, and double ζs for $5d$ orbitals, (b) Sm composed of Sm double ζs for $6s$, single ζ for $5d$ and $4f$, and single ζ polarised for $6p$, and (c)/(d) S/Se constituted by double ζs each for $3s/4s$ and $3p/4p$ along with a single ζ for $3d/4d$. (e)/(f) depict default Siesta split-valence LNAO S/Se basis where the radial cut-offs for $3s/4s$ orbitals are less by 0.7 Å than $3p/4p$ and $3d/4d$ with the $3d/4d$ orbitals taken to be polarised.

Our aim is to finally do DMFT calculations where we will be dealing with Sm $4f$-orbitals making the thin film which will have interface effects of the leads (W). We

know from Afbau's principle that $5d$ orbitals are close in energy to $4f$. Therefore, even though the predictions of a and B with DZP basis are good enough, we decide to include W-$5d$ orbitals in the basis definition. With this inspiration and the above discussion on radial and angular flexibilisation in mind, our final basis-ζs for W, using a SplitNorm of 0.15 and EnergyShift of 0.01 Ry, looks like fig.(5.4a). This choice also leads to a substantial reduction in energy in the bulk unit cell ($\sim$1 eV) as compared to DZP basis.

Coming to SmS and SmSe, we start from the typical split DZP basis and test various combinations of basis parameters against experimental data keeping in mind the aforementioned purpose of the calculations. Since the expected MIT involves the Sm $4f$ and $5d$ physics primarily, we construct the Sm basis to have $4f$ and $5d$ shells in the valence explicitly along with the $6s$ and $6p$ orbitals suggested by the Siesta scheme (fig. 5.4b). One thing to note is that the default Siesta split type DZP basis for S and Se are slightly erroneous, as depicted in fig.(5.4e) and fig.(5.4f). Looking at the radial extension of the basis, we find that both for S and Se, the extent of the 3s and the $4s$ orbitals end $\sim$ 0.7 Å before the $4d$ and $4p$. The S-$3d$ and Se-$4d$ orbitals are also considered to be polarised which in the SmX material. Since the expected transition is from Sm-$4f$ to Sm-$5d$, the S-$3d$ and Se-$4d$ orbitals are not expected to be polarised. These two corrections are crucial not only in stabilising the structures further energetically but also to the prediction of the correct lattice constant as their inclusion increases the predicted lattice constant by $\sim$ 0.05 Å (fig. 5.5). The final SmX basis along with the specifications seen in fig.(5.4) used a SplitNorm of 0.15 and EnergyShift of 0.01 Ry.

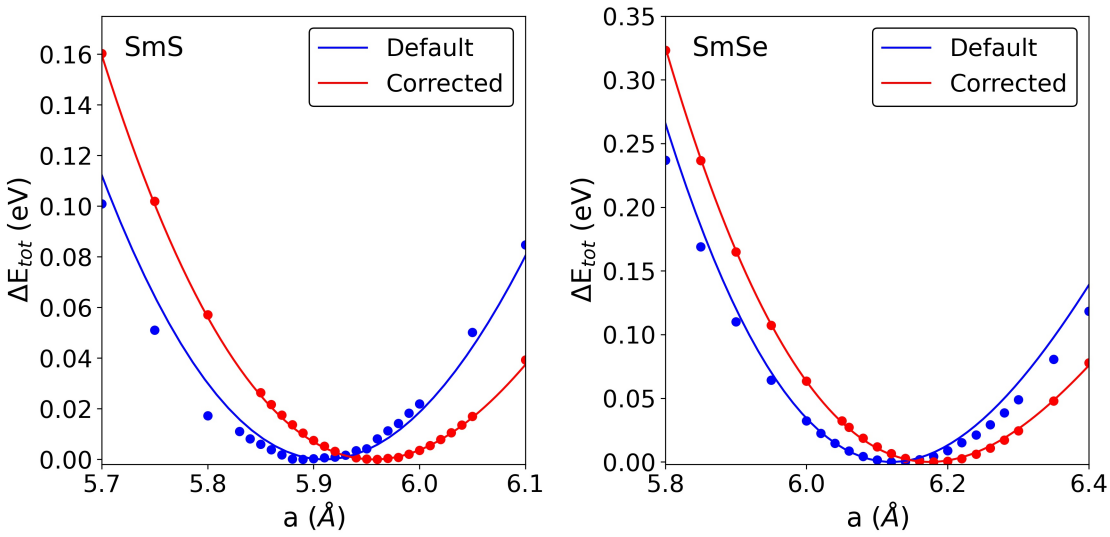


Figure 5.5: The difference in predicted lattice constants for (a) SmS and (b) SmSe with each of the default Siesta S, Se basis as shown in fig.(5.4e, f) and the corrected basis as shown in fig.(5.4c, d).

We also found, as seen in fig.(5.6), that spin polarised LDA or GGA based relaxation minima values are consistently nearer the experimentally predicted values for SmSe. This was also observed for SmS. An important point to note is that ferromagnetic SmS/SmSe does not exist in nature, but we use this *"trick"* to have a structure with a value of the lattice constant as close to the experimentally observed value as possible in order to make the interface. Since we are using a computational self-consistency based approach, the initial heterostructure configuration for this isostructural transition is crucial, and given the large computational cost, we would like to initiate the future DMFT runs nearer to the expected values whose approximate range can be guessed from section 4. Now, albeit for the wrong reasons, the lattice constants obtained with a ferromagnetic Sm-atom in DFT are closer to the SmX DMFT values as obtained with CASTEP as well as the experimental values as already reported in tab.(4.1). Given we also expect that the converged DFT+DMFT values will be comparable irrespective of the basis and the code used, we decide to use the spin-polarised DFT further in the following work with Siesta.

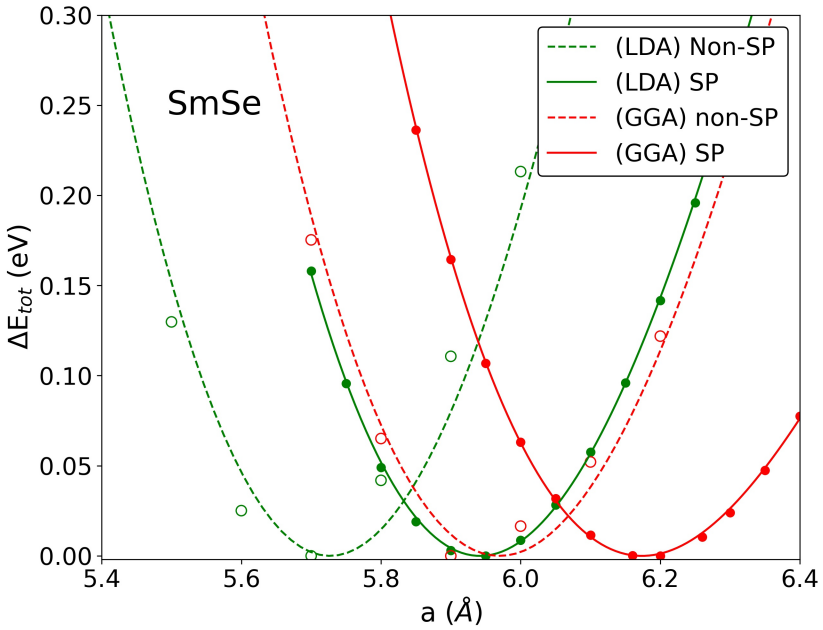


Figure 5.6: The difference in predicted lattice constant values for SmSe with the system taken to be non-spin polarised (non-SP) and spin-polarised (SP) with LDA and GGA.

The final election has to be of the pseudopotential. We need a suitable choice of a norm-conserving pseudopotential as an all-electron calculation even with LNAO basis will prove computationally challenging for this system. We find that even with spin polarisation enabled, LDA underestimates the lattice constant considerably whereas ferromagnetic GGA gives a lattice constant close to the experimental and CASTEP-DMFT insulating values. Note that both the choice of basis and pseudopotential affects the lattice constant and bulk modulus, but the trends followed by multiple-ζ basis sets

Material	Pseudopotential	a_{Siesta} (Å)	a_{exp} (Å)
W	LDA	3.16	3.2
	GGA	3.20	
SmS	LDA	5.75	5.97
	GGA	5.96	
SmSe	LDA	5.94	6.19
	GGA	6.17	

Table 5.3: Comaprision of lattice structures of (a) W, (b) SmS, (c) SmSe obtained with LDA and GGA with experimental predictions [198], [239], [244], [243]

for GGA (PBE) and LDA, as implemented in SIESTA, are the same. Note that even with all this, the DOS is always metallic at the equilibrium i.e., the zero pressure state for both SmS and SmSe, as expected.

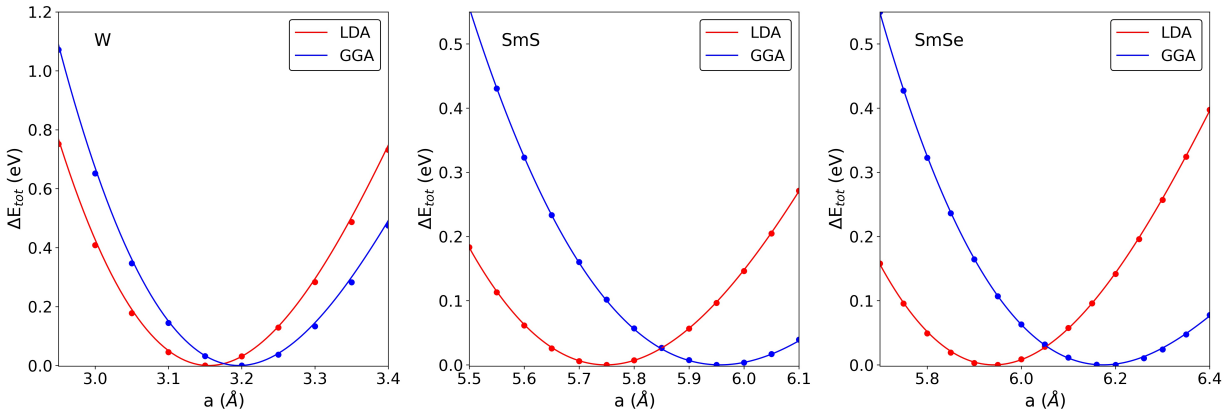
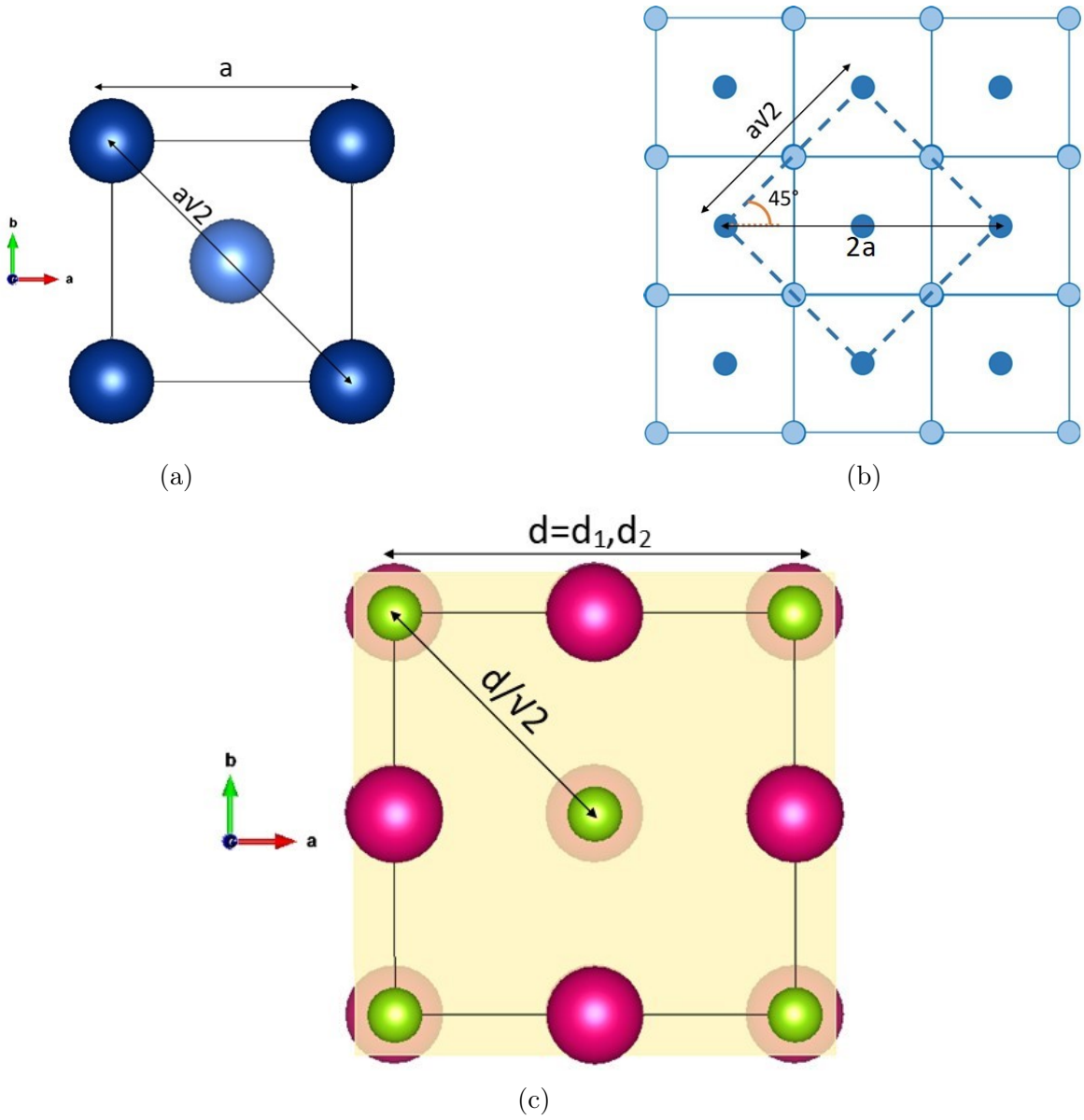


Figure 5.7: DFT based energy minimisation for (a) W, (b) SmS, and (c) SmSe with the final basis as described in fig.(5.4a, b, c, d) with LDA and GGA pseudopotentials.

Setting up the heterostructure

One aim of using Dynamical Mean Field Theory corrections for the strongly correlated Sm-4f orbitals on top of Density Functional Theory is for improved predictions of the I-V characteristics for the possible PR candidates of a Piezoelectric transistor. Before we perform the transport runs to calculate the I-V characteristics, it is necessary to set-up a stable heterostructure junction that mimics the experimental system we wish to compare our results with. We have already performed the first step for this and relaxed bulk W, which serves as our lead material and followed by SmX which serve as our piezoresistive materials in the form of thin films. The heterostructure that we will obtain at the end of this section will comprise of semi-infinite W-leads sandwiching a few layers of the PR materials along the z-direction, which is the direction of electron transport.

5.4.2 Setting up the interface



(a) (b)

(c)

Figure 5.8: (a) *Front-view* of a W bcc unit cell [261] with W atoms in blue. The a-b axes refer to the x-y plane or the plane of the paper. Shades of blue depict the depth along the c(z)-axis. (b) The blue dotted line connects 4 W-atoms in a plane with the $5th$ W-atom at the face-centre. This corresponds to the orientation of the W-atoms at the interface. (c) *Front-view* of SmX NaCl-like structure with Sm, and X=S, Se atoms in magenta and green, respectively. The Sm-Sm, X-X distance $d < 2a$ (d_1 for SmS, d_2 for SmSe). The W-SmX cross-section made to match the distance between W atoms at the ends of the square ($a\sqrt{2}$) in (b) to the 1st-nn distance ($d/\sqrt{2}$) of Sm-Sm, X-X.

The structure of W-SmX interface isn't unique. There is some inexactness that we need to sort through aiming to optimise the structure for the future quantum transport calculations to be performed. We have already fixed the basis and selected the

pseudopotential for the bulk. Our aim is to get to a transport set-up structurally as close to experiments as possible within our DFT-based theoretical framework which can serve as a good starting point for DMFT runs. The first few degrees of freedom to fix pertains to the relative positions of Sm and X (=S, Se) atoms with respect to the W atoms, and this choice isn't unique.

W crystallises with a body-centred cubic (bcc) structure in bulk (fig. 5.8a, 5.8b) with *almost* but not exactly half the lattice constant as SmX with SmX having an NaCl-like rock-salt structure (Fig. 5.8c). This mismatch presents us with a choice to compress or expand either the leads or the thin film materials viz., SmX. Since our motivation is to build a piezoresistive element based transistor, we decide to compress the W-lead x-y distances to suit SmSe/SmS lattice constant value and keep the thin films fully relaxed as electronically the main role of the electrodes comes from their metallic behaviour which doesn't change even if they are compressed in W, and thus is expected to have little effect on the transport properties.

We are aware that with this choice we are inherently making this assumption that an experimental set-up is be grown such that the substrate, i.e., the lead material W, adjusts to the thin film (a few monolayers long). This is an unusual supposition as usually films are grown on substrates, and at the interface both relax with respect to each other and might have some strain or strain induced defects. That is why this choice, although reasonable for our aim to calculate transport properties, is a possible source of error when comparing to experiments. Given that along with the piezoresistive behaviour we are interested in electronic properties of SmX, we will stay with this choice for our theoretical studies in this thesis. But tipping the scales back again against this motivation, it is important to remember that such a mismatch can have possible defects and/or defect induced disorders around the interface and SmX thin film properties in a realistic set-up might be prone to such effects as they can be possibly induced by an intra-structural pressure. But given that we are dealing with strongly correlated materials with interesting though arduous $4f$-physics, it is only utilitarian and reasonable to first understand the electronic degree of freedom to the best possible approximation before looking at the effects of lattice distortions which not only require larger computational effort but also deals with an energy scale usually about 10^{-3} times smaller than the electronic energy scales. Thus the possible issue of disorder has not been dealt with in this thesis and remains as a possible topic of interest in the future of this project.

When we make this choice, it becomes necessary to fix W-a_x and W-a_y values to suit the corresponding films. As we observe from tab.(5.4), this implies that the lead material, W, will be under strain in the x and y direction which can lead to significant expansion along the z-direction. Since the z-direction is the direction of transport as well, we first need to re-relax the structure along the z-direction to minimise the intra-structural forces inside the W-leads. It is important to note that, as discussed in 2.3.3, Pulay terms can be significant in codes based on atomic orbitals making this check

Interface Material	Quantity	Actual Value	Implemented Value
	a = W-W	3.20	
	d_1 = Sm-Sm, S-S	5.96	
	d_2 = Sm=Sm, Se-Se	6.17	
W	a_x, a_y	$a\sqrt{2} = 4.52$	$d_1/\sqrt{2} = 4.21$, $d_2/\sqrt{2} = 4.36$
SmS	a_x, a_y ($=d_1$)	$d_1/\sqrt{2}$	$d_1/\sqrt{2}$
SmSe	a_x, a_y ($=d_2$)	$d_2/\sqrt{2}$	$d_2/\sqrt{2}$

Table 5.4: A summary of lattice size mismatch at the interface between the lead W and the films of SmS and SmSe, respectively.

additionally important. Fixing the W-a_z is concurrent with the choice of the interface orientation of atoms and will be computationally expensive if done with the whole leads + thin-film structure. We avoid that by creating a 4-atom W unit cell with W-a_x and W-a_y kept fixed at the respective film-dependant values, and relaxing the W-a_z. We find that, matching our expectations, the now compressed W elongates along the z-direction to (a) 3.49 Å for SmS and (b) 3.30 Å for SmSe from the previous value of 3.20 Å. The expansion is more for SmS as compared to SmSe as with SmS being the smaller cell, W has been compressed more in the x-y direction for SmS than for SmSe. Additionally SmS being the smaller cell will have more electronic repulsion than SmSe elongating it in the z-direction. We now fix these values for W-a_z in the leads in order to set up the interface.

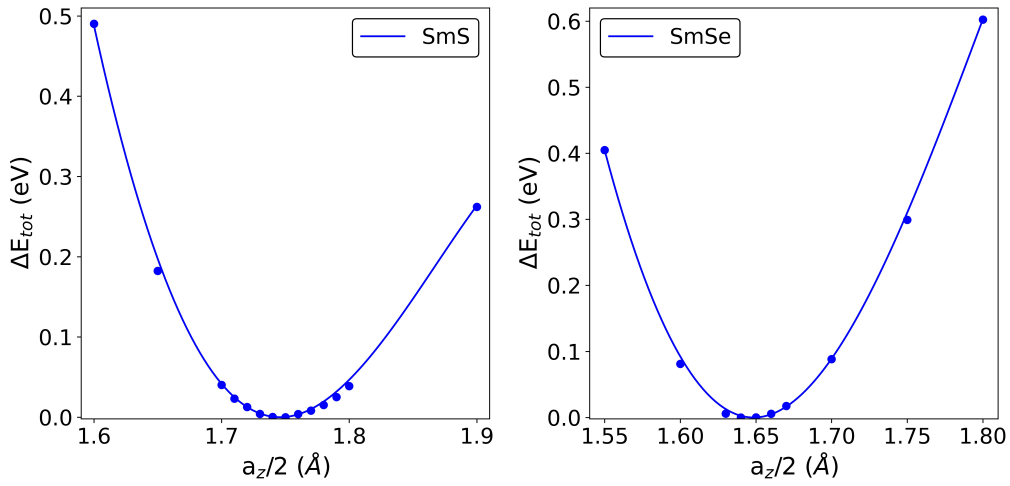


Figure 5.9: Relaxing a_z of the substrate W with respect to the new a_x, a_y set as per the reference thin film bulk lattice minimum denoted by the figure legend.

d(W-SmS) Å	$\Delta E = E_{top} - E_{hollow}$ (eV)
1.8	3.66
2.0	1.64
2.2	0.55

Table 5.5: The variation of total energy difference for the *top* and the *hollow* configurations of W-SmS interface for three selected distances.

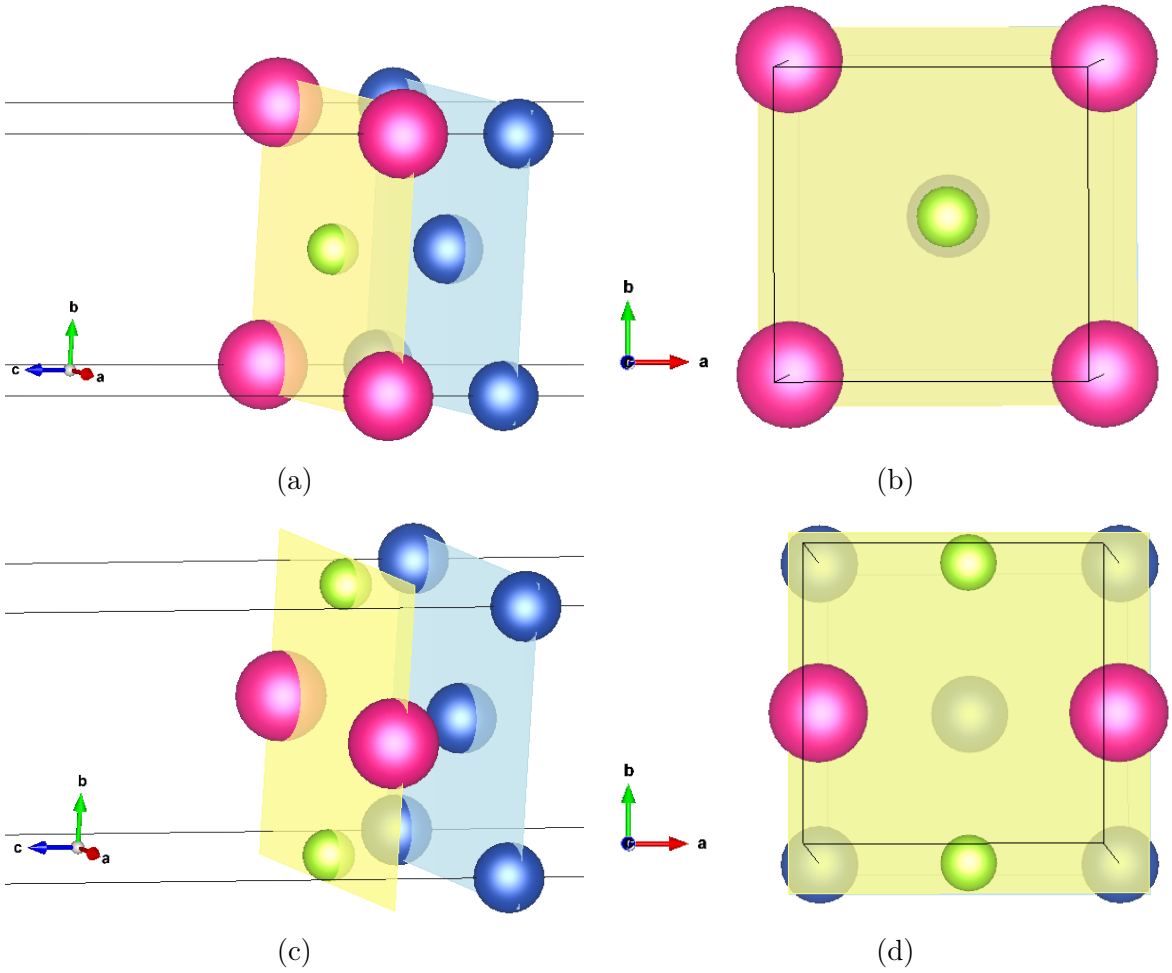


Figure 5.10: The (a), (c) side-views and (b), (d) top-views of the *top* and *hollow* configurations of the W-SmX interface [261], respectively with magenta, green and blue atoms representing Sm, X = S or Se and W, respectively. The shaded planes show the respective layer cross-sections. In (a), (b) Sm and X atoms sit right on top of all five W atoms. In (c), (d) the Sm and X atoms sit between the boundary W-atoms. There can be infinitely many configurations where the Sm or X atoms sit somewhere in-between.

The next step is to choose the orientations of W with respect to either Sm or X. One choice is to make the interface such that Sm atoms sit on top of the W atoms at the junction, as in fig.(5.10a, 5.10b). This configuration with periodic boundary condition also has the X atoms sitting on top of the W atoms at the first layer as well. We call this

the *'top'* configuration. A second choice is to place Sm exactly between two W atoms as depicted in fig.(5.10c, 5.10d) which we name the *'hollow'* configuration. There can be many other choices where the Sm atom is placed somewhere in between its position of the *top* and *hollow* configurations. We will select the structure which is energetically most stable. We expect the *hollow* configuration to have the lowest energy as Sm being the largest atom will have least electronic repulsion with the electron clouds of W atoms at this position. Another parameter to fix concurrently is the distance between the W lead and the SmX film. But since the whole set-up of a semi-infinite lead with a few layers of SmS is computationally expensive, we compare the energies of the two configurations for select distances of W-SmS. We expect that at the optimal distance the energy difference between the configurations will reach a minimum but the trends will remain the same.

In tab.(5.5), we find expectantly that the *hollow* configuration is more stable energetically as it minimises the electronic repulsion and thus decreases the energy. A secondary point to note from tab.(5.5) is that as the W-SmS distance nears 2.2 Å, the energy difference reduces. This is a hint at the optimum interface distance ranges for SmS.

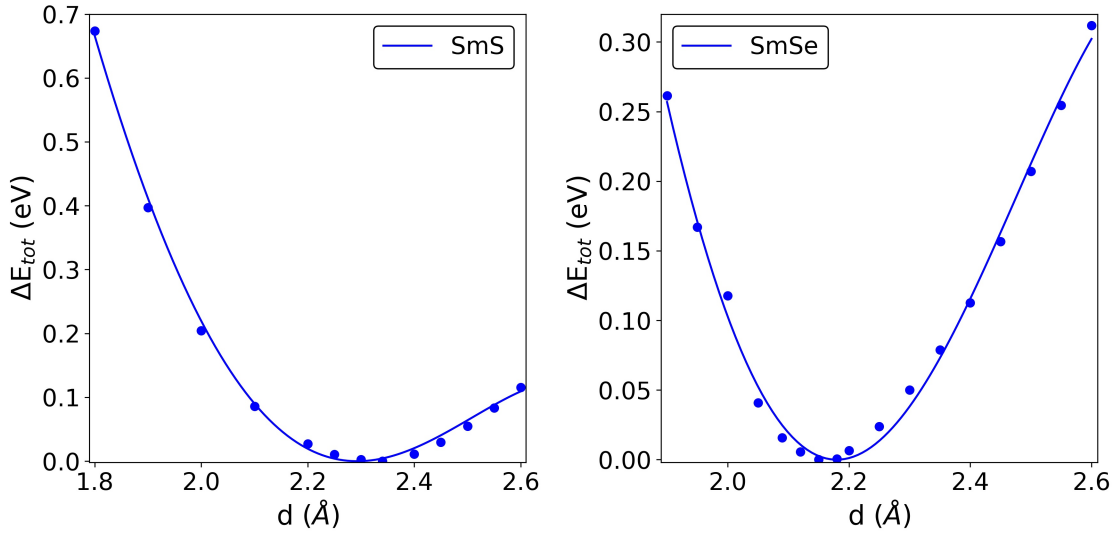


Figure 5.11: W-SmX (X = S, Se) interface distance relaxation. The minimum d is used as the interface lead-film distance in transport calculations.

The succeeding step is to use the *hollow* configuration as our final interface configuration, as shown in fig.(5.12), and find the optimal lead-film distance at the interface by relaxing the left lead-film set-up to complete the heterostructure construction. This distance was found to be (a) 2.29 Å for W-SmS, and (b) 2.18 Å for W-SmSe interface as shown in fig.(5.11). Note that our system is isotropic and we use multiple layers of SmX in the *thin*-film such that the interface effects of the left and right leads are independent of each other, and hence doing relaxations, as above, for one is good enough

for constructing the other by symmetry.

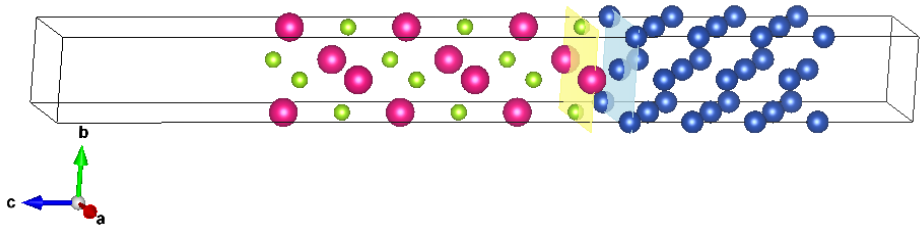


Figure 5.12: The W-SmX interface [261] for the *hollow* configuration with 6 SmX film layers and 7 W lead layers. The Sm, X and W atoms are denoted by the colours magenta, green and blue, respectively.

5.4.3 Calibrating the pressure

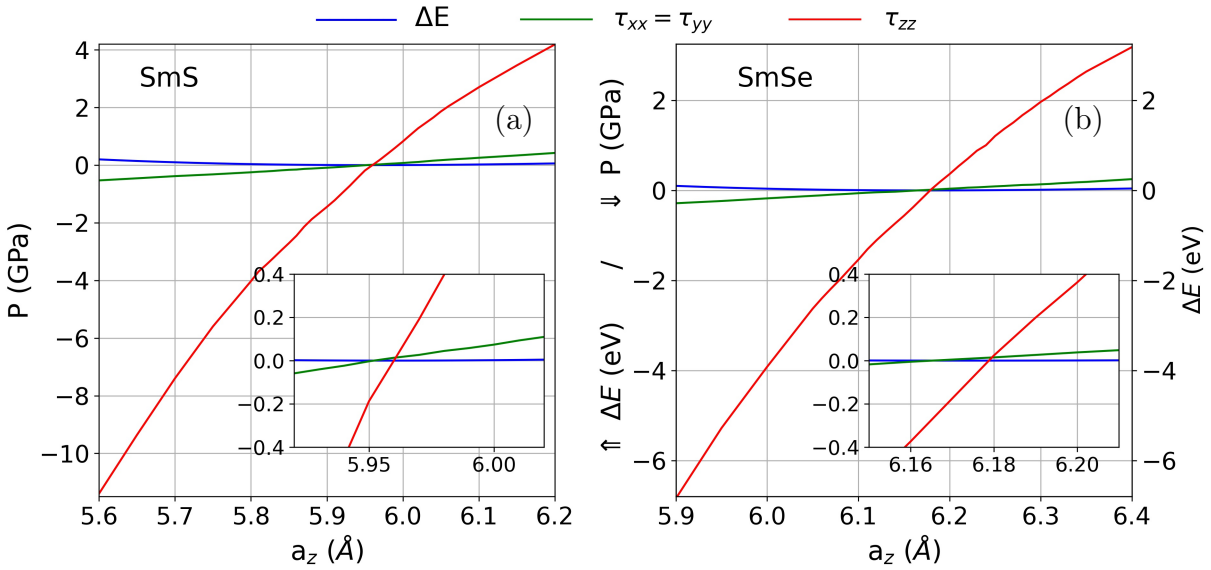


Figure 5.13: Concurrence of minimum energy and zero pressure state for thinfilm materials used (a) SmS, (b) SmSe

The final job is calibrating the values of pressure to be used in the transport. The pressure will be applied along the z-direction which is the direction of the transport. For that we again create a 4-atom unit cell of SmX and keep $a_{x/y}$ fixed as per their respective minimum bulk lattice constants. Then we change a_z and note the total energy and the stress tensor. Ideally the energy curve with respect to the change in a_z should have a minimum when $a_x = a_y = a_z$. This should coincide when the pressure in all three directions is zero. So, in a perfect world we should see the three curves coincide at zero pressure. This serves as a test for the correctness of the structure as well because the most stable configuration that we want to start from is expected to be under ambient conditions. On running the calculations, we note from fig.(5.13)

that the zero of the parabola and that of the τ_{xx}, τ_{yy} curves match. However the zero of the τ_{zz} graph is shifted towards the right by ∼0.007 Å for SmS and by ∼0.012 Å for SmSe. Given that we are using a mean field approach to determine the structural stability of a large structure with an element of strong correlation present, and since our expected MIT behaviour change will be observed in the range > 0.1 Å, as shown by our previous CASTEP bulk calculations tabulated in tab.(4.1), these differences in the bilayer pressure zeros are acceptable and transferable to the heterostructure. From the curve of the stress tensor along the z-direction τ_z vs a_z, we select the pressure values that we want to perform the transport calculations for, and note the corresponding a_z values of SmX to be set in the structure to attain that.

This concludes our search for the heterostructure closest to experiments aimed at performing quantum transport calculations using DFT+NEGF and DFT+DMFT+NEGF on. These details were supplied to our Industry collaborators at NPL for performing the quantum transport calculations using the NEGF code SMEAGOL interfaced with Siesta.

5.5 Quantum Transport with DFT and DMFT

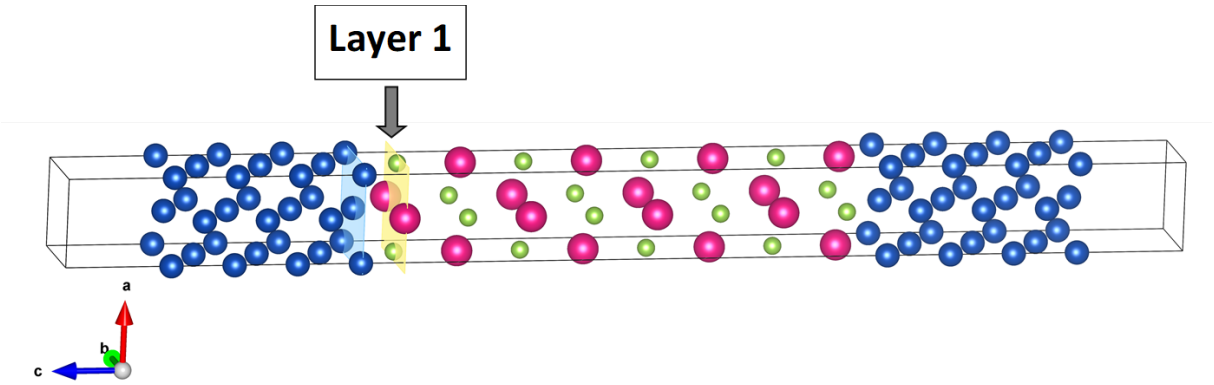


Figure 5.14: Structure of the W-SmSe-W junction with the W and SmSe as electrode and film materials respectively for the *hollow* configuration. The interface is optimised with Siesta to be used with SMEAGOL by collaborators at NPL for transport calculations. The atoms in blue, magenta and green stand for W, Sm and Se, respectively.

We first extend the W-SmX transport heterostructure by adding the W-lead on the other side of fig.(5.12). This gives us the thin film, SmX, at the junction between the two W electrodes as shown in fig.(5.14). As calculation of transmission with the DFT+DMFT framework introduces more technicalities to be addressed, in this section we focus on SmSe as our piezoresistive thin film candidate. Since the qualitative behaviour of the density of states is similar across all three chalcogenides as seen in chapter 4 and since estimating the electronic current through thin films at finite tem-

perature depends on the position of various energy levels especially around the Fermi level which influence the conductance, we expect the results to be similar across the group. The question regarding the difference in the nature of transition between SmS and SmSe has not been addressed as a result. An additional reason for choosing SmSe is that its lattice constant is such that the size mismatch with the leads will be smaller than for SmS where the first few W layers will be more compressed, and than for SmTe, where the first few layers have to be expanded artificially (see tab.(5.4) and tab.(4.1)).

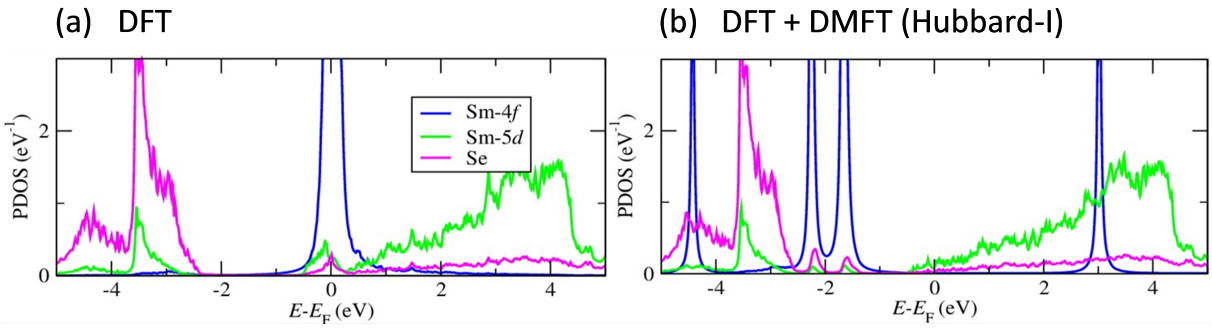


Figure 5.15: Partial density of states (PDOS) obtained with SMEAGOL with (a) DFT and (b) 1-shot DFT+DMFT using the Hubbard-1 solver as implemented in SMEAGOL for a heterostructure with 8 monolayers (ML) of SmSe with W semi-infinite electrodes, a DMFT-U = 8.1 eV on Sm-4f orbitals, Hund's coupling, J = 0.8 eV, and nominal valence of 5.5. (Simulation and figure by: Dr. Ivan Rungger)

Now we have the correct structure to do DMFT for the transport calculations[2]. For DMFT, the Hubbard-1 solver was used with a U = 8.1 eV, and J = 0.8 eV with an input nominal valence of 5.5, which has been set from the output occupancy from the DFT self-consistency loop. The chemical potential for 1-shot DMFT has been set to 0 (equal to the Fermi energy). Note that the values of U and J are different from the ones used in chapter 4. This is due to the fact that the transferability of such parameters between codes that use different basis sets isn't usually guaranteed. Every work with a different code demands initial benchmark studies determining the appropriate value of U for the relevant property of interest to serve as a reference which were done for both the codes separately.

As observed in chapter 4 with CASTEP plane-wave basis based implementation, in the SMEAGOL implementation of DFT with the SIESTA numeric localised atomic orbital basis predicts the system to be metallic under ambient conditions. Both DFT+U and DFT+U+SOC both open a gap. DFT+U+SOC with U=6 eV, finds the gap in SmSe to close when the material is compressed by 9%, as described in detail in Appendix II. As the next step, we include the many-body effects by correcting the Sm-4f levels with DMFT within the Hubbard-I framework. This can be done in two ways in SMEAGOL where the many-body self energy can either be read from an external code

[2]This structure was sent to our industry collaborators at NPL to perform the DMFT simulations.

(SIESTA DFT) following which a 1-shot DMFT calculation can be performed. Another way is to calculate the many-body self-energy with charge self-consistency criteria as discussed in section 2.10.4. We first perform a 1-shot DMFT calculation with the above parameters.

In fig.(5.15) it can be seen that for the 4^{th} layer of SmSe, indicated in fig.(5.17a), the DOS obtained with SMEAGOL DFT+DMFT (Hubbard-I solver) is qualitatively the same as that obtained with CASTEP DMFT (Hubbard-I solver). There are two occupied Sm-4f peaks between -1 and -3 eV and one occupied Sm-4f peak between -4 and -5 eV. These correspond to the three occupied Sm-4f peaks between 0 and -2 eV in fig.(4.9c). However note that the splitting changes with increasing J even with CASTEP DMFT as verified from fig.(4.10) for SmS where out these three peaks, two shift to between -1 and -3 eV, whereas the other one between -4 and -5 eV, exactly as seen in fig.(5.15). This is expected to happen for all three Sm-monochalcogenides. The benchmark of SMEAGOL layer-4 with the bulk SmSe as obtained with CASTEP validates the calculations done on the heterostructure so constructed with SMEAGOL.

However, going back to fig.(5.15b), we observe that there is a finite density of Sm-5d electrons at the Fermi level of the electrodes (which is set to zero and coincides with the Fermi level of the film). This means that even under zero bias and pressure, there is a small but finite electron density present at the Fermi level even when the phase is supposed to be insulating. Thus this junction is not locally charge neutral. The DMFT corrections, as discussed, apply only to the chosen correlated subspace (Sm-4f levels here). However, the remaining electronic structure outside this correlated subspace that includes the Sm-5d bands might react to these corrections for the local Coulomb interactions. This relaxing of the weakly-correlated electronic structure can then again change the orbital occupations of the correlated subspace. Interweaving of these effects is crucial for orbital occupations and total energies of complex heterostructures, especially in regimes near a metal-insulator transition [262]. Although systematic studies deciphering quantitative and qualitative impact of charge self-consistency on *ab-initio* approaches are few, in general combining DFT and corrections to a small correlated subspace based on either DMFT [262] or GW-approximation [263] benefit from applied charge self-consistency. This motivates us to implement charge self-consistency.

Thus the next step is to implement charge self-consistency on the electron density initiating from a nominal valence of 6, as discussed in section 2.10.4. This solves the issue of charge neutrality by fixing the chemical potential of the system to the Fermi level. We find that this moves the two occupied Sm-4f peaks which in fig.(5.15) were between -1 and -3 eV to approximately between 0 and -1 eV. This position exactly matches the CASTEP DOS within this energy range as seen in fig.(4.9c). However the third occupied Sm-4f peak moves up to -3 eV but is still substantially deeper when compared to the CASTEP insulating DOS. We also see in both fig.(5.15) and fig.(5.16) that occupied Se-4p states hybridise heavily with filled Sm-4f states. This observation has already been observed and corrected for in chapter 4 by introducing a static DFT

U on the chalcogenide valence Se-p shells. A DMFT-U on the Se-p shells might also be applied but that will prove to be computationally expensive as for p-levels hybridisation will need to be considered. Also, since in this section we are primarily interested in conduction properties around the Fermi energy, energy levels which are > 2 eV deeper than the Fermi level are of little consequence.

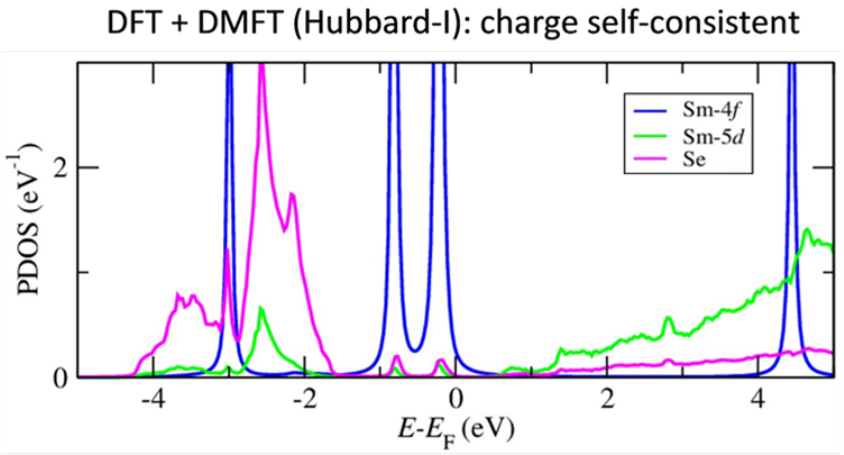
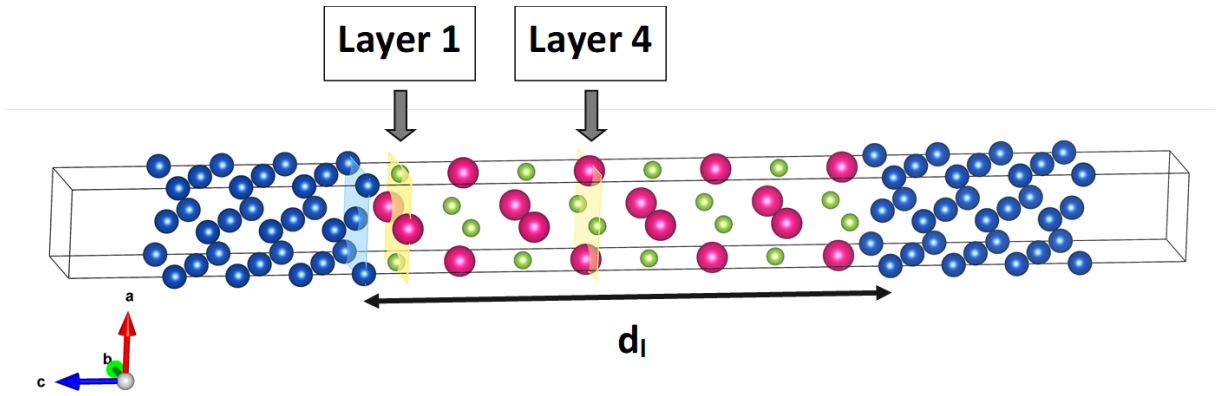


Figure 5.16: Partial density of states (PDOS) obtained with the SMEAGOL implementation of DFT+DMFT using the Hubbard-1 solver with charge self-consistency for a W-SmSe-W heterostructure with 8 monolayers (ML) of SmSe and semi-infinite W leads, DMFT-U = 8.1 eV on Sm-4f orbitals, a Hund's coupling, J = 0.8 eV, and nominal valence of 6. (Simulation and figure by: Dr. Ivan Rungger)

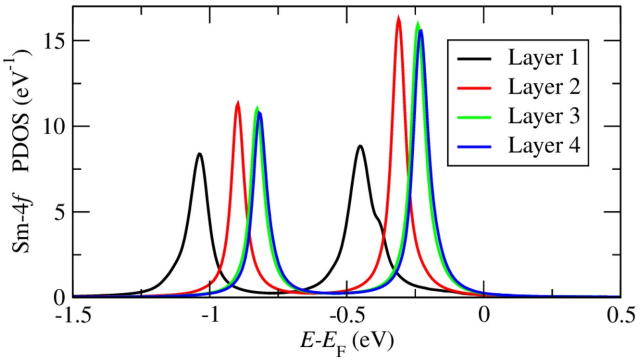
Next we look at the evolution of the Sm-4f DOS with DMFT corrections layer by layer from layer 1 to layer 4 which is the middle layer from either side, as shown in fig.(5.17a), in an 8 monolayer structure. The Sm-4f peaks for the second Sm layer shifts by ~ 0.25 eV from the first layer towards the Fermi level and then a smaller variation in the third layer with a higher density near the Fermi level.

- The DOS for layers 3 and 4 remain almost same in character and position which implies that the bulk-like behaviour has been reached.
- In the first layer the Sm-4f DOS is less localised and more smeared out in energy than the middle layers because they are positioned next to atoms of metallic character. We observe the effect to remain partially till layer 2. The extent of the smearing will also depend on the distance of the layer from the terminal electrode layer.

Finally we study the transmission as a function of energy for zero bias such that the chemical potential at the left W-SmSe interface is same as the right. The system, as per its size and presence of a gap in ambient pressure, is expected to be in the tunnelling regime where the transition can have an exponential behaviour for different energy ranges as well as junction thicknesses. That's why the transmission is plotted



(a)



(b)

Figure 5.17: (a) Structure of the W-SmSe-W junction with W atoms (blue) as electrodes and SmSe (magenta, green) as the sandwiched film with shaded regions in xy-plane. Layer 1 is the first SmSe layer at the metal interface of length $d_l = 2.5255$ nm and layer 4 is the layer in the middle. (b) Partial density of states (PDOS) of Sm-4f levels for 4 consecutive layers of SmSe showing the evolution of occupied Sm-4f levels in energy with distance from the interface. (Simulation and figure of (b) by Dr. Ivan Rungger)

on a logarithmic scale. The observations from the transmission plot in fig.(5.18) are listed below.

- The transmission peak between -0.5 eV to 0 ($= E_F$) matches the patterns in the density of states as shown in fig.(5.16) and fig.(5.17b). Since the total DOS is dominated by the Sm-4f peaks in that energy regime, it confirms that the Sm-4f electrons do contribute to transmission in spite of their localisation.

- When comparing DFT+U+SOC (U=6 eV), as discussed in Appendix II, with DMFT we note that -

  (i) DFT+U+SOC finds a local minimum in transmission at the Fermi level which moves above it with DMFT corrections.

(ii) The value of the transmission coefficient at the Fermi level almost remains the same for both ~ 0.01 increasing slightly when computed with DMFT. This is approximately a value at the border of metallic and insulating behaviour. We expect this peak to shift with an applied bias inducing metallicity.

(iii) DMFT splits a single broad transmission peak of DFT+U+SOC between -1 and 0 eV into two which agree with the respective density of states of the Sm-4f levels.

(iv) The 1^{st} peak in DMFT transmission within 0.3 eV of the Fermi level is not fully localised and is near the Fermi level and can be expected to contribute to the current. This peak can be expected to shift towards left or right depending on the material or temperature or pressure, as discussed in 4.

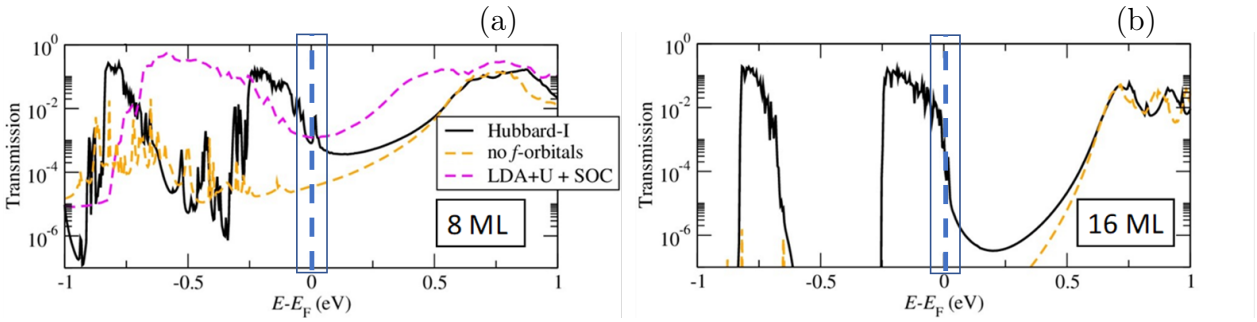


Figure 5.18: Comparison between transmission plotted as a function of energy from the Fermi level for W-SmSe-W heterostructure with (a) 8 monolayers (ML), and (b) 16 MLs of SmSe as the PR thin-film with DMFT-Hubbard1 solver and DFT+U+SOC with the basis as described in 5.4 compared with the DFT results obtained without the contribution of f-orbitals. (Simulation and figure by: Dr. Ivan Rungger)

- If the contribution of the Sm-4f levels is removed by using the projection scheme specified in ref. [138] (the contribution of the f-electrons is removed from the background DFT+NEGF transmission within the code), the transmission reduces by about 2 orders of magnitude at the Fermi level. For 16 monolayers, the transmission essentially vanishes without the contribution of the 4f electrons. These results roughly correspond to a standard model of lanthanides where the f-orbitals are completely localised and do not contribute to the conductance. The true SmSe conductance at this nanoscale is expected to be somewhere between the calculated DFT+DMFT transmission and the results where the f-electron contribution is removed from the conductance.

- Regarding the thickness-dependence we find that -

  (i) The transmission for 8 ML junction (~ 0.01) is still rather large when compared to a fully insulating system. Compressing this further might change the resistance, but not significantly owing to the fact that the conductance

itself is still rather large. From this we can conclude that for junction lengths $d_l \geq 2.5$ nm corresponding the 8 ML heterostructure, fig.(5.17a), the PR material can potentially act as a memory element but not a transistor element.

(ii) The transmission at and within ~ 0.05 eV around the Fermi level, represented by the blue dashed line and the blue rectangle in fig.(5.18), decreases exponentially when the number of layers is doubled, thus indicating tunnelling behaviour.

(iii) For the 16 ML junction, $T(E_F) = 10^{-4}$ that quickly decays to 10^{-6} within 0.05 eV past E_F. The corresponding junction thickness is $d_l = 4.62$ nm. The local minimum in transmission just above the Fermi level for 16 ML junction decreases by three orders of magnitude just above E_F, at ~ 0.15 eV, and goes below 10^{-6} following the sharp decrease at the Fermi level. As per IBM and NPL internal reports, the OFF-state resistivity for transistor operation should be $1\Omega m$, which corresponds to a $T(E_F) = 10^{-6}$. Since the system is in tunnelling regime, and its exponential decay with junction thickness has been established already, increasing the junction thickness to ~ 6 nm corresponding to about 24 monolayers can be expected to reduce the transmission as described. The position of the Fermi level (E_F) could be changed within the band gap region by changing the electrode material or the interface chemistry. Thus, if this regime is made accessible by adding a few more layers of the PR material, a stable OFF state could be achieved for switching operations.

(iv) A smaller thickness (i.e., $d_l < 2.5$ nm) will increase the conductance of the set-up as the terminal two film layers on either side will remain smeared due to their closeness with the metallic leads. The first layer without that effect is layer 3. So, we can extrapolate and say that we need at least 6 layers for any tunnelling-like behaviour to be observed. This corresponds to a junction thickness of 2 nm.

(v) From 0.2 eV till 0.7 eV, the transmission for both cases gradually rises albeit from different minima but then attain similar values. This corresponds to the conduction through Sm-5d conduction bands as seen from fig.(5.16). This shows that thermionic electrons, which are thermally excited to the SmSe conduction band, get transmitted across the thicker junction with small scattering. For thick SmSe films these thermally excited electrodes in the SmSe conduction band dominate the transmission.

5.6 Conclusion and outlook

To summarise, we started with Samarium chalcogenides, more specifically SmS and SmSe, that show promise as piezoresistive elements in a piezoelectric transistor. On

studying their bulk properties and by accounting the role of strongly correlated $4f$ orbitals in chapter 4 we saw that on application of pressure an insulator to metal transition happens due to a shift of the energy levels owing to compression. This shift leads to the $4f$ levels crossing the Fermi level making the system metallic while the $4f$ electrons simultaneously become heavier. This demands a closer inspection on the role of the $4f$ electrons in transmission in a PET-like PR set-up.

Experimentally it is known that in the macroscopic regime the the exponential rise in conductance with pressure happens via thermionic emission. However, when approaching nano scales as designed for PR films in the PET model, the conduction mechanism is expected to be based on quantum tunnelling. Owing to the closeness of the f levels to the Fermi level in ambient conditions, this demands an independent scrutiny of the behaviour of the Sm-$4f$ electrons in a heterostructure based thin film set-up and in depth layer-by-layer study of interface properties which can be influenced heavily by pressure or compression of the material.

Confirming the conclusions drawn in chapter 4, we see that the f-electrons in a thin-film set-up are described as rather strongly itinerant by DFT calculations. With DFT they are always at the Fermi energy, whereas DFT+U+SOC opens a gap parametrically depending on the value of U. But both overestimate the contribution of the f-electrons to the conductance, which is in contrast to the common notion that such electrons are highly localised, almost atomic-like. Given the true degree of localisation is not known for such systems, its calculation requires the use of the dynamical mean field theory (DMFT) corrections on top of the DFT for the strongly correlated $4f$ orbitals.

Given the high computational expense of DMFT corrections in a heterostructure set-up, *appropriate* construction of the initial structure is very important given that the DFT and DMFT predicted lattice constants can vary by up to ~ 0.5 Å. The initial zero pressure structure for calculating transmission through an SmS or SmSe thin film is constructed to be as close to the *expected* DMFT structure as possible. Also, since the compression of the PR film in a PET is uniaxial, resultant expansions along other two planes have to be accounted for along with an optimal lead-film interface distance in the heterostructure. A large part of this chapter is dedicated to the technicalities of this process and explanation of the logical steps followed to attain it.

With the optimised structures we then calculate the transmission through the W/SmSe/W heterostructure. We confirm that as with bulk, even in a thin-film set-up, an inclusion of the strong correlations of the $4f$ orbitals at the appropriate level using Dynamical mean field theory is crucial in determining their contribution to transmission which is related to the calculation of current through the PR junction. We show that for the unstrained system of SmSe as a prospective piezoresistive film, the behaviour $4f$-electron peaks as reflected in the density of states of the film layers around the Fermi level and associated changes with thickness can be used to define the OFF states for memory and transistor operation in a Piezoelectric transistor as mentioned in tab.(5.6). However, memory operation also requires a hysteretic change which is shown by SmS

and not SmSe, but we expect similar order in scaling for SmS.

Operation type	Approximated OFF Scale (nm)
Memory	$2 \lesssim d_l \lesssim 6$
Transistor	$d_l \gtrsim 6$

Table 5.6: Predicted junction length scales (d_l) for OFF-state PR functionality corresponding to memory and transistor operations for SmSe.

The structures calibrated corresponding to the high-pressure phases need to be simulated next to quantify a reliable ON/OFF ratio. The map for that work is discussed in the next section.

5.7 Future plan of action

- To predict what thickness of the PR film will be experimentally required for device operations for technologies suggested in tab.(5.1), a similar study has to be done for different pressures calibrated with thin film structural parameters as per 5.4.3 and fig.(5.13). This will define the ON states. For low voltage bias, the ratio of the resistance between the strained (high pressure) and unstrained (zero pressure) PR films will be inversely proportional to their transmission at the Fermi level as,

$$\frac{R_{\text{strained}}}{R_{\text{unstrained}}} = \frac{T_{\text{unstrained}}(E_F)}{T_{\text{strained}}(E_F)} \tag{5.4}$$

  One could plot the above ratio as a function of volume stress or pressure, and predict operational ON/OFF length scales to conclude device operation regimes mentioned in tab.(5.1).

- A similar work can be done for SmS. The behaviour of the transmission around the Fermi level and the associated density of states could be studied with the increasing and decreasing compression corresponding to increasing and decreasing pressure each associated with a many-body self-energy that is fed to the next pressure value to infer why SmS shows a hysteretic change in resistance whereas SmSe shows a reversible change.

- Although $4f$ orbitals are atomic like such that their hybridisation with other energy levels can be ignored, it is still a strong assumption. The coherent transmission is expected to change depending on the impact of the hybridisation term. Thus using an impurity solver that includes the effect of hybridisation is another direction of work that can be regarded to paint a better picture of the impact of strong correlations in this phenomena.

Chapter 6

Disorder and defects in rare-earth metal oxide structures

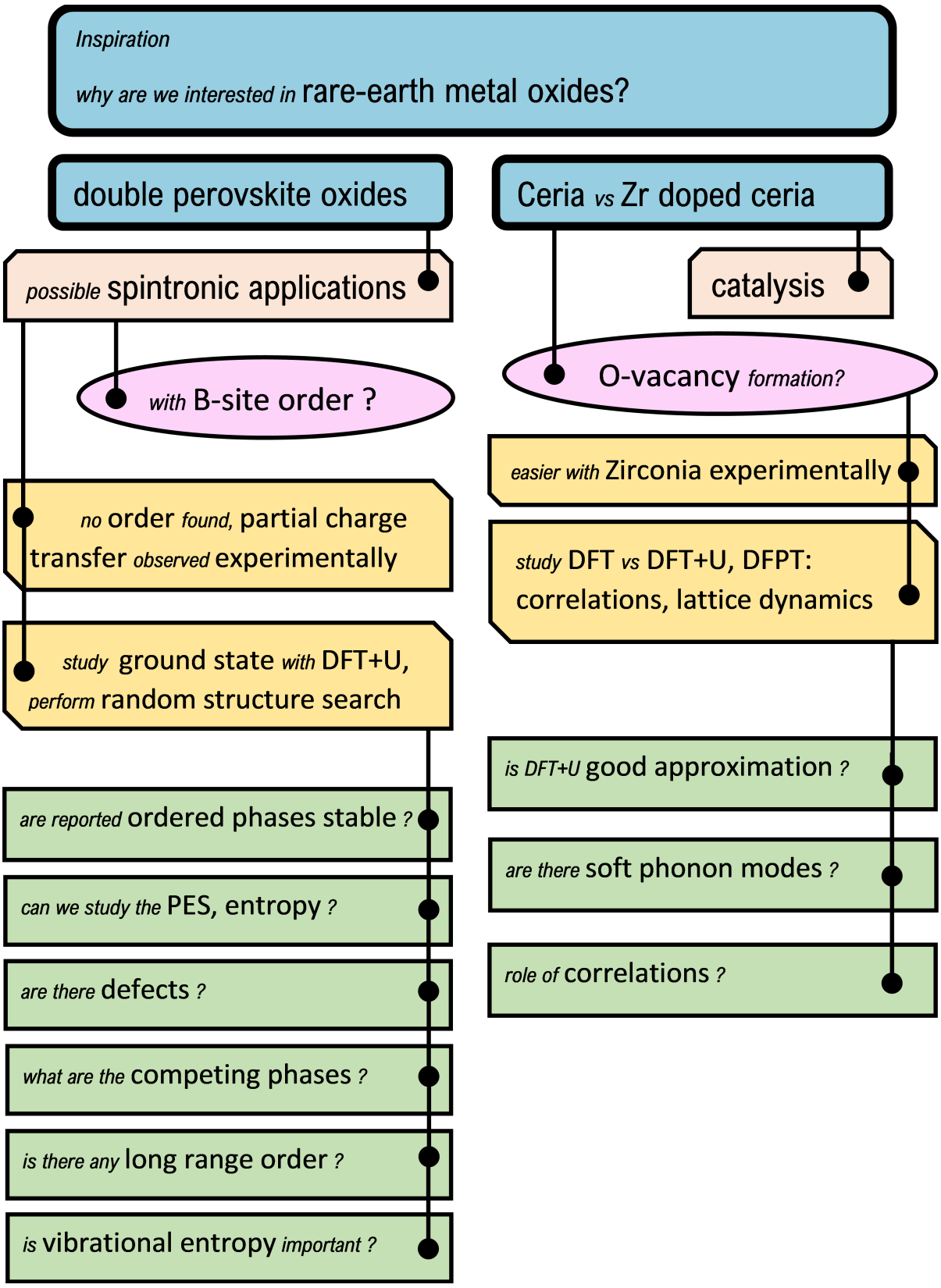


Figure 6.1: Chapter objectives and keyword map: highlighting the main questions asked, topics addressed and keywords used.

6.1 Introduction

In this chapter we will study structural properties of two different sets of rare-earth transition metal oxides each relevant for a specific industrial application. In the first part of this chapter we will employ a first-principle structure search method for double perovskite oxides which can have possible spintronic application and will analyse the role of disorder in determining the observed cationic order. In the second part we will study doped ceria where lattice dynamics impacts the facilitation of oxygen vacancies which is responsible for their popular use as heterogeneous catalyst.

6.1.1 Disorder in Double perovskite oxides

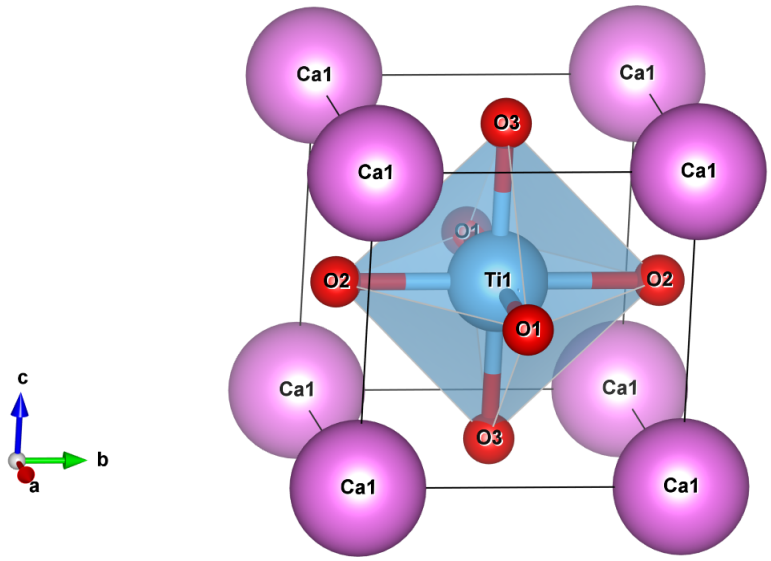


Figure 6.2: The prototypical perovskite structure of $CaTiO_3$ (ABX_3) [264].

Perovskites are a class of materials with a general formula of ABX_3 where A and B are cations of different sizes and X is an anion which binds to both A and B [265]. The B-site cation, usually a transition metal, has a six-fold coordination of six corner-sharing anions, often oxygen, forming an octahedron as shown in fig.(6.2). The A cation, usually an alkaline-earth or a rare-earth material, has a 12-fold coordination of 12 anions. An interesting aspect of these materials is that structural distortions like various octahedral distortions or tilting along with the prevalence of $d-$ or even $f-$orbital physics leads to these materials exhibiting a plethora of interesting properties like ionic conductivity, high-T_c superconductivity, magnetoresistance, ferroelectricity and ferromagnetism [266].

Double perovskites, as the name suggests, have double the formula unit of perovskites with one of the B-cationic sites replaced by B′ making its general formula

$A_2BB'O_6$, as seen in fig.(6.3). Usually two different transition metal cations constitute the B and the B′ sites, with sometimes even the A-site hosting different cations. Possibile multiple combinations, structural distortions, defects, along with having the $d-$ or $f-$shells gives a larger playing ground to double perovskites in terms of their magnetic and transport properties tunable for various applications [267], [268]. A a result, they also serve as testing grounds for role of various levels of theories of electronic correlations that can be compared with experiments.

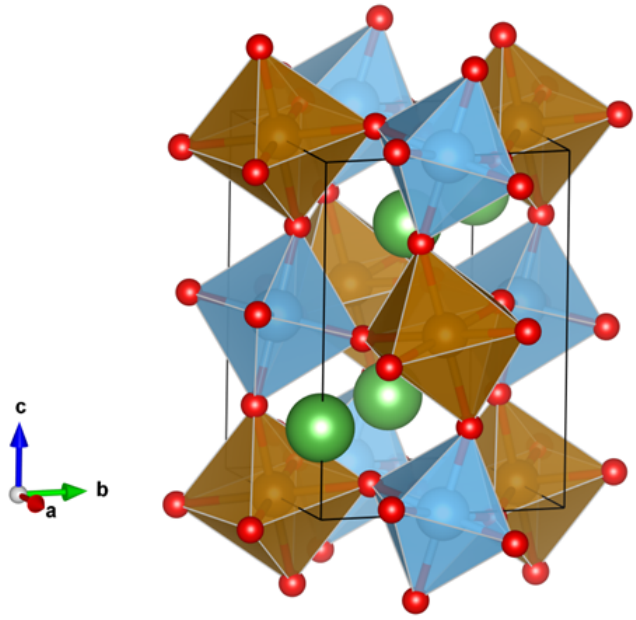


Figure 6.3: The rock-salt phase of La_2TiFeO_6, a double-perovskite comprising of two formula units. The atoms are identified by colours as - La:green, Ti:blue, Fe:brown, and O:red. The above structure corresponds to the charge-transfer type ground state with $a^-b^-c^+$ octahedral rotations with Ti, Fe in 4+, 2+ states, respectively.

Charge transfer (CT) between the B-site cations in complex oxide heterostructures can result in different oxidation states for the B-site cations as compared to the respective complex bulk oxides containing B, B′ cations individually [268]. This can lead to a greater diversity in emergent properties if one can create conditions in the laboratory where this charge transfer (CT) process can be controlled reversibly by pressure or temperature or polarisation of various sample planes. We study two double perovskites comprising of two different 3d-transition elements at the B and B′ sites , namely, La_2TiFeO_6 (LTFO) and La_2VCuO_6 (LVCO) where CT can be expected between $Fe^{3+}/Ti^{3+} \rightarrow Fe^{2+}/Ti^{4+}$ and $Cu^{2+}/V^{4+} \rightarrow Cu^{+}/V^{5+}$, respectively.

Following the prospect of a tunable CT based device, a previous work by Lupo, Sheridan *et al* [269] studied $LaTiO_3/LaFeO_3$ heterostructures strained on $SrTiO_3$ and $LaAlO_3(100)$ substrates using DFT+U. They found that CT between Fe and Ti can be observed as a function of a uniaxial strain. Also, the polarisation of the LaO plane could be changed as a function of the nominal charge on TiO_2 and FeO_2 planes. This

associates to this CT a tunable ferroelectric behaviour, thus promising potential spintronic applications. Another work [270] reported that La_2VCuO_6 is a half-metal in the Cu^{2+}/V^{4+} states whereas in the Cu^{+}/V^{5+} state it is an insulator. This inspires one to question whether a metal-insulator transition can be induced in these materials as a function of the charge transfer.

However neither of these double perovskites have been realised experimentally in their respective B-site ordered form. In general for double perovskites, the B-site ordering plays an important role in determining properties of the concerned material. An example is La_2MnNiO_6 which is ferromagnetic when the B-site elements (Mn, Ni) are rock-salt ordered but becomes antiferromagnetic when they are randomly distributed [271]. Thus controlling the B-site ordering and a detailed understanding of the concerned mechanism is crucial for synthesising samples with desirable properties. However a spontaneous ordering corresponding to a desired property is notoriously difficult to obtain. This is primarily why in spite of the literature predicting novel combinations of $A_2BB'O_6$, only a few have been realised experimentally, and those double perovskites usually differ substantially in cation valence or size. Given the promising study by by Lupo, Sheridan *et al* [269] on controlling the LTFO charge transfer with pressure, our first goal is to experimentally obtain stable perovskite phases for both LTFO and LVCO.

6.2 Experimental observations

LTFO and LVCO crystals were grown on STO (001) and STO (111) substrates using Puled Laser Deposition (PLD), and then their phases were studied using ray diffraction (XRD). Although the films were perovskites, neither planar nor rock-salt ordering of B-site cations was found by XRD scans along different planes. Then using X-ray Photoemission spectroscopy (XPS) the oxidation states of Fe and Ti were examined. The experimental workflow is presented in fig.(6.4). It showed Ti atoms to be entirely in 4+ states whereas Fe ions were only partly in 2+ states i.e., only a partial charge transfer had occurred.

Although the experiments performed fall short of an exhaustive growth study and more growth parameters need to be investigated to draw confident conclusions on the possibility of obtaining order in double perovskites, they necessitate further study of the observed B-site disorder by using high-fidelity ab-initio theoretical modelling which forms the basis of this section. Give that our aim is to study material growth during which various structures are likely to compete, merely searching and studying the ground state isn't enough, and an extensive exploration of the entire energy landscape is needed.

Aim:
Obtain a stable perovskite phase and use strain to change B-site order

Synthesis:
1. Grown La_2TiFeO_6 (LTFO) and La_2VCuO_6 (LVCO) on $SrTiO_3$ (001) and $SrTiO_3$ (111) substrates using Puled Laser Deposition (PLD).
2. Ensured layer-by-layer growth during deposition using Reflection High-Energy Electron Diffraction (RHEED).

Analysis:
1. Studied the crystalline structure of grown films using X-ray diffraction (XRD) and found:
(i) LTFO, LVCO have single perovskite phase
(ii) No rock-salt or planar ordering of B-site cations
2. Lattice parameters obtained by Reciprocal space mapping shows tetragonal symmetry with:

Material	a (Å)	b (Å)	c (Å)
LTFO	3.91	3.91	4.01
LVCO	3.91	3.91	3.97

Table 6.1: Experimentally obtained lattice parameters for LTFO and LVCO using XPS

3. High quality of the film is confirmed by studying surface morphology using Atomic Force Microscopy (AFM).
4. High structure quality confirmed again and no B-site order found using Scanning Transmission Electron Microscopy (STEM).
5. Oxidation states of Fe, Ti in LTFO studied using X-ray Photoemission spectroscopy (XPS) and observes:
(i) Fe: partly in 2+
(ii) Ti: Fully in 4+
$\longrightarrow$ CT observed with complete oxidation of Ti but only partial reduction of Fe.

Result and outlook:
1. No B-site order found. 2. Partial charge transfer occurs.
Possible explanations: over-oxidation during/post-growth, La-vacancies

Figure 6.4: Summary of experimental workflow and methods used to synthesise and study of La_2TiFeO_6 (LTFO) and La_2VCuO_6 (LVCO) aimed at controlling the B-site charge transfer and ordering by varying internal pressure. See tab.(I) for further details.

6.3 Ordered phases

Following the experimental work, our aim is different now and is to understand why we observe a B-site disorder in these materials. Understanding the origins of the observed disorder could potentially suggest ways to search more exhaustively for the desirable ordered phases. And to effectuate that, we first take a detailed look into the ordered phases as reported in the literature.

As per the theoretical work done in the literature before using DFT+U [269], LTFO is characterised by a charge transfer ground state with Fe^{2+} and Ti^{4+} oxidation states different from its individual constituents $LaFeO_3$ and $LaTiO_3$ with Fe^{3+} and Ti^{3+} oxidation states respectively. The CT-type and non CT-type ground states could be obtained as a function of strain with same $a^-b^-c^+$ octahedral rotations. For LVCO, the individual components $LaVO_3$ and $LaCuO_3$ could not be stabilised in V^{3+} and Cu^{3+} oxidation states, respectively. But charge transfer led to a stable ground state with G-type layered rock-salt and planar orders with Cu^{2+} and V^{4+} oxidation states. Transfer of an additional electron leads to a non-magnetic (NM) state with Cu$-d^{10}$ and Vd^0. Both states are insulators where on application of octahedral rotations, the gaps are suppressed. This finding is in contrast with another work [270] with DFT+U that finds LVCO in Cu^{2+} and V^{4+} order to be a half-metal for certain choices of U.

As the first step of investigation, the ordered phases of LTFO and LVCO were modelled as bulk, grown on $SrTiO_3$ (100) and $LaAlO_3$ (100) using DFT+U as implemented in Quantum Espresso 6.5 with U(Fe)=4.8 eV, U(Ti)=3 eV, U(V)=4 eV, and U(Cu)=8 eV. Plane wave basis with energy cut-off of 800 eV, a k-mesh of 4×4×3 and energy and force tolerance of 0.1 meV and 1.0 meV/Årespectively we used. Ultrasoft pseudopotentials were used with valence configurations La ($4f$, $5s$, $5p$, $5d$, $6s$, $6p$), Ti ($3s$, $3p$, $4s$, $3d$), Fe ($3s$, $3p$, $3d$, $4s$, $4p$), V ($3s$, $3p$, $4s$, $3d$), Cu ($3s$, $3p$, $3d$, $4s$, $4p$), and O ($2s$, $2p$). To model the materials grown on a substrate, the lattice vectors were constrained matching the particular substrate plane. Relaxations were allowed in the direction of the growth, and internal coordinates were free to relax as well. The initial internal atomic positions were taken for the bulk with G-type initial magnetic orientations for both the rock-salt and layered phases. The energy per formula unit was calculated for all the combinations of substrate dependent strain and phases.

Results

La_2VCuO_6:

- Rock-salt and layered G-type phases compete within 10 meV for all the values of strain, as seen in fig.(6.5). This difference from LTFO can be attributed to the observation that the octahedra sizes for LVCO do not differ much between the rock-salt and layered phases as compared to LTFO, as seen in table.(6.2).

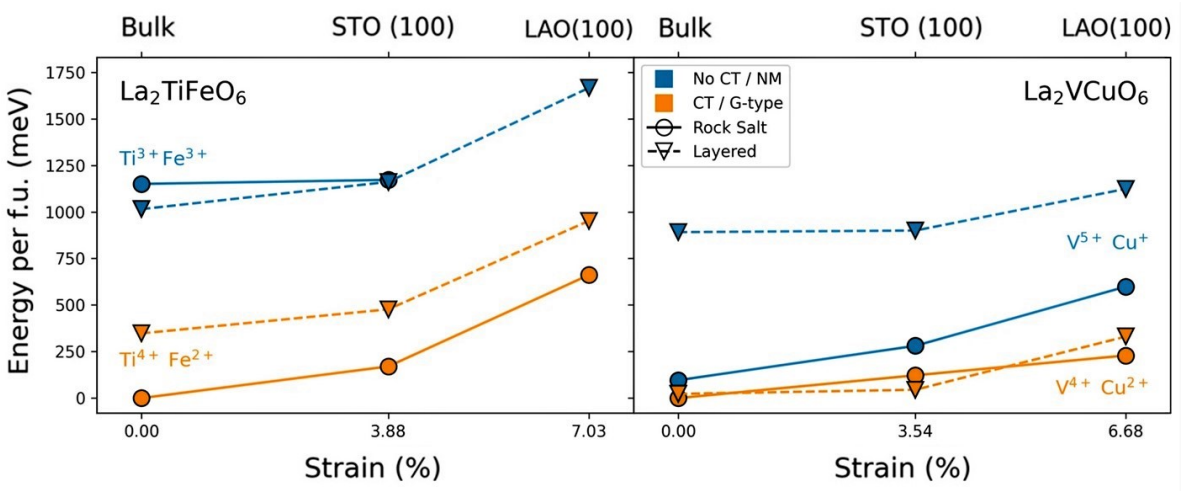


Figure 6.5: Energy difference per formula unit (f.u.) of the ground state of the rock-salt and layered phases plotted as a function of strain in bulk (zero strain), strained on $SrTiO_3$ (100) and on $LaAlO_3$ (100), respectively. For La_2TiFeO_6, the charge transfer phases correspond to Ti^{4+} and Fe^{2+}, and the non-charge transfer phases stand for Ti^{3+} and Fe^{3+} oxidation states. For La_2VCuO_6, the charge transfer phases with oxidation states V^{4+} and Cu^{2+} refer to the G-type magnetic states whereas V^{5+} and Cu^{+} refer to the non-magnetic non-charge transfer phases. (reprinted from coauthored citation [272])

Phase	d(Fe-O) (Å)	d(Ti-O) (Å)
RS-CT	2.11-2.22	1.98-2.01
RS-No CT	2.05-2.10	2.04-2.13
L-CT	2.04-2.26	1.93-2.07
L-No CT	2.05-2.08	2.02-2.13

Phase	d(Cu-O) (Å)	d(V-O) (Å)
RS-CT	2.00-2.32	1.85-2.06
RS-No CT	2.12-2.38	1.89-1.91
L-CT	2.01-2.37	1.85-2.05
L-No CT	2.02-2.42	1.82-2.02

Table 6.2: Bond distance ranges for La_2TiFeO_6 and La_2VCuO_6 for charge transfer (CT) and non charge transfer (No CT) states each for the rock-salt (RS) and layered (L) type B-site ordering. The ranges include the zero strain bulk structures and those strained on STO (100) and LAO (100) as shown in fig.(6.5)

- Gap between CT (G-type) and non-CT (NM) type phases increases as strain increases for the rock-salt structure whereas for the layered structure this gap is always $\sim$ 800 meV. This might arise because the non CT type Cu^{+} ionic radii is larger than that of $V^{5}+$ by 0.25 Å as compared to the difference in ionic radii of CT type Cu^{2+} and V^{4+}. This can lead to an increased strain on the Cu and V octahedra for the non CT layered structure making it energetically unfavourable.

- **Conclusion:** The observed competition between the rock-salt and layered CT type phases justifies the experimentally observed disorder in LVCO.

La_2TiFeO_6:

- Rock salt phase after charge transfer is the most stable phase for all strains. No competition with any other phase is noted at the level of DFT+U, contrary to

experimental observations.

- The Fe and Ti ionic radii are comparable in size. Thus a study of ionic radii alone cannot explain the observed stability of the rock-salt phase.

- **Conclusion:** Study of the ground state structure for LTFO is not sufficient to understand the observed disorder. More phases should be studied to understand the disordered growth. Effect of defects by over-oxygenation and by La-vacancies need to be considered for the disorder.

6.4 Disordered phases

As inferred above, studying more such phases which are relevant during experimentally observed disordered growth translates to theoretical studies as computationally searching for low lying energy minima in the available configurational space. Now as discussed in 2.14, one cannot study the entire configurational space practically due to its sheer size, so one has to find ways to restrictively select the phase space in order to make the problem more palatable. There are various ways to do that and arrive at thermodynamically stable configurations using DFT to optimize a particular structure energetically among a great many others to be of any statistical relevance. We focus on two particular techniques below.

- A class of structures can evolve if one selects a few relevant criteria and then either favours or penalises structures as they evolve energetically based on those. In this approach the initial choice of relevant properties are crucial to the phases determined, and future phases depend on the past history of chosen phases. Oganov-Glass algorithm [273], particle swarm optimisation by Wang *et al.* [274] are popular methods in this group.

- Structures can be randomly generated with some chemically intuitive constraints to limit the size of configurational space and then be optimised by electronic structure methods like DFT. Here the generated structures are independent of each other and hence can evolve in parallel and go beyond selective characterisation of the low-lying energy landscape. This is called Random Structural sampling (RSS) method. Within the applied constraints, RSS can map even the entire energy landscape. Although it comes with substantial computational cost, given the mere number of structures that can be sampled and analysed parallelly and the span of the phase space that can be sampled, it enables the calculation thermodynamically relevant quantities like configurational entropy. Due to this reason along with the development of some excellent DFT codes and with the rapid development of high performance computing in the past two decades, these codes

are being widely used. Some popular codes in this category include *ab-initio* Random Structure Search (AIRSS) [154], [155], USPEX [275], [276] and CALYPSO [277].

Computational details

Given our results from the study of the ordered phases, it is necessary for us to explore phases which might be missed by structural optimisation of select cells, and thus we decided to use AIRSS in this work interfaced with Quantum Espresso.

The random structure search using AIRSS was performed at zero pressure with a target volume within 20% of 125 $Å^3$, the experimentally observed volume of the thin films grown on STO(100) surfaces. A compact cell was preferred by forcing a Niggli reduction of the unit cell wherever possible for choosing more efficient grids for Brillouin zone integrations. The distance constraints were so chosen that a loss of 20% of the ordered $LaFeO_3$ interatomic distances could be allowed. The associated DFT runs had an energy cut-off of 500 eV on a grid of $2\pi \times 0.1$ Å. Pseudopotentials and Hubbard U values were same as used in the study of ordered phases. The final structures were further relaxed with higher levels of accuracy. The structure search was performed for La_1TiFeO_6, $La_{1.5}TiFeO_6$ and $La_1TiFeO_{6.5}$ by sampling them separately with random space groups and 2-4 symmetry operations with initial magnetic moments of Ti and Fe ions being randomly generated. $La_{1.5}TiFeO_6$ and $La_1TiFeO_{6.5}$ were chosen to study the role of La-vacancies and over-oxygenation, as inspired by the discussion before and will be analysed in further detail in the following part. A total of 400 random structures were obtained respecting the relevant chemistry as described above and as expected for double perovskites.

Our attempt is to understand the competition between different microstates in the observed disordered phase by trying to understand the role of configurational entropy. To do this, we first sample the randomly generated and then optimised structures and calculate the frequency of occurrence of different structures corresponding to different phases within an energy window, as was discussed in 2.14.1. Following that we calculate the Entropy forming ability (EFA) of the respective phases, as was discussed in 2.14.2.

6.4.1 Relative frequency of occurrence

After having performed the random sampling search, we can now count how many times a particular phase of LTFO occurs. As discussed in 2.14.1, we can relate this frequency of occurrence, f_i, to the probability of occurrence of a state related via the volume of basins of attraction of the associated local minima. This can tell us if a particular phase is more or less accessible than another and gives us a comparison between the associated configurational entropies.

To do that we choose a window of 400 meV above the AIRSS predicted ground state and identify the local minima in that energy window. We identify five minima each

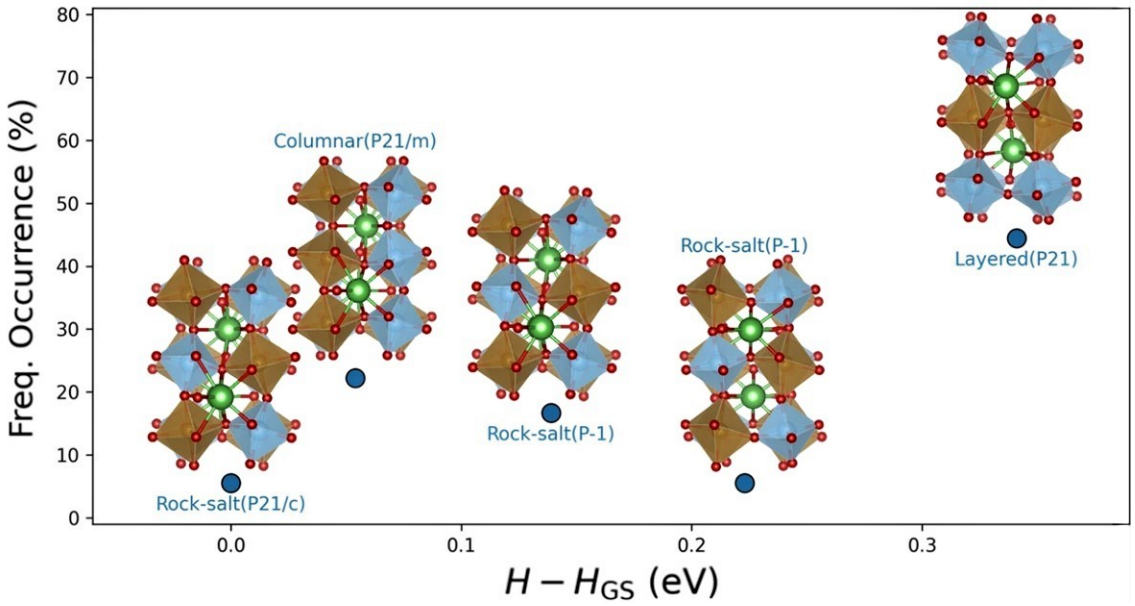


Figure 6.6: Frequency of occurrence plotted as a function of the energy (H, enthalpy at zero pressure) difference within 400 meV of the ground state among all La_2TiFeO_6 double perovskite structures captured by AIRSS. The $P2_1/C$ rock-salt and the layered orders correspond to the ground state with the lowest frequency and the highest energy state with highest frequency. Along with three new B-site ordered structures, these low-lying competing phases are associated with higher configurational entropy and observed experimental disorder. The atoms are identified by colours- La:green, Ti:blue, Fe:brown, and O:red. (reprinted from coauthored citation [272])

associated with a B-site ordered perovskite. The rock-salt phase with symmetry $P2_1/C$ is the ground state. This supports the findings of 6.3. However, the layered structure which has the highest energy in this window has the maximum frequency of occurrence. In addition to these, three new phases which were not considered by our original ground state structural optimisation of 6.3 were found. The metastable configuration about $\sim$ 50 meV next to the ground state was a columnar ordered phase with the second largest frequency of occurrence in this window. The other two phases were distorted rock-salt phases with different $a^-b^-c^-$ octahedral rotations. Surprisingly the rock-salt phase occurred fewer number of times than the layered and the columnar phases. The observance of these phases account for the observed disorder at the B-site of LTFO.

Apart from the fact that multiple low-lying phases are observed in the randomly sampled structures, the frequency of occurrence of all the structures above the ground state within 400 meV are substantially higher. This associates all those structures to a larger basin of attraction with a bigger hypervolume in the phase space as described in fig.(2.11), fig.(2.12) and eq.(2.149) and eq.(2.150). Then as per eq.(2.151) could be connected to a higher probability of creating these phases in the aforementioned PLD growth process, and thus a higher configurational entropy and associated randomness or disorder. However we can only draw qualitative inferences from the frequency of occur-

rence because the number of sampled structures (400 in total, including structures with defects) is not enough to predict a confident quantitative description of configurational entropy. It is so because entropy being a quantity obtained by statistical averaging cannot be ideally estimated from the above sample size and associated frequency of occurrences for each phase. This calls for additional scrutiny of the inference drawn.

6.4.2 Entropy Forming Ability (EFA) and the role of defects

To solidify the pictures obtained above by studying the frequency of occurrence, we further investigate the system by calculating its entropy forming ability (EFA) as discussed in 2.14.2. It studies the spectrum of accessible quasi-degenerate configurations to capture the predisposition of a material to form high-entropy single-phase crystals and is another way to quantify configurational entropy or randomness. Typically EFA values are calculated for a particular material and is used as a characteristic of the material to estimate its predisposition to disorder as compared to another material. Although we use the logic behind eq.(2.155) and eq.(2.157) but our use of and way to calculate EFA is slightly different.

We calculate our EFA values as a continuous function over the entire observed spectrum as occupied by all the 400 structures optimised with AIRSS. This way of defining the EFA leads to its interpretation as a measure of expected entropy and disorder within the spectrum. The benefit of doing this is that now we can study the change of EFA with respect to enthalpy for a single material exhibiting disorder and compare its various phases corresponding to different orders and their respective structures for different experimental conditions and potentially infer an insight into possible ways one could use to stabilise the ordered phase.

$$\text{EFA} \quad = \quad \{\sigma[\text{spectrum}(H_i)]_{T=0K}\}^{-1} \tag{6.1}$$

$$\sigma(\{H_i\}, H_{ref}) \quad = \quad \sqrt{\frac{\sum_{i=1}^{n} g_i \left(H_i - H_{ref}\right)}{\left(\sum_{i=1}^{n} g_i\right) - 1}} \;, \text{ where} \tag{6.2}$$

H_i and g_i are the enthalpy and degeneracy of the collected data points each representing one of the AIRSS converged structures. H_{ref} is reference energy, usually taken to be the ground state energy H_0.

Our aim is to understand the experimental observations as discussed in 6.2 and fig.(6.4) and one inference is to study the potential effect of defects that can emerge in a realistic growth processes. The PLD growth occurs in oxygen-rich conditions and therefore, we consider the effect of 8% overoxidation in $La_2TiFeO_{6.5}$ by adding an O-

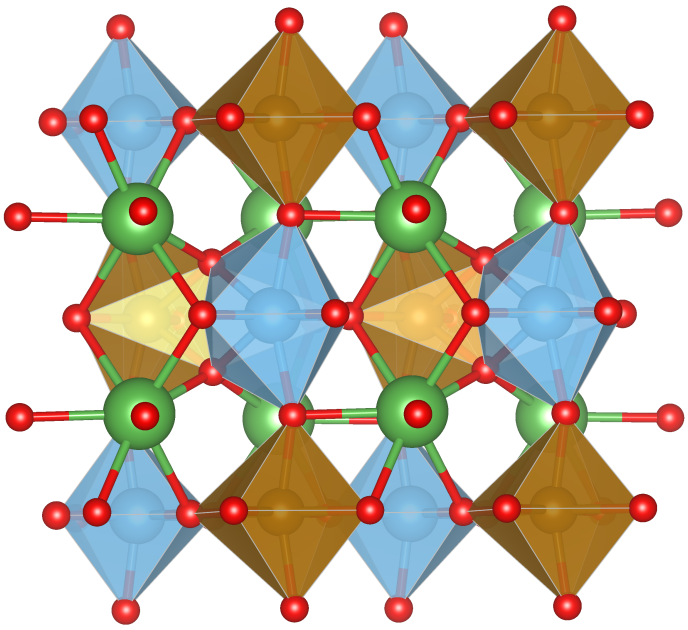


Figure 6.7: An AIRSS optimised configuration of $La_2TiFeO_{6.5}$ with an extra O-atom between two edge sharing B-site octahedra accounting for 8% overoxygenation representing the PLD growth in oxygen-rich conditions. The atoms are identified by their colours- La:green, Ti:blue, Fe:brown, and O:red. (reprinted from coauthored citation [272])

atom to the existing LTFO unit cell and running structure searches for a 21-atom unit cell and 13 O-atoms, as shown in fig.(6.7). Also, post-growth the samples are cooled down after being deposited on a hot substrate motivating us to consider the effect of 25% La-vacancies by removing one of the four La-atoms and running AIRSS with a 19-atom unit cell for $La_{1.5}TiFeO_6$.

Since we will be comparing a system with no defect with two systems with different kind of defects, it is crucial that we consider the effect of defect formation energies. This will be relevant especially for eq.(6.2) because we are comparing configurations with different number of atoms, and thus have to account for the resultant energetic difference. The formation energy of a defect is defined as the difference between the energy of the system concerned and its components in their reference states. Since we are removing or adding a whole atom, our unit cell is still charge neutral, and thus we consider our defects to be charge neutral as well.

We follow the definition of defect formation energy, ΔH_f, from [278]. H_{def} and H_0 are the total energies of the same relaxed supercells with and without the defect, respectively. H_x is the elemental reference energy of the defect i.e., the energy of the defect element in its standard state which can be, say, a pure metal, irrespective of the material it is a part of in the supercell. For La the reference state was La-metal and for O it was the triplet O molecule i.e., ${}^3O_2$ in a supercell. μ_x is the x^{th} defect element's chemical potential which has to be experimentally determined based on physical factors

like partial pressure of constituents, their temperature, etc., and is not a unique choice.

$$\Delta H_f = H_{def} - H_0 \pm \sum_x n_x(H_x - \mu_x) \ , \text{ where} \tag{6.3}$$

Note that following above eq.(6.3), we replace H_{ref} in eq.(6.2) by $H_0 + \Delta H_f$. In absence of any defects $\Delta H_f = 0$, this value becomes H_0, as expected. This makes the EFA value highly dependent on μ_x whose choice in turn is dependent on experimental conditions. In Pulsed Laser Deposition of thin films, different chemical potential (μ_x) regimes are scanned depending on the physical conditions.

Since $LaFeO_3$ is one of the building blocks of our original material La_2TiFeO_6, we follow the work of Taylor *et al.* [279] which studies the formation of $LaFeO_3$ from its constituents. We consider the μ_x ranges between two extreme regimes where $LaFeO_3$ is stable and its formation is preferred with respect to other competing phases made of La, Fe and O like La_2O_3, metallic Fe. This reference for μ is used because the conditions for La-vacant and O-rich phases are similar for both the experimental set-ups.

- Extreme 1: The major competing phases are La_2O_3 and $LaFeO_3$ and represents lanthanum poor and oxygen rich conditions.

Condition	Chemical potential (eV)
$\mu_{La-poor}$	-8.89
μ_{O-rich}	0.00

Table 6.3: Estimated chemical potential bounds obtained from reference $LaFeO_3$ formation [279] in La-poor and O-rich conditions.

- Extreme 2: The major competing phases are La_2O_3 and Fe metal and represents lanthanum rich and oxygen poor conditions with

Condition	Chemical potential (eV)
$\mu_{La-rich}$	-3.09
μ_{O-poor}	-3.87

Table 6.4: Estimated chemical potential bounds obtained from reference $LaFeO_3$ formation [279] in La-rich and O-poor conditions.

Since the growth happens in oxygen-rich conditions covering the oxygen-rich to oxygen-poor conditions account for the experimental conditions where varying oxygen partial pressure affects the material and defect formation.

We observe that the values of the EFA depend heavily on μ_{La} and μ_O. The values have a tendency of becoming higher as we approach La-poor and O-rich phases and reach values ~ 1.3 eV^{-1} around the energy window of $\sim 1.2-1.4$ eV. In these situations the formation of defects can be considered to be more favourable. By inspecting regions

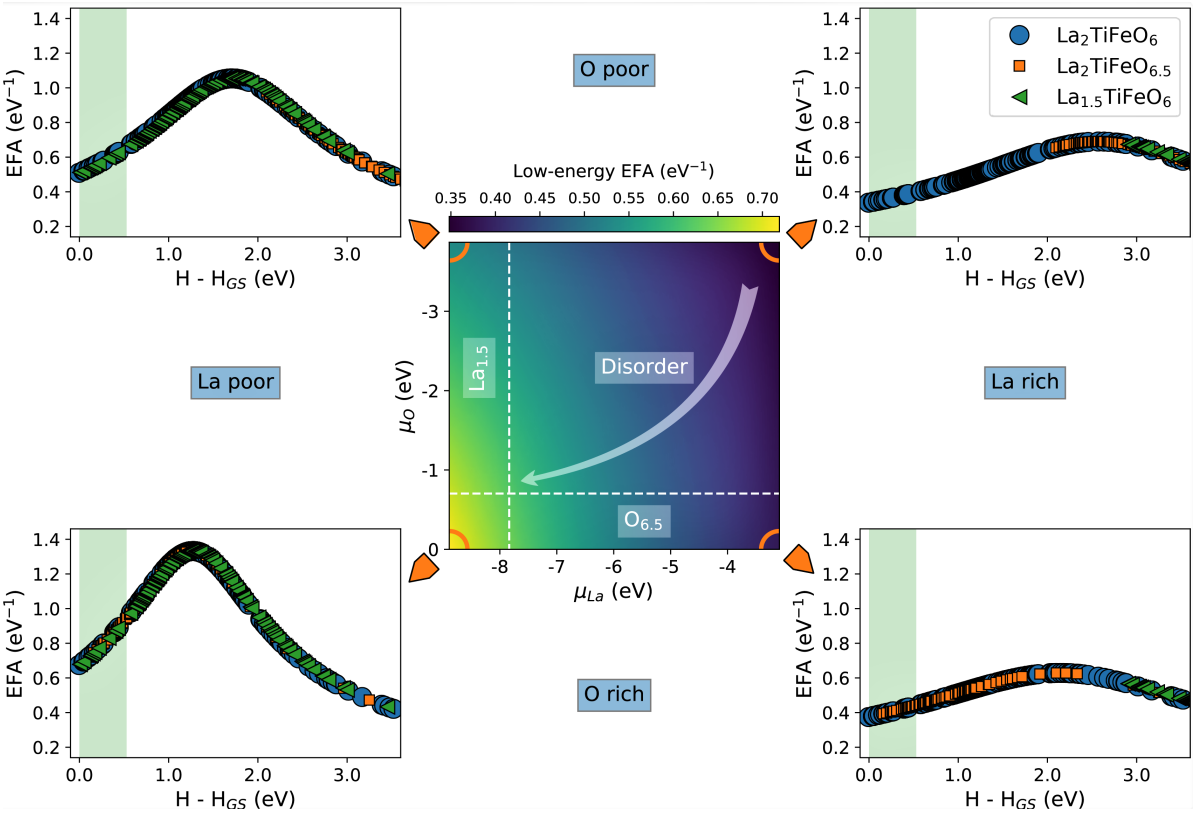


Figure 6.8: (*Central panel*) Entropy Forming Ability (EFA) computed within the energy window of 0-400 meV for La_2TiFeO_6 depicted by the colour gradient proportional to the EFA values. The EFA is explicitly dependent on the defect chemical potential via the defect formation energies. The dashed white lines denote the value of the chemical potential where the defects emerge and accentuate the disorder. (*Corner panels*) The change of EFA with energy for four combinations of defect chemical potentials. The green shaded region corresponds to the energy window of 0-400 eV where the low-lying competing structures are observed. (reprinted from coauthored citation [272])

at four extreme limits of the chemical potential, we observe that the disorder becomes maximum between 1-2.5 eV among all four cases. This is the energy window where disorder will play a crucial role and obtaining ordered phases will be difficult as it corresponds to highest number of minima obtained in the PES. As the energy becomes higher, the number of states increase but energetically are more divergent from each other which leads to a reduction of the EFA value.

If we now zoom into between 0-400 meV i.e., the window where we found the five low lying ordered phases of fig.(6.8) corresponding to the green shaded region if fig(6.8), we find that for all chosen windows of scrutiny, the EFA value increases almost monotonically as a function of energy. This rate of increase is much steeper in the La-poor and O-rich conditions corresponding to growth conditions in presence of La-vacancy and over-oxygenation which increases the tendency of disorder. This implies that in crystals grown under these experimental conditions several low-lying microstates will compete and thus the entropy will be larger which can be a factor behind increasing

the disorder.

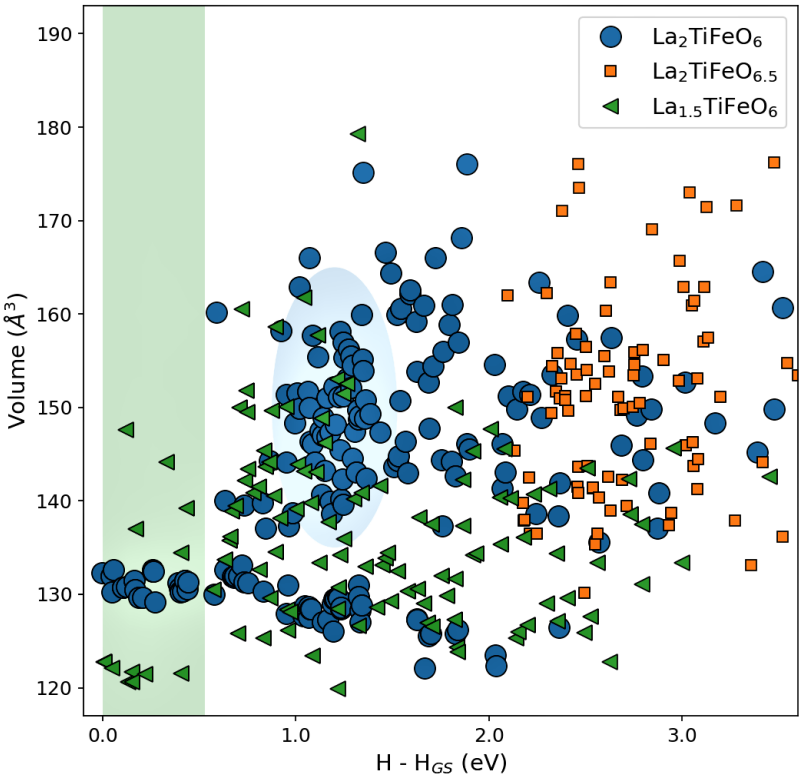


Figure 6.9: Volume distribution of AIRSS optimised structures for $La_{1.5}TiFeO_6$, $La_2TiFeO_{6.5}$ and La_2TiFeO_6 in La-poor and O-poor conditions. The green shaded region corresponds to the energy window of 0-400 eV. The blue shaded region between $\sim 1 - 1.5$ eV corresponds to the expanse with highest concentration of minima responsible for the incoming EFA peak at ~ 1.1 eV in the upper left corner panel of fig.(6.8). (reprinted from coauthored citation [272])

Fig.(6.9) depicts the volume distribution of minima each for $La_{1.5}TiFeO_6$, $La_2TiFeO_{6.5}$ and La_2TiFeO_6 in La-poor and O-poor conditions. If we observe the energy window where we found the five ordered double perovskite phases of La_2TiFeO_6 i.e., between 0-400 meV, the volumes are around 130 $Å^3$. This matches well with the volume of the films grown on $SrTiO_3$ (100) surfaces which are around 125 $Å^3$. This agreement validates our AIRSS predictions.

The disordered phases, as expected, have a broader distribution. We can observe from fig.(6.9) that for $La_2TiFeO_{6.5}$, the presence of the extra oxygen makes this structure energetically unfavourable when compared to $La_{1.5}TiFeO_6$ and La_2TiFeO_6. On the other hand, $La_{1.5}TiFeO_6$ with 25% of La removed has competing phases with La_2TiFeO_6.

We also observe from fig.(6.8) that as μ_{La} increases from -8.89 eV to -3.09 eV i.e., as we go from La-poor to La-rich conditions the EFA maximum decreases for both extremes of μ_O. The overall effect of μ_{La} is also more pronounced than that of μ_O. This is supported by the observation from fig.(6.9) where we see that the $La_{1.5}TiFeO_6$

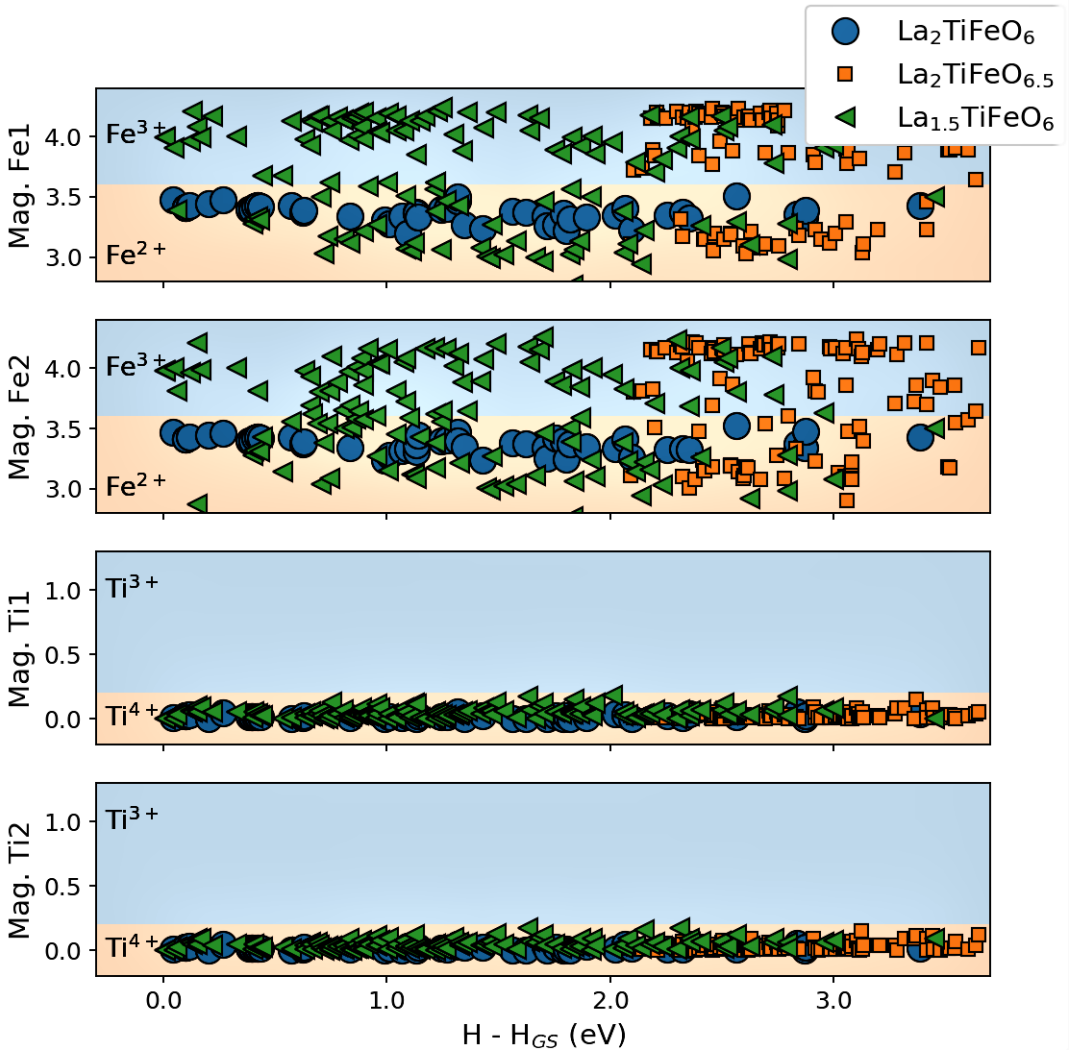


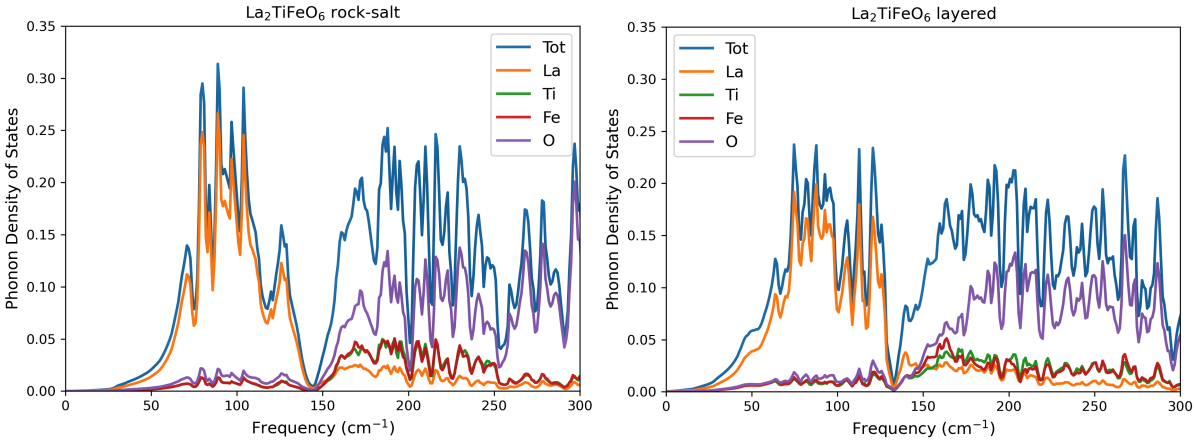
Figure 6.10: Distribution of magnetic moments of La_2TiFeO_6, $La_{1.5}TiFeO_6$ and $La_2TiFeO_{6.5}$ as function of energy. In La_2TiFeO_6, the charge transfer type Fe^{2+} and Ti^{4+} states are most favoured. Oxidised Fe^{3+} states emerge more when defects are included. (reprinted from coauthored citation [272])

minima have a wider spread over the spectrum than $La_2TiFeO_{6.5}$. These observations signify the role of La-vacancies as the more significant cause of the observed disorder when compared to over-oxygenation.

Since the disorder concerns the B-site cations, we also explore the distribution of final magnetic moments corresponding to minima for each of $La_{1.5}TiFeO_6$, $La_2TiFeO_{6.5}$ and La_2TiFeO_6. We observe from fig.(6.10) that the magnetic moments of both Ti atoms are always 0 for all minima of all three phases. This corresponds to the Ti^{4+} state which is what we observe from the XPS data. For La_2TiFeO_6, the magnetic moments of Fe are between 3 and 3.5 which correspond to the Fe^{2+} high-spin state post partial charge transfer. But both $La_{1.5}TiFeO_6$ and $La_2TiFeO_{6.5}$ show a distribution between Fe^{2+} and Fe^{3+} states. This observation with local intermixing of primarily La-vacant and also possible overoxidised structures validates the observed partial reduction of Fe.

Note again that EFA is an empirically defined quantity and serves as a qualitative measure of disorder. Although inferences drawn from both the frequency of occurrence and EFA signify the role of configurational entropy unequivocally, not being able to calculate it by going beyond this sample size due to the restrictive computational costs remains a limitation.

6.4.3 Vibrational entropy and long-range order



(a) (b)

Figure 6.11: Atom resolved phonon density of states obtained using DFPT for the La_2TiFeO_6 rock-salt and layered structures. (reprinted from coauthored citation [272])

So far our discussion has been within the confines of the configurational phase space. But as the configurational space becomes larger, an even larger 'phase space' is explored by the atomic constituents as they vibrate. This 'phase space' is spanned by the momentum coordinates of the system in addition to its position coordinates and describes the lattice vibrations which might have a contribution to the total entropy. Since in LTFO, disorder and defects are relevant, the contribution from vibrational entropy could be an important factor in describing the observed behaviour [280], [281].

However neither the frequency of occurrence nor the EFA formalism captures the role of vibrational entropy. This is because the description is based on a DFT+U dependent estimate of the ground state with Born-Oppenheimer (BO) approximation applied by 'freezing' the atoms. We know that atomic vibrations are also accentuated by temperature, and since the PLD deposition temperature of La_2TiFeO_6 is 730 °C, a correct description of high-temperature behaviour of this material could potentially be a substantial contributing factor to the picture we obtained so far.

So as a first step we analyse the Ph-DOS for the rock-salt and the layered structures of LTFO. For that we use Density Functional Perturbation Theory as implemented in Quantum Espresso with a self-consistency threshold of 1×10^{-14} eV. We observe in fig.(6.11) that the phonon dispersion is dominated by vibrational modes associated

with Lanthanum followed by Oxygen for both the rock-salt and the layered structures which are two competing low-energy ordered phases similar to each other in volume. We then proceed to study the vibrational entropy using the post-processing tool as available in thermo_pw driver [282] of Quantum Espresso within the quasi-harmonic approximation.

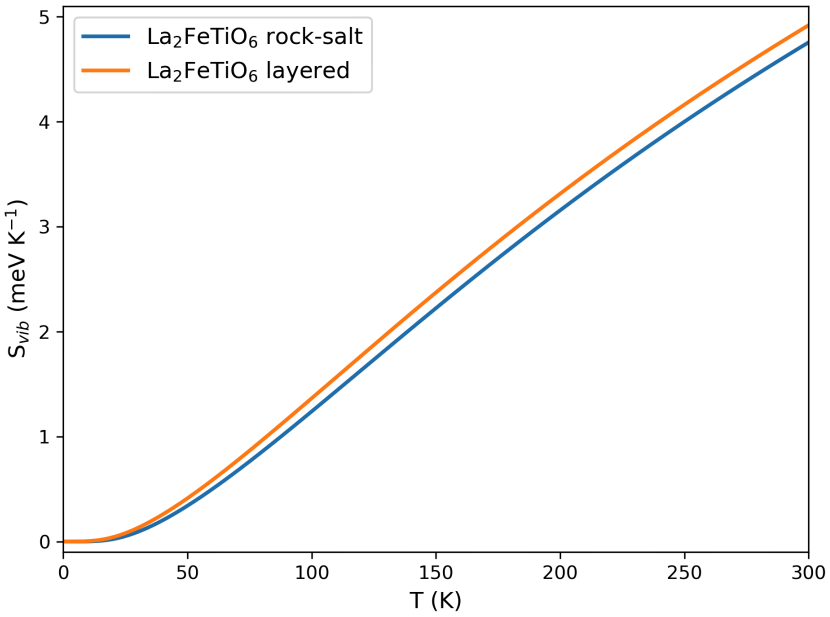


Figure 6.12: Evolution of vibrational entropy of La_2TiFeO_6 rock-salt and layered structures with temperature within the quasi-harmonic approximation. The entropies for both the structures are almost identical as the largest contribution arises from the La-cage as observed in fig.(6.11). (reprinted from coauthored citation [272])

The most common approximation to study phonons is called the Harmonic approximation (HA) that treats the bonds between atoms as springs obeying Hooke's law. This makes the Harmonic potential a quadratic function of atomic displacements. The electrons are considered to make the *interatomic glue*, and within the BO approximation, the nuclei is assumed to respond instantaneously to displacements. However assuming the spring constants as fixed implies that the observed atomic volumes are independent of temperature. Although this is a good approximation for lower temperatures where the vibrations are small and thus the quadratic nature of the potential is more accurate but as the temperature increases, not only the potential differs from its quadratic form but as more phonons populate the material, the chances of phonon-phonon interactions are also larger.

To rectify some of these shortcomings, we use the quasi-harmonic approximation (QHA) which still has non-interacting phonons but *softens* the atomic spring constants by having a harmonic potential as a function of temperature. This results in temperature induced changes in volume and phonon spectra. As a result of this *softening*, the equilibrium atomic positions grow further apart and the same lattice displacement as

the HA leads to lesser potential energy being stored in the springs. This results in a decrease in phonon frequencies with increasing volume, and consequently is reflected in the vibrational entropy.

Fig.(6.12) shows that the two vibrational entropies for the rock-salt and layered B-site ordering of LTFO are almost identical with their evolution with temperature. This can be attributed to the observation from fig.(6.11) that the largest contribution of vibrational modes arise from the Lanthanum cage in both the rock-salt and the layered structures. In spite of the absence of an exhaustive study of phonon dynamics for all possible configurations, given the importance of La-defects, as discussed before, and the relevance of the La-cage in the phonon spectra, we can qualitatively infer that when we compare competing phases to study the emergence of disorder, the role of configurational entropy, as discussed in 2.14.2, is the not the dominating factor.

In addition to this, we also searched for any possible long-range order phenomena. For that we constructed cells of 4 formula units by repeating the 2 formula unit ground state cell along all the lattice vectors. Then we applied random displacements to the atomic positions up to 0.1 Å and re-optimised the structures and studied the converged states. All the structural relaxations with the 4 formula unit cells lead to the same ground state minima as with the 2 formula unit cells with energy differences $< 10^{-7}$ eV. Note that this is not sufficient to confidently comment on the absence of any long-range order because given the computational cost, it would be prohibiting to repeat this for all studied phases. However the absence of any new superstructures in the ground state of the larger cells justify the size for the cell we considered to study disorder and the dominating role of configurational entropy in bringing that.

6.5 Soft phonons in lanthanides

Even though in the previous section vibrational motion wasn't the dominating factor in determining the observed disorder in La_2TiFeO_6 and La_2VCuO_6, in general systems with f-electrons are often associated with large soft phonons modes [283] and a wide range of magnetic properties [284]. This makes materials with f-systems privy to a complex phase diagram associated with structural transitions along with a wide range of magnetic properties leading to a diverse range of applications in the field of spintronics, quantum information processing and ultra high density storage among others [285]. For example in lanthanide-based nanocrystals, which are luminescent nanomaterials [286], the phonon density of states (Ph-DOS) governs both the inter-ion and intra-ion non-radiative relaxation processes between narrowly spaced electronic energy levels [287]. This along with the fair abundance on lanthanides in earth's crust[1] attracts the use of ab-initio methods for reliable predictability of various associated properties in these

[1] An irony to the *rare*-earth nomenclature. However their geochemical properties are such that they are typically dispersed and are not found in concentrations viable for mining mine. This is the *rarity* in rare earths.

systems [288].

Soft phonon modes within the DFPT or finite-difference framework are associated with the observation of large acoustical and/or optical imaginary phonon frequencies. This happens when the phonon frequencies which are the square roots of the eigenvalues of the dynamical matrix, as discussed in 2.13, are imaginary. The sign of the eigenvalues signify if the curvature of the potential energy surface (PES) in which the nuclei move is positive or negative in the direction of the corresponding eigenvector, as depicted in chapter 2 in fig.(2.11). A positive value implies that this energy refers to a local minimum along the direction of that associated eigenvector whereas a negative value refers to a local maximum. Thus, a soft mode referring to an imaginary frequency stems from a local maximum in the potential energy surface which means that if the atoms in the system are displaced along the eigenvector, a structure with lower value of total energy can be obtained.

However all imaginary phonon modes are not soft phonon modes. To elaborate further, soft phonon modes are usually associated with the onset of a displacive phase transition with a dynamical character. Occurrence of soft phonon modes describes a collective movement of atoms that is associated with a transformation from a higher-symmetry crystal structure to a lower symmetry one. It signifies that the existing static perfect crystal structure with higher symmetry provides an incomplete picture of the lattice dynamics. As the phase transition begins, the frequency of the soft phonon starts to decrease until it reaches zero at the phase transition when the phonon has *completely softened* or *frozen* and is no longer dynamical. This corresponds to another structure with lower symmetry signifying that the structural transformation has taken place. Such modes are often observed in materials which have more than one stable crystal structure in the vicinity of each other in the PES. For example $PbTiO_3$, above 492 K, assumes a cubic structure with space group $Pm\bar{3}m$ but below that it becomes tetragonal with space group $P4mm$ and simultaneously acquires a spontaneous ferroelectric polarisation [289]. This phenomenon is associated with the observation of a soft phonon mode.

Before a soft mode corresponding to a structural phase transition is confirmed, technical origins of imaginary phonon modes have to be examined. In case of lanthanides and perovskites, they often might correspond to the following scenarios which must be corrected for to ascertain the result [2].

- inadequate structural relaxation
- poorly converged DFT parameters that give rise to large dynamical forces like the SCF convergence criteria, k-mesh density, etc.
- interpolation artefacts that rely on the size of supercells for finite differences and of q-grid for DFPT to commensurate with the associated wavevector

[2] A student-friendly review : [290]

- strong correlations which might make it important to go beyond DFT to DFT+U or Hybrids or DMFT
- spin-phonon coupling which might need inclusion of spin and/or spin-orbit coupling
- considering the wrong magnetic order where the information about magnetic ordering is lacking or there are competing phases

Also, as discussed in 4, lanthanides show appreciable volume collapse under pressure. In $4f$ materials the volume collapse mechanism [291] might involve the valence change or band formation of the $4f$ electrons or a $s \rightarrow d$ transfer among conduction electrons among other factors [292]. In many rare-earths, compression is associated with softening of optical as well as acoustic phonon modes along with elastic anomalies and defects and associated novel applications [293], [294], [295]. How a soft phonon evolves into a lattice defect and interacts with electronic properties is still unclear and draws attention to the study of lanthanides [296] where these different degrees of freedom come to play. As we will see in the upcoming part of this chapter, they are active playgrounds of strong correlation induced phenomena, and disentangling if an imaginary phonon mode is merely an artefact of the use of an inefficient theory or refers to an actual phase transition is an interesting question.

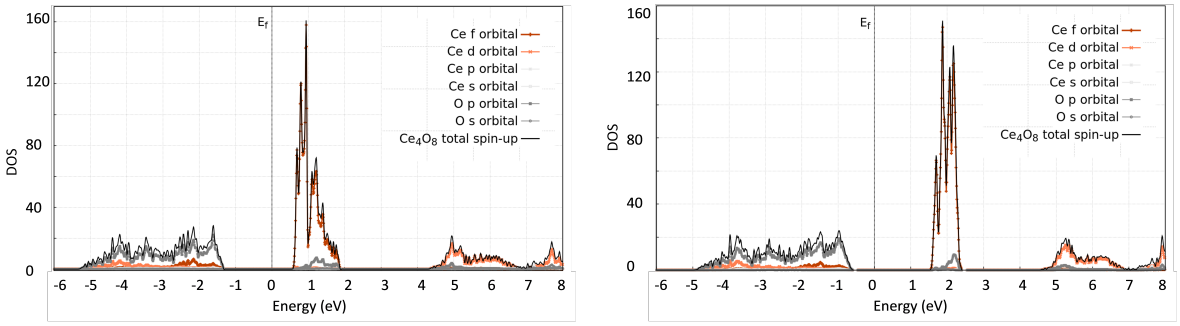
6.5.1 Catalytically relevant oxides

Rare-earth oxides have been famous for their various catalytic applications for more than four decades now [297]. Their catalytic activity stems from typically solid rare-earth surfaces with different possible phases of reactants and products classifying them as heterogeneous catalysts. Heterogeneous catalysis has emerged as a promising way to provide an effective pathway for removing atmospheric pollutants like nitrogen oxides, carbon monoxide (CO), soot, automotive exhausts, methane and volatile organic compounds [298].

One such rare-earth oxide is CeO_2, or ceria whose applications range from being ingredients in sunscreens due to its UV shielding photocatalytic activity and photocytotoxicity in colloidal solutions [299] to its use as a three-way catalyst [300] performing simultaneous multiple oxidation (e.g., oxidising hydrocarbons and CO) and reduction (e.g., reducing nitrogen oxides) reactions converting air pollutants present in exhaust to harmless gases. Also ceria has high oxygen mobility with inclination for reversible conversion to a non-stoichiometric oxide [301] many of which show promising uses for energy conversions and environmental applications. Recent advances in synthetic methods can control the final morphology and size of ceria compounds, and thus can successfully influence its resulting catalytic activity [302]. These properties paired with its high abundance in earth's crust makes ceria and its mixed oxides e.g., CeO_2+ZrO_2 materials of interest in the present times.

Apart from this, Ce-based compounds attract interest in theoretical modelling due to Ce ([Xe] $4f^1$ $5d^1$ $6s^2$) being the simplest element with one d and one f electron making it the ideal testing ground for theoretical models studying the role of strong correlations.

6.5.2 Ceria



(a) Ce_4O_8: DFT (b) Ce_4O_8: DFT+U

Figure 6.13: Projected density of states for ceria (CeO_2) as obtained with a 4-formula unit supercell of Ce_4O_8 with (a) DFT, (b) DFT+U, $U = 5$ eV. (Simulation by Dr. Rachel Kerber, JM. See footnotes 3 and 4)

We[3] study four ceria compounds, namely Ce_4O_8, Ce_4O_7, $ZrCe_3O_8$ and $ZrCe_3O_7$. Ceria in bulk has fluorite structure belonging to $Fm\bar{3}m$ spacegroup where Ce and O atoms have 8-fold and 4-fold coordination respectively with Ce^{4+} and O^{2-} oxidation states. We study these systems in this thesis with an interest in understanding the role of strong correlations in them within the scope of DFT and DFT+U as employed in the plane wave basis code Quantum Espresso[4] [303], [304]. Full volume relaxations were obtained with energy and force tolerances of 10^{-5} eV and 10^{-3} eV/Å with projected augmented Wave (PAW) pseudopotential and PBE [305] scalar relativistic functional taking into account non linear core corrections with valence configurations Ce ($4f$, 5s, 5p, 5d, 6s, 6p) [306] and O (2s, 2p) [307] in the UPF format. Van der Waals corrections [308] were enabled with Marzari-Vanderbilt-DeVita-Payne cold smearing [309] and Thomas-Fermi mixing scheme with self-consistency threshold of 10^{-7}.

CeO_2 is a wide gap insulator with a band gap of $2.7 - 3.1$ eV [310] between the O-$2p$ and Ce-$4f$ states. The gap between O-$2p$ and Ce-$5g$ states is usually noted to be ~ 6 eV. DFT reports CeO_2 (Ce_4O_8) as an insulator with a band gap ~ 2 eV. This is a significant underestimation over the experimentally observed band gap[5]. Application

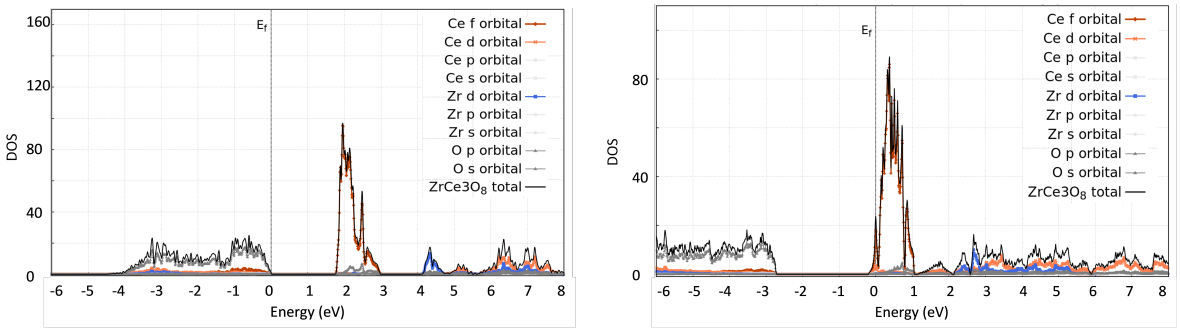
[3]This work is part of a bigger collaboration, with some results presented in this thesis based on work done by various collaborators. See declaration for details.

[4]Parallel simulations using VASP were performed by me with computational details as mentioned on page 176 to benchmark the correctness of the results and disentangle possible errors depending on the choice and implementation of the simulation algorithm for reasons mentioned in the following pages.

[5]See Appendix III for bandstructure.

of a static U within the DFT+U framework does not affect the band gap between O-2p and Ce-4f states substantially. The unoccupied Ce-4f states and even the occupied O-p states shift to higher values of energy with application of U. This shows that the double counting corrections with DFT+U is insufficient to correctly account for the properties of this highly correlated system, and beyond static mean field corrections need to be accounted for using the dynamical mean field theory.

6.5.3 Zirconia-ceria oxide



(a) $ZrCe_3O_8$: DFT (b) $ZrCe_3O_8$: DFT+U

Figure 6.14: Projected density of states for ceria-zirconia ($ZrCe_3O_8$) in the fluorite structure with (a) DFT, (b) DFT+U, $U = 5$ eV. (Simulation by Dr. Rachel Kerber, JM. See footnotes 3 and 4)

The catalytic and electrochemical properties of ceria are also carried over to mixed ceria compounds especially with other metal oxides where the metal usually belongs to the 3d or the 4d transition series. Some well known examples include nickel-manganese mixed metal oxide doped with nano cerium oxide [311] useful as catalysts for organic transformations, ceria-titania hybrid composites which have shown usefulness as electrochemical enzyme biosensors [312] and in production of hydrogen through photocatalytic splitting of water [313], etc. We study ceria-zirconia mixed oxide (CeO_2+ ZrO_2) which shows a better efficiency than ceria in the three-way catalysis as oxygen storage among other uses in photocatalysis, catalytic combustion of pollutants, etc [314].

We substitute one of the four Ce atoms by Zr in Ce_4O_8, thus giving $ZrCe_3O_8$. We notice both with DFT and DFT+U, the addition of Zr drives the system towards metallicity. In the DFT framework, Zr doping pushes the oxygen occupied states to higher energies whereas in DFT+U ($U = 5$ eV), the 4f states are lowered in energy when compared to ceria, as compared between fig.(6.14) and fig.(6.13).

XRD results show that with Zr doping till 2 mol %, the direct band gap remain the same as ceria whereas the indirect band gap is reduced by $0.8 - 0.9$ eV depending on the doping percentage [315]. This result is in contrast with the metallic behaviour that we see. However, note that our doping percentage is significantly larger, $\sim 14\%$ and hence a metallic result might correspond to expected trends. The crystal structure

and properties of ceria-zirconia depend largely on the Zr:Ce ratio, surface chemistry, temperature and other synthesis conditions [316]. Larger supercells with smaller Zr doping percentages need to be simulated to draw further conclusions.

We observe that the volume of $ZrCe_3O_8$ is contracted by > 30 Å^3 i.e., by $> 3\%$, as expected given the ionic radius of Zr is smaller compared to Ce, as tabulated in tab.(6.5). The lattice parameter contracts by 0.06 Å on zirconium incorporation into the cubic fluorite ceria lattice, and matches experiments well [317]. XRD shows that lattice constant gradually decreases as the concentration of Zr increases in ceria-zirconia mixture, by ~ 0.01 Å for a doping of 2 mol % [315]. Our results with larger doping % thus conform with the observed trends in volume within an error bar.

Note that $ZrCe_3O_8$, as studied here, is volume relaxed after being initiated from the cubic fluorite structure. However experimentally the fluorite structure is only observed at very low Zr concentrations. Since in DFT, the initial structure is important in determining the final structure, this can be a possible cause of error in determining properties of the final state.

6.5.4 Oxygen vacancies

The usefulness and active interest in ceria stems a lot from its interesting defect chemistry. Among many defects, most prominent ones which are stable under a wide range of physical conditions are oxygen vacancies. Potentially oxygen vacancies can induce local distortions and related short-range, non-periodic features which might be missed by conventional X-ray powder diffraction studies. As a result this subject remains an active field of interest both for discovery of tunable applications as well as serving as a common ground of comparison for theoretical modelling and experimental understanding [318].

Introduction of zirconium into ceria is expected to accelerate the formation of defect sites owing to the smaller size of Zr atom when compared to Ce, leading to increase in the displacement of oxygen atoms and formation of oxygen vacancies, and which in turn can also displace the Ce and Zr further in the cell. Thus, Zr replacement of Ce in Ce_4O_8 supercell is expected to lower the energy required for formation of defects, and alter the phonon modes.

In this work, we focus on neutral oxygen vacancies in bulk ceria whose introduction can be associated with a reversible change in oxidation state of two cerium ions from Ce^{4+} to Ce^{3+} as,

$$O^{2-} + 2Ce^{4+} \rightarrow 2Ce^{3+} + \frac{1}{2}O_2(g) \tag{6.4}$$

i.e., an oxygen ion O^{2-} leaves as neutral $\frac{1}{2}$ $O_2(g)$ with two electrons left behind. Those are trapped and localised at two Ce sites which might occupy an otherwise empty Ce-4f state, as seen in fig.(6.13) for both DFT and DFT+U implementations. One can then expect that the highly localised Ce-4f bands, in presence of a neutral oxygen vacancy,

will be split into two bands with one band being occupied and the other unoccupied.

S1 → S2	DFT	DFT+U
$Ce_4O_8 \rightarrow Ce_4O_7$	+1.19	+1.31
$Ce_4O_8 \rightarrow ZrCe_3O_8$	-3.33	-3.86
$Ce_4O_8 \rightarrow ZrCe_3O_7$	-2.39	-2.96
$ZrCe_3O_8 \rightarrow ZrCe_3O_7$	+0.97	+0.94

Table 6.5: Percent volume collapse ($\Delta V\%$) observed in relaxed volume for structure S2 from the relaxed volume of structure S1 for each respective method with ± corresponding to an enlargement or collapse of volume respectively.

Introducing a 12.5% oxygen vacancy in Ce_4O_8 gives us Ce_4O_7 in bulk, which as per DFT is metallic, as shown in fig.(III.1a). It also does not show the expected splitting of the Ce-4f bands, as seen from fig.(III.2b). For ceria-zirconia, the f-levels are driven closer to the Fermi level, as seen from fig.(III.2). On comparing the relaxed volumes, as shown in tab.(6.5), we see that oxygen vacancies lead to an expansion of the volume by 1.19% in ceria and by 0.97% in ceria-zirconia with DFT. The increase in volume increases with DFT+U in ceria but decreases for zirconia. This is expected as an onsite U has been applied on Ce which increases electronic repulsion and leads to a volume increase in ceria. With three Ce atoms in the supercell, one would expect similar trend for zirconia which is not observed. This calls for further studying the impact of correlations in Zr which has an open 4d shell as well as beyond the DFT+U framework. For both ceria and ceria with oxygen vacancy, introduction of Zr doping leads to volume contractions by $> 3\%$, in agreement with experimental data [317], [319].

If the defect formation energy ΔE_{vac} is defined as,

$$\Delta E_{\text{vac}} = E_{\text{vac}} + E_{\text{O}} - E_{\text{ideal}} \tag{6.5}$$

where E_{vac} is the total energy of the defect supercell, E_{ideal} is the total energy of the ideal bulk supercell without the defect, and E_{O} is energy of a reference state computed using the same level of approximation as the compounds. The reference state can be half the energy of an oxygen molecule in triplet state relaxed with DFT or a difference between the total energies of H_2O and H_2 using DFT. Defect formation energies are usually less well defined when compared to the respective structure in bulk. Another variation of the above equation was eq.(6.3) which took into account the influence of experimental conditions via the chemical potential and reference energy of the element concerned. In the above eq.(6.5) although, E_{O} is found using a reference configuration with DFT or DFT+U which, depending on the system concerned, can have limited relevance when compared to experiments as it will reflect the errors from the approximation, correlation functional, cell size, etc. However in this thesis we aim for a comparative study of vacancy formation between Ce_4O_8 and $ZrCe_3O_8$ within the chosen frameworks and try to comment on the trend observed within that chosen framework to comment

on its validity.

We also observe a large reduction in the formation energy, defined as eq.(6.5), of defects by 0.34 eV with Zr substitution of a Ce atom with DFT. This shows that at this level of Zr-doping, the catalytic activities fuelled by oxygen vacancies will be more favourable which match experimental observations. However, on the contrary in the DFT+U framework this difference reduces to 0.06 eV.

System	DFT	DFT+U
$Ce_4O_8 \rightarrow Ce_4O_7$	2.03	2.08
$ZrCe_3O_8 \rightarrow ZrCe_3O_7$	1.69	2.02

Table 6.6: Defect formation energy (in eV) for oxygen vacancy for ceria and ceria-zirconia starting from an oxygen reference state calculated by difference of total energies of electronic relaxation of H_2O and H_2. A different reference state, like the oxygen molecule in triplet form, will shift all the above energies by a constant for the method used.

6.5.5 Soft phonon modes

Before discussing further the quantitative discrepancy between DFT and DFT+U, we would go back to our discussion on soft phonon modes in rare-earths from section 6.5. Since we are discussing vacancy formation energies for ascertaining the correctness of this result, the stability of the original lattice has to be verified. For that we employ Density-Functional Perturbation Theory (DFPT) as implemented in the plane wave code VASP [234], [232], [320]. For that we first benchmark the DFT+U results from Quantum Espresso, VASP [233], [235] with the PBE [305] potentials, an energy cutoff of 520 eV with the tetrahedron method and Blöchl corrections and a 7×7×7 Monkhorst k-grids. DFT and DFT+U ($U = 3$ eV) with VASP results matched the Quantum Esspresso DFT and DFT+U ($U = 5$ eV) results respectively. Thus difference in the value of U is acceptable owing to the pseudopotentials used in both the implementations. The energy scales for electronic and vibrational degrees of freedom are expected to be comparable between VASP and Quantum Espresso. Thus, DFPT is performed to study the displacements commensurate with the supercell i.e., phonons at the Gamma point without the use of symmetry.

Ce_4O_8 is found to be stable with acoustic imaginary modes < 0.18 meV, attributable to numerical instabilities. Note that the final relaxed structures of Ce_4O_8 obtained with QE and VASP are similar within a different of ~ 0.1 Å in lattice parameters and ~ 0.01 Å in atomic positions. This verifies the coherence of results and inferences drawn between two codes.

For $ZrCe_3O_8$, the initial structure shows a large imaginary frequency of ~ 20 meV, as seen in fig.(6.15b). To inspect whether this is a soft phonon mode or not, we displace the structure in the direction of the corresponding eigenvector by Δd times the eigenvector.

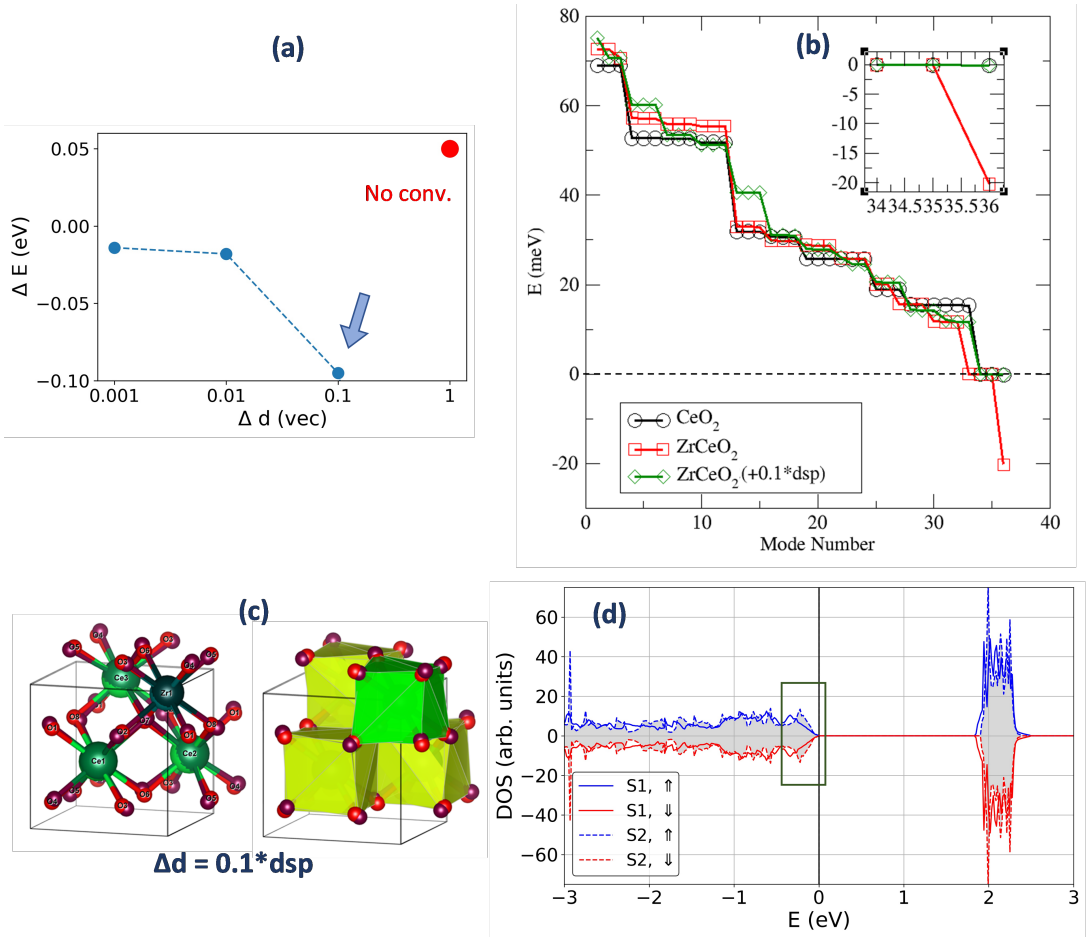


Figure 6.15: (a) Energy difference of the structure displaced Δd times with respect to the original structure in the direction of the soft-mode. The red point signifies no convergence. (b) Phonon eigenvalues in meV at Gamma (0,0,0) point for ceria and zirconia-ceria oxides. (c) Relaxed structure of $ZrCe_3O_8$ corresponding to the large soft phonon mode, with the new structure formed by tilted oxygen (red) planes. (d) Density of states corresponding to the old $ZrCe_3O_8$ *(straight lines)* and the new displaced relaxed *(dashed lines)* structures denoting the structure induced energetic stabilisation.

We find that as the atoms are displaced towards the eigenvector, the structure becomes stabler with a minimum for $\Delta d = 0.1$. On doing a full volume relaxation, we find the the energy to be stabilised by 0.1 eV, as seen in fig.(6.15a) as the imaginary phonon mode vanishes, as seen in fig.(6.15b). A difference of 0.1 eV is larger by two orders of magnitude than can be attributed to noise. The new $ZrCe_3O_8$ stable structure corresponds to a slight shift of the oxygen positions in the cell that leads to a distorted cuboidal structure around the cations, as shown in fig.(6.15c, 6.15d). If this difference in energy is accounted for, then as per DFT+U oxygen vacancy formation is favoured in $ZrCe_3O_8$ by 0.17 eV when compared to Ce_4O_8.

On inspecting the electronic density of states we observe that although the band gap of new structure is almost identical to the old, however the slope of the occupied states below the Fermi level for the new structure is almost twice that of the older

structure, as seen in fig.(6.15e). The steepness of the density of state below the Fermi level determines the effective mass of the electrons.

Thus we observe that when comparing DFT and DFT+U studies if lattice dynamics is also considered, energetically the formation of defects is favoured in zirconia. This is identified via an imaginary mode in the phonon spectrum at Gamma which leads to a new supercell and owing to lattice displacements prefers the formation of an oxygen defect. So, vibrational modes can facilitate symmetry breaking and the formation of superstructures which is an important factor for lanthanides and surface reconstruction with interfaces in a catalyst as zirconia. This structural reconstruction mediated by the soft phonon mode also leads to an increase of the effective mass. This is a trademark of correlated systems, and such effects usually increase when dynamical correlations are accounted for.

The above scenario of lattice dynamics facilitated structural reconstruction and the crucial role of correlations is a trait of lanthanide compounds. The above study motivates us for a deeper investigation into the role of dynamic strong correlations beyond the DFT+U framework [6]. Apart from this, in ceria based compounds, temperature and defects have a big role in estimating stability [321]. This usually requires inclusion of anharmonic terms in the calculation to account for subtle phonon-phonon interactions, and is one possible avenue for future investigations [322].

6.6 Conclusion and outlook

In this chapter we investigate two groups of rare-earth metal oxides where correlations lead to interesting applications. The first group we studied comprises of two double perovskites La_2TiFeO_6 and La_2VCuO_6 where previous theoretical studies of charge transfer phenomena between $Fe^{3+}/Ti^{3+} \rightarrow Fe^{2+}/Ti^{4+}$ and $Cu^{2+}/V^{4+} \rightarrow Cu^{+}/V^{5+}$ associated with specific B-site orders can be used in spintronic applications. However no such B-site order could be found experimentally and only a partial charge transfer was observed.

Within the DFT+U framework, the observed disorder for La_2VCuO_6 could be explained by the competition between its layered and rock-salt phases. For La_2TiFeO_6, studying ground state properties were inconclusive and we investigated further. We performed random structure search with DFT+U and observed that within 400 meV of the ground state there are five competing local minima each associated with a different B-site order such that the frequency of occurrence of the structures farther from the ground state are substantially higher. These low-lying competing phases qualitatively stressed the role of configurational entropy for the observed disorder. We then calculated

[6] These systems were also studied with QSGW (using the Questaal code with LMTO basis) and DMFT (using the DCore code) for an improved estimation of the effect of the degrees of correlation, but this work, done as a part of collaboration with Johnson Matthey, Rahko, and AWS has not been included in this thesis, and is under embargo.

the entropy forming ability values for the 400 optimised structures and found that they are highest in presence of Lanthanum vacancies and over oxygenation. These defects were also responsible for the observed partial charge transfer. By comparing the volume distribution of all the optimised structures with experimental data, La-vacancies were found to have a dominating effect on the observed disorder. Additionally we saw that lattice vibrations, although an important aspect in determining stability of a material are not the driving factor in observation of high entropic disordered phases because the largest contribution originated from vibrational modes associated with Lanthanum atoms in the ordered phases which are always similar to each other.

In the second part of this chapter we studied another set of rare-earth metal oxides ceria and zirconia aiming at understanding the role of oxygen vacancies in their use as heterogeneous catalysts. DFT+U corrections correctly predicted CeO_2 to be an insulator but underestimated the band gap. Doping with Zr renders the system as metallic. Since experimental data is only available for smaller doping percentages, this part of the work concluded with a stress on simulating larger supercells with smaller Zr doping percentages need to be simulated to draw further conclusions. We confirmed that with Zr doping the volume contracted and with introduction of Oxygen vacancy the volume expanded, matching experiments. We obtained formation energies for oxygen defects and found that both DFT and DFT+U show Zr adsorbed on CeO_2 to be energetically favourable. However, contrary to expectations, on including the effect of correlations in the DFT+U framework this vacancy favorability reduces. But on including the effect of lattice dynamics, a soft phonon mediated symmetry breaking is found to facilitate vacancy formation along with an increase in effective mass. This calls for further investigation of the interplay of correlation effects with phonons in these systems.

Chapter 7

Conclusion & Outlook

7.1 Conclusion

We started this thesis with a simple question. *Why electrons behave the way they do?* We mapped a brief historical account of how the quest to understand electrons has altered the philosophical definition of *fundamental* physics. Alongside it has morphed into a pursuit of understanding the complexities introduced by correlations which stem from simple electron-electron interaction in materials. The effect of correlations are intricately linked to many desirable practical applications. Therefore, understanding the role of correlations in lanthanide interfaces and lanthanide metal oxides associated with specific real world applications is the central theme of this thesis.

We begin this pursuit in chapter 3 by studying a model correlated interface that serves as a simplified prototype double well potential. By solving a Hubbard-like Hamiltonian using dynamical mean field theory (DMFT) we examine how the competition between kinetic energy and Coulomb repulsion terms can lead to the occurrence of Mott transition. We conclude with an analysis of the conditions associated with the occurrence of resonant tunnelling at non-interacting and interacting limits. In future, inferences drawn from this model can be used as a reference to design a realistic interface with real materials imitating a quantum double well to obtain a Mott transistor like function.

Chapters 4 and 5 are coupled under a single broader aim, to comprehend the functioning of a piezoelectric transistor (PET). A PET is an alternative transistor design that attempts to overcome the saturation of trends predicted by Moore's law in traditional CMOS based transistors owing to their voltage and frequency dependent energy losses. We focus on understanding a class of materials chosen to serve as piezoresistive elements in the PET, namely Samarium monochalcogenides (SmX). SmX show a pressure dependent insulating to metal transition with a concomitant change in valence.

In chapter 4 our focus is on understanding SmX in bulk. We observe that density functional theory (DFT) fails to capture this transition associated with the presence of a mixed valent state due to the presence of strongly correlated Sm-4f orbitals. However using DMFT within the Hubbard-I approximation, owing to an access of fractional electronic occupations, the insulating and the metallic phases emerge as a function of changing valence with increasing pressure. Inclusion of the charge and spin fluctuations via DMFT directly lead to significantly improved predictions of the equilibrium lattice constants and bulk moduli for all of SmX, thus verifying experiments. Nudged Elastic Band inspired analysis reveals that the insulating states are characterised by a finite quasiparticle weight which decreases as the band gap closes. This implies that this transition is not a Mott-like. The electronic energy levels change as the structure is compressed and although that makes the Sm-4f electrons heavier, they cross the Fermi level as the system becomes metallic. Therefore we classify these materials as correlated band insulators. We notice that the difference between the discontinuous and continuous nature of transitions between SmS and SmSe, SmTe can be qualitatively

attributed to the closeness of the sharply resonant Sm-4f peaks to the Fermi level in the predicted metallic states. Further work can be done to inspect the transition path to confirm whether there is any regime where this transition might be Mott-like. Another possible direction can be using a DMFT solver that includes the hybridisation term which could provide a more conclusive insight into the difference between the nature of piezoresistive behaviour in SmS versus SmSe and SmTe.

In chapter 5 we focus on the behaviour of SmX in a PET-like set-up. We review experimental predictions for the length scales at which the piezoresistive functionality is needed for various technological applications. Unlike bulk, in a PET-like set up the transmission mechanism is tunnelling. This requires a separate investigation into the role of Sm-4f levels in transmission. We discuss the technical details for the choice of electrodes and the construction of the heterostructure that due to the computational complexity of a large system as this, must be optimised. These include accounting for the structural expansion that will occur after the application of a uniaxial strain and optimisation of the electrode-film distance. We note that the 4f-electrons in SmS and SmSe are described as strongly itinerant by DFT. DFT+U+SOC opens a gap parametrically depending on the value of U. Nonetheless both incorrectly estimate the contribution of the Sm-4f electrons in transmission. By including DMFT corrections over DFT in the Hubbard-I framework implemented within the NEGF formalism, we calculate transmission through the W/SmSe/W heterostructure. We find that for the unstrained system of SmSe, the change in density of states around the Fermi level is such that an SmSe film thickness $\geq$ 6 nm can act as a transistor in a PET-like set-up. This defines the insulating OFF state for device operations. To determine the ON states, transmission has to be calculated for the calibrated structures corresponding to various pressures. Those structures, derived in this work, have been provided to our industry collaborators at NPL. Another future direction, as with bulk SmX, can include a study of the effect of hybridisation term on transmission.

In chapter 6, we study two separate groups of rare-earth metal oxides each motivated by a specific application. The first set comprises of two double perovskites, viz., La_2TiFeO_6 and La_2VCuO_6. Previous DFT+U based studies on these materials had predicted charge transfer between $Fe^{3+}/Ti^{3+} \rightarrow Fe^{2+}/Ti^{4+}$ with pressure for La_2TiFeO_6 and between $Cu^{2+}/V^{4+} \rightarrow Cu^{+}/V^{5+}$ along with a half-metal to insulator transition for La_2VCuO_6, each associated with a particular B-site order. However experimental studies with structures obtained using pulsed laser deposition found no B-site ordering and only a partial charge transfer showing that they are not good candidates for charge-transfer based transistors. We investigate the reason behind this. For La_2VCuO_6, a competition between the ground states of its layered and rock-salt phases within 10 meV of each other in the DFT+U framework is attributed as the cause of the observed disorder. For La_2TiFeO_6, the study of ground state properties of ordered phases is inconclusive. Therefore, a random structure search has to be performed with DFT+U giving 400 optimised structures. We find that within 400 meV of the ground state, five

local energy minima exist. Each is associated with a specific structural symmetry and B-site order. The frequency of occurrence of the four structures above ground state are substantially higher than that of the ground state. This can be qualitatively associated with a higher configurational entropy. We then calculate the entropy forming ability for these optimised structures. We find that competition between low lying structures with Lanthanum vacancies and, to a lesser extent, over oxygenation are also responsible for the the high configurational entropy and observed partial charge transfer. We then inspect the role of vibrational entropy and find its role insignificant. Although this description is a qualitative picture and not an exhaustive and definitive theory describing the growth of these double perovskites, it provides valuable insights into the competing phases that drive the observed disorder.

In the second part of chapter 6 we study CeO_2 (ceria) and Zr+CeO_2 (zirconia) to understand the comparative ease of formation of oxygen vacancies that is responsible for their use as heterogeneous catalysts. Both DFT and DFT+U correctly predict CeO_2 to be an insulator but largely underestimate the band gap. Doping with Zr renders the system as metallic in both the frameworks. Since experimental data is only available for smaller doping percentages which show a decrease of band gap with Zr doping, even with correct prediction of trends the results are inconclusive. However we confirm the volume contraction observed with Zr doping and expansion with Oxygen vacancy in both the systems. We then obtain defect formation energies and observe that in both DFT and DFT+U frameworks Zr adsorption on CeO_2 is favourable. Zirconia has shown to be a better catalyst experimentally. However including correlations with DFT+U puts ceria and zirconia at a more equal footing which is only reinstated by including the effect of lattice dynamics where a soft phonon mediated symmetry breaking facilitates vacancy formation in zirconia. This phenomenon occurs with an increase in effective mass just below the Fermi level highlighting that dynamic strong correlations play an important role. This serves as inspiration for future studies with DMFT so that the interplay of dynamic correlation effects with phonons can be understood. Further experimental work with higher Zr doping can also provide a larger ground for inspection.

7.2 Outlook

To summarise we started this thesis by exploring the role of strong correlations in a layered model system to understand the occurrence of resonant tunnelling and Mott behaviour for a prototype *Mott-transistor*. Following this we looked at Samarium monochalcogenides in bulk and as thin films, to see how the response of the strongly correlated Sm-4f levels to pressure is utilised, for them to serve as the piezoresistive component of a *piezoelectric transistor*. Then we inspected double perovskites that were predicted by the literature to serve as *charge transfer based transistors* and found that a high configurational entropy hinders this application. Finally we studied a lanthanide

oxide and its mixed metal oxide to understand how vacancy formation that leads to their use as *catalysts* can be theoretically studied by accounting for the right degree of correlations and lattice dynamics.

As a perspective gain, I found that for theory to guide experiments and device design, accurate description of electron-electron interactions is crucial in this quantum era of material science. I observed that DMFT applied in conjunction to DFT or DFT+GW emerges as a successful formalism for describing strongly correlated materials such as lanthanides or transition metal oxides. However a major drawback is that the application of these methods are restricted to small systems due to prohibitive computational costs. Its relevance is more significant for developing economies and smaller institutions where HPC resources are scarce and therefore cannot facilitate an active participation from scientists even though many open problems of practical significance exist. For non-equilibrium systems, this is even more challenging. Based on this understanding, my future research interests will include the following.

- Alternative transistor designs e.g., the PET, a Mott transistor or memristor, etc., comprise of rare-earth and/or transition metal oxides where strong correlations are important. Research using material modelling to comprehend such physical mechanisms and guide such device design is promising field.

- In a realistic set-up, applications rely on more than just the effect of correlations. Studying lattice dynamics, disorder and defects at par with correlations are crucial to harness reliable applications. However such investigations are usually done independently due to restrictive computational costs. Studying them on an equal footing is a desirable future direction to address real-world problems.

- Systematic inclusion of non-local correlations together with local correlations as done in numerical cluster DMFT extensions, although usually restricted to nearest neighbour effects, is a promising avenue.

- On conventional computers, the prohibitive computational cost is a major drawback. I would like to work towards developing faster DMFT solvers with broader applicability. Two possible starting points are developing (i) a data-driven machine learning based process for solving the Anderson Impurity Model [323], and (ii) a quasi-continuous-time impurity solver for DMFT where determinantal quantum Monte Carlo calculations are solved with a multigrid extrapolation procedure [324].

- A more ambitious personal research interest (almost exotic, in line with the above point) is in understanding, development and application of quantum algorithms to simulate DMFT on existing quantum computers [325].

Appendix I

A quick overview of experimental methods for theorists

Method	Description	Applications
X-Ray **P**hotoemission **S**pectroscopy (**XPS**)	• Irradiate a material with X-ray beams in vacuum, under usually high pressure • Obtain electron population spectra and electron kinetic energy	Used for chemical analysis on the basis of determining which elements are present in a sample. Can • infer about bonding between sample components • determine band gaps of materials • profile elemental composition of a surface • qualitatively profile materials after cleavage, scraping, exposure to heat, reactive gasses or solutions, ultraviolet light, or during ion implantation **• Used in 4 and 6 to characterise SmS, SmSe and LTFO and LVCO samples.**
Angle **R**esolved **P**hoto**E**mission **S**pectroscopy **ARPES**	Based on the photoelectric effect • Monochromatic beam of photons incident on a material surface in within an ultra-high vacuum environment • Measures electron kinetic energy, velocity, absolute momentum, emission angle with respect to sample structure normal, two in-plane or all three momentum components	Very useful in determining the role of many-body effects experimentally by measuring • electronic bandstructure along a specific momentum direction • dispersion of electronic bands near the Fermi level and map Fermi surfaces by exciting bound electrons in a substrate with a given photon energy • Spin polarisation of the emitted electrons **• Used in 4 to study SmS bandstructure**

Method	Description	Applications
Pulsed **L**aser **D**eposition **(PLD)**	• Physical vapour deposition of a material in a vaccuum/gas(e.g., oxygenated) chamber targetted by a high-power laser beam • A thin film vaporises on a usually hot substrate	• Layer-by-layer growth of materials • 3D growth • Typical thickness 10-200 nm • **Used in 6.2 to grow of 45 monolayers of LTFO and 30 monolayers of LVCO films on TiO_2 terminated STO(001) and STO(111) substrates using 248 nm KrF laser at** 2×10^{-6} **Torr and** 700 °**C**
Low **E**nergy **E**lectron **D**iffraction (**LEED**)	• Fire electrons normal to the solid surface • Detect diffracted electrons • Detector screen shows an image of the reciprocal lattice of sample surface	Detects changes in surface structure and symmetry of the first 1 or 2 layers- • Surface cleanliness • Surface reconstructions • Lattice types • (even) Lattice constants
Reflection **H**igh-**E**nergy **E**lectron **D**iffraction (**RHEED**)	• Fire electrons parallel to the solid surface • Detects diffracted electrons • Detector screen shows an image of the reciprocal lattice of sample surface	Detects changes in surface symmetry • *in-situ* monitoring technique inside growth chambers e.g., in Molecular Beam Epitaxy (MBE) chambers • Monitors growth of single monolayers, island formation • **Used in 6.2 to ensure layer-by-layer growth of LTFO and LVCO films during deposition on STO(001) and STO(111) substrates**

Table I.1: A quick overview of experimental methods concerning the work done and compared with in this thesis for the *lay-person* theorist. It includes a brief description of the experimental method and its usual application with a mention of where and how that was used in this thesis.

Appendix II

Precursor to many-body quantum transport

As a first attempt of using the NEGF+DFT formalism to evaluate the density of states and transmission of an electrode-film-electrode heterostructure, along the lines of fig.(5.14) and compare them to bulk properties of the film material, artificial simplified metal electrodes were used. These electrodes were made up of gold-like atoms with a single s-type orbital per atom. Actual gold atoms will have similar valence configuration, Au: [Xe] ($4f^{14}$ $5d^{10}$) $6s^1$, and although its $5d$ and $4f$ shells are filled and are reasonably inert within the pressure ranges zero to a few GPa, a heterostructure with $\sim$ 30 Au lead atoms to be studied with a SIESTA basis including the $4f$, $5d$ shells (filled but included for better accuracy) will make the computation heavier while having insignificant physical impact. This justifies using artificial Au-like leads for testing purposes as this overlooking of the nature of a the real substrate material makes the calculations faster by using still a reasonable metal electrode with a smooth density of states around the Fermi level.

For the film, 8 monolayers of SmSe are used with $d_l = 2.6$ nm, constructed as in fig.(5.17a). This thickness of the PR film approximately corresponds to the thickness predicted for PET transistors for VLSI units as mentioned in table.(5.1).

The highly localised Sm 4f-shells were studied with a static DFT+U treatment with $U = 6$ eV. Since Sm is a heavy element, relativistic corrections in general are important and thus at the level of first approximation within a mean-field treatment, spin-orbit corrections (SOC) were included. Although it was later found, as reported in fig.(4.6), that SOC as implemented in a DFT framework can be safely neglected while evaluating structural and integral properties due to the smallness of its energy scale when compared to the energy scale of on-site Coulomb repulsion of the Sm 4f electrons.

The main observations from the DFT+U+SOC study of the bulk and test heterostructures are listed below:

- In this framework, at 0 pressure the observed gaps of bulk SmS and SmSe are ~ 0.2 and ~ 0.5 eV, respectively, in agreement with [209] and [326]. The bandgap

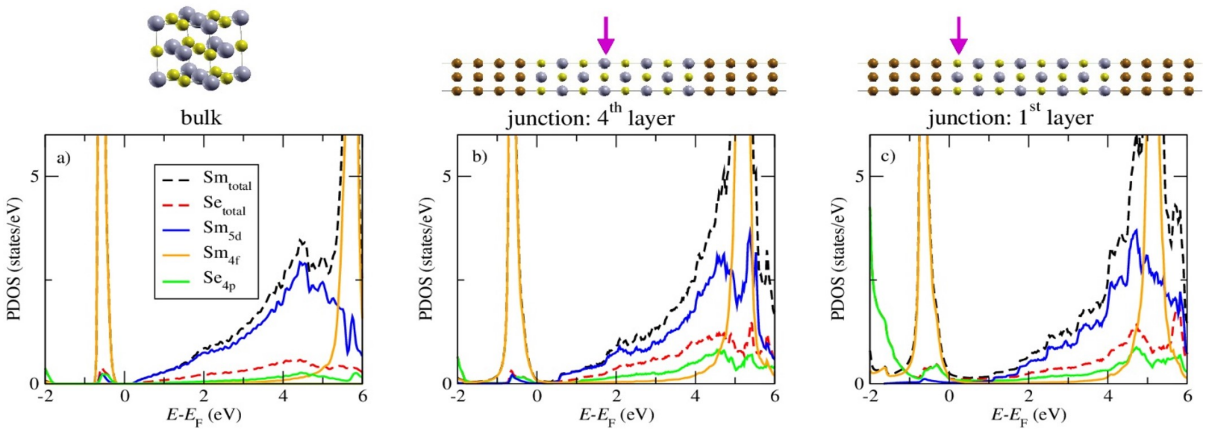


Figure II.1: Layer dependent projected density of states (PDOS) obtained with DFT+U+SOC (spin orbit corrections) with U=6 eV for (a) bulk SmSe, (b) the 4^{th} layer of SmSe in an 8-monolayer film, and (c) the 1^{st} layer of SmSe . Study of the layer dependence of DOS shows that at the 4^{th} layer, the DOS becomes visibly similar to the bulk. (Simulation and figure by: Dr. Ivan Rungger)

closes for this value of $U = 6$ eV when the volume was isotropically compressed by $\sim 9\%$ for SmSe and for a smaller value of $\sim 6\%$ for SmS (data not shown).

- The partial density of states (PDOS) of the middle layer 4, fig.(II.1(b)), qualitatively matches the bulk PDOS as shown in fig.(II.1(a)). The gap between occupied Sm-4f states below the Fermi level to the unoccupied Sm-5d above the Fermi level is ~ 0.5 eV in both scenarios. This is because beyond a few layers from the interface, the bulk properties are acquired again as the physical effects of the interface diminish. Thus it serves as a confirmation for correctness of the implementation within the scope of this DFT+U+SOC framework.

- The PDOS of layer 1 i.e., the layer of SmSe at the interface, shown in fig.(II.1(c)), differs qualitatively from the bulk and layer 4 in terms of the energetic ordering of Se-4p orbitals. For the interface layers, the occupied Se-4p orbitals move up in energy. Also the Sm-4f and Sm-5d gap is smeared out as the interface layer is spatially closer to the metal electrodes.

- In Smeagol, the total current through a nanojunction is obtained by using the Landauer formula, as discussed in eq.(2.122), and is proportional to integral of energy dependent transmission $T(E)$ coefficient over an energy (E) range that is equal to the range of the applied bias around E_F. The conduction of the system at low bias voltage will be proportional to the transmission in a small energy range around E_F, as discussed below. The observations on transmission (data not shown) through the heterostructure:

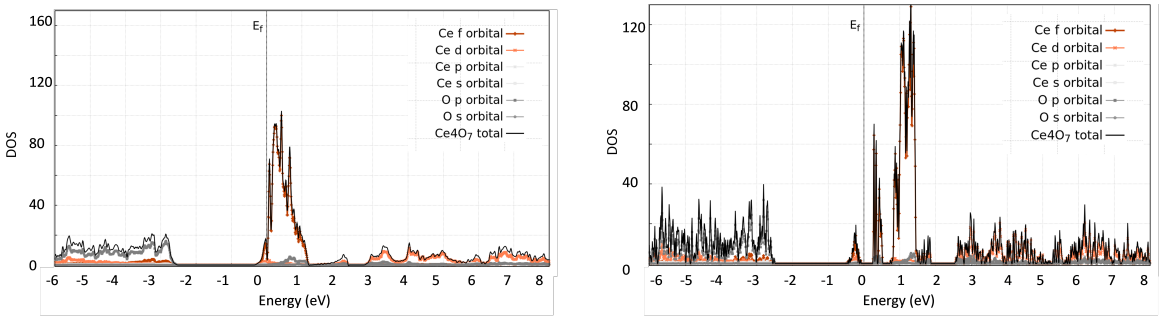
- **Zero pressure-**

1. For $-1 < E < 0$ (E_F) (eV), the high peak in DOS as seen in fig.(II.1) coming from the occupied Sm-4f states. This corresponds to a high peak in transmission, as expected.
2. For 0 (E_F) $< E < 0.5$ (eV) i.e., around the Fermi level, the DOS decreases exponentially with increasing distance of the concerned layer from the Fermi level. Even at the 4^{th} SmSe layer, the DOS at E_F is small but non-zero and the resultant transmission is exponentially small but finite. This corresponds to a non-zero finite tunnelling conductance in the given heterostructure.
3. For $E > 0.5$ eV, the DOS contributions from Sm-5d states is reflected in an increase in transmission.

Appendix III

Ceria

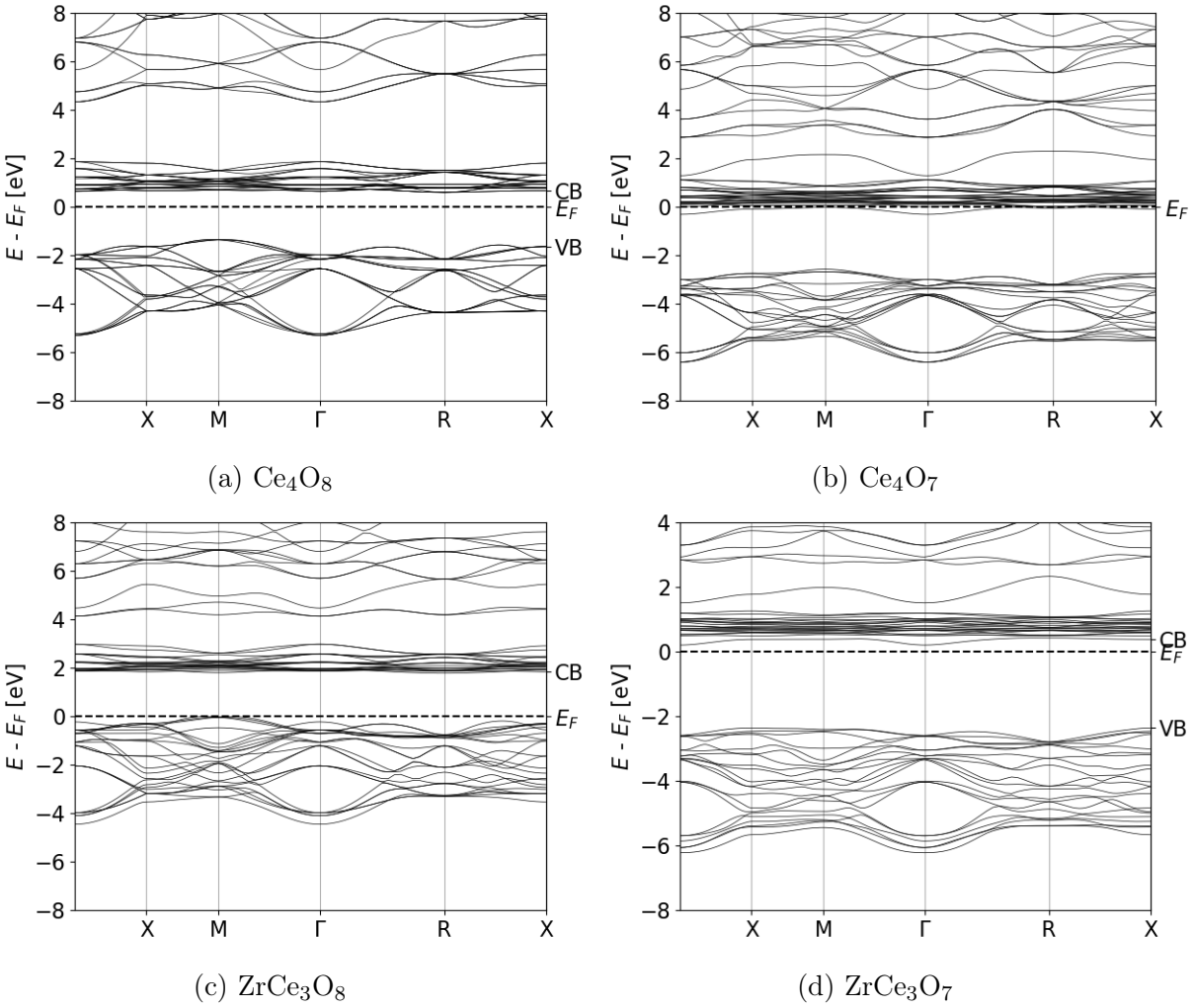
III.1 Projected DOS for ceria compounds



(a) Ce_4O_7: DFT (b) Ce_4O_7: DFT+U

Figure III.1: Projected density of states for ceria with 12.5% oxygen vacancy with a Ce_4O_7 supercell with (a) DFT, and (b) DFT+U with $U = 5$ eV. (Simulation by Dr. Rachel Kerber, JM. See footnotes 3 and 4)

III.2 Bandstructures for ceria compounds



(a) Ce_4O_8 (b) Ce_4O_7

(c) $ZrCe_3O_8$ (d) $ZrCe_3O_7$

Figure III.2: Band-structure for various ceria oxides: (a)Ce_4O_8 bulk, (b) Ce_4O_7 with 12.5% O-vacancy, (c) $ZrCe_3O_8$ bulk, and (d) $ZrCe_3O_7$ with 12.5% O-vacancy obtained with DFT as implemented in Quantum Espresso code with plane-wave basis and PBE functional and other comparable parameters as obtained with VASP as described in 6.5.2. E_F, CB and VB stand for the Fermi level, conduction band and valence band respectively. (Simulation by Dr. Rachel Kerber, JM. See footnotes 3 and 4)

Bibliography

[1] Iwan Rhys Morus. "When Physics Became King". In: 1427 E. 60th Street Chicago, IL 60637 USA: The University of Chicago Press, 2005. ISBN: 9780226542003. URL: https://press.uchicago.edu/ucp/books/book/chicago/W/bo3534126.html.

[2] *The Nobel Prize in Physics 1956*. 1956. URL: https://www.nobelprize.org/prizes/physics/1956/summary/.

[3] Marvin L. Cohen. "Essay: Fifty Years of Condensed Matter Physics". In: *Phys. Rev. Lett.* 101 (2008), p. 250001. DOI: 10.1103/PhysRevLett.101.250001.

[4] Joseph D. Martin. "When condensed-matter physics became king". In: *Physics Today* 72.1 (2019), pp. 30–37. DOI: 10.1063/PT.3.4110. eprint: https://doi.org/10.1063/PT.3.4110. URL: https://doi.org/10.1063/PT.3.4110.

[5] P. W. Anderson. "More Is Different". In: *Science* 177.4047 (1972), pp. 393–396. DOI: 10.1126/science.177.4047.393. eprint: https://www.science.org/doi/pdf/10.1126/science.177.4047.393. URL: https://www.science.org/doi/abs/10.1126/science.177.4047.393.

[6] Hans Primas. "Reductionism, Holism and Complementarity". In: *Chemistry, Quantum Mechanics and Reductionism: Perspectives in Theoretical Chemistry*. Berlin, Heidelberg: Springer Berlin Heidelberg, 1983. ISBN: 978-3-642-69365-6. DOI: 10.1007/978-3-642-69365-6_6. URL: https://doi.org/10.1007/978-3-642-69365-6_6.

[7] R. B. Laughlin and David Pines. "The Theory of Everything". In: *Proceedings of the National Academy of Sciences* 97.1 (2000), pp. 28–31. DOI: 10.1073/pnas.97.1.28. eprint: https://www.pnas.org/doi/pdf/10.1073/pnas.97.1.28. URL: https://www.pnas.org/doi/abs/10.1073/pnas.97.1.28.

[8] *The Nobel Prize in Physics 1933*. 1933. URL: https://www.nobelprize.org/prizes/physics/1933/summary/.

[9] Paul Adrien Maurice Dirac and Ralph Howard Fowler. "Quantum mechanics of many-electron systems". In: *Proceedings of the Royal Society of London. Series A, Containing Papers of a Mathematical and Physical Character* 123.792 (1929), pp. 714–733. DOI: 10.1098/rspa.1929.0094. eprint: https://royalsocietypublishing.

org/doi/pdf/10.1098/rspa.1929.0094. URL: https://royalsocietypublishing.org/doi/abs/10.1098/rspa.1929.0094.

[10] D. R. Hartree. "The Wave Mechanics of an Atom with a Non-Coulomb Central Field. Part I. Theory and Methods". In: *Mathematical Proceedings of the Cambridge Philosophical Society* 24.1 (1928), pp. 89–110. DOI: 10.1017/S0305004100011919.

[11] Robert Bruce Lindsay. "On the Atomic Models of the Alkali Metals". In: *Journal of Mathematics and Physics* 3.4 (1924), pp. 191–236. DOI: https://doi.org/10.1002/sapm192434191. eprint: https://onlinelibrary.wiley.com/doi/pdf/10.1002/sapm192434191. URL: https://onlinelibrary.wiley.com/doi/abs/10.1002/sapm192434191.

[12] W. Pauli. "Über den Zusammenhang des Abschlusses der Elektronengruppen im Atom mit der Komplexstruktur der Spektren". In: *Zeitschrift für Physik* 31.1 (Feb. 1925), pp. 765–783. ISSN: 0044-3328. DOI: 10.1007/BF02980631. URL: https://doi.org/10.1007/BF02980631.

[13] J. C. Slater. "Note on Hartree's Method". In: *Phys. Rev.* 35 (2 Jan. 1930), pp. 210–211. DOI: 10.1103/PhysRev.35.210.2. URL: https://link.aps.org/doi/10.1103/PhysRev.35.210.2.

[14] V. Fock. "Näherungsmethode zur Lösung des quantenmechanischen Mehrkörperproblems". In: *Zeitschrift für Physik* 61.1 (Jan. 1930), pp. 126–148. ISSN: 0044-3328. DOI: 10.1007/BF01340294. URL: https://doi.org/10.1007/BF01340294.

[15] Christina V Kraus and J Ignacio Cirac. "Generalized Hartree–Fock theory for interacting fermions in lattices: numerical methods". In: *New Journal of Physics* 12.11 (Nov. 2010), p. 113004. DOI: 10.1088/1367-2630/12/11/113004. URL: https://dx.doi.org/10.1088/1367-2630/12/11/113004.

[16] N. W. Ashcroft and N. D. Mermin. *Solid State Physics*. Holt-Saunders, 1976.

[17] Felix Bloch. "Über die Quantenmechanik der Elektronen in Kristallgittern". In: *Zeitschrift für Physik* 52.7 (July 1929), pp. 555–600. DOI: 10.1007/BF01339455. URL: https://doi.org/10.1007/BF01339455.

[18] M.L. Cohen. "Chapter 1 Overview: A Standard Model of Solids". In: *Conceptual Foundations of Materials*. Ed. by Steven G. Louie and Marvin L. Cohen. Vol. 2. Contemporary Concepts of Condensed Matter Science. Elsevier, 2006, pp. 1–8. DOI: https://doi.org/10.1016/S1572-0934(06)02001-4. URL: https://www.sciencedirect.com/science/article/pii/S1572093406020014.

[19] Martin C. Gutzwiller. "Effect of Correlation on the Ferromagnetism of Transition Metals". In: *Phys. Rev. Lett.* 10 (5 Mar. 1963), pp. 159–162. DOI: 10.1103/PhysRevLett.10.159. URL: https://link.aps.org/doi/10.1103/PhysRevLett.10.159.

[20] Junjiro Kanamori. "Electron Correlation and Ferromagnetism of Transition Metals". In: *Progress of Theoretical Physics* 30.3 (Sept. 1963), pp. 275–289. ISSN: 0033-068X. DOI: 10.1143/PTP.30.275. eprint: https://academic.oup.com/ptp/article-pdf/30/3/275/5278869/30-3-275.pdf. URL: https://doi.org/10.1143/PTP.30.275.

[21] J. Hubbard and Brian Hilton Flowers. "Electron correlations in narrow energy bands". In: *Proceedings of the Royal Society of London. Series A. Mathematical and Physical Sciences* 276.1365 (1963), pp. 238–257. DOI: 10.1098/rspa.1963.0204. eprint: https://royalsocietypublishing.org/doi/pdf/10.1098/rspa.1963.0204. URL: https://royalsocietypublishing.org/doi/abs/10.1098/rspa.1963.0204.

[22] "The Hubbard model at half a century". In: *Nature Physics* 9.9 (Sept. 2013), pp. 523–523. ISSN: 1745-2481. DOI: 10.1038/nphys2759. URL: https://doi.org/10.1038/nphys2759.

[23] J. Bardeen. "Theory of the Meissner Effect in Superconductors". In: *Phys. Rev.* 97 (6 Mar. 1955), pp. 1724–1725. DOI: 10.1103/PhysRev.97.1724. URL: https://link.aps.org/doi/10.1103/PhysRev.97.1724.

[24] Leon N. Cooper. "Bound Electron Pairs in a Degenerate Fermi Gas". In: *Phys. Rev.* 104 (4 Nov. 1956), pp. 1189–1190. DOI: 10.1103/PhysRev.104.1189. URL: https://link.aps.org/doi/10.1103/PhysRev.104.1189.

[25] J. Bardeen, L. N. Cooper, and J. R. Schrieffer. "Microscopic Theory of Superconductivity". In: *Phys. Rev.* 106 (1 Apr. 1957), pp. 162–164. DOI: 10.1103/PhysRev.106.162. URL: https://link.aps.org/doi/10.1103/PhysRev.106.162.

[26] J. G. Bednorz and K. A. Müller. "Possible highTc superconductivity in the Ba-La-Cu-O system". In: *Zeitschrift für Physik B Condensed Matter* 64.2 (June 1986), pp. 189–193. ISSN: 1431-584X. DOI: 10.1007/BF01303701. URL: %5Curl%7Bhttps://doi.org/10.1007/BF01303701%7D.

[27] Jan M. Tomczak and Silke Biermann. "Optical properties of correlated materials - Or why intelligent windows may look dirty". In: *physica status solidi (b)* 246.9 (2009), pp. 1996–2005. DOI: https://doi.org/10.1002/pssb.200945231. URL: https://onlinelibrary.wiley.com/doi/abs/10.1002/pssb.200945231.

[28] Max Planck. "Ueber das Gesetz der Energieverteilung im Normalspectrum". In: *Annalen der Physik* 309.3 (1901), pp. 553–563. DOI: https://doi.org/10.1002/andp.19013090310. eprint: https://onlinelibrary.wiley.com/doi/pdf/10.1002/andp.19013090310. URL: https://onlinelibrary.wiley.com/doi/abs/10.1002/andp.19013090310.

[29] Molly Kao. "Unification and the Quantum Hypothesis in 1900–1913". In: *Philosophy of Science* 82.5 (2015), pp. 1200–1210. DOI: 10.1086/683648.

[30] A. Einstein. "Über einen die Erzeugung und Verwandlung des Lichtes betreffenden heuristischen Gesichtspunkt". In: *Annalen der Physik* 322.6 (1905), pp. 132–148. DOI: https://doi.org/10.1002/andp.19053220607. eprint: https://onlinelibrary.wiley.com/doi/pdf/10.1002/andp.19053220607. URL: https://onlinelibrary.wiley.com/doi/abs/10.1002/andp.19053220607.

[31] LOUIS DE BROGLIE. "Waves and Quanta". In: *Nature* 112.2815 (Oct. 1923), pp. 540–540. ISSN: 1476-4687. DOI: 10.1038/112540a0. URL: https://doi.org/10.1038/112540a0.

[32] M. Born and R. Oppenheimer. "Zur Quantentheorie der Molekeln". In: *Annalen der Physik* 389.20 (1927), pp. 457–484. DOI: https://doi.org/10.1002/andp.19273892002. eprint: https://onlinelibrary.wiley.com/doi/pdf/10.1002/andp.19273892002. URL: https://onlinelibrary.wiley.com/doi/abs/10.1002/andp.19273892002.

[33] Pablo Echenique and J. L. Alonso. "A mathematical and computational review of Hartree–Fock SCF methods in quantum chemistry". In: *Molecular Physics* 105.23-24 (2007), pp. 3057–3098. DOI: 10.1080/00268970701757875. eprint: https://doi.org/10.1080/00268970701757875. URL: https://doi.org/10.1080/00268970701757875.

[34] Hans-Joachim Werner and Peter J. Knowles. "An efficient internally contracted multiconfiguration–reference configuration interaction method". In: *The Journal of Chemical Physics* 89.9 (1988), pp. 5803–5814. DOI: 10.1063/1.455556. eprint: https://doi.org/10.1063/1.455556. URL: https://doi.org/10.1063/1.455556.

[35] Darwin W. Smith. "N-Representability Problem for Fermion Density Matrices. I. The Second-Order Density Matrix with N =3". In: *The Journal of Chemical Physics* 43.10 (1965), S258–S264. DOI: 10.1063/1.1701504. eprint: https://doi.org/10.1063/1.1701504. URL: https://doi.org/10.1063/1.1701504.

[36] L. H. Thomas. "The calculation of atomic fields". In: *Mathematical Proceedings of the Cambridge Philosophical Society* 23.5 (1927), pp. 542–548. DOI: 10.1017/S0305004100011683.

[37] P. Hohenberg and W. Kohn. "Inhomogeneous Electron Gas". In: *Phys. Rev.* 136 (3B Nov. 1964), B864–B871. DOI: 10.1103/PhysRev.136.B864.

[38] W. Kohn and L. J. Sham. "Self-Consistent Equations Including Exchange and Correlation Effects". In: *Phys. Rev.* 140 (4A Nov. 1965), A1133–A1138. DOI: 10.1103/PhysRev.140.A1133.

[39] P. A. M. Dirac. "Note on Exchange Phenomena in the Thomas Atom". In: *Mathematical Proceedings of the Cambridge Philosophical Society* 26.3 (1930), pp. 376–385. DOI: 10.1017/S0305004100016108.

[40] D. M. Ceperley and B. J. Alder. "Ground State of the Electron Gas by a Stochastic Method". In: *Phys. Rev. Lett.* 45 (7 Aug. 1980), pp. 566–569. DOI: 10.1103/PhysRevLett.45.566. URL: https://link.aps.org/doi/10.1103/PhysRevLett.45.566.

[41] Axel D. Becke. "Perspective: Fifty years of density-functional theory in chemical physics". In: *The Journal of Chemical Physics* 140.18 (2014), 18A301. DOI: 10.1063/1.4869598. eprint: https://doi.org/10.1063/1.4869598. URL: https://doi.org/10.1063/1.4869598.

[42] A. D. Becke. "Density-functional exchange-energy approximation with correct asymptotic behavior". In: *Phys. Rev. A* 38 (6 Sept. 1988), pp. 3098–3100. DOI: 10.1103/PhysRevA.38.3098. URL: https://link.aps.org/doi/10.1103/PhysRevA.38.3098.

[43] John P. Perdew, Kieron Burke, and Matthias Ernzerhof. "Generalized Gradient Approximation Made Simple". In: *Phys. Rev. Lett.* 77 (18 Oct. 1996), pp. 3865–3868. DOI: 10.1103/PhysRevLett.77.3865.

[44] John P. Perdew et al. "Atoms, molecules, solids, and surfaces: Applications of the generalized gradient approximation for exchange and correlation". In: *Phys. Rev. B* 46 (11 Sept. 1992), pp. 6671–6687. DOI: 10.1103/PhysRevB.46.6671. URL: https://link.aps.org/doi/10.1103/PhysRevB.46.6671.

[45] D. R. Hartree. "The Wave Mechanics of an Atom with a Non-Coulomb Central Field. Part II. Some Results and Discussion". In: *Mathematical Proceedings of the Cambridge Philosophical Society* 24.1 (1928), pp. 111–132. DOI: 10.1017/S0305004100011920.

[46] Axel D. Becke. "Density-functional thermochemistry. III. The role of exact exchange". In: *The Journal of Chemical Physics* 98.7 (1993), pp. 5648–5652. DOI: 10.1063/1.464913. eprint: https://doi.org/10.1063/1.464913. URL: https://doi.org/10.1063/1.464913.

[47] Axel D. Becke. "A new mixing of Hartree–Fock and local density-functional theories". In: *The Journal of Chemical Physics* 98.2 (1993), pp. 1372–1377. DOI: 10.1063/1.464304. eprint: https://doi.org/10.1063/1.464304. URL: https://doi.org/10.1063/1.464304.

[48] Dimitar Pashov et al. "Questaal: A package of electronic structure methods based on the linear muffin-tin orbital technique". In: *Computer Physics Communications* 249 (2020), p. 107065. ISSN: 0010-4655. DOI: https://doi.org/10.

1016/j.cpc.2019.107065. URL: https://www.sciencedirect.com/science/article/pii/S0010465519303868.

[49] M Methfessel, Mark van Schilfgaarde, and RA Casali. "Electronic Structure and Physical Properties of Solids: The Uses of the LMTO Method". In: *Lecture Notes in Physics* 535 (2000), p. 114.

[50] David Vanderbilt. "Soft self-consistent pseudopotentials in a generalized eigenvalue formalism". In: *Phys. Rev. B* 41 (11 Apr. 1990), pp. 7892–7895. DOI: 10.1103/PhysRevB.41.7892. URL: https://link.aps.org/doi/10.1103/PhysRevB.41.7892.

[51] Andrew Zangwill. "The education of Walter Kohn and the creation of density functional theory". In: *Archive for History of Exact Sciences* 68.6 (Nov. 2014), pp. 775–848. ISSN: 1432-0657. DOI: 10.1007/s00407-014-0140-x. URL: https://doi.org/10.1007/s00407-014-0140-x.

[52] Klaus Capelle. *A bird's-eye view of density-functional theory*. 2002. DOI: 10.48550/ARXIV.COND-MAT/0211443. URL: https://arxiv.org/abs/cond-mat/0211443.

[53] Lars Goerigk and Nisha Mehta. "A Trip to the Density Functional Theory Zoo: Warnings and Recommendations for the User*". In: *Australian Journal of Chemistry* 72.8 (2019), pp. 563–573. DOI: 10.1071/CH19023. URL: https://doi.org/10.1071/CH19023.

[54] Erich Runge and E. K. U. Gross. "Density-Functional Theory for Time-Dependent Systems". In: *Phys. Rev. Lett.* 52 (12 Mar. 1984), pp. 997–1000. DOI: 10.1103/PhysRevLett.52.997. URL: https://link.aps.org/doi/10.1103/PhysRevLett.52.997.

[55] Jeffrey M. McMahon et al. "The properties of hydrogen and helium under extreme conditions". In: *Rev. Mod. Phys.* 84 (4 Nov. 2012), pp. 1607–1653. DOI: 10.1103/RevModPhys.84.1607. URL: https://link.aps.org/doi/10.1103/RevModPhys.84.1607.

[56] N. David Mermin. "Thermal Properties of the Inhomogeneous Electron Gas". In: *Phys. Rev.* 137 (5A Mar. 1965), A1441–A1443. DOI: 10.1103/PhysRev.137.A1441. URL: https://link.aps.org/doi/10.1103/PhysRev.137.A1441.

[57] Justin C. Smith, Francisca Sagredo, and Kieron Burke. "Warming Up Density Functional Theory". In: *Frontiers of Quantum Chemistry*. Ed. by Marek J. Wójcik et al. Singapore: Springer Singapore, 2018, pp. 249–271. ISBN: 978-981-10-5651-2. DOI: 10.1007/978-981-10-5651-2_11. URL: https://doi.org/10.1007/978-981-10-5651-2_11.

[58] Aurora Pribram-Jones, David A. Gross, and Kieron Burke. "DFT: A Theory Full of Holes?" In: *Annual Review of Physical Chemistry* 66.1 (2015). PMID: 25830374, pp. 283–304. DOI: 10.1146/annurev-physchem-040214-121420. eprint: https://doi.org/10.1146/annurev-physchem-040214-121420. URL: https://doi.org/10.1146/annurev-physchem-040214-121420.

[59] Emmanuel Fromager et al. "Strong correlation in density functional theory: general discussion". In: *Faraday Discuss.* 224 (0 2020), pp. 373–381. DOI: 10.1039/D0FD90025G. URL: http://dx.doi.org/10.1039/D0FD90025G.

[60] J. P. Perdew and Alex Zunger. "Self-interaction correction to density-functional approximations for many-electron systems". In: *Phys. Rev. B* 23 (10 May 1981), pp. 5048–5079. DOI: 10.1103/PhysRevB.23.5048. URL: https://link.aps.org/doi/10.1103/PhysRevB.23.5048.

[61] W. M. Temmerman et al. "On the Implementation of the Self-Interaction Corrected Local Spin Density Approximation for d- and f-Electron Systems". In: *Electronic Structure and Physical Properies of Solids*. Ed. by Hugues Dreyssé. Berlin, Heidelberg: Springer Berlin Heidelberg, 2000, pp. 286–312. ISBN: 978-3-540-46437-2.

[62] A. Svane and O. Gunnarsson. "Transition-metal oxides in the self-interaction–corrected density-functional formalism". In: *Phys. Rev. Lett.* 65 (9 Aug. 1990), pp. 1148–1151. DOI: 10.1103/PhysRevLett.65.1148. URL: https://link.aps.org/doi/10.1103/PhysRevLett.65.1148.

[63] Arti Garg, Mohit Randeria, and Nandini Trivedi. "Strong correlations make high-temperature superconductors robust against disorder". In: *Nature Physics* 4.10 (Oct. 2008), pp. 762–765. ISSN: 1745-2481. DOI: 10.1038/nphys1026. URL: https://doi.org/10.1038/nphys1026.

[64] John Schliemann, S. M. Girvin, and A. H. MacDonald. "Strong Correlation to Weak Correlation Phase Transition in Bilayer Quantum Hall Systems". In: *Phys. Rev. Lett.* 86 (9 Feb. 2001), pp. 1849–1852. DOI: 10.1103/PhysRevLett.86.1849. URL: https://link.aps.org/doi/10.1103/PhysRevLett.86.1849.

[65] K. Mizushima et al. "LixCoO2 (0<x<-1): A new cathode material for batteries of high energy density". In: *Materials Research Bulletin* 15.6 (1980), pp. 783–789. ISSN: 0025-5408. DOI: https://doi.org/10.1016/0025-5408(80)90012-4. URL: https://www.sciencedirect.com/science/article/pii/0025540880900124.

[66] Nicholas A. Besley. "Density Functional Theory Based Methods for the Calculation of X-ray Spectroscopy". In: *Accounts of Chemical Research* 53.7 (July 2020), pp. 1306–1315. ISSN: 0001-4842. DOI: 10.1021/acs.accounts.0c00171. URL: https://doi.org/10.1021/acs.accounts.0c00171.

[67] Soumen Ghosh et al. “Combining Wave Function Methods with Density Functional Theory for Excited States”. In: *Chemical Reviews* 118.15 (Aug. 2018), pp. 7249–7292. ISSN: 0009-2665. DOI: 10.1021/acs.chemrev.8b00193. URL: https://doi.org/10.1021/acs.chemrev.8b00193.

[68] Trygve Helgaker et al. “Recent Advances in Wave Function-Based Methods of Molecular-Property Calculations”. In: *Chemical Reviews* 112.1 (Jan. 2012), pp. 543–631. ISSN: 0009-2665. DOI: 10.1021/cr2002239. URL: https://doi.org/10.1021/cr2002239.

[69] George Green. *An Essay on the Application of mathematical Analysis to the theories of Electricity and Magnetism*. 2008. DOI: 10.48550/ARXIV.0807.0088. URL: https://arxiv.org/abs/0807.0088.

[70] F. J. Dyson. “The S Matrix in Quantum Electrodynamics”. In: *Phys. Rev.* 75 (11 June 1949), pp. 1736–1755. DOI: 10.1103/PhysRev.75.1736. URL: https://link.aps.org/doi/10.1103/PhysRev.75.1736.

[71] R. P. Feynman. “Space-Time Approach to Non-Relativistic Quantum Mechanics”. In: *Rev. Mod. Phys.* 20 (2 Apr. 1948), pp. 367–387. DOI: 10.1103/RevModPhys.20.367. URL: https://link.aps.org/doi/10.1103/RevModPhys.20.367.

[72] Julian Schwinger. *The Greening of Quantum Field Theory: George and I*. 1993. DOI: 10.48550/ARXIV.HEP-PH/9310283. URL: https://arxiv.org/abs/hep-ph/9310283.

[73] Gordon Baym and Leo P. Kadanoff. “Conservation Laws and Correlation Functions”. In: *Phys. Rev.* 124 (2 Oct. 1961), pp. 287–299. DOI: 10.1103/PhysRev.124.287. URL: https://link.aps.org/doi/10.1103/PhysRev.124.287.

[74] Mariana M. Odashima, Beatriz G. Prado, and E. Vernek. “Pedagogical introduction to equilibrium Green’s functions: condensed-matter examples with numerical implementations”. In: *Revista Brasileira de Ensino de Fıé sica* 39.1 (Sept. 2016). DOI: 10.1590/1806-9126-rbef-2016-0087. URL: https://doi.org/10.1590%5C%2F1806-9126-rbef-2016-0087.

[75] Gunnar Källén. “On the Definition of the Renormalization Constants in Quantum Electrodynamics”. In: *Helvetica Physica Acta* 25.IV (1952), p. 417. ISSN: 0018-0238. DOI: 10.5169/seals-112316. URL: https://doi.org/10.5169/seals-112316.

[76] H. Lehmann. “Über Eigenschaften von Ausbreitungsfunktionen und Renormierungskonstanten quantisierter Felder”. In: *Il Nuovo Cimento (1943-1954)* 11.4 (Apr. 1954), pp. 342–357. ISSN: 1827-6121. DOI: 10.1007/BF02783624. URL: https://doi.org/10.1007/BF02783624.

[77] Lucia Reining. "The GW approximation: content, successes and limitations". In: *WIREs Computational Molecular Science* 8.3 (2018), e1344. DOI: https://doi.org/10.1002/wcms.1344. eprint: https://wires.onlinelibrary.wiley.com/doi/pdf/10.1002/wcms.1344. URL: https://wires.onlinelibrary.wiley.com/doi/abs/10.1002/wcms.1344.

[78] Gökhan Esirgen and N. E. Bickers. "Fluctuation-exchange theory for general lattice Hamiltonians". In: *Phys. Rev. B* 55 (4 Jan. 1997), pp. 2122–2143. DOI: 10.1103/PhysRevB.55.2122. URL: https://link.aps.org/doi/10.1103/PhysRevB.55.2122.

[79] Vijay B. Shenoy. *Lecture Notes: Fermions in Disorder*. 2007. URL: http://www.physics.iisc.ac.in/%5C~shenoy/LectureNotes/disorder.pdf.

[80] P. W. Anderson. "Localized Magnetic States in Metals". In: *Phys. Rev.* 124 (1 Oct. 1961), pp. 41–53. DOI: 10.1103/PhysRev.124.41. URL: https://link.aps.org/doi/10.1103/PhysRev.124.41.

[81] C. L. Kane and E. J. Mele. "Z_2 Topological Order and the Quantum Spin Hall Effect". In: *Phys. Rev. Lett.* 95 (14 Sept. 2005), p. 146802. DOI: 10.1103/PhysRevLett.95.146802. URL: https://link.aps.org/doi/10.1103/PhysRevLett.95.146802.

[82] N F Mott and R Peierls. "Discussion of the paper by de Boer and Verwey". In: *Proceedings of the Physical Society* 49.4S (Aug. 1937), p. 72. DOI: 10.1088/0959-5309/49/4S/308. URL: https://dx.doi.org/10.1088/0959-5309/49/4S/308.

[83] J. Hubbard and Brian Hilton Flowers. "Electron correlations in narrow energy bands III. An improved solution". In: *Proceedings of the Royal Society of London. Series A. Mathematical and Physical Sciences* 281.1386 (1964), pp. 401–419. DOI: 10.1098/rspa.1964.0190. eprint: https://royalsocietypublishing.org/doi/pdf/10.1098/rspa.1964.0190. URL: https://royalsocietypublishing.org/doi/abs/10.1098/rspa.1964.0190.

[84] Markus Greiner et al. "Quantum phase transition from a superfluid to a Mott insulator in a gas of ultracold atoms". In: *Nature* 415.6867 (Jan. 2002), pp. 39–44. ISSN: 1476-4687. DOI: 10.1038/415039a. URL: https://doi.org/10.1038/415039a.

[85] Leticia Tarruell and Laurent Sanchez-Palencia. "Quantum simulation of the Hubbard model with ultracold fermions in optical lattices". In: *Comptes Rendus Physique* 19.6 (2018). Quantum simulation / Simulation quantique, pp. 365–393. ISSN: 1631-0705. DOI: https://doi.org/10.1016/j.crhy.2018.10.013. URL: https://www.sciencedirect.com/science/article/pii/S1631070518300926.

[86] Iurii Timrov, Nicola Marzari, and Matteo Cococcioni. "HP – A code for the calculation of Hubbard parameters using density-functional perturbation theory". In: *Computer Physics Communications* 279 (2022), p. 108455. ISSN: 0010-4655. DOI: https://doi.org/10.1016/j.cpc.2022.108455. URL: https://www.sciencedirect.com/science/article/pii/S0010465522001746.

[87] A. I. Liechtenstein, V. I. Anisimov, and J. Zaanen. "Density-functional theory and strong interactions: Orbital ordering in Mott-Hubbard insulators". In: *Phys. Rev. B* 52 (8 Aug. 1995), R5467–R5470. DOI: 10.1103/PhysRevB.52.R5467. URL: https://link.aps.org/doi/10.1103/PhysRevB.52.R5467.

[88] Burak Himmetoglu et al. "Hubbard-corrected DFT energy functionals: The LDA+U description of correlated systems". In: *International Journal of Quantum Chemistry* 114.1 (2014), pp. 14–49. DOI: https://doi.org/10.1002/qua.24521. eprint: https://onlinelibrary.wiley.com/doi/pdf/10.1002/qua.24521. URL: https://onlinelibrary.wiley.com/doi/abs/10.1002/qua.24521.

[89] Vladimir I Anisimov, F Aryasetiawan, and A I Lichtenstein. "First-principles calculations of the electronic structure and spectra of strongly correlated systems: the LDA+ U method". In: *Journal of Physics: Condensed Matter* 9.4 (Jan. 1997), p. 767. DOI: 10.1088/0953-8984/9/4/002. URL: https://dx.doi.org/10.1088/0953-8984/9/4/002.

[90] F. M. F. de Groot et al. "2p x-ray absorption of 3d transition-metal compounds: An atomic multiplet description including the crystal field". In: *Phys. Rev. B* 42 (9 Sept. 1990), pp. 5459–5468. DOI: 10.1103/PhysRevB.42.5459. URL: https://link.aps.org/doi/10.1103/PhysRevB.42.5459.

[91] F. Aryasetiawan et al. "Frequency-dependent local interactions and low-energy effective models from electronic structure calculations". In: *Phys. Rev. B* 70 (19 Nov. 2004), p. 195104. DOI: 10.1103/PhysRevB.70.195104. URL: https://link.aps.org/doi/10.1103/PhysRevB.70.195104.

[92] O. Gunnarsson. "Calculation of parameters in model Hamiltonians". In: *Phys. Rev. B* 41 (1 Jan. 1990), pp. 514–518. DOI: 10.1103/PhysRevB.41.514. URL: https://link.aps.org/doi/10.1103/PhysRevB.41.514.

[93] V. I. Anisimov and O. Gunnarsson. "Density-functional calculation of effective Coulomb interactions in metals". In: *Phys. Rev. B* 43 (10 Apr. 1991), pp. 7570–7574. DOI: 10.1103/PhysRevB.43.7570. URL: https://link.aps.org/doi/10.1103/PhysRevB.43.7570.

[94] A. M. Oles and G. Stollhoff. "Correlation effects in ferromagnetism of transition metals". In: *Phys. Rev. B* 29 (1 Jan. 1984), pp. 314–327. DOI: 10.1103/PhysRevB.29.314. URL: https://link.aps.org/doi/10.1103/PhysRevB.29.314.

[95] Vladimir I. Anisimov, Jan Zaanen, and Ole K. Andersen. "Band theory and Mott insulators: Hubbard U instead of Stoner I". In: *Phys. Rev. B* 44 (3 July 1991), pp. 943–954. DOI: 10.1103/PhysRevB.44.943. URL: https://link.aps.org/doi/10.1103/PhysRevB.44.943.

[96] M. T. Czyżyk and G. A. Sawatzky. "Local-density functional and on-site correlations: The electronic structure of La_2CuO_4 and $LaCuO_3$". In: *Phys. Rev. B* 49 (20 May 1994), pp. 14211–14228. DOI: 10.1103/PhysRevB.49.14211. URL: https://link.aps.org/doi/10.1103/PhysRevB.49.14211.

[97] V. I. Anisimov et al. "Density-functional theory and NiO photoemission spectra". In: *Phys. Rev. B* 48 (23 Dec. 1993), pp. 16929–16934. DOI: 10.1103/PhysRevB.48.16929. URL: https://link.aps.org/doi/10.1103/PhysRevB.48.16929.

[98] K. Held. "Electronic structure calculations using dynamical mean field theory". In: *Advances in Physics* 56.6 (2007), pp. 829–926. DOI: 10.1080/00018730701619647. eprint: https://doi.org/10.1080/00018730701619647. URL: https://doi.org/10.1080/00018730701619647.

[99] S. L. Dudarev et al. "Electron-energy-loss spectra and the structural stability of nickel oxide: An LSDA+U study". In: *Phys. Rev. B* 57 (3 Jan. 1998), pp. 1505–1509. DOI: 10.1103/PhysRevB.57.1505. URL: https://link.aps.org/doi/10.1103/PhysRevB.57.1505.

[100] A. G. Petukhov et al. "Correlated metals and the LDA + U method". In: *Phys. Rev. B* 67 (15 Apr. 2003), p. 153106. DOI: 10.1103/PhysRevB.67.153106. URL: https://link.aps.org/doi/10.1103/PhysRevB.67.153106.

[101] Berenike Stahl and Thomas Bredow. "Critical Assessment of the DFT + U Approach for the Prediction of Vanadium Dioxide Properties". In: *Journal of Computational Chemistry* 41.3 (2020), pp. 258–265. DOI: https://doi.org/10.1002/jcc.26096. eprint: https://onlinelibrary.wiley.com/doi/pdf/10.1002/jcc.26096. URL: https://onlinelibrary.wiley.com/doi/abs/10.1002/jcc.26096.

[102] Takeo Matsubara and Yutaka Toyozawa. "Theory of Impurity Band Conduction in Semiconductors: An Approach to Random Lattice Problem". In: *Progress of Theoretical Physics* 26.5 (Nov. 1961), pp. 739–756. ISSN: 0033-068X. DOI: 10.1143/PTP.26.739. eprint: https://academic.oup.com/ptp/article-pdf/26/5/739/5455052/26-5-739.pdf. URL: https://doi.org/10.1143/PTP.26.739.

[103] Raymond Frésard and Gabriel Kotliar. "Interplay of Mott transition and ferromagnetism in the orbitally degenerate Hubbard model". In: *Phys. Rev. B* 56 (20 Nov. 1997), pp. 12909–12915. DOI: 10.1103/PhysRevB.56.12909. URL: https://link.aps.org/doi/10.1103/PhysRevB.56.12909.

[104] R D Mattuck. “Guide to Feynman diagrams in the many-body problem”. In: Jan. 1967. URL: https://www.osti.gov/biblio/7347199.

[105] Walter Metzner and Dieter Vollhardt. “Correlated Lattice Fermions in $d = \infty$ Dimensions”. In: *Phys. Rev. Lett.* 62 (3 Jan. 1989), pp. 324–327. DOI: 10.1103/PhysRevLett.62.324.

[106] Antoine Georges and Gabriel Kotliar. “Hubbard model in infinite dimensions”. In: *Phys. Rev. B* 45 (12 Mar. 1992), pp. 6479–6483. DOI: 10.1103/PhysRevB.45.6479.

[107] Gunnar Källén. “On the Definition of the Renormalization Constants in Quantum Electrodynamics”. In: *Helvetica Physica Acta* 25.IV (1952), p. 417. ISSN: 0018-0238. DOI: 10.5169/seals-112316. URL: https://doi.org/10.5169/seals-112316.

[108] M. J. Rozenberg, G. Kotliar, and X. Y. Zhang. “Mott-Hubbard transition in infinite dimensions. II”. In: *Phys. Rev. B* 49 (15 Apr. 1994), pp. 10181–10193. DOI: 10.1103/PhysRevB.49.10181. URL: https://link.aps.org/doi/10.1103/PhysRevB.49.10181.

[109] M. J. Rozenberg et al. “Optical Conductivity in Mott-Hubbard Systems”. In: *Phys. Rev. Lett.* 75 (1 July 1995), pp. 105–108. DOI: 10.1103/PhysRevLett.75.105. URL: https://link.aps.org/doi/10.1103/PhysRevLett.75.105.

[110] Henrik Kajueter and Gabriel Kotliar. “New Iterative Perturbation Scheme for Lattice Models with Arbitrary Filling”. In: *Phys. Rev. Lett.* 77 (1 July 1996), pp. 131–134. DOI: 10.1103/PhysRevLett.77.131. URL: https://link.aps.org/doi/10.1103/PhysRevLett.77.131.

[111] A Martıén-Rodero et al. “Interpolative solution for the periodic Anderson model of mixed-valence compounds”. en. In: *Phys Rev B Condens Matter* 33.3 (Feb. 1986), pp. 1814–1822.

[112] H. Padé. “Sur la représentation approchée d’une fonction par des fractions rationnelles”. fre. In: *Annales scientifiques de l’École Normale Supérieure* 9 (1892), pp. 3–93. URL: http://eudml.org/doc/81047.

[113] H. A. Bethe and William Lawrence Bragg. “Statistical theory of superlattices”. In: *Proceedings of the Royal Society of London. Series A - Mathematical and Physical Sciences* 150.871 (1935), pp. 552–575. DOI: 10.1098/rspa.1935.0122. eprint: https://royalsocietypublishing.org/doi/pdf/10.1098/rspa.1935.0122. URL: https://royalsocietypublishing.org/doi/abs/10.1098/rspa.1935.0122.

[114] E. Müller-Hartmann. "The Hubbard model at high dimensions: some exact results and weak coupling theory". In: *Zeitschrift für Physik B Condensed Matter* 76.2 (June 1989), pp. 211–217. ISSN: 1431-584X. DOI: 10.1007/BF01312686. URL: https://doi.org/10.1007/BF01312686.

[115] O. W. Richardson. "On the Negative Radiation from Hot Platinum". In: *Proceedings of the Cambridge Philosophical Society: Mathematical and physical sciences*. Vol. 11. Cambridge Univ. Press., 1901, pp. 286–295. URL: https://doi.org/10.1007/3-540-37586-4_1.

[116] C.R. Crowell. "The Richardson constant for thermionic emission in Schottky barrier diodes". In: *Solid-State Electronics* 8.4 (1965), pp. 395–399. ISSN: 0038-1101. DOI: https://doi.org/10.1016/0038-1101(65)90116-4. URL: https://www.sciencedirect.com/science/article/pii/0038110165901164.

[117] Shi-Jun Liang and L. K. Ang. "Electron Thermionic Emission from Graphene and a Thermionic Energy Converter". In: *Phys. Rev. Applied* 3 (1 Jan. 2015), p. 014002. DOI: 10.1103/PhysRevApplied.3.014002. URL: https://link.aps.org/doi/10.1103/PhysRevApplied.3.014002.

[118] Yee Sin Ang et al. "Generalized High-Energy Thermionic Electron Injection at Graphene Interface". In: *Phys. Rev. Applied* 12 (1 July 2019), p. 014057. DOI: 10.1103/PhysRevApplied.12.014057. URL: https://link.aps.org/doi/10.1103/PhysRevApplied.12.014057.

[119] In: *Handbook of Charged Particle Optics*. Ed. by J. Orloff. Vol. 11. CRC Press, 2009, pp. 5–6. URL: https://doi.org/10.1201/9781420045550.

[120] Yee Sin Ang, Hui Ying Yang, and L. K. Ang. "Universal Scaling Laws in Schottky Heterostructures Based on Two-Dimensional Materials". In: *Phys. Rev. Lett.* 121 (5 Aug. 2018), p. 056802. DOI: 10.1103/PhysRevLett.121.056802. URL: https://link.aps.org/doi/10.1103/PhysRevLett.121.056802.

[121] L. Esaki, Y. Kurose, and T. Suzuki. "19F-23 Ge P-N Junction Internal Field Emission". In: *Meeting Abstracts of the Physical Society of Japan* 12.5.0 (1957), p. 85. ISSN: 2433-1163. DOI: 10.11316/jpsgaiyoi.12.5.0_85. URL: https://cir.nii.ac.jp/crid/1390001206165405440.

[122] Chulbum Kim et al. "11.4 A 512Gb 3b/cell 64-stacked WL 3D V-NAND flash memory". In: *2017 IEEE International Solid-State Circuits Conference (ISSCC)*. 2017, pp. 202–203. DOI: 10.1109/ISSCC.2017.7870331.

[123] G. Binnig and H. Rohrer. "Scanning tunneling microscopy". In: *Helvetica Physica Acta* 55.6 (1982), p. 726. ISSN: 0018-0238. DOI: 10.5169/seals-115309. URL: https://doi.org/10.5169/seals-115309.

[124] Soudip Sinha Roy. "Simplification of master power expression and effective power detection of QCA device (Wave nature tunneling of electron in QCA device)". In: *2016 IEEE Students' Technology Symposium (TechSym)*. 2016, pp. 272–277. DOI: 10.1109/TechSym.2016.7872695.

[125] Adrian M. Ionescu and Heike Riel. "Tunnel field-effect transistors as energy-efficient electronic switches". In: *Nature* 479.7373 (Nov. 2011), pp. 329–337. ISSN: 1476-4687. DOI: 10.1038/nature10679. URL: https://doi.org/10.1038/nature10679.

[126] A. B. Balantekin and N. Takigawa. "Quantum tunneling in nuclear fusion". In: *Rev. Mod. Phys.* 70 (1 Jan. 1998), pp. 77–100. DOI: 10.1103/RevModPhys.70.77. URL: https://link.aps.org/doi/10.1103/RevModPhys.70.77.

[127] Saumitra Raj Mehrotra and Gerhard Klimeck. *Resonant Tunneling Diode operation*. Apr. 2010. URL: https://nanohub.org/resources/8799.

[128] Mark Sweeny and Jingming Xu. "Resonant interband tunnel diodes". In: *Applied Physics Letters* 54.6 (1989), pp. 546–548. DOI: 10.1063/1.100926. eprint: https://doi.org/10.1063/1.100926. URL: https://doi.org/10.1063/1.100926.

[129] Sean L. Rommel et al. "Room temperature operation of epitaxially grown Si/Si0.5Ge0.5/Si resonant interband tunneling diodes". In: *Applied Physics Letters* 73.15 (1998), pp. 2191–2193. DOI: 10.1063/1.122419. eprint: https://doi.org/10.1063/1.122419. URL: https://doi.org/10.1063/1.122419.

[130] R. Landauer. "Spatial Variation of Currents and Fields Due to Localized Scatterers in Metallic Conduction". In: *IBM Journal of Research and Development* 1.3 (1957), pp. 223–231. DOI: 10.1147/rd.13.0223.

[131] Rolf Landauer. "Electrical resistance of disordered one-dimensional lattices". In: *The Philosophical Magazine: A Journal of Theoretical Experimental and Applied Physics* 21.172 (Apr. 1970), pp. 863–867. ISSN: 0031-8086. DOI: 10.1080/14786437008238472. URL: https://doi.org/10.1080/14786437008238472.

[132] M. Büttiker et al. "Generalized many-channel conductance formula with application to small rings". In: *Phys. Rev. B* 31 (10 May 1985), pp. 6207–6215. DOI: 10.1103/PhysRevB.31.6207. URL: https://link.aps.org/doi/10.1103/PhysRevB.31.6207.

[133] A. R. Rocha et al. "Spin and molecular electronics in atomically generated orbital landscapes". In: *Phys. Rev. B* 73 (8 Feb. 2006), p. 085414. DOI: 10.1103/PhysRevB.73.085414. URL: https://link.aps.org/doi/10.1103/PhysRevB.73.085414.

[134] Alexandre R. Rocha et al. "Towards molecular spintronics". In: *Nature Materials* 4.4 (Apr. 2005), pp. 335–339. ISSN: 1476-4660. DOI: 10.1038/nmat1349. URL: https://doi.org/10.1038/nmat1349.

[135] Rungger I. *Computational methods for electron transport and their application in nanodevices [PhD dissertation]*. Trinity College (Dublin, Ireland). School of Physics, 2009. URL: http://hdl.handle.net/2262/90575.

[136] Ivan Rungger and Stefano Sanvito. "Algorithm for the construction of self-energies for electronic transport calculations based on singularity elimination and singular value decomposition". In: *Phys. Rev. B* 78 (3 July 2008), p. 035407. DOI: 10.1103/PhysRevB.78.035407. URL: https://link.aps.org/doi/10.1103/PhysRevB.78.035407.

[137] A. Droghetti and I. Rungger. *Nanophysics sourcebook. Quantum Transport Simulations of Nano-systems: An Introduction to the Green's Function Approach*. Springer Handbook of Materials. Volume 1 Methods: Theory and Modelling, 2018. URL: http://nano-bio.ehu.es/non-equilibrium-green-s-functions-spin-transport-and-dynamics.

[138] Andrea Droghetti and Ivan Rungger. "Quantum transport simulation scheme including strong correlations and its application to organic radicals adsorbed on gold". In: *Phys. Rev. B* 95 (8 Feb. 2017), p. 085131. DOI: 10.1103/PhysRevB.95.085131. URL: https://link.aps.org/doi/10.1103/PhysRevB.95.085131.

[139] M.J. Verstraete and Z. Zanolli. *Density Functional Perturbation Theory*. 2013. URL: https://zeilazanolli.files.wordpress.com/2019/04/2013_dfpt_c2_verstraete_zanolli.pdf.

[140] Rolf Heid. *Density Functional Perturbation Theory and Electron Phonon Coupling*. 2013. URL: https://www.cond-mat.de/events/correl13/manuscripts/heid.pdf.

[141] M. T. Yin and Marvin L. Cohen. "Microscopic Theory of the Phase Transformation and Lattice Dynamics of Si". In: *Phys. Rev. Lett.* 45 (12 Sept. 1980), pp. 1004–1007. DOI: 10.1103/PhysRevLett.45.1004. URL: https://link.aps.org/doi/10.1103/PhysRevLett.45.1004.

[142] R. P. Feynman. "Forces in Molecules". In: *Phys. Rev.* 56 (4 Aug. 1939), pp. 340–343. DOI: 10.1103/PhysRev.56.340. URL: https://link.aps.org/doi/10.1103/PhysRev.56.340.

[143] Stefano Baroni et al. "Phonons and related crystal properties from density-functional perturbation theory". In: *Rev. Mod. Phys.* 73 (2 July 2001), pp. 515–562. DOI: 10.1103/RevModPhys.73.515. URL: https://link.aps.org/doi/10.1103/RevModPhys.73.515.

[144] D K Blat, N E Zein, and V I Zinenko. "Calculations of phonon frequencies and dielectric constants of alkali hydrides via the density functional method". In: *Journal of Physics: Condensed Matter* 3.29 (July 1991), p. 5515. DOI: 10.1088/0953-8984/3/29/006. URL: https://dx.doi.org/10.1088/0953-8984/3/29/006.

[145] N.E. Zein. "Ab initio calculations of phonon dispersion curves. Application to Nb and Mo". In: *Physics Letters A* 161.6 (1992), pp. 526–530. ISSN: 0375-9601. DOI: https://doi.org/10.1016/0375-9601(92)91086-7. URL: https://www.sciencedirect.com/science/article/pii/0375960192910867.

[146] Stefano Baroni, Paolo Giannozzi, and Andrea Testa. "Green's-function approach to linear response in solids". In: *Phys. Rev. Lett.* 58 (18 May 1987), pp. 1861–1864. DOI: 10.1103/PhysRevLett.58.1861. URL: https://link.aps.org/doi/10.1103/PhysRevLett.58.1861.

[147] Paolo Giannozzi et al. "Ab initio calculation of phonon dispersions in semiconductors". In: *Phys. Rev. B* 43 (9 Mar. 1991), pp. 7231–7242. DOI: 10.1103/PhysRevB.43.7231. URL: https://link.aps.org/doi/10.1103/PhysRevB.43.7231.

[148] P. Delhaès et al. "Polymorphism and Structure of Carbons". In: *Understanding Carbon Nanotubes: From Basics to Applications*. Ed. by Annick Loiseau et al. Berlin, Heidelberg: Springer Berlin Heidelberg, 2006, pp. 1–47. ISBN: 978-3-540-37586-9. DOI: 10.1007/3-540-37586-4_1. URL: https://doi.org/10.1007/3-540-37586-4_1.

[149] Eric B. Jones and Vladan Stevanović. "Polymorphism in elemental silicon: Probabilistic interpretation of the realizability of metastable structures". In: *Phys. Rev. B* 96 (18 Nov. 2017), p. 184101. DOI: 10.1103/PhysRevB.96.184101. URL: https://link.aps.org/doi/10.1103/PhysRevB.96.184101.

[150] Bianca Haberl, Timothy A. Strobel, and Jodie E. Bradby. "Pathways to exotic metastable silicon allotropes". In: *Applied Physics Reviews* 3.4 (2016), p. 040808. DOI: 10.1063/1.4962984. eprint: https://doi.org/10.1063/1.4962984. URL: https://doi.org/10.1063/1.4962984.

[151] Azadeh Amiri and Reza Shahbazian-Yassar. "Recent progress of high-entropy materials for energy storage and conversion". In: *J. Mater. Chem. A* 9 (2 2021), pp. 782–823. DOI: 10.1039/D0TA09578H. URL: http://dx.doi.org/10.1039/D0TA09578H.

[152] Scott M. Woodley et al. "The prediction of inorganic crystal structures using a genetic algorithm and energy minimisation". In: *Phys. Chem. Chem. Phys.* 1 (10 1999), pp. 2535–2542. DOI: 10.1039/A901227C. URL: http://dx.doi.org/10.1039/A901227C.

[153] X. Zhang et al. "Prediction of A_2BX_4 metal-chalcogenide compounds via first-principles thermodynamics". In: *Phys. Rev. B* 86 (1 July 2012), p. 014109. DOI: 10.1103/PhysRevB.86.014109. URL: https://link.aps.org/doi/10.1103/PhysRevB.86.014109.

[154] Chris J. Pickard and R. J. Needs. "High-Pressure Phases of Silane". In: *Phys. Rev. Lett.* 97 (4 July 2006), p. 045504. DOI: 10.1103/PhysRevLett.97.045504. URL: https://link.aps.org/doi/10.1103/PhysRevLett.97.045504.

[155] Chris J Pickard and R J Needs. "*Ab initio* random structure searching". In: *Journal of Physics: Condensed Matter* 23.5 (Jan. 2011), p. 053201. DOI: 10.1088/0953-8984/23/5/053201. URL: https://doi.org/10.1088/0953-8984/23/5/053201.

[156] Vladan Stevanović. "Sampling Polymorphs of Ionic Solids using Random Superlattices". In: *Phys. Rev. Lett.* 116 (7 Feb. 2016), p. 075503. DOI: 10.1103/PhysRevLett.116.075503. URL: https://link.aps.org/doi/10.1103/PhysRevLett.116.075503.

[157] Sergey V. Krivovichev. "Structural complexity and configurational entropy of crystals". In: *Acta Crystallographica Section B* 72.2 (Apr. 2016), pp. 274–276. DOI: 10.1107/S205252061501906X. URL: https://doi.org/10.1107/S205252061501906X.

[158] Vinothan N. Manoharan. "Colloidal matter: Packing, geometry, and entropy". In: *Science* 349.6251 (2015), p. 1253751. DOI: 10.1126/science.1253751. eprint: https://www.science.org/doi/pdf/10.1126/science.1253751. URL: https://www.science.org/doi/abs/10.1126/science.1253751.

[159] Christopher J. Bartel et al. "Physical descriptor for the Gibbs energy of inorganic crystalline solids and temperature-dependent materials chemistry". In: *Nature Communications* 9.1 (Oct. 2018), p. 4168. ISSN: 2041-1723. DOI: 10.1038/s41467-018-06682-4. URL: https://doi.org/10.1038/s41467-018-06682-4.

[160] Pranab Sarker et al. "High-entropy high-hardness metal carbides discovered by entropy descriptors". In: *Nature Communications* 9.1 (Nov. 2018), p. 4980. ISSN: 2041-1723. DOI: 10.1038/s41467-018-07160-7. URL: https://doi.org/10.1038/s41467-018-07160-7.

[161] Andrew Burke et al. "Long-term survival following a single treatment of kidney tumors with multiwalled carbon nanotubes and near-infrared radiation". en. In: *Proc Natl Acad Sci U S A* 106.31 (July 2009), pp. 12897–12902.

[162] Mahmoud Enieb and Aboelkasim Diab. "Characteristics of asphalt binder and mixture containing nanosilica". In: *International Journal of Pavement Research and Technology* 10.2 (2017), pp. 148–157. ISSN: 1996-6814. DOI: https://doi.org/10.1016/j.ijprt.2016.11.009. URL: https://www.sciencedirect.com/science/article/pii/S1996681416301262.

[163] Elena Serrano, Guillermo Rus, and Javier García-Martínez. "Nanotechnology for sustainable energy". In: *Renewable and Sustainable Energy Reviews* 13.9 (2009), pp. 2373–2384. ISSN: 1364-0321. DOI: https://doi.org/10.1016/j.rser.2009.06.003. URL: https://www.sciencedirect.com/science/article/pii/S1364032109001087.

[164] Peng-Cheng Chen et al. "Interface and heterostructure design in polyelemental nanoparticles". In: *Science* 363.6430 (2019), pp. 959–964. DOI: 10.1126/science.aav4302. eprint: https://www.science.org/doi/pdf/10.1126/science.aav4302. URL: https://www.science.org/doi/abs/10.1126/science.aav4302.

[165] Lei Zhu et al. "Noble-Metal-Free CdS Nanoparticle-Coated Graphene Oxide Nanosheets Favoring Electron Transfer for Efficient Photoreduction of CO2". In: *ACS Applied Materials & Interfaces* 12.11 (Mar. 2020), pp. 12892–12900. ISSN: 1944-8244. DOI: 10.1021/acsami.0c00163. URL: https://doi.org/10.1021/acsami.0c00163.

[166] Yoshitaka Kawasugi et al. "Field-Induced Carrier Delocalization in the Strain-Induced Mott Insulating State of an Organic Superconductor". In: *Phys. Rev. Lett.* 103 (11 Sept. 2009), p. 116801. DOI: 10.1103/PhysRevLett.103.116801. URL: https://link.aps.org/doi/10.1103/PhysRevLett.103.116801.

[167] M. Nakano et al. "Collective bulk carrier delocalization driven by electrostatic surface charge accumulation". In: *Nature* 487.7408 (July 2012), pp. 459–462. ISSN: 1476-4687. DOI: 10.1038/nature11296. URL: https://doi.org/10.1038/nature11296.

[168] Zhicheng Zhong et al. "Electronics with Correlated Oxides: $SrVO_3/SrTiO_3$ as a Mott Transistor". In: *Phys. Rev. Lett.* 114 (24 June 2015), p. 246401. DOI: 10.1103/PhysRevLett.114.246401. URL: https://link.aps.org/doi/10.1103/PhysRevLett.114.246401.

[169] L. V. Keldysh. "Diagram technique for nonequilibrium processes". In: *Zh. Eksp. Teor. Fiz.* 47 (1964), pp. 1515–1527.

[170] R. Tsu and L. Esaki. "Tunneling in a finite superlattice". In: *Applied Physics Letters* 22.11 (1973), pp. 562–564. DOI: 10.1063/1.1654509. eprint: https://doi.org/10.1063/1.1654509. URL: https://doi.org/10.1063/1.1654509.

[171] T. C. L. G. Sollner et al. “Resonant tunneling through quantum wells at frequencies up to 2.5 THz”. In: *Applied Physics Letters* 43.6 (1983), pp. 588–590. DOI: 10.1063/1.94434. eprint: https://doi.org/10.1063/1.94434. URL: https://doi.org/10.1063/1.94434.

[172] Daryoosh Saeedkia. “Handbook of terahertz technology for imaging, sensing and communications”. In: 2013.

[173] R. Yukawa et al. “Resonant tunneling driven metal-insulator transition in double quantum-well structures of strongly correlated oxide”. In: *Nature Communications* 12.1 (Dec. 2021), p. 7070. ISSN: 2041-1723. DOI: 10.1038/s41467-021-27327-z. URL: https://doi.org/10.1038/s41467-021-27327-z.

[174] V. Meden et al. “Correlation effects on resonant tunneling in one-dimensional quantum wires”. In: *Phys. Rev. B* 71 (4 Jan. 2005), p. 041302. DOI: 10.1103/PhysRevB.71.041302. URL: https://link.aps.org/doi/10.1103/PhysRevB.71.041302.

[175] Rajinder Mavi and Jeffrey Schenker. “Resonant tunneling in a system with correlated pure point spectrum”. In: *Journal of Mathematical Physics* 60.5 (2019), p. 052103. DOI: 10.1063/1.5075623. eprint: https://doi.org/10.1063/1.5075623. URL: https://doi.org/10.1063/1.5075623.

[176] Irakli Titvinidze et al. “Resonance effects in correlated multilayer heterostructures”. In: *Phys. Rev. B* 94 (24 Dec. 2016), p. 245142. DOI: 10.1103/PhysRevB.94.245142. URL: https://link.aps.org/doi/10.1103/PhysRevB.94.245142.

[177] Gordon E Moore. “Cramming more components onto integrated circuits”. In: *Electronics,* 38.8 (1965).

[178] CARLENE STEPHENS and MAGGIE DENNIS. “Engineering time: inventing the electronic wristwatch”. In: *The British Journal for the History of Science* 33.4 (2000), pp. 477–497. DOI: 10.1017/S0007087400004167.

[179] C. Batten et al. *42 Years of Microprocessor Trend Data*. https://github.com/karlrupp/microprocessor-trend-data. 2018.

[180] Kihyun Choi et al. “Reliability on Evolutionary FinFET CMOS Technology and Beyond”. In: *2020 IEEE International Electron Devices Meeting (IEDM)*. 2020, pp. 9.3.1–9.3.4. DOI: 10.1109/IEDM13553.2020.9371930.

[181] Hasan Goktas and Mona E. Zaghloul. “Tuning In-Plane Fixed-Fixed Beam Resonators With Embedded Heater in CMOS Technology”. In: *IEEE Electron Device Letters* 36.2 (2015), pp. 189–191. DOI: 10.1109/LED.2014.2381557.

[182] Dennis M. Newns et al. “High Response Piezoelectric and Piezoresistive Materials for Fast, Low Voltage Switching: Simulation and Theory of Transduction Physics at the Nanometer-Scale”. In: *Advanced Materials* 24.27 (2012), pp. 3672–3677. DOI: https://doi.org/10.1002/adma.201104617.

[183] Stanley Kon, Kenn Oldham, and Roberto Horowitz. "Piezoresistive and piezoelectric MEMS strain sensors for vibration detection". In: *Sensors and Smart Structures Technologies for Civil, Mechanical, and Aerospace Systems 2007*. Ed. by Masayoshi Tomizuka, Chung-Bang Yun, and Victor Giurgiutiu. Vol. 6529. International Society for Optics and Photonics. SPIE, 2007, p. 65292V. DOI: 10.1117/12.715814. URL: https://doi.org/10.1117/12.715814.

[184] P Ciureanu. *Thin Film Resistive Sensors, (Sensors Series)*. CRC Press, 1992.

[185] Hari S Nalwa. *Handbook of Thin Film Materials*. Vol. 3. Academic Press, 2002.

[186] D. M. Newns et al. "The piezoelectronic transistor: A nanoactuator-based post-CMOS digital switch with high speed and low power". In: *MRS Bulletin* 37.11 (Nov. 2012), pp. 1071–1076. ISSN: 1938-1425. DOI: 10.1557/mrs.2012.267. URL: https://doi.org/10.1557/mrs.2012.267.

[187] Hwang-Pill Kim et al. "5 - Piezoelectrics". In: *Advanced Ceramics for Energy Conversion and Storage*. Ed. by Olivier Guillon. Elsevier Series on Advanced Ceramic Materials. Elsevier, 2020, pp. 157–206. ISBN: 978-0-08-102726-4. DOI: https://doi.org/10.1016/B978-0-08-102726-4.00005-3. URL: https://www.sciencedirect.com/science/article/pii/B9780081027264000053.

[188] S. H. Baek et al. "Giant Piezoelectricity on Si for Hyperactive MEMS". In: *Science* 334.6058 (2011), pp. 958–961. DOI: 10.1126/science.1207186. eprint: https://www.science.org/doi/pdf/10.1126/science.1207186. URL: https://www.science.org/doi/abs/10.1126/science.1207186.

[189] Seung-Eek Park and Thomas R. Shrout. "Ultrahigh strain and piezoelectric behavior in relaxor based ferroelectric single crystals". In: *Journal of Applied Physics* 82.4 (1997), pp. 1804–1811. DOI: 10.1063/1.365983. eprint: https://doi.org/10.1063/1.365983. URL: https://doi.org/10.1063/1.365983.

[190] Dennis Newns et al. "A low-voltage high-speed electronic switch based on piezoelectric transduction". In: *Journal of Applied Physics* 111.8 (2012), p. 084509. DOI: 10.1063/1.4704391. eprint: https://doi.org/10.1063/1.4704391. URL: https://doi.org/10.1063/1.4704391.

[191] Zhengping Jiang et al. "Electron transport in nano-scaled piezoelectronic devices". In: *Applied Physics Letters* 102.19 (2013), p. 193501. DOI: 10.1063/1.4804601. eprint: https://doi.org/10.1063/1.4804601. URL: https://doi.org/10.1063/1.4804601.

[192] A. Alvin Barlian et al. "Review: Semiconductor Piezoresistance for Microsystems". In: *Proceedings of the IEEE* 97.3 (2009), pp. 513–552. DOI: 10.1109/JPROC.2009.2013612.

[193] A. Jayaraman et al. “Pressure-Induced Metal-Semiconductor Transition and $4f$ Electron Delocalization in Sm Te”. In: *Phys. Rev. Lett.* 25 (6 Aug. 1970), pp. 368–370. DOI: 10.1103/PhysRevLett.25.368.

[194] A Jayaraman et al. “Continuous and Discontinuous Semiconductor-Metal Transition in Samarium Monochalcogenides Under Pressure”. In: *Phys. Rev. Lett.* 25.20 (Nov. 1970), p. 1430.

[195] M. B. Maple and D. Wohlleben. “Nonmagnetic $4f$ Shell in the High-Pressure Phase of SmS”. In: *Phys. Rev. Lett.* 27 (8 Aug. 1971), pp. 511–515. DOI: 10.1103/PhysRevLett.27.511.

[196] P. P. Deen et al. “Structural and electronic transitions in the low-temperature, high-pressure phase of SmS”. In: *Phys. Rev. B* 71 (24 June 2005), p. 245118. DOI: 10.1103/PhysRevB.71.245118.

[197] M. Copel et al. “Giant Piezoresistive On/Off Ratios in Rare-Earth Chalcogenide Thin Films Enabling Nanomechanical Switching”. In: *Nano Letters* 13.10 (Oct. 2013), pp. 4650–4653. ISSN: 1530-6984. DOI: 10.1021/nl401710f. URL: https://doi.org/10.1021/nl401710f.

[198] Andreas Sousanis et al. “Switchable Piezoresistive SmS Thin Films on Large Area”. In: *Sensors* 19.20 (2019). ISSN: 1424-8220. DOI: 10.3390/s19204390.

[199] Andreas Sousanis, Philippe F. Smet, and Dirk Poelman. “Samarium Monosulfide (SmS): Reviewing Properties and Applications”. In: *Materials* 10.8 (2017). ISSN: 1996-1944. DOI: 10.3390/ma10080953.

[200] Liu C. “Foundations of MEMS”. In: Pearson/Prentice Hall, 2006.

[201] T. Toriyama, Y. Tanimoto, and S. Sugiyama. “Single crystal silicon nano-wire piezoresistors for mechanical sensors”. In: *Journal of Microelectromechanical Systems* 11.5 (2002), pp. 605–611. DOI: 10.1109/JMEMS.2002.802905.

[202] Rongrui He and Peidong Yang. “Giant piezoresistance effect in silicon nanowires”. In: *Nature Nanotechnology* 1.1 (Oct. 2006), pp. 42–46. ISSN: 1748-3395. DOI: 10.1038/nnano.2006.53. URL: https://doi.org/10.1038/nnano.2006.53.

[203] Yangmu Li et al. “Strongly-overdoped La$_{2-x}$Sr$_x$CuO$_4$: Evidence for Josephson-coupled grains of strongly-correlated superconductor”. In: 2022.

[204] A. Sigel and H. Sigel. “The lanthanides and their interrelations with biosystems”. In: New York: Marcel Dekker, 2003.

[205] Barry T. Kilbourn. “The role of the lanthanides in applied catalysis”. In: *Journal of the Less Common Metals* 126 (1986). Proceedings of the Seventeenth Rare Earth Research Conference - Part 1, pp. 101–106. ISSN: 0022-5088. DOI: https://doi.org/10.1016/0022-5088(86)90254-7. URL: https://www.sciencedirect.com/science/article/pii/0022508886902547.

[206] A A Palizban, H Sadeghi-Aliabadi, and F Abdollahpour. "Effect of cerium lanthanide on Hela and MCF-7 cancer cell growth in the presence of transferring". en. In: *Res Pharm Sci* 5.2 (July 2010), pp. 119–125.

[207] Hans L. Skriver. "Crystal structure from one-electron theory". In: *Phys. Rev. B* 31 (4 Feb. 1985), pp. 1909–1923. DOI: 10.1103/PhysRevB.31.1909.

[208] U. Lundin et al. "Modification of the standard model for the lanthanides". In: *Solid State Communications* 115.1 (2000), pp. 7–12. ISSN: 0038-1098. DOI: https://doi.org/10.1016/S0038-1098(00)00126-5. URL: https://www.sciencedirect.com/science/article/pii/S0038109800001265.

[209] V. N. Antonov, B. N. Harmon, and A. N. Yaresko. "Electronic structure of mixed-valence semiconductors in the LSDA + U approximation. I. Sm monochalcogenides". In: *Phys. Rev. B* 66 (16 Oct. 2002), p. 165208. DOI: 10.1103/PhysRevB.66.165208.

[210] A. Svane et al. "Electronic structure of Sm and Eu chalcogenides". In: *phys. Stat. Sol. (b)* 241 (14 Oct. 2004), pp. 3185–3192. DOI: 10.1002/pssb.200405226.

[211] A. Svane et al. "Electronic structure of samarium monopnictides and monochalcogenides". In: *Phys. Rev. B* 71 (4 Jan. 2005), p. 045119. DOI: 10.1103/PhysRevB.71.045119.

[212] L. Petit et al. "Rare-earth pnictides and chalcogenides from first-principles". In: *Journal of physics. Condensed matter* 28 (22 June 2016), p. 223001. DOI: 10.1088/0953-8984/28/22/223001.

[213] D C Gupta and Subhra Kulshrestha. "Pressure induced magnetic, electronic and mechanical properties of SmX (X = Se, Te)". In: *Journal of Physics: Condensed Matter* 21.43 (Oct. 2009), p. 436011. DOI: 10.1088/0953-8984/21/43/436011.

[214] M. Singh, A. Gour, and S. Singh. In: *High Pressure Phase Transition and Allied Behavior of Samarium Compounds*. 2013.

[215] Shilpa Kapoor, Namrata Yaduvanshi, and Sadhna Singh. "Analysis of structural and elastic properties of SmS under high pressure including temperature effects". In: *Ferroelectrics* 519.1 (2017), pp. 139–144. DOI: 10.1080/00150193.2017.1361228.

[216] Ritu Dubey and Sadhna Singh. "High pressure phase transition in samarium monochalcogenides SmX (X=S, Se, Te) and their alloy $SmS_{1-x}Se_x$". In: *Journal of Molecular Structure* 1052 (2013), pp. 204–213. ISSN: 0022-2860. DOI: https://doi.org/10.1016/j.molstruc.2013.08.062.

[217] Shinji Watanabe. "Interplay of Valence and Semimetal-to-Insulator Transitions in SmS". In: *Journal of the Physical Society of Japan* 90.2 (2021), p. 023706. DOI: 10.7566/JPSJ.90.023706.

[218] P. Per Söderlind et al. “Ground-state properties of rare-earth metals: an evaluation of density-functional theory”. In: *Journal of Physics: Condensed Matter* 26.41 (Sept. 2014), p. 416001. DOI: 10.1088/0953-8984/26/41/416001.

[219] Antoine Georges et al. “Dynamical mean-field theory of strongly correlated fermion systems and the limit of infinite dimensions”. In: *Rev. Mod. Phys.* 68 (1 Jan. 1996), pp. 13–125. DOI: 10.1103/RevModPhys.68.13.

[220] G. Kotliar et al. “Electronic structure calculations with dynamical mean-field theory”. In: *Rev. Mod. Phys.* 78 (3 Aug. 2006), pp. 865–951. DOI: 10.1103/RevModPhys.78.865.

[221] John B. Goodenough. “The two components of the crystallographic transition in VO2”. In: *Journal of Solid State Chemistry* 3.4 (1971), pp. 490–500. ISSN: 0022-4596. DOI: https://doi.org/10.1016/0022-4596(71)90091-0.

[222] W. H. Brito et al. “Metal-Insulator Transition in VO_2: A DFT + DMFT Perspective”. In: *Phys. Rev. Lett.* 117 (5 July 2016), p. 056402. DOI: 10.1103/PhysRevLett.117.056402.

[223] M. J. Rozenberg et al. “Optical Conductivity in Mott-Hubbard Systems”. In: *Phys. Rev. Lett.* 75 (1 July 1995), pp. 105–108. DOI: 10.1103/PhysRevLett.75.105.

[224] Masatoshi Imada, Atsushi Fujimori, and Yoshinori Tokura. “Metal-insulator transitions”. In: *Rev. Mod. Phys.* 70 (4 Oct. 1998), pp. 1039–1263. DOI: 10.1103/RevModPhys.70.1039.

[225] P. Limelette et al. “Universality and Critical Behavior at the Mott Transition”. In: *Science* 302.5642 (2003), pp. 89–92. DOI: 10.1126/science.1088386.

[226] Chang-Jong Kang et al. “Topological Properties and the Dynamical Crossover from Mixed-Valence to Kondo-Lattice Behavior in the Golden Phase of SmS”. In: *Phys. Rev. Lett.* 114 (16 Apr. 2015), p. 166404. DOI: 10.1103/PhysRevLett.114.166404.

[227] M. C. Payne et al. “Iterative minimization techniques for ab initio total-energy calculations - molecular-dynamics and conjugate gradients”. In: *Rev. Mod. Phys.* 64 (1992), pp. 1045–1097.

[228] S. J. Clark et al. “First principles methods using CASTEP”. In: *Z. Kristall.* 220 (2005), pp. 567–570.

[229] John P. Perdew et al. “Restoring the Density-Gradient Expansion for Exchange in Solids and Surfaces”. In: *Phys. Rev. Lett.* 100 (13 Apr. 2008), p. 136406. DOI: 10.1103/PhysRevLett.100.136406.

[230] H. J. Monkhorst and J. D. Pack. “Special points for Brillouin-zone integrations”. In: *Phys. Rev. B* 13 (1976), pp. 5188–5192.

[231] Soner Steiner et al. "Calculation of the magnetic anisotropy with projected-augmented-wave methodology and the case study of disordered $Fe_{1-x}Co_x$ alloys". In: *Phys. Rev. B* 93 (22 June 2016), p. 224425. DOI: 10.1103/PhysRevB.93.224425.

[232] J. Furthmüller G. Kresse. "Efficiency of ab-initio total energy calculations for metals and semiconductors using a plane-wave basis set". In: *Computational Materials Science* 6 (1 July 1996), pp. 15–50. DOI: https://doi.org/10.1016/0927-0256(96)00008-0.

[233] G. Kresse and J. Furthmüller. "Efficient iterative schemes for ab initio total-energy calculations using a plane-wave basis set". In: *Phys. Rev. B* 54 (16 Oct. 1996), pp. 11169–11186. DOI: 10.1103/PhysRevB.54.11169.

[234] P. E. Blöchl. "Projector augmented-wave method". In: *Phys. Rev. B* 50 (24 Dec. 1994), pp. 17953–17979. DOI: 10.1103/PhysRevB.50.17953.

[235] G. Kresse and D. Joubert. "From ultrasoft pseudopotentials to the projector augmented-wave method". In: *Phys. Rev. B* 59 (3 Jan. 1999), pp. 1758–1775. DOI: 10.1103/PhysRevB.59.1758.

[236] Helena Kurzen et al. "Electronic structure and magnetic properties of lanthanide 3+ cations". In: *Chemical Physics Letters* 574 (2013), pp. 129–132. ISSN: 0009-2614. DOI: https://doi.org/10.1016/j.cplett.2013.04.070. URL: https://www.sciencedirect.com/science/article/pii/S0009261413005848.

[237] John M. Wills et al. "Dynamical Mean Field Theory". In: *Full-Potential Electronic Structure Method: Energy and Force Calculations with Density Functional and Dynamical Mean Field Theory*. Berlin, Heidelberg: Springer Berlin Heidelberg, 2010, pp. 75–87. ISBN: 978-3-642-15144-6. DOI: 10.1007/978-3-642-15144-6_7. URL: https://doi.org/10.1007/978-3-642-15144-6_7.

[238] Evgeny Plekhanov et al. "Many-body renormalization of forces in f-electron materials". In: *Phys. Rev. B* 98 (7 Aug. 2018), p. 075129. DOI: 10.1103/PhysRevB.98.075129.

[239] Jürgen Röhler. "Chapter 71 X-ray absorption and emission spectra". In: *High Energy Spectroscopy*. Vol. 10. Handbook on the Physics and Chemistry of Rare Earths. Elsevier, 1987, pp. 453–545. DOI: https://doi.org/10.1016/S0168-1273(87)10013-X.

[240] T. Ito et al. "Electronic structure of black SmS. II. Angle-resolved photoemission spectroscopy". In: *Phys. Rev. B* 65 (15 Mar. 2002), p. 155202. DOI: 10.1103/PhysRevB.65.155202.

[241] Francis Birch. "Finite Elastic Strain of Cubic Crystals". In: *Phys. Rev.* 71 (11 June 1947), pp. 809–824. DOI: 10.1103/PhysRev.71.809.

[242] F. D. Murnaghan. "The Compressibility of Media under Extreme Pressures". In: *Proceedings of the National Academy of Sciences* 30.9 (1944), pp. 244–247. ISSN: 0027-8424. DOI: 10.1073/pnas.30.9.244.

[243] O. Vogt et al. In: *Phase Transformation of the Monochalcogenides SmX (X = S, Se, Te)*. 1995.

[244] P. Wachter. *Handbook on the Physics and Chemistry of Rare Earths*. Vol. 19. Elsevier, 1994. Chap. 132.

[245] H. Jonsson, G. Mills, and J. C. Karsten. *Nudged elastic band method for finding minimum energy paths of transitions*. World Scientific, 1998. DOI: https://doi.org/10.1142/9789812839664_0016.

[246] K. Imura et al. "Angle-resolved photoemission spectroscopy on mixed-valent $Sm_{1-x}Y_xS$". In: *Journal of the Korean Physical Society* 62 (2013), pp. 2028–2031. DOI: https://doi.org/10.3938/jkps.62.2028.

[247] T. Penney and F. Holtzberg. "Virtual Bound States and Configurational Mixing in $Sm_{1-x}Y_xS$ Alloys". In: *Phys. Rev. Lett.* 34 (6 Feb. 1975), pp. 322–325. DOI: 10.1103/PhysRevLett.34.322.

[248] G Martyna. "Nanostructured stress transduction device: Combining piezoelectric and piezoresistive functional materials to drive metal insulator transitions for fast, low power electronics". In: *ABSTRACTS OF PAPERS OF THE AMERICAN CHEMICAL SOCIETY*. Vol. 251. AMER CHEMICAL SOC 1155 16TH ST, NW, WASHINGTON, DC 20036 USA. 2016.

[249] Matthew W. Copel et al. *Piezoelectronic switch device for RF applications, US Patent No. 9472368, Application number 14529380*. 2016.

[250] H. Zhang et al. "Young's modulus of thin SmS films measured by nanoindentation and laser acoustic wave". In: *Surface and Coatings Technology* 421 (2021), p. 127428. ISSN: 0257-8972. DOI: https://doi.org/10.1016/j.surfcoat.2021.127428. URL: https://www.sciencedirect.com/science/article/pii/S0257897221006022.

[251] E. Artacho et al. "Linear-Scaling ab-initio Calculations for Large and Complex Systems". In: *physica status solidi (b)* 215.1 (1999), pp. 809–817. DOI: https://doi.org/10.1002/(SICI)1521-3951(199909)215:1<809::AID-PSSB809>3.0.CO;2-0. eprint: https://onlinelibrary.wiley.com/doi/pdf/10.1002/%28SICI%291521-3951%28199909%29215%3A1%3C809%3A%3AAID-PSSB809%3E3.0.CO%3B2-0. URL: https://onlinelibrary.wiley.com/doi/abs/10.1002/%5C%28SICI%5C%291521-3951%5C%28199909%5C%29215%5C%3A1%5C%3C809%5C%3A%5C%3AAID-PSSB809%5C%3E3.0.CO%5C%3B2-0.

[252] José M Soler et al. "The SIESTA method for *ab initio* order-N materials simulation". In: *Journal of Physics: Condensed Matter* 14.11 (Mar. 2002), pp. 2745–2779. DOI: 10.1088/0953-8984/14/11/302. URL: https://doi.org/10.1088/0953-8984/14/11/302.

[253] Javier Junquera et al. "Numerical atomic orbitals for linear-scaling calculations". In: *Phys. Rev. B* 64 (23 Nov. 2001), p. 235111. DOI: 10.1103/PhysRevB.64.235111. URL: https://link.aps.org/doi/10.1103/PhysRevB.64.235111.

[254] John Bardeen. "Surface States and Rectification at a Metal Semi-Conductor Contact". In: *Phys. Rev.* 71 (10 May 1947), pp. 717–727. DOI: 10.1103/PhysRev.71.717. URL: https://link.aps.org/doi/10.1103/PhysRev.71.717.

[255] D. Cahen and A. Kahn. "Electron Energetics at Surfaces and Interfaces: Concepts and Experiments". In: *Advanced Materials* 15.4 (2003), pp. 271–277. DOI: https://doi.org/10.1002/adma.200390065. eprint: https://onlinelibrary.wiley.com/doi/pdf/10.1002/adma.200390065. URL: https://onlinelibrary.wiley.com/doi/abs/10.1002/adma.200390065.

[256] Sayanti Samaddar et al. "Equal variations of the Fermi level and work function in graphene at the nanoscale". In: *Nanoscale* 8 (33 2016), pp. 15162–15166. DOI: 10.1039/C6NR04606A. URL: http://dx.doi.org/10.1039/C6NR04606A.

[257] J. C. Slater. "Atomic Radii in Crystals". In: *The Journal of Chemical Physics* 41.10 (1964), pp. 3199–3204. DOI: 10.1063/1.1725697. eprint: https://doi.org/10.1063/1.1725697. URL: https://doi.org/10.1063/1.1725697.

[258] Beatriz Cordero et al. "Covalent radii revisited". In: *Dalton Trans.* (21 2008), pp. 2832–2838. DOI: 10.1039/B801115J. URL: http://dx.doi.org/10.1039/B801115J.

[259] V. Monteseguro et al. "Phase stability and electronic structure of iridium metal at the megabar range". In: *Scientific Reports* 9.1 (June 2019), p. 8940. ISSN: 2045-2322. DOI: 10.1038/s41598-019-45401-x. URL: https://doi.org/10.1038/s41598-019-45401-x.

[260] Tsutomu Mashimo et al. "Effect of shear strength on Hugoniot-compression curve and the equation of state of tungsten (W)". In: *Journal of Applied Physics* 119.3 (2016), p. 035904. DOI: 10.1063/1.4939725. eprint: https://doi.org/10.1063/1.4939725. URL: https://doi.org/10.1063/1.4939725.

[261] Koichi Momma and Fujio Izumi. "*VESTA3* for three-dimensional visualization of crystal, volumetric and morphology data". In: *Journal of Applied Crystallography* 44.6 (Dec. 2011), pp. 1272–1276. DOI: 10.1107/S0021889811038970. URL: https://doi.org/10.1107/S0021889811038970.

[262] Alexander Hampel, Sophie Beck, and Claude Ederer. "Effect of charge self-consistency in DFT + DMFT calculations for complex transition metal oxides". In: *Phys. Rev. Res.* 2 (3 July 2020), p. 033088. DOI: 10.1103/PhysRevResearch.2.033088. URL: https://link.aps.org/doi/10.1103/PhysRevResearch.2.033088.

[263] Swagata Acharya et al. "Importance of charge self-consistency in first-principles description of strongly correlated systems". In: *npj Computational Materials* 7.1 (Dec. 2021), p. 208. ISSN: 2057-3960. DOI: 10.1038/s41524-021-00676-5. URL: https://doi.org/10.1038/s41524-021-00676-5.

[264] Michael J. Mehl et al. "The AFLOW Library of Crystallographic Prototypes: Part 1". In: *Computational Materials Science* 136 (2017), S1–S828. ISSN: 0927-0256. DOI: https://doi.org/10.1016/j.commatsci.2017.01.017. URL: https://www.sciencedirect.com/science/article/pii/S0927025617300241.

[265] V. M. Goldschmidt. "Die Gesetze der Krystallochemie". In: *Naturwissenschaften* 14.21 (May 1926), pp. 477–485. ISSN: 1432-1904. DOI: 10.1007/BF01507527. URL: https://doi.org/10.1007/BF01507527.

[266] Jin Young Kim et al. "High-Efficiency Perovskite Solar Cells". In: *Chemical Reviews* 120.15 (Aug. 2020), pp. 7867–7918. ISSN: 0009-2665. DOI: 10.1021/acs.chemrev.0c00107. URL: https://doi.org/10.1021/acs.chemrev.0c00107.

[267] Tanusri Saha-Dasgupta. "Double perovskites with 3d and 4d/5d transition metals: compounds with promises". In: *Materials Research Express* 7.1 (Jan. 2020), p. 014003. DOI: 10.1088/2053-1591/ab6293. URL: https://doi.org/10.1088/2053-1591/ab6293.

[268] Hanghui Chen and Andrew Millis. "Charge transfer driven emergent phenomena in oxide heterostructures". In: *Journal of Physics: Condensed Matter* 29.24 (May 2017), p. 243001. DOI: 10.1088/1361-648x/aa6efe. URL: https://doi.org/10.1088/1361-648x/aa6efe.

[269] Carla Lupo et al. "From Slater to Mott physics by epitaxially engineering electronic correlations in oxide interfaces". In: *npj Computational Materials* 7.1 (June 2021), p. 94. ISSN: 2057-3960. DOI: 10.1038/s41524-021-00563-z. URL: https://doi.org/10.1038/s41524-021-00563-z.

[270] Victor Pardo and Warren E. Pickett. "Evaluation of compensated magnetism in La_2VCuO_6: Exploration of charge states". In: *Phys. Rev. B* 84 (11 Sept. 2011), p. 115134. DOI: 10.1103/PhysRevB.84.115134. URL: https://link.aps.org/doi/10.1103/PhysRevB.84.115134.

[271] Steven R. Spurgeon et al. “Competing Pathways for Nucleation of the Double Perovskite Structure in the Epitaxial Synthesis of La2MnNiO6”. In: *Chemistry of Materials* 28.11 (June 2016), pp. 3814–3822. ISSN: 0897-4756. DOI: 10.1021/acs.chemmater.6b00829. URL: https://doi.org/10.1021/acs.chemmater.6b00829.

[272] Edoardo Fertitta et al. “Study of disorder in pulsed laser deposited double perovskite oxides by first-principle structure prediction”. In: *npj Computational Materials* 7.1 (June 2021), p. 92. ISSN: 2057-3960. DOI: 10.1038/s41524-021-00561-1. URL: https://doi.org/10.1038/s41524-021-00561-1.

[273] Artem R. Oganov and Colin W. Glass. “Crystal structure prediction using ab initio evolutionary techniques: Principles and applications”. In: *The Journal of Chemical Physics* 124.24 (2006), p. 244704. DOI: 10.1063/1.2210932. eprint: https://doi.org/10.1063/1.2210932. URL: https://doi.org/10.1063/1.2210932.

[274] Yanchao Wang et al. “Crystal structure prediction via particle-swarm optimization”. In: *Phys. Rev. B* 82 (9 Sept. 2010), p. 094116. DOI: 10.1103/PhysRevB.82.094116. URL: https://link.aps.org/doi/10.1103/PhysRevB.82.094116.

[275] Andriy O. Lyakhov et al. “New developments in evolutionary structure prediction algorithm USPEX”. In: *Computer Physics Communications* 184.4 (2013), pp. 1172–1182. ISSN: 0010-4655. DOI: https://doi.org/10.1016/j.cpc.2012.12.009. URL: https://www.sciencedirect.com/science/article/pii/S0010465512004055.

[276] Artem R. Oganov, Andriy O. Lyakhov, and Mario Valle. “How Evolutionary Crystal Structure Prediction Works—and Why”. In: *Accounts of Chemical Research* 44.3 (Mar. 2011), pp. 227–237. ISSN: 0001-4842. DOI: 10.1021/ar1001318. URL: https://doi.org/10.1021/ar1001318.

[277] Yanchao Wang et al. “CALYPSO: A method for crystal structure prediction”. In: *Computer Physics Communications* 183.10 (Oct. 2012), pp. 2063–2070. DOI: 10.1016/j.cpc.2012.05.008. arXiv: 1205.2264 [cond-mat.mtrl-sci].

[278] Felicity H. Taylor, John Buckeridge, and C. Richard A. Catlow. “Screening Divalent Metals for A- and B-Site Dopants in LaFeO3”. In: *Chemistry of Materials* 29.19 (Oct. 2017), pp. 8147–8157. ISSN: 0897-4756. DOI: 10.1021/acs.chemmater.7b01993. URL: https://doi.org/10.1021/acs.chemmater.7b01993.

[279] Felicity H. Taylor, John Buckeridge, and C. Richard A. Catlow. “Defects and Oxide Ion Migration in the Solid Oxide Fuel Cell Cathode Material LaFeO3”. In: *Chemistry of Materials* 28.22 (Nov. 2016), pp. 8210–8220. ISSN: 0897-4756. DOI: 10.1021/acs.chemmater.6b03048. URL: https://doi.org/10.1021/acs.chemmater.6b03048.

[280] Freeman J. Dyson. "The Dynamics of a Disordered Linear Chain". In: *Phys. Rev.* 92 (6 Dec. 1953), pp. 1331–1338. DOI: 10.1103/PhysRev.92.1331. URL: https://link.aps.org/doi/10.1103/PhysRev.92.1331.

[281] P. DEAN. "The Vibrational Properties of Disordered Systems: Numerical Studies". In: *Rev. Mod. Phys.* 44 (2 Apr. 1972), pp. 127–168. DOI: 10.1103/RevModPhys.44.127. URL: https://link.aps.org/doi/10.1103/RevModPhys.44.127.

[282] Andrea Dal Corso. *Welcome to Thermo_pw*. 2020. URL: https://dalcorso.github.io/thermo_pw/ (visited on 10/15/2022).

[283] W. A. Grosshans, Y. K. Vohra, and W. B. Holzapfel. "Evidence for a Soft Phonon Mode and a New Structure in Rare-Earth Metals under Pressure". In: *Phys. Rev. Lett.* 49.21 (Nov. 1982), pp. 1572–1575. DOI: 10.1103/PhysRevLett.49.1572.

[284] Lorenzo Sorace and Dante Gatteschi. "Electronic Structure and Magnetic Properties of Lanthanide Molecular Complexes". In: *Lanthanides and Actinides in Molecular Magnetism*. John Wiley & Sons, Ltd, 2015. Chap. 1, pp. 1–26. ISBN: 9783527673476. DOI: https://doi.org/10.1002/9783527673476.ch1. eprint: https://onlinelibrary.wiley.com/doi/pdf/10.1002/9783527673476.ch1. URL: https://onlinelibrary.wiley.com/doi/abs/10.1002/9783527673476.ch1.

[285] Simon G. McAdams et al. "Molecular single-ion magnets based on lanthanides and actinides: Design considerations and new advances in the context of quantum technologies". In: *Coordination Chemistry Reviews* 346 (2017). SI: 42 iccc, Brest–by invitation, pp. 216–239. ISSN: 0010-8545. DOI: https://doi.org/10.1016/j.ccr.2017.03.015. URL: https://www.sciencedirect.com/science/article/pii/S0010854517300747.

[286] Z. H. Li et al. "Phonon density of states in lanthanide-based nanocrystals". In: *Phys. Rev. B* 102 (16 Oct. 2020), p. 165409. DOI: 10.1103/PhysRevB.102.165409. URL: https://link.aps.org/doi/10.1103/PhysRevB.102.165409.

[287] Rui Shi and Anja-Verena Mudring. "Phonon-Mediated Nonradiative Relaxation in Ln3+-Doped Luminescent Nanocrystals". In: *ACS Materials Letters* 4.10 (Oct. 2022), pp. 1882–1903. DOI: 10.1021/acsmaterialslett.2c00595. URL: https://doi.org/10.1021/acsmaterialslett.2c00595.

[288] Liviu Ungur and Liviu F. Chibotaru. "Computational Modelling of the Magnetic Properties of Lanthanide Compounds". In: *Lanthanides and Actinides in Molecular Magnetism*. John Wiley & Sons, Ltd, 2015. Chap. 6, pp. 153–184. ISBN: 9783527673476. DOI: https://doi.org/10.1002/9783527673476.ch6. eprint: https://onlinelibrary.wiley.com/doi/pdf/10.1002/9783527673476.ch6. URL: https://onlinelibrary.wiley.com/doi/abs/10.1002/9783527673476.ch6.

[289] J.P. Remeika and A.M. Glass. "The growth and ferroelectric properties of high resistivity single crystals of lead titanate". In: *Materials Research Bulletin* 5.1 (1970), pp. 37–45. ISSN: 0025-5408. DOI: https://doi.org/10.1016/0025-5408(70)90071-1. URL: https://www.sciencedirect.com/science/article/pii/0025540870900711.

[290] Ioanna Pallikara et al. "The physical significance of imaginary phonon modes in crystals". In: *Electronic Structure* 4.3 (July 2022), p. 033002. DOI: 10.1088/2516-1075/ac78b3. URL: https://dx.doi.org/10.1088/2516-1075/ac78b3.

[291] J Lim et al. "Origin of the volume collapse under pressure in elemental Dy". In: *Journal of Physics: Conference Series* 500.19 (May 2014), p. 192009. DOI: 10.1088/1742-6596/500/19/192009. URL: https://dx.doi.org/10.1088/1742-6596/500/19/192009.

[292] G. Fabbris et al. "Different routes to pressure-induced volume collapse transitions in gadolinium and terbium metals". In: *Phys. Rev. B* 88 (24 Dec. 2013), p. 245103. DOI: 10.1103/PhysRevB.88.245103. URL: https://link.aps.org/doi/10.1103/PhysRevB.88.245103.

[293] Jordi Ibáñez et al. "Structural and Lattice-Dynamical Properties of Tb2O3 under Compression: A Comparative Study with Rare Earth and Related Sesquioxides". In: *Inorganic Chemistry* 59.14 (July 2020), pp. 9648–9666. ISSN: 0020-1669. DOI: 10.1021/acs.inorgchem.0c00834. URL: https://doi.org/10.1021/acs.inorgchem.0c00834.

[294] Arup Kumar Pathak and Tijo Vazhappilly. "Ab Initio Study on Structure, Elastic, and Mechanical Properties of Lanthanide Sesquioxides". In: *physica status solidi (b)* 255.6 (2018), p. 1700668. DOI: https://doi.org/10.1002/pssb.201700668. eprint: https://onlinelibrary.wiley.com/doi/pdf/10.1002/pssb.201700668. URL: https://onlinelibrary.wiley.com/doi/abs/10.1002/pssb.201700668.

[295] Olijnyk, H. and Jephcoat, A. P. "Lattice dynamics of the lanthanides: Samarium at high pressure". In: *Europhys. Lett.* 69.3 (2005), pp. 385–389. DOI: 10.1209/epl/i2004-10354-7. URL: https://doi.org/10.1209/epl/i2004-10354-7.

[296] Xiaohui Liu et al. "Crystal metamorphosis at stress extremes: how soft phonons turn into lattice defects". In: *NPG Asia Materials* 8.10 (Oct. 2016), e320–e320. ISSN: 1884-4057. DOI: 10.1038/am.2016.154. URL: https://doi.org/10.1038/am.2016.154.

[297] G.N. Sauvion and P. Ducros. "Catalysis: A growing market for rare earths". In: *Journal of the Less Common Metals* 111.1 (1985), pp. 23–35. ISSN: 0022-5088. DOI: https://doi.org/10.1016/0022-5088(85)90165-1. URL: https://www.sciencedirect.com/science/article/pii/0022508885901651.

[298] Zhiquan Hou et al. "Rare earth oxides and their supported noble metals in application of environmental catalysis". In: *Journal of Rare Earths* 38.8 (2020). Special Issue of Rare Earth Catalysis, pp. 819–839. ISSN: 1002-0721. DOI: https://doi.org/10.1016/j.jre.2020.01.011. URL: https://www.sciencedirect.com/science/article/pii/S1002072119309238.

[299] N.M. Zholobak et al. "UV-shielding property, photocatalytic activity and photocytotoxicity of ceria colloid solutions". In: *Journal of Photochemistry and Photobiology B: Biology* 102.1 (2011), pp. 32–38. ISSN: 1011-1344. DOI: https://doi.org/10.1016/j.jphotobiol.2010.09.002. URL: https://www.sciencedirect.com/science/article/pii/S1011134410002150.

[300] A.F. Diwell et al. "The Role of Ceria in Three-Way Catalysts". In: ed. by A. Crucq. Vol. 71. Studies in Surface Science and Catalysis. Elsevier, 1991, pp. 139–152. DOI: https://doi.org/10.1016/S0167-2991(08)62975-4. URL: https://www.sciencedirect.com/science/article/pii/S0167299108629754.

[301] W. Hayes and A. M. Stoneham. "Defects and defect processes in nonmetallic solids". In: 1985.

[302] Xin-Song Huang et al. "Morphology effects of nanoscale ceria on the activity of Au/CeO2 catalysts for low-temperature CO oxidation". In: *Applied Catalysis B: Environmental* 90.1 (2009), pp. 224–232. ISSN: 0926-3373. DOI: https://doi.org/10.1016/j.apcatb.2009.03.015. URL: https://www.sciencedirect.com/science/article/pii/S0926337309001039.

[303] Paolo Giannozzi et al. "QUANTUM ESPRESSO: a modular and open-source software project for quantum simulations of materials". en. In: *J Phys Condens Matter* 21.39 (Sept. 2009), p. 395502.

[304] P Giannozzi et al. "Advanced capabilities for materials modelling with Quantum ESPRESSO". en. In: *J Phys Condens Matter* 29.46 (Oct. 2017), p. 465901.

[305] John P. Perdew, Kieron Burke, and Matthias Ernzerhof. "Generalized Gradient Approximation Made Simple". In: *Phys. Rev. Lett.* 77 (18 Oct. 1996), pp. 3865–3868. DOI: 10.1103/PhysRevLett.77.3865. URL: https://link.aps.org/doi/10.1103/PhysRevLett.77.3865.

[306] M. Topsakal and R.M. Wentzcovitch. "Accurate projected augmented wave (PAW) datasets for rare-earth elements (RE=La–Lu)". In: *Computational Materials Science* 95 (2014), pp. 263–270. ISSN: 0927-0256. DOI: https://doi.org/10.1016/j.commatsci.2014.07.030. URL: https://www.sciencedirect.com/science/article/pii/S0927025614005059.

[307] Andrea Dal Corso. "Pseudopotentials periodic table: From H to Pu". In: *Computational Materials Science* 95 (2014), pp. 337–350. ISSN: 0927-0256. DOI: https://doi.org/10.1016/j.commatsci.2014.07.043. URL: https://www.sciencedirect.com/science/article/pii/S0927025614005187.

[308] Stefan Grimme. "Semiempirical GGA-type density functional constructed with a long-range dispersion correction". In: *Journal of Computational Chemistry* 27.15 (2006), pp. 1787–1799. DOI: https://doi.org/10.1002/jcc.20495. eprint: https://onlinelibrary.wiley.com/doi/pdf/10.1002/jcc.20495. URL: https://onlinelibrary.wiley.com/doi/abs/10.1002/jcc.20495.

[309] Nicola Marzari et al. "Thermal Contraction and Disordering of the Al(110) Surface". In: *Phys. Rev. Lett.* 82 (16 Apr. 1999), pp. 3296–3299. DOI: 10.1103/PhysRevLett.82.3296. URL: https://link.aps.org/doi/10.1103/PhysRevLett.82.3296.

[310] Klaus Reinhardt and Herwig Winkler. "Cerium Mischmetal, Cerium Alloys, and Cerium Compounds". In: *Ullmann's Encyclopedia of Industrial Chemistry*. John Wiley & Sons, Ltd, 2000. ISBN: 9783527306732. DOI: https://doi.org/10.1002/14356007.a06_139. eprint: https://onlinelibrary.wiley.com/doi/pdf/10.1002/14356007.a06_139. URL: https://onlinelibrary.wiley.com/doi/abs/10.1002/14356007.a06_139.

[311] S.S.P. Sultana et al. "Ceria doped mixed metal oxide nanoparticles as oxidation catalysts: Synthesis and their characterization". In: *Arabian Journal of Chemistry* 8.6 (2015), pp. 766–770. ISSN: 1878-5352. DOI: https://doi.org/10.1016/j.arabjc.2015.05.008. URL: https://www.sciencedirect.com/science/article/pii/S1878535215001446.

[312] John Njagi, Cristina Ispas, and Silvana Andreescu. "Mixed Ceria-Based Metal Oxides Biosensor for Operation in Oxygen Restrictive Environments". In: *Analytical Chemistry* 80.19 (Oct. 2008), pp. 7266–7274. ISSN: 0003-2700. DOI: 10.1021/ac800808a. URL: https://doi.org/10.1021/ac800808a.

[313] Aaron C. Johnston-Peck et al. "Nature of the Mixed-Oxide Interface in Ceria–Titania Catalysts: Clusters, Chains, and Nanoparticles". In: *The Journal of Physical Chemistry C* 117.28 (July 2013), pp. 14463–14471. ISSN: 1932-7447. DOI: 10.1021/jp3125268. URL: https://doi.org/10.1021/jp3125268.

[314] Damma Devaiah et al. "Ceria–zirconia mixed oxides: Synthetic methods and applications". In: *Catalysis Reviews* 60.2 (2018), pp. 177–277. DOI: 10.1080/01614940.2017.1415058. eprint: https://doi.org/10.1080/01614940.2017.1415058. URL: https://doi.org/10.1080/01614940.2017.1415058.

[315] S.K. Sahoo, M. Mohapatra, and S. Anand. "Absorption and emission properties of Zr-doped nanoceria synthesised by co-precipitation-hydrothermal treatment route". In: *Journal of Experimental Nanoscience* 10.13 (2015), pp. 1012–1027. DOI: 10.1080/17458080.2014.951411. eprint: https://doi.org/10.1080/17458080.2014.951411. URL: https://doi.org/10.1080/17458080.2014.951411.

[316] Noelia Guillén-Hurtado, Agustín Bueno-López, and Avelina García-García. "Catalytic performances of ceria and ceria-zirconia materials for the combustion of diesel soot under NOx/O2 and O2. Importance of the cerium precursor salt". In: *Applied Catalysis A: General* 437-438 (2012), pp. 166–172. ISSN: 0926-860X. DOI: https://doi.org/10.1016/j.apcata.2012.06.028. URL: https://www.sciencedirect.com/science/article/pii/S0926860X12003924.

[317] Aling Chen et al. "Redox properties and catalytic performance of ceria–zirconia nanorods". In: *Catal. Sci. Technol.* 5 (8 2015), pp. 4184–4192. DOI: 10.1039/C5CY00564G. URL: http://dx.doi.org/10.1039/C5CY00564G.

[318] Rafael Schmitt et al. "A review of defect structure and chemistry in ceria and its solid solutions". In: *Chem. Soc. Rev.* 49 (2 2020), pp. 554–592. DOI: 10.1039/C9CS00588A. URL: http://dx.doi.org/10.1039/C9CS00588A.

[319] Gilberto Vlaic et al. "Redox Property–Local Structure Relationships in the Rh-Loaded CeO2–ZrO2Mixed Oxides". In: *Journal of Catalysis* 182.2 (1999), pp. 378–389. ISSN: 0021-9517. DOI: https://doi.org/10.1006/jcat.1998.2335. URL: https://www.sciencedirect.com/science/article/pii/S0021951798923351.

[320] M. Gajdo š et al. "Linear optical properties in the projector-augmented wave methodology". In: *Phys. Rev. B* 73 (4 Jan. 2006), p. 045112. DOI: 10.1103/PhysRevB.73.045112. URL: https://link.aps.org/doi/10.1103/PhysRevB.73.045112.

[321] Gege Zhou et al. "Thermal stability of zirconia-doped ceria surfaces: A first-principles molecular dynamics study". In: *Applied Surface Science* 507 (2020), p. 144942. ISSN: 0169-4332. DOI: https://doi.org/10.1016/j.apsusc.2019.144942. URL: https://www.sciencedirect.com/science/article/pii/S0169433219337596.

[322] Michèle Pijolat et al. "Thermal stability of doped ceria: experiment and modelling". In: *J. Chem. Soc., Faraday Trans.* 91 (21 1995), pp. 3941–3948. DOI: 10.1039/FT9959103941. URL: http://dx.doi.org/10.1039/FT9959103941.

[323] Evan Sheridan et al. In: *Phys. Rev. B* 104 (20 Nov. 2021), p. 205120.

[324] D. Rost, F. Assaad, and N. Blümer. In: *Phys. Rev. E* 87 (5 May 2013), p. 053305.

[325] I. Rungger et al. 2020. arXiv: 1910.04735 [quant-ph].

[326] Marcelo A. Kuroda et al. “Anisotropic strain in SmSe and SmTe: Implications for electronic transport”. In: *Phys. Rev. B* 90 (24 Dec. 2014), p. 245124. DOI: 10.1103/PhysRevB.90.245124. URL: https://link.aps.org/doi/10.1103/PhysRevB.90.245124.

The middle-earth of correlations

Meandering around a single proton there lived an electron. Not a confused, Mott-transitioning, screened electron, not yet a loose, metallic, vagabond electron enamouring confused physicists with puckered brows: it was a hydrogen-atom electron, and that means comfort.

When the delicious stew of quantum mechanics was being cooked around a fire with Planck, Einstein, Rutherford, Bohr, de Briglie, Bose, Pauli, Hund, Heisenberg, Born, Schrödinger, Oppenheimer, Fermi, Dirac and an entire battalion, the hydrogen electron fascinated the world by being a fully solvable problem in quantum mechanics with the beautiful hydrogen spectrum dazzling the masses. The next step in Jacob's ladder was to extend the understanding to a few more of its brothers and its sisters hanging around and describe the physics of multi-electronic systems, and we will see many including the likes of Hartree, Fock, Kohn, Anderson, and their armies tried. But, ...

Alas, ambition is a sin.

As years went by the secret brotherhood of electronic structure scientists grew more worried. There were a few successes. The Hartree-Fock theory and the affluent Density functional theory made realistic materials accessible. The BCS theory, Landau's theory of superfluidity signalled success with quasiparticles, but each time a big secret was revealed, like the asura Raktabeej in Indian mythology, more demon heads sprung up to take its place, like when people were content with the BCS theory, someone found Type-II superconductor and all correlated hell was let loose (, and still is. But people say it is fun, and so we are okay with it!). Throughout the past century brave warriors have tried to defeat the omnipresent demon, and they were indeed immensely successful especially our DMFT cult leaders, the great Vollhardt, Metzner, Georges, Kotliar, Lichtenstein among many others, but the mystery and correlated chaos of the Pandora's box was far from being solved and understood.

Now, I don't want the reader to think that I dislike those demon heads, neither am I a pessimist because actually I am in awe (, and I think you are too, if you have reached this sentence even though with a few eye-rolls!), but this is how fantastic the mysterious world of correlated electrons is, and am a baby apprentice in this field. I have also been told that scientists don't like vague phantasmal stories, and prefer equations and graphs for a better quantitative and qualitative attack, so let me change the gear.

In the mystical land of azimuthal quantum numbers, there lived some strange electrons in the d-, and f- villages of the city of correlations ... .. .

Oh, sorry. Not again!

Couldn't stop.

Will try again. Let's go back to the second sentence of page 14. :)

. . .

Enough of Science and of Art;
Close up those barren leaves;
Come forth, and bring with you a heart
That watches and receives.

∼ The Tables Turned, William Wordsworth